UNIVERSITY OF CALIFORNIA, SAN DIEGO

Continental Rifting Across the Southern Gulf of California

A dissertation submitted in partial satisfaction of the
requirements for the degree Doctor of Philosophy
in
Earth Sciences

by

Fiona Helen Sutherland

Committee in charge:

Alistair Harding, Co-Chair
Graham Kent, Co-Chair
Joel Conte
Neal Driscoll
John Orcutt
Frank Vernon

2006

The dissertation of Fiona Helen Sutherland is approved, and it is acceptable in quality and form for publication on microfilm:

_____

_____

_____

_____

_____

Co-chair

_____

Co-chair

2006

To my family.

TABLE OF CONTENTS

LIST OF FIGURES

LIST OF TABLES

ACKNOWLEDGMENTS

I would like to thank my advisors, Alistair Harding and Graham Kent, for their help and support over the last few years. I would also like to thank John Orcutt for taking me on as a graduate student, and Frank Vernon for his supervision and help with the OSNPE project. I have to thank Neal Driscoll for his help and encouragement over the years. Despite having an ever-expanding group of his own students, he has always found time to help and advise me.

There are many other researchers in involved in the Gulf of California project: Dan Lizarralde, Paul Umhoefer, Steve Holbrook, Gary Axen, John Fletcher and Antonio Gonzalez-Fernandez, my interactions with them over the past four years were an invaluable education. I also need to mention my fellow Gulf of California gradate students, Hillary Brown and Pedro Paramo, who provided support and encourgement along the way. In particular, I would like to thank Dan Lizarralde for all his help and support, especially with the rayinvr code and gravity modeling, but also for his never-ending enthusiasm and encouragement. Paul Umhoefer and Neal Driscoll both helped me with seismic stratigraphy and lots of geology advice, helping shape the interpretations of the multi-channel seismic data. The tomographic inversions would not have been completed without a huge effort from Alistair, for which I am very grateful.

I must also thank my fellow graduate students at IGPP; I would not have survived the first year without the help of my fellow first-years in the Keller: Katie Phillips, Jasper Konter, Jeremy Bassis, Geoff Ely and Alex Hutko. I also need to thank all the IGPP graduate students, past and present, who have provided help and support over the years. The faculty at IGPP have a wide range of interests, and I am grateful for all the helpful discussions and advice they have provided.

Chaper IV, in full, is a reprint of the material as it appears in: Sutherland, F.H., Vernon, F.L., Orcutt, J.A., Collins, J.A., Stephen, R.A. Results from OSNPE: Improved Teleseismic Earthquake Detection at the Seafloor, Bulletin of

the Seismological Society of America, vol. 94, No 5, pp. 1868-1878, 2004. The dissertation author was the primary investigator and author of this paper.

VITA

1977	Born - Bromley, Kent, U.K.
2000	M.Geophys. (1st Class Honors), Geophysical Sciences University of Leeds
2000-2006	Research Assistant Scripps Institution of Oceanography University of California, San Diego
2006	Ph.D. Earth Science University of California, San Diego

PUBLICATIONS

Sutherland, F.H., F.L. Vernon, J.A. Orcutt, J.A. Collins and R.A. Stephen, 2004: Results from OSNPE: Improved Teleseismic Earthquake Detection at the Seafloor. *Bull. Seis. Soc. Am.*, **94**, No. 5 pp. 1868-1878.

Kendall, J.M., Sol, S., Thomson, C.J., White, D.J., Asudeh, I., Snell, C.S., Sutherland, F.H., 2002: Seismic Heterogeneity and Anisotropy in the Western Superior Province, Canada; Insights into the Evolution of an Archaean Craton. *Geological Society Special Publications*, **199**, pp. 27-44.

ABSTRACT OF THE DISSERTATION

Continental Rifting Across the Southern Gulf of California

by

Fiona Helen Sutherland
Doctor of Philosophy in Earth Science
University of California, San Diego, 2006
Doctor Alistair Harding, Co-chair
Doctor Graham Kent, Co-chair

This study of continental rifting in the Gulf of California has two aims: 1. To better understand the tectonic evolution of the Gulf of California, and 2. To gain insight into continental rifting processes. The combination of seismic reflection and refraction techniques provides a robust method to analyze crustal structure, allowing for the amount, style, and temporal evolution of continental extension over conjugate rifted margins to be assessed.

Multi-channel seismic data spanning 600 km image basins created by upper crustal extension. These basins appear to have formed in two phases: an initial phase beginning at or near 14 Ma, forming large basins and a second phase beginning around 6 Ma forming smaller half-grabens. There is a reflective, ropey layer seen mantling basement along much of the transect; modeling of velocity-depth profiles in the upper crust show that this layer has a velocity of 2.5 km/s and is a few hundred meters thick. This layer is interpreted as the arc-related 20-11 Ma Comondú formation, and its continuity across the Tamayo Bank and Trough suggests it was deposited either synchronous or after faulting of the Tamayo Trough. This provides compelling evidence for onset of NW-SE oriented extension in the Gulf before 11 Ma.

Refraction data spanning an 881 km profile over conjugate rifted margins between the Baja peninsula and mainland Mexico were used to construct a seismic velocity model. This model shows that the crust has experienced an overall pure shear mode of extension and, on average, has thinned to half its original thickness. Estimated total opening across the southern Gulf of California is 495 km, indicating an alternative tectonic evolution characterized by oblique NW-SE extension and dextral slip in the Gulf since ∼14 Ma. Average lower crustal velocity of ∼6.3 km/s on both margins indicates there was no large-scale magmatism during rifting, and significant Moho topography suggests brittle deformation of the whole crust and no lower crustal flow, indicating rifting of cold lithosphere. However, some magmatism is seen at the in the regions of greatest crustal thinning at the continent-ocean transition and allowed for the transition from rifting to seafloor spreading.

I

Introduction

The rifting of continental lithosphere and subsequent transition to seafloor spreading is a fundamental part of the Wilson Cycle of plate tectonics (Wilson, 1966), where crust is created at mid-ocean ridges and is assimilated back into the mantle at deep-sea trenches. It allows for large-scale plate reorganization, and the passive continental margins it creates contain large reservoirs of hydrocarbons. Consequently, a significant amount of research has been conducted on rifted continental margins over the past 30 years. The majority of these studies have looked at the rifted margins of the Atlantic and Indian Oceans, which formed as a result of the breakup of Pangea during the Jurassic and Cretaceous periods, and that seafloor spreading has now separated by thousands of kilometers. This research has provided great insight into the nature of rifted continental margins, particularly the variations in volcanism and the role of pure shear (McKenzie, 1978) and simple shear (Wernicke, 1984) during passive continental margin formation. However, conjugate margin pairs are difficult to establish given their large geographical separation (sometimes thousands of kilometers), and without the complete margin and associated geodynamical context it is challenging to fully understand rifting processes.

The bulk of this thesis concerns continental rifting within the southern

Gulf of California: I have analyzed and interpreted seismic reflection (Chapter II) and refraction (Chapter III) data across the Alarcón Basin, the southernmost basin in the Gulf of California. The refraction data span 881 km starting about 40 km southwest of Loreto on the unextended crust of the Baja peninsula, cross conjugate extended margins and oceanic crust, and finish on mainland Mexico near the city of Tepic. Tomographic inversions of this refraction data were carried out, and this work is shown in Chapter IV. Chapter V concerns work I completed earlier in my graduate career as part of the Ocean Seismic Network Pilot Experiment (OSNPE), investigating earthquake detection levels at the seafloor, and was published in 2004 (Sutherland et al., 2004). This work was motivated by the desire to create a truly global seismic network by installing broadband seismometers in the oceans.

I.1 Gulf of California

The Gulf of California is a young, highly oblique, rifted continental margin with significant differences in extensional style from north to south. The northern and central Gulf are buried under kilometers of sediment from the Colorado River and show a diffuse zone of continental deformation without recognizable oceanic seafloor spreading (Nagy and Stock, 2000; Persaud et al., 2003; Gonzalez-Fernandez et al., 2005), whereas the southern Gulf is poorly sedimented and has an active mid-oceanic ridge system (Larson, 1972). The Gulf of California plate boundary connects the East Pacific Rise mid-ocean ridge system in the south to the San Andreas transform fault in California and is characterized by short spreading centers, where extension is concentrated within discreet basins, separated by longer transform faults. A two-ship experiment with Research Vessels Maurice Ewing and New Horizon was conducted in Fall 2002 in the Gulf of California and collected marine seismic refraction and reflection data. This experiment was designed to study and compare continental rifting along the axis of the Gulf, with 2D transects oriented parallel and perpendicular to transform faults (NW-SE) across the

Guaymas Basin, and parallel to transform faults crossing the Alarcón Basin (this study) and at the northern end of the East Pacific Rise (Figure I.1a). The refraction profiles were extended onto land through the deployment of IRIS-PASSCAL seismographs on the Baja peninsula and on mainland Mexico. A cross-peninsula profile traversing the Baja Peninsula near El Cien was also collected to constrain pre-rift crustal thickness near the intersection with the Alarcón profile.

I.1.A Previous Gulf of California Research

Between 1958-1963 several scientists from Scripps Institution of Oceanography collected the first extensive bathymetry dataset in the Gulf of California using depth soundings. They were the first to see the *en echelon* fault pattern of the Gulf and interpreted these faults as tensional cracks from right-lateral movement connecting to the San Andreas Fault system to the north. They concluded that the Baja Peninsula had moved between 160 and 240 miles (260- 385 km) to the northwest, following crustal breakup, and that the tip of the peninsula had originally been located near Banderas Bay (Rusnak et al., 1964). During this period, the first seismic refraction experiment was carried out along the axis of the Gulf, and the results from that experiment led Phillips (1964) to conclude that the center of the southern Gulf was similar in structure to that of the East Pacific Rise. These results and others were published in the 1964 AAPG memoir 'Marine Geology of the Gulf of California' (van Andel and Shor, 1964). These observations predated the plate tectonic revolution, and the tectonic history was not understood until the plate reconstructions of Atwater (1970) described the demise of the Farallon plate, the rifting of continental crust, and the inland jump of the North American plate boundary, which created the Gulf of California.

Although this early research established an overall framework of the formation of the Gulf of California, many questions still remained regarding its kinematic evolution. In the southern Gulf, bathymetry and magnetic data collected

by Lonsdale (1989, 1995) show that seafloor spreading is occurring within the Alarcón Basin, the southernmost basin in the Gulf, but that there is no organized spreading in the northern Gulf, only diffuse extension. The bathymetric data also highlight extensive faulting of the surrounding continental crust. However, there has been only one seismic refraction/reflection experiment in the Gulf of California since the 1960s Phillips (1964): The Cortes Experiment conducted in 1996 (Gonzalez-Fernandez et al., 2005) crossed the northernmost Gulf, complementing additional northern Gulf reflection profiles collected by Pemex, the national Mexican oil company. In contrast, the central and southern Gulf has seen little or no modern seismic profiling; the underlying crustal structure and the true amount of extension is still unknown.

I.1.B Tectonic History

The western edge of the North American continent was a convergent margin from the Cretaceous through to the mid-Miocene. During this time, the now extinct Farallon plate was subducting beneath the North American continent and the Pacific plate was located to its west. At about 29 Ma a portion of the Pacific-Farallon spreading ridge approached the western edge of North America, stalling seafloor spreading and subduction and creating the new Pacific- North America transform plate boundary (Atwater, 1970). This transform boundary spread north and south along the western edge of North America bounded, respectively, by the Mendocino and Rivera triple junctions. Between 15-12 Ma, the Rivera triple junction migrated to the tip of what is now the Baja Peninsula leaving abandoned spreading centers and creating the dextral San Benito and Tosco-Abreojos faults just to the east of the fossil trench, traversing the continental forearc (Figure I.1). Relative Pacific-North America plate motion in northwestern Mexico was not exactly parallel to this strike-slip fault orientation, so an additional component of east-west extension was needed and accommodated in the proto-Gulf. However,

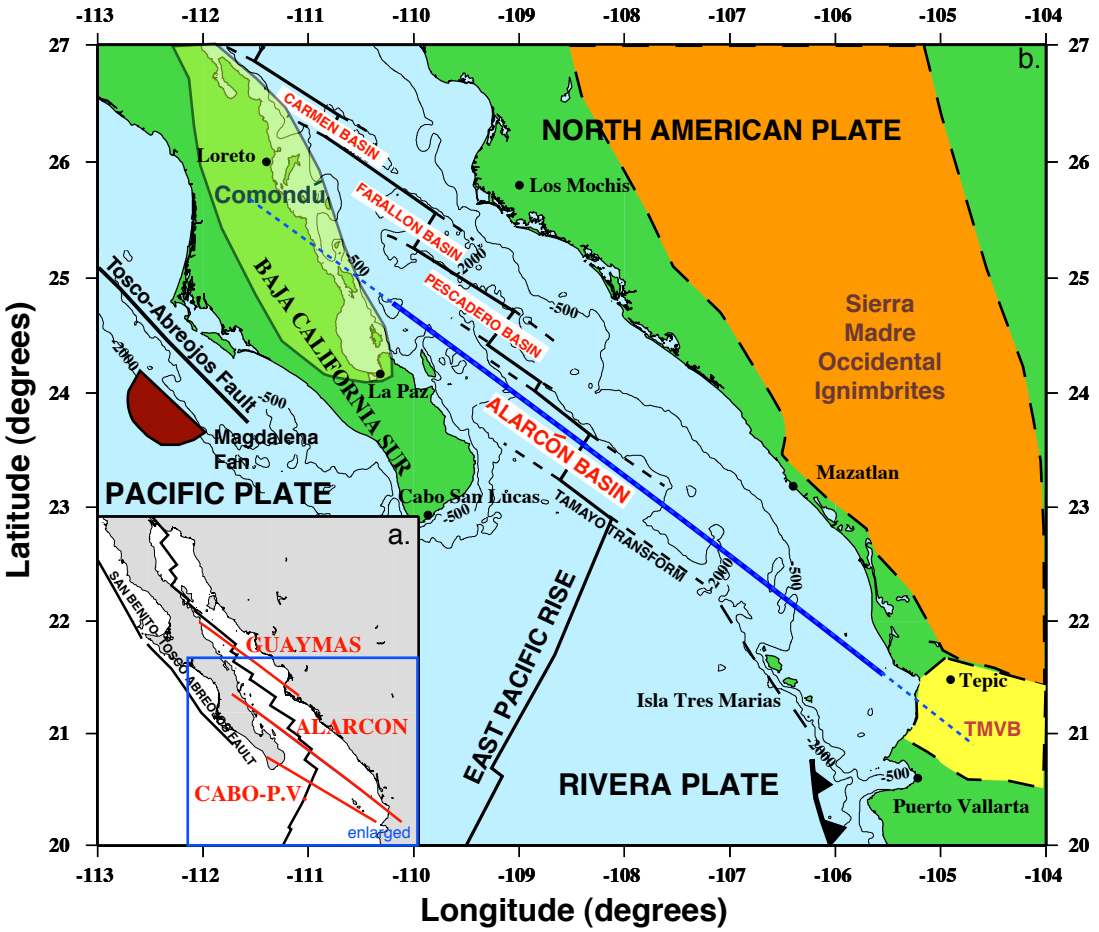

Figure I.1 Southern Gulf of California map showing major geologic and tectonic features. Inset (a) Three cross-gulf transects (Guaymas, Alarcón and Cabo- P.V.) collected in this experiment are shown in red. (b) Southern Gulf of California: the Alarcón line is shown in blue: dashed indicates entire line including refraction data, solid line shows the extent of MCS data. Major geologic provinces (Comondú Formation (light green), Sierra Madre Occidental (orange) and Trans-Mexican Volcanic Belt (TMVB) (orange)) are outlined.

the partitioning of significant slip onto the Tosco-Abreojos fault was only short-lived, and this dextral motion was ultimately accommodated ∼400 km to the east, initiating major extension in what is now the Gulf of California. Near 6 Ma, the style of rifting in the Gulf is thought to have dramatically changed from a system characterized by small amounts of orthogonal separation, to a more dextral dominated system with most of the slip that was accommodated along the Tosco-

Abreojos/ San Benito faults transferred eastward, providing a significant amount of dextral slip along the transform boundaries in the Gulf.

However, the direction, amount, and timing of extension in the Gulf and, consequently, the amount of slip on the Tosco-Abreojos fault are still unresolved. Movement on the Tosco-Abreojos fault is estimated by the displacement of the Magdalena Fan: this thick sedimentary sequence formed before the onset of formation of the Gulf of California and is bounded by the Tosco-Abreojos fault (Spencer and Normark, 1979), hence it is a clear indicator of the amount of slip on that fault. The traditional model of Gulf of California evolution (Figure I.2.1) places ∼300 km slip on the Tosco-Abreojos fault system between 12- 6 Ma, synchronous with only small amounts of E-W oriented extension in the region of the Gulf of California. At 6 Ma, strike-slip motion is thought to have jumped onto transform faults in the Gulf, initiating oblique extension. The main evidence supporting this model is the translation of the Magdalena Fan from its proposed original location at the mouth of the Gulf to its current position (Yeats and Haq, 1981) (Figure I.1b), and the careful matching of the San Felipe Tuff, which is now split between coastlines, in the northern Gulf by Oskin and Stock (2003b), showing ∼300 km extension since 6 Ma with very little preceding extension. The total requirement of dextral slip between the Pacific and North American plates since 12 Ma is around 600 km (Stock and Hodges, 1989), and this can be accommodated in more than one way. An alternative model for Gulf of California tectonic evolution (Figure I.2.2) puts less motion on the Tosco-Abreojos fault and envisions oblique extension in the Gulf since ∼12 Ma (Gans, 1997). A smaller amount of slip on the faults west of Baja is supported by dating of zircons from the Magdalena Fan, placing its source only ∼100 km south of its current location (Fletcher et al., 2006). Hence, to accommodate 600 km total dextral slip, 500 km dextral slip and NW-SE oriented extension must have occurred in the Gulf. It is known that there has been 300 km since 6 Ma (Oskin and Stock, 2003b). Consequently, for the alternative tectonic

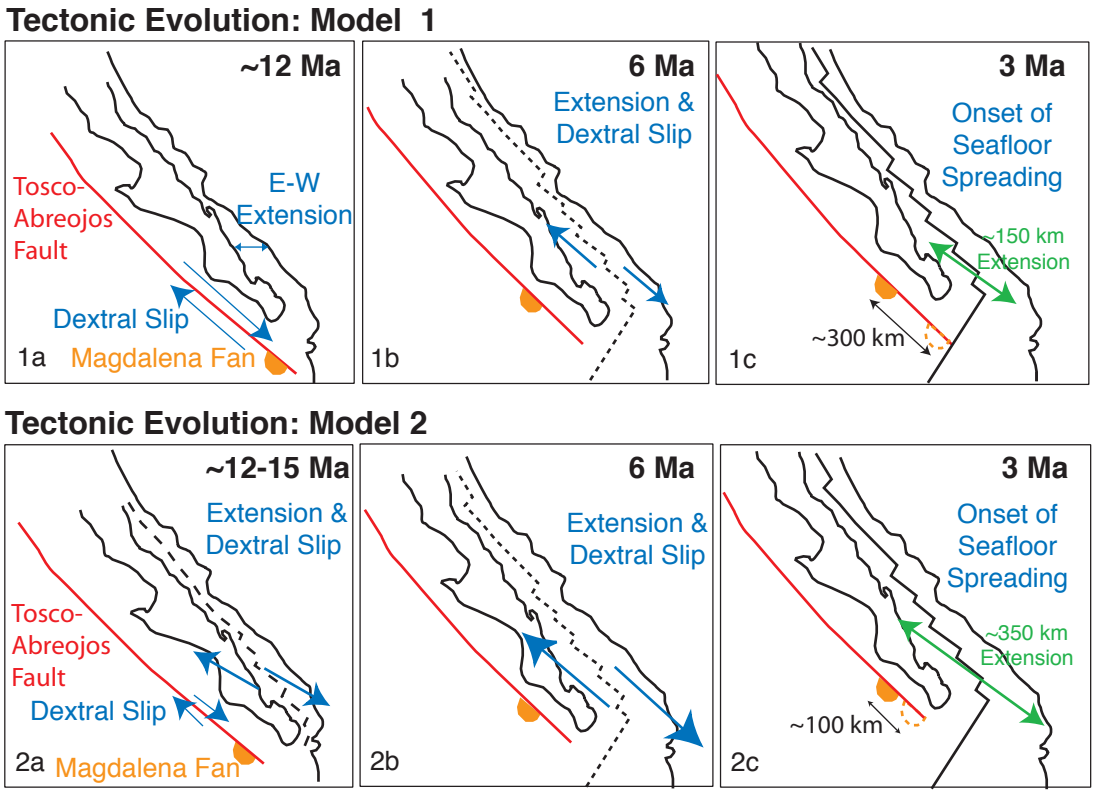

Figure I.2 Two models for the tectonic evolution of the Gulf of California. Tectonic model 1 is the traditional model, where there was limited east-west extension between 12-6 Ma in the Gulf region and 300 km slip on the Tosco-Abreojos fault. At 6 Ma the strike-slip motion jumped inboard initiating oblique extension. In this model there is ~150 km extension in the Gulf before seafloor spreading. Tectonic model 2 has oblique extension beginning at 12 Ma, with no 2 stage extension and ~350 km extension in the Gulf before seafloor spreading. In the two-stage model the original position of the land that now comprises the Baja Peninsula was further north than in the initial oblique rifting model.

model to be viable there must have been an additional 200 km NW-SE extension and dextral slip during 12- 6 Ma time-frame. This extra 200 km of extension is not observed within the marine basins of the central and northern Gulf, and is likely located further east (Gans, 1997).

I.1.C Volcanism

The geological history of Baja California and western Mexico has been dominated by volcanism associated with the subduction of the Farallon plate beneath North America. The oldest outcrops on the Baja Peninsula are the Cretaceous Peninsula Ranges batholith, emplaced from 26^o - 32^o N, and a smaller late Cretaceous batholith, which outcrops at the cape of the Baja Peninsula and also near Puerto Vallarta on mainland Mexico (Gastil et al., 1978). During the early Cenozoic, compression far inland from the trench prompted the start of the Laramide orogeny. In the Oligocene this compression changed to extension, prompting the initiation of Basin and Range extension (Dickinson and Snyder, 1978), which extended from western Mexico up to southern Oregon and Idaho. Beneath Mexico, a possible asthenospheric window opened up initiating the eruption of the Sierra Madre Occidental (SMO) ignimbrites, which were erupted on mainland Mexico from 21^o S northwards past the United States-Mexico border. This event produced one of the largest silicic igneous provinces on Earth (Ferrari et al., 2002). The southern SMO saw two large ignimbrite pulses, first in the mid-Oligocene (31.5-28 Ma) and then moving further west in the early Miocene (23.5-20 Ma) (Ferrari et al., 2002). Across Baja California Sur an unconformity separates older sandstones and Cretaceous granites from the Miocene volcanoclastic sequences. The base of this volcano-clastic sequence, the La Paz formation, is dated to 20-21 Ma (Umhoefer et al., 2001) and corresponds to the distal facies of the last SMO ignimbrite flare-up seen on mainland Mexico (Ferrari et al., 2002).

Around 19 Ma the volcanic arc completed its westward migration, and the early-mid Miocene calc-alkaline Comondú group was emplaced along the eastern edge of what is now the Baja Peninsula (Hausback, 1984). The Comondú arc remained active until arc volcanism ceased near 11 Ma. Post-subduction volcanism on the Baja Peninsula is less extensive, and is found north of 25^oN. Many of the Comondú outcrops around the Sierra Gigántica and north of La Paz are

capped by 10 Ma basalts, and basalt flows are also observed within the Comondú formation (Gastil et al., 1979). There are also recent volcanoes, such as the Tres Virgenes- Reforma caldera (Portugal et al., 2000) and the Pliocene- Quaternary Cerro Mencenares volcano located 30 km north of Loreto (Bigioggero et al., 1995) Ongoing subduction of the Rivera Plate beneath Mexico is producing volcanism in the Trans-Mexican Volcanic Belt (TMVB), which runs east-west starting near Tepic (Figures I.1, I.4). In this area there is also significant normal faulting from the extension across the Gulf of California, seen in two episodes, 9-12 Ma and 3.5-5.5 Ma (Ferrari and Rosas-Elguera, 1999).

I.1.D Geology

Insight into the geology of the submarine extended continental crust comes from Baja's numerous offshore islands. The Islas Coronados, Carmen and Monseratt located around 26^oN have a Miocene Comondú basement overlain by Pliocene marine sediments that have experienced late Pliocene- Quaternary uplift (Backus et al., 2005; Johnson et al., 2005). Isla Carmen has been mapped extensively by Dorsey et al. (2001), who found subsidence occurred rapidly between 4-8 Ma, with one unit dated at 3.1-3.5 Ma that was deposited in approximately 500 m water depth. Subsequent rapid uplift has placed Quaternary limestones 20 m above sea level. Located at 25^oN, Isla San Jose (Figure I.3) experienced normal faulting and subsidence, with older syn-rift deposits (Schwennicke et al., 2005). It has been uplifted in the past 3 Ma and there is no active faulting.

Quaternary uplift is being experienced along the Baja Peninsula, and further north in California (Ortlieb, 1991), but the exact cause is unclear. Offshore of La Paz, Isla Espiritu de Santo (Figure I.3) has a granitic basement overlain by Comondú andesite flows and tuff, indicating close proximity to the volcanic arc (Hausback, 1984). Isla Cerralvo (Figure I.3) is the southernmost island along the eastern coast of the Baja Peninsula. The island has a Cretaceous granitic basement

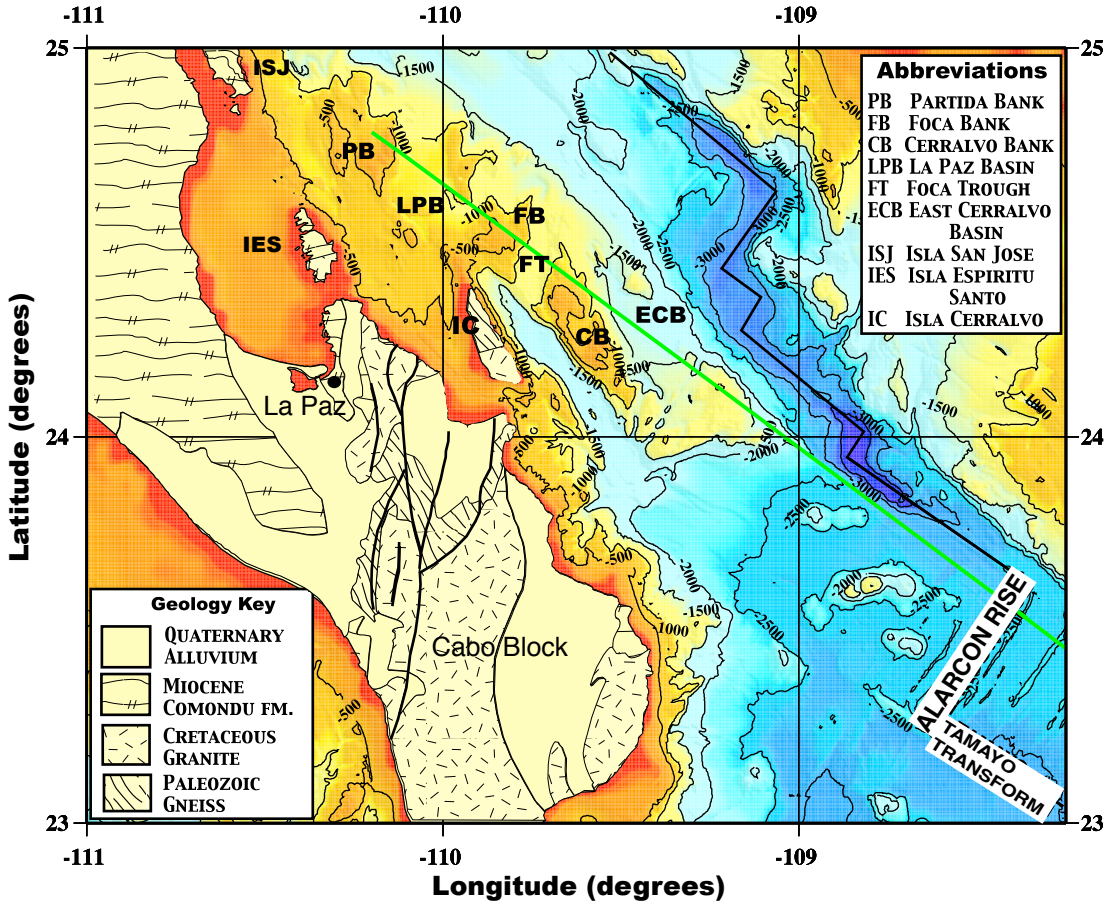

Figure I.3 Northwestern (Baja) margin bathymetry and geology. Location of MCS data shown in green, the northwestern-most point of which corresponds to 170 km along transect (refraction data not shown here continues onto the Baja Peninsula). Bathymetry data is a combination of satellite data (Smith and Sandwell, 1997) and high resolution multi-beam data supplied by P. Lonsdale: simplified geology of the Baja peninsula by P. Umhoefer (*pers. comm.*)

of similar age to the western Cabo block (90-120 Ma), and is highly metamorphosed indicating it has been exhumed from depth (Grove et al., 2005). The Cabo block itself is in two distinct parts: the older western half dates from 90-120 Ma and has experienced about 4 km exhumation, whilst the eastern half is younger than 90 Ma and does not seem to have experienced much tectonic uplift (Fletcher et al., 2000).

The Islas Tres Marías, at the mouth of the Gulf between 21^o and 22^{o}N (Figure I.4), are the only islands on the eastern conjugate margin. Following the

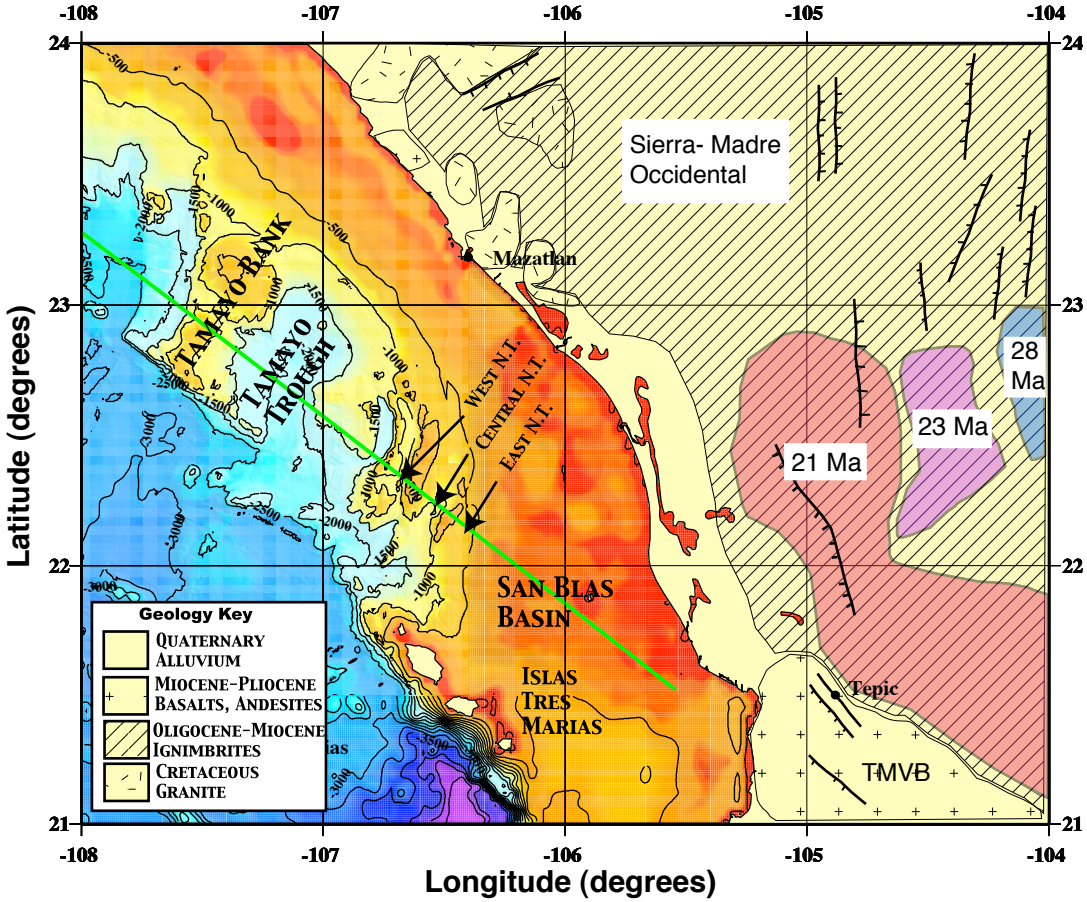

Figure I.4 Southeastern (Mainland Mexico) margin bathymetry and geology. The MCS transect is shown in green. Bathymetry data is a combination of satellite data (Smith and Sandwell, 1997) and high resolution multi-beam data supplied by P. Lonsdale. Simplified geology interpreted from INEGI maps and Ferrari et al. (2002). SMO, Sierra Madre Occidental, with dated ignimbrites flares outlined; TMVB, Trans-Mexican Volcanic Belt.

study of McCloy et al. (1988), Maria Madre Island, the largest of the Islas Tres Marías has the oldest known Neogene sedimentary sequence in the southern Gulf of California. The island has a Cretaceous granite basement and possibly some Tertiary andesites and rhyolites. Subsidence began 8.2 Ma allowing the deposition of Miocene non-marine to shallow marine sandstones. Continued subsidence into deeper depositional environments in the upper Miocene produced diatomites, mudstones and siltstones. In the lower Pliocene, the area was still in about 1 km water depth and sandstones and siltstones were laid down until uplift began in

the late Pliocene. The total sedimentary sequence is about 1145 m thick. The first marine incursion into the Gulf was in the mid-Miocene (11-14 Ma), indicated by the presence of marine fossils in the southern and central Gulf (McDougall, 2006). A second marine incursion in the southern Gulf is also seen ∼8 Ma (McCloy et al., 1988), but in the northern Gulf the youngest marine sediments date to latest Miocene- early Pliocene, indicating marine incursion around 6 Ma (Oskin and Stock, 2003a).

I.2 Active Source Seismology

Active source seismology provides an efficient and robust method to study the Earth's crust. Although, in theory, earthquake data can be used to image the crust, there is no control over the location or temporal distribution of the earthquakes (sources). This may mean years to collect a dataset, and that dataset may be biased by one active region producing the majority of the sources, with other areas sparsely sampled. In addition, the exact earthquake location is difficult to decipher, leading to uncertainties in source-receiver paths. In contrast, an active seismic source produced, for example, by airguns, provides rapid data collection, and the exact position of each source is measured by a global positioning system (GPS), providing excellent knowledge of source-receiver paths. Data can also be collected in any region, seismically active or not. There are two complimentary methods in active source seismology: reflection, or multi-channel seismic (MCS) data collection, which images the upper crust in great detail, and refraction, or wide-angle data, which images the whole crust down to the upper mantle at a lower resolution.

MCS data provide key information about sedimentary basins and upper crustal structure. These data are collected using a research vessel equipped with a streamer of hydrophones (receivers) which is towed behind the ship. The air-gun array, which is also towed by the same ship, is tuned to provide an impulsive source

with little or no ringing, allowing greater temporal resolution within sedimentary and volcanic sequences. When the seismic wavefield reaches an impedance contrast (a change in velocity and/or density) within the crust, some of the energy is reflected back and is recorded by the array of hydrophones. These impedance contrasts are typically the seafloor, sedimentary layers, and the sediment/basement interface. We may also see internal structure within the basement, and Moho reflections are often observed some ∼6.0 km or deeper below the seafloor.

To collect wide-angle data the seismometers need to be located far from the source (energy can be recorded 100 km or more from the ship). In marine settings, ocean-bottom seismometers (OBS) are deployed at regularly spaced intervals along a line (for a 2D experiment) by dropping them from the ship, before airguns are used as a seismic source and are fired along the same transect. OBS are constructed with an acoustic release mechanism that allow them to release their anchor so they can float to the surface and be retrieved at the end of the experiment. Refraction data provide travel-time curves that indicate the velocity of the material sampled by each source-receiver path. This information about the velocity of the crust and depth to Moho allow for a model of crustal structure to be formed.

I.3 Continental Rifting

Many rifted margins around the globe have been studied in great detail, especially those of the Atlantic Ocean (e.g. Holbrook et al. (1994); Chian and Louden (1994); Kelemen and Holbrook (1995); Whitmarsh et al. (1996); Manatschal and Bernoulli (1999); Korenaga et al. (2000); Funck et al. (2003); Perez-Gussinye et al. (2003)), Red Sea/ Gulf of Aden (e.g. Bonatti (1985); Bohannon et al. (1989); Fournier et al. (2004)), the East African Rift system (e.g. McKenzie et al. (1970); Moore and Davidson (1978); Ebinger (1989); Mackenzie et al. (2005); Kendall et al. (2005)), the Indian Ocean (e.g. Mutter and Larson (1989);

Driscoll and Karner (1998); Chand and Subrahmanyam (2003); Henstock and Minshull (2004)), the South China Sea (e.g. Westaway (1994); Clift et al. (2002)) and the Woodlark Basin (e.g. Taylor et al. (1995, 1999); Abers et al. (2002)). These studies, along with theoretical, analog and numerical models have yielded a huge amount of information and ideas concerning the causes and styles of deformation observed at rifted continental margins. The major parameters that affect the deformation of continental lithosphere and the amount of magmatism are believed to be crustal thickness, rheology, temperature and strain rate. However, in many previously studied rifted margins, rifting occurs within ancient terrain, and some of these parameters are difficult to decipher today. Studying a recent rifted system, like the Gulf of California, promises to bring new insights and clarity to the process of rifting continental lithosphere.

The amount of stretching varies across a margin, typically increasing toward the continent-ocean transition, but overall the average stretching factor is usually stated, as a gauge of the total extension created by rifting. The degree of crustal extension is usually measured with the stretching factor, β. The continental crust of a margin before extension has a width, x, and a thickness, z. After extension the width increases to ($x^*\beta$), and consequently the crustal thickness decreases to (z/β).

An assessment of symmetry in conjugate rifted margins was the first major characteristic used to classify rifting style. Pure shear (McKenzie, 1978) is ductile stretching of the crust producing a symmetric margin. Simple shear (Wernicke, 1984) emphasizes brittle deformation and achieves rifting by a large low-angle detachment fault extending through the lithosphere in an upper and lower plate, producing an asymmetric margin. The upper plate margin will consist of faulted upper crustal rocks, while the conjugate lower plate margin will have mid-lower crustal rocks exposed at the surface. The purely kinematic models of pure shear and simple shear are too simple to describe all the processes at work

during continental rifting but the notion of symmetric and asymmetric rifting is a useful way of describing rifted margins and dynamical models.

Analog models of rifting suggest that a more common scenario is a combination of both: pure shear occurs on a lithospheric scale, as crust thins due to passive rifting, and mantle material upwells to fill the space. However, on a smaller scale the deformation may be asymmetric with varying sizes and styles of faulting in the upper crust (Brun and Beslier, 1996). Recent work with numerical modeling has shown that the degree of symmetry may differ between the upper crust and lithospheric mantle, with upper crustal asymmetry being accompanied by mantle symmetry (Huismans and Beaumont, 2002). A strong control on symmetry is the degree of strain softening that occurs during rifting (Huismans and Beaumont, 2002, 2003). If rifting occurs quickly, the dominant rheology produces ductile deformation, and the margins are symmetric. During slower rifting, strain softening of the upper crust provides a positive feedback of increasing strain in areas already weakened, thereby enhancing asymmetry. Symmetric margins appear to be produced mostly by models with strongly coupled crust and mantle lithosphere, lacking a weak lower crustal layer. Moreover, during rifting the strength of the crust or the velocity of rifting must dominate the process to produce symmetry (Huismans and Beaumont, 2003).

Another classification of rifted margins is width: Buck (1991) described three types of rift: narrow, wide and core complex, and the width of the rifted margins is largely controlled by temperature, strain rate and crustal thickness. A narrow rift has a focused zone of extension $\leq$100 km (e.g. East African Rift), is thought to result from higher strain with a thicker crust and low heat flow. A cold, thick brittle layer is significantly weakened by one fault and extension is concentrated into a narrow region by strain softening. Narrow rifting appears to occur most commonly and is also observed by moderate extension of average lithosphere (Buck, 1991). Wide rifts, with areas of upper crustal faulting up to

1000 km wide (e.g. Basin and Range), are consequently thought to be the result of lower strain rates, higher heat flow and weaker lithosphere. With low strain rates the rising lithosphere has time to cool, strengthening the rifting area and causing deformation to migrate to a new weak zone. A warmer and weaker lithosphere has only a thin brittle layer, so the affects of faulting are not as severe on overall lithospheric strength and extension is less concentrated. It is debated whether the core complex mode is a third style of extension or a local effect that can occur within a wide rift (Brun, 1999). This mode of extension is highly asymmetric and occurs in very hot, weak lithosphere where there is also a high strain over a narrowly confined region. Extension produces significant lower crustal flow that subsequently smoothes out any changes in Moho topography created by extension and high grade metamorphic mid-lower crustal rocks are often exposed at the surface. However, the exhumation of mid-lower crustal rocks is not dependent on this core complex mode of extension, at the Iberian margin it is thought to have been the result of connecting crust and mantle shear zones in regions of high stretching (Brun and Beslier, 1996).

Magmatism is another important factor used to classify rifting; Buck (2004) states that ten times the tectonic force is required to rift continental lithosphere without magmatism than with it, due to the weakening effects magmatic intrusions have on the crust. A synthesis of current available data estimates that up to 90% of rifted margins globally are volcanic (Menzies et al., 2002). Indicators of volcanic rifted margins include seaward dipping reflector sequences (SDRS) seen in multi-channel seismic data, upper crustal dikes, fast crustal velocities and observed volcanism (e.g. Mutter et al. (1982); Funck et al. (2003); Holbrook and Kelemen (1993); Holbrook et al. (2001); Nielsen et al. (2002)). There is also evidence from subsidence: a volcanic margin will experience initial uplift from increased temperature and then undergo long-term thermal subsidence, whereas a non-volcanic margin will experience large amounts of subsidence during rifting along with faults

rather than dikes in the upper crust (Buck, 2004). Classifying a margin as volcanic is easy if SDRS are observed, but classification as completely non-volcanic is difficult: crustal structure derived from wide-angle refraction data has limited resolution, especially in the lower crust, and it is unlikely that small intrusions in the lower crust would produce notable travel-time anomalies. As crust is thinned, mantle material upwells in response and, partial melting of the upwelling mantle occurs due to decompression. The volume of partial melt depends on mantle temperature, thus a hotter mantle will produce greater volumes of partial melt. Strain rate is also important: if rifting is slow the upwelling mantle has time to cool and little or no partial melt is produced. However, if rifting is fast enough there is no time for conductive cooling, hence mantle material remains hot close to the surface, which is more likely to produce volcanism. The degree of magmatism is also dependent on the amount of stretching, as greater degrees of extension cause melt to rise higher, thus causing greater volumes of decompression melting (Pedersen and Ro, 1992).

II

Mid-Miocene to early Pliocene NW-SE upper crustal extension across conjugate margins in the southern Gulf of California

II.1 Abstract

A multi-channel seismic (MCS) profile spanning 600 km across conjugate rifted margins in the southern Gulf of California provides insight into the spatial and temporal evolution of extension during the rifting of the Baja peninsula away from mainland Mexico. Stratigraphic analysis of multiple rifted basins within the Alarcón spreading corridor indicates an initial stage of extension starting near or after 14 Ma. This initial phase is characterized by the formation of several large, widely distributed basins that show little or no syn-rift sedimentation. Following the large-scale faulting of each basin, extension was likely accommodated by small-scale faulting which offsets basement within these basins. This initial phase of rifting was then followed by a second phase of extension, likely synchronous with

basin opening in the central and northern Gulf of California beginning at or near 6 Ma. This latter phase of extension is characterized by the formation of smaller half-grabens spread throughout both conjugate margins, with a syn-rift record of sedimentary deposition. The Alarcón Basin, which modeling of magnetic anomalies indicates started robust seafloor spreadingat 2.5 Ma along this profile, shows only recent post-rift sediment drape, although the style of extension is similar to that seen in the older basins.

A ropey layer imaged in the MCS profile, interpreted to have a volcanic origin, is observed mantling basement along the majority of the seismic profile and can be used to help constrain the timing of initial rifting. The results of velocity-depth modeling of common midpoint (CMP) supergathers, reveal that this layer is a few hundred meters thick and has a relatively low velocity of around 2.5 km/s, which is consistent with a volcano-clastic origin. Beneath this layer, the velocity increases to around 4 km/s in the upper crust. This likely volcano-clastic layer is continuous over the Tamayo Bank and down into the bottom of the Tamayo Trough, and hence seems to be either synchronous or post-dates the formation of the Tamayo Trough. This volcanic layer conceals the total amount of upper crustal extension imaged along faults, but its age and origin will provide evidence for the earliest possible onset of NW-SE extension in the Gulf of California. This layer is interpreted to be the 20-11 Ma Comondú formation. The 11 Ma youngest age of Comondú deposits and the estimated ∼11 Ma age and the NW-SE orientation of the Tamayo bank and trough, along with multiple basins estimated to have formed significantly earlier than 6 Ma, suggest an alternative tectonic history for the Gulf of California, with dextral slip and NW-SE extension in the Gulf beginning at the onset of Gulf of California rifting. The continuity of the volcano-clastic stratigraphy and velocity structure across both conjugate margins, combined with equivalent amounts of observed extension, indicates an essentially symmetric, pure-shear mode of extension for the southern Gulf of California.

II.2 Introduction

The richness of the geological information on the Baja peninsula and on mainland Mexico, along with the analysis of seismic sequence stratigraphy within the Gulf will produce a first-order interpretation of our MCS data and the evolution of the southern Gulf of California across the Alarcón transect. Extension in the upper crust is most noticeably accommodated by faulting in this brittle layer, and multi-channel seismic (MCS) profiling provides an excellent technique for imaging layered sediments and faulted basement, allowing for basin analysis. The lack of drilling constraints in the southern Gulf of California, however, impedes any straightforward correlation between the seismic profile-derived structure and the exact timing of rift initiation and evolution. Nonetheless, there has been a significant amount of research into the geology of Baja California and mainland Mexico, which provides insight into submarine geology. The extensive volcanism and tectonic history of western North America in this area has also been detailed by many authors (e.g. Gastil et al. (1979); Hausback (1984); Gans (1997); Ferrari and Rosas-Elguera (1999); Dorsey and Kidwell (1999)).

II.3 Multi-channel Seismic Data

Multi-channel seismic data for the Alarcón profile span the middle 600 km of the 881 km total profile length (Figure II.1), which incorporates the wide-angle refraction data from the land-based IRIS-PASSCAL and ocean-bottom seismographs (Chapter III). The most northwestern location of MCS data is at 167 km along the 881 km transect, and continues to 767 km (Figure II.1). Data were collected by the R/V Maurice Ewing using a 480-channel 6-km-long streamer with 12.5 m receiver groups, recording energy from a 7860 in.^{3} tuned 20 airgun array. Data were collected in three separate profiles, shot west-east. Data northwest of the Alarcón Rise was collected at 50 m shot-spacing (Figure II.1), yielding 60-fold

data with 6.25 m CMP spacing. Due to problems at sea, the two profiles south of the Alarcón Rise were shot at a lower repetition rate, 150 m shot spacing, which is better suited to refraction profiling as recorded by both the ocean-bottom and PASSCAL seismographs. This lower shot rate could have reduced fold to 20, but CMP spacing was doubled to 12.5 m, yielding 40 fold data. This reduction in data density prevented the use of several processing techniques to improve image quality, such as f-k demultiple techniques, which would have greatly improved imaging beneath the shallow marine shelf across the San Blas basin. Velocity analysis using semblance was carried out every 150-250 CMP's for the 50 m shot-spacing data, and every 100 CMP's on the 150 m shot-spacing data. The data were filtered using a trapezoidal bandpass filter 15-40 Hz, normal move-out was applied and the data were stacked. Post-stack time migration was followed by gain correction. Clear images of the basement and sedimentary structures were produced, but no lower crustal or Moho reflections were observed.

II.3.A Northwestern Margin

The northwestern MCS transect spans 230 km between the Partida Bank (170 km along transect) and the Alarcón Rise (400 km along transect) (Figures II.1, II.2). We image two major basins on the extended continental crust of this margin, the La Paz Basin and the East Cerralvo Basin, before the continent-ocean transition and change to oceanic crust in the Alarcón Basin. The topography of the extended continental terrain is hummocky with multiple highs and basins, both of which are poorly sedimented, the result of the arid climate of Baja California Sur where most sediment supply is storm run-off, trapped in basins close to the peninsula (Nava-Sanchez et al., 2001). The northwestern-most basin imaged by these data is a deeper part of the La Paz Basin, located 185 km along the Alarcón transect (Figure II.3). This basin has a simple structure, with a bounding normal fault northwest providing down-to-the-southeast motion. Maximum sediment

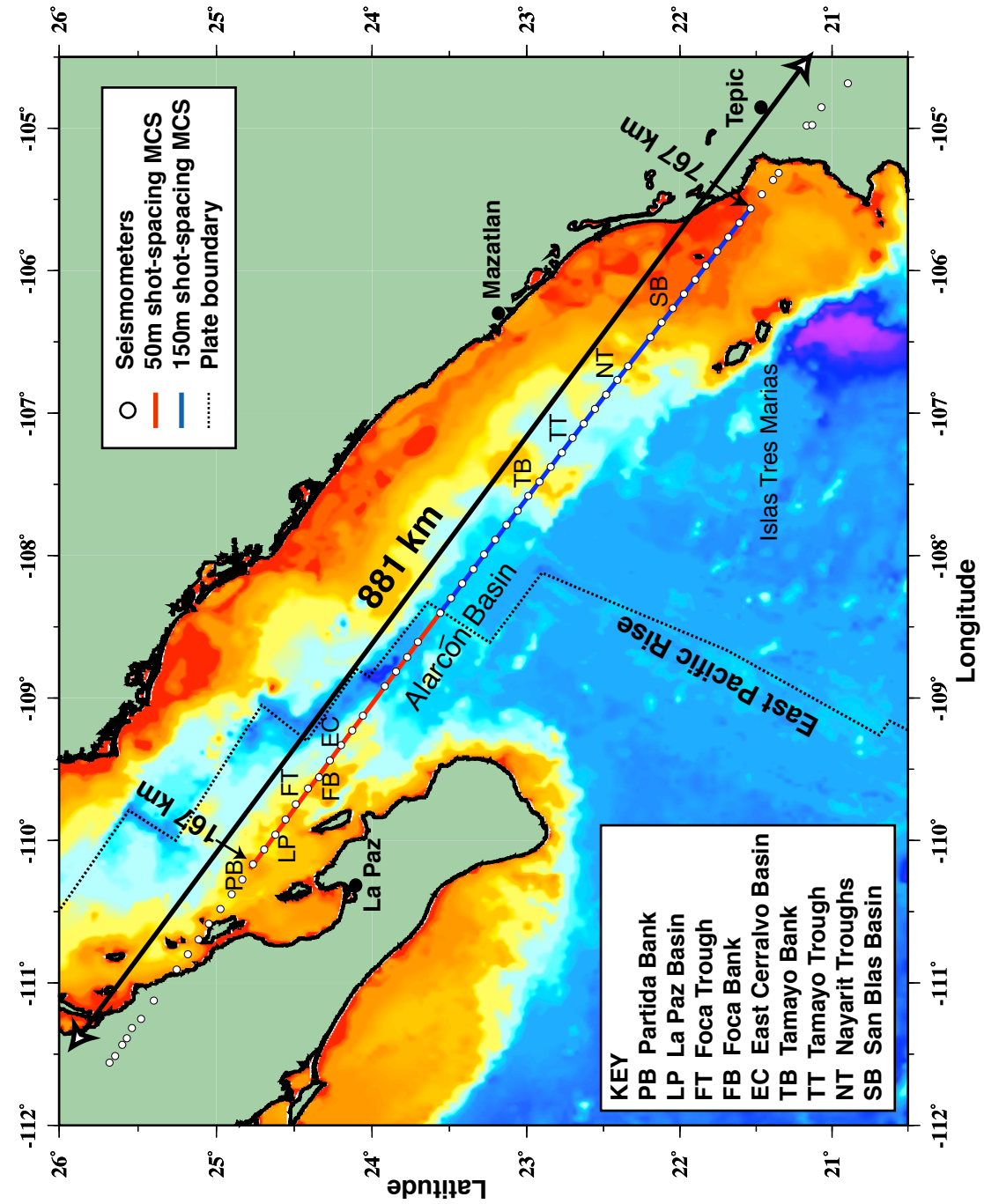

Figure II.1 Map showing location of Alarcón transect and the major basins long it.

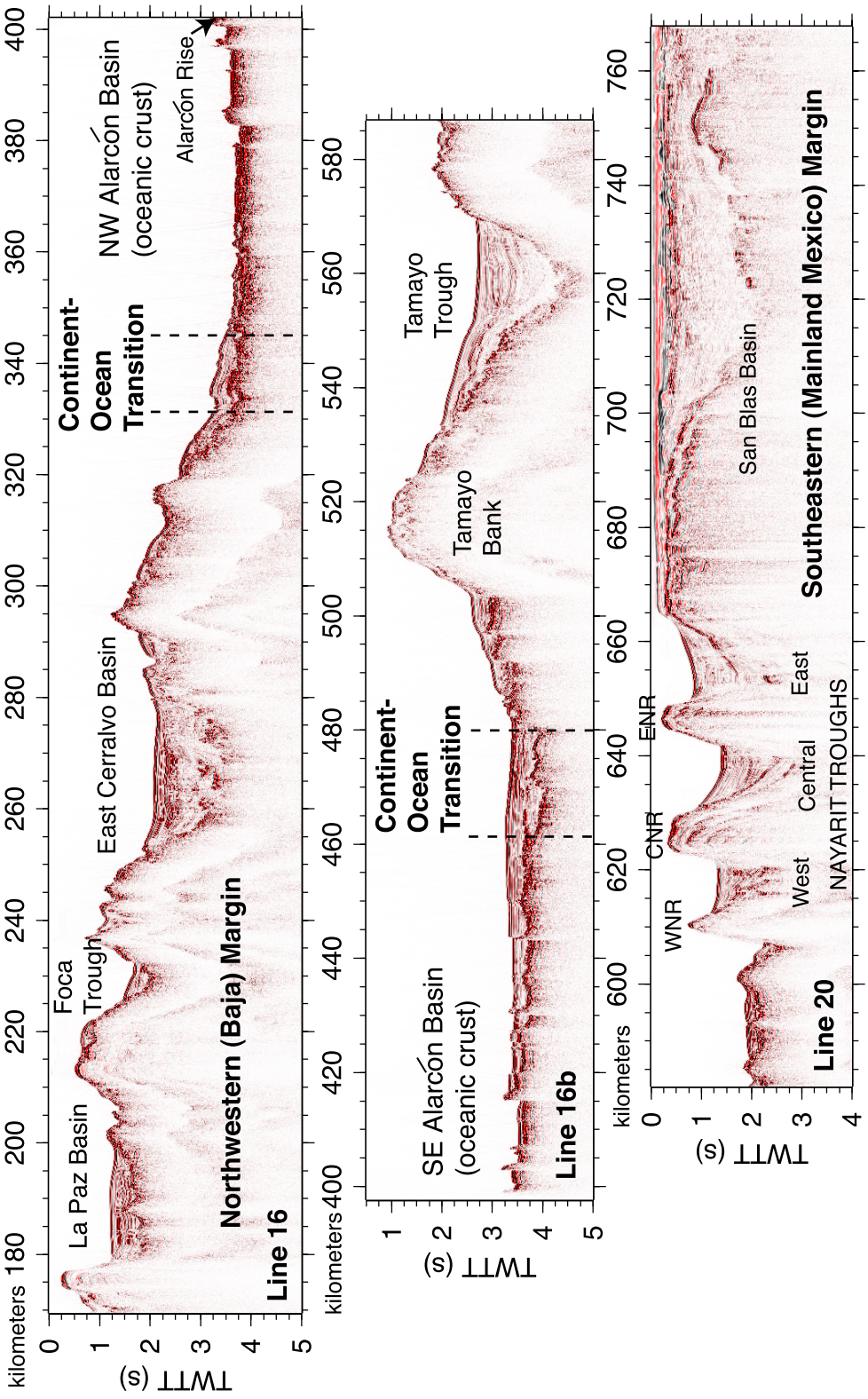

Figure II.2 Migrated multi-channel seismic (MCS) data in two-way travel time (TWTT). Location shown in Figure II.1.

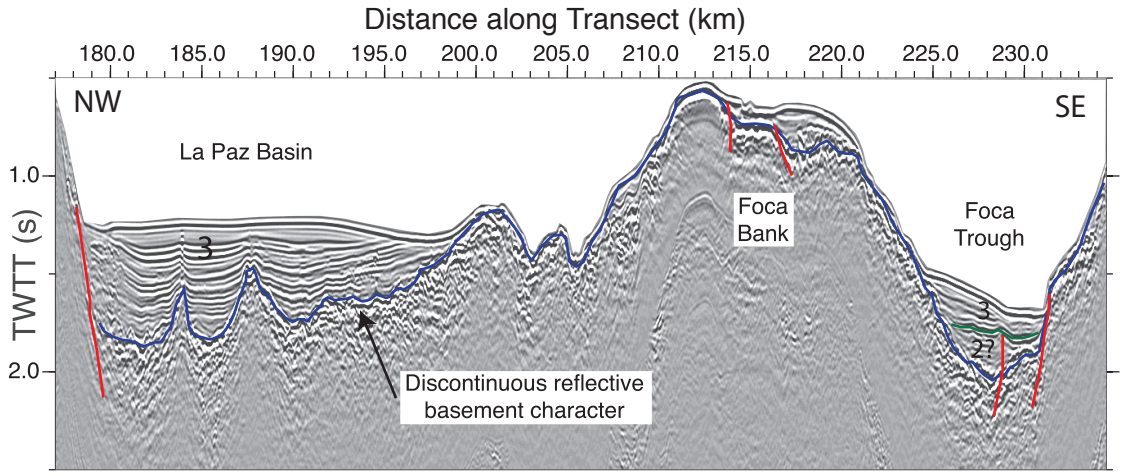

Figure II.3 La Paz Basin and Foca Trough. Basement is indicated by blue, with faults shown in red. The basement of the La Paz Basin shows topography, possibly related to its volcanic character; sediments are post-rift. The Foca Bank shows some small-scale faulting and the Foca Trough may have a small lower syn-rift sedimentary sequence (indicated in green).

thickness is 0.6 seconds two-way travel time (TWTT; all thicknesses here are given in two way travel-time, and later converted into depth after estimating sediment velocity). The sediments thin towards the south, but conformable layering implies that the sedimentation is post-rift. The basement has a distinctive ropey character that is interpreted to be of volcanic origin. The next basin along the MCS profile is the narrow Foca Trough (Figure II.3), which has a maximum 0.4 s of sediment with a lower syn-rift sequence, and a pair of northwest-facing normal faults along its southeast scarp.

At 265 km along the profile, to the east of the Cerralvo Bank, a deep basin exhibits the most complicated sedimentary sequences along this line. This basin is previously unnamed and we will refer to it as the East Cerralvo Basin (Figure II.4). The basement character is similar to that of the La Paz Basin and Foca Trough and may also be of volcanic origin. There is no visible basin-bounding fault, so it is likely that the majority of the accommodation space was created in a rapid episode of faulting not recorded in the sedimentary sequences. The majority of the observed

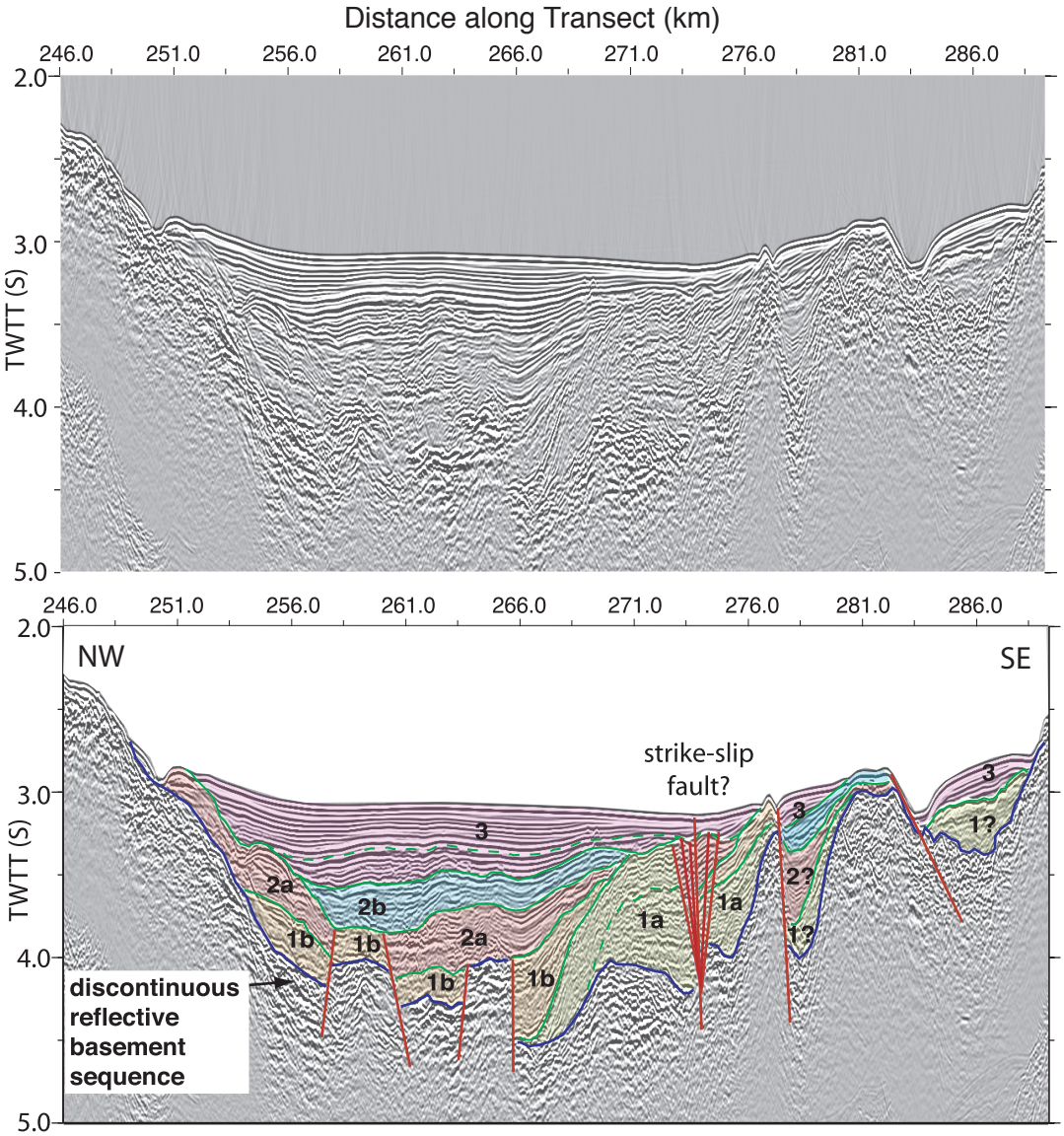

Figure II.4 East Cerralvo Basin. The top plot shows the uninterpreted section, the lower plot is interpreted. Basement is shown by a blue line, sedimentary sequence boundaries are in green, faults are shown in red. Basement has a reflective discontinuous appearance. Unit 1 (divided into 1a and 1b) a syn-rift deposit with a chaotic character; unit 2 (divided into 2a and 2b) is possibly syn-rift and shows an increase in layering; unit 3 consists of post-rift, layered marine sediments. The two surface-cutting normal faults at the southeast end appear younger than the main basin, but exact correlation to the main basin is unclear.

faulting is on a smaller-scale with only a few kilometers offset, and affects only the basement and the lowest sedimentary sequences. Total sedimentary thickness is 1.3 s and five sedimentary units have been identified based on unconformities, with three syn-rift and two post-rift sequences. From either side, the lowest unit (1a) thickens towards a possible fault at 274 km. An interpretation of this sequence provides evidence for two opposite-sense normal faults early in the basin's history to create the stratal relationship of these deposits, which have more recently been cut by a strike-slip fault at 274 km. As this 2D transect is parallel to the main transform faults in the Gulf, this is an unlikely orientation for a strike-slip fault; we suggest, however, that it may be a fault resulting from mass-wasting of Isla Cerralvo prior to the opening of the Cerralvo Trough. Unit 1b was deposited synchronous with slip on the fault at 265 km, but was deposited and faulted later in the northwest of the basin. Unit 2a shows a possible slump feature at 254 km, and may also be syn-rift along with unit 2b. The youngest unit (3) appears to be a typical post-rift, layered, deep marine deposit. The change in character through the sequences is most likely indicative of changing sediment sources, from possibly sub-aerial and shallow marine units that are seismically less reflective with chaotic layering, to layered deep water pelagic sedimentation. To the southeastern side of the basin there are two possibly younger faults at 277 km and 283 km, which form smaller basins and appear to break the surface. It is difficult to relate the sedimentary sequences in these smaller basins to those seen in the main basin, but the oldest layer in both sub-basins has a more chaotic, unlayered appearance similar to the older units in the main basin and may have been deposited during the early stages of rifting. The stratal character of sediments abutting the fault at 277 km suggests the initiation of fault movement and sub-basin formation during the deposition of unit 2, and may continue to move at slow rates through the present. The fault at 283 km seems to be more recent, creating a small bathymetric low.

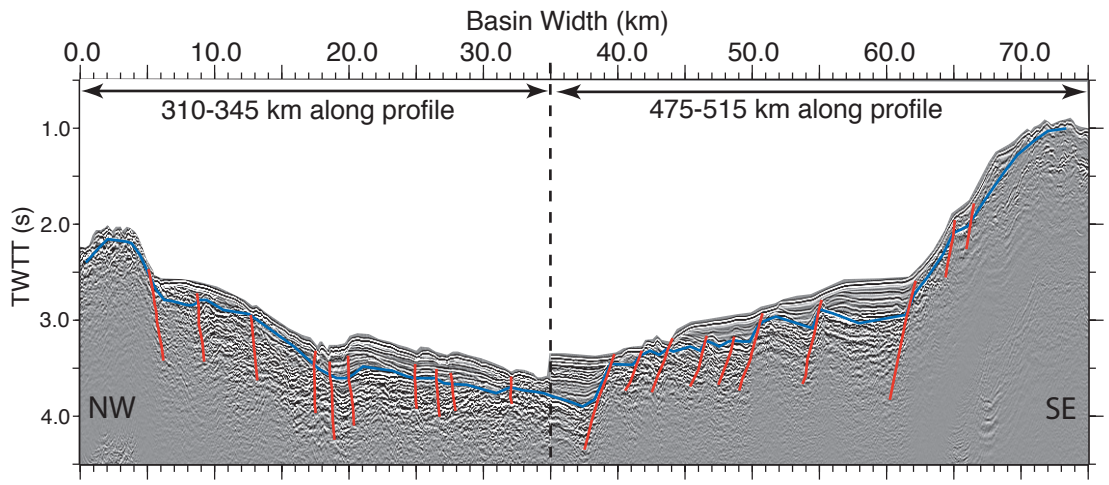

Figure II.5 Reconstructed Alarcón Basin. Basement is indicated with a blue line and faults are shown in red. Sediments appear to be post-rift and drape the faulted, volcanic basement.

II.3.B Alarcón Basin

The Alarcón Basin experienced full rifting and is now undergoing seafloor spreading (Figure II.6). The flanks of the basin prior to the onset of seafloor spreading have been reconstructed (Figure II.5). The southeast side of the basin is marked by a large sequence of inactive down-to-the-northwest normal faults which step up to the Tamayo Bank. These fault show basement offsets up to 0.5 s, and basement is draped with post-rift sediment which also reaches a thickness of 0.5 s. The basement shows the same volcanic character observed elsewhere along the profile, and faulting occurred after the deposition of this volcanic layer.

II.3.C Oceanic Crust

The continent-ocean transitions on both sides of the Alarcón Basin are sharp: basement depths across the northwest boundary suggest the transition is located between 330 and 345 km, whilst the southeastern transition occurs 457-480 km along transect (Figure II.2). To help constrain the continent-ocean transition further, modeling of magnetic anomalies (Cande and Kent, 1995) has been done

using a lineation orientation of 215^o and an intensity of 8 A$^-$1m for a 0.5 km thick layer, with varying spreading rates (Figure II.6). Magnetic anomalies are of low quality along the northwestern side of the oceanic crust, possibly due to the proximity to the transform fault less than 10 km north and the seamounts on the northwestern side of the oceanic crust. In the northwest we are confident that seafloor spreading has been active since 2.5 Ma, although the deep basement (at oceanic crustal depths) suggests the continent-ocean transition may be located further to the northwest, corresponding to an onset of seafloor spreading as early as 4 Ma.

The oceanic crust southeast of the spreading center has thicker sediment relative to the northwest half (Figure II.2), which is most likely related to enhanced sediment supply and delivery from mainland Mexico. Magnetic anomalies along this portion of the transect are higher quality and modeling of the southeastern magnetic anomaly shows a reasonable fit of 3.7 Ma at 480 km along transect (Figure II.6). However there appears to be a transition zone between 457-480 km where the basement is deeper with older sedimentary sequence (Figure II.2). This transition from normal sedimentation to deeper basement occurs at 2.5 Ma, matching the northwestern side.

The magnetic anomaly on the northwestern side has a significantly lower amplitude than that of the southeastern oceanic crust. The estimated spreading rates from the magnetic anomaly (Figure II.2) are asymmetric, and it may be that the initiation of seafloor spreading was asymmetric also. It is also possible that the 2A chron on the southeastern side is the result of intrusion and underplating, rather than true seafloor spreading. This may explain the low amplitude (as the source of the anomaly is deeper) and the low basement depth (as this was the location of extreme extension before the creation of oceanic crust). The low amplitude on the northwestern oceanic crust may also be a combination of proximity to the transform fault, located less than 10 km to the northeast, and the presence of the

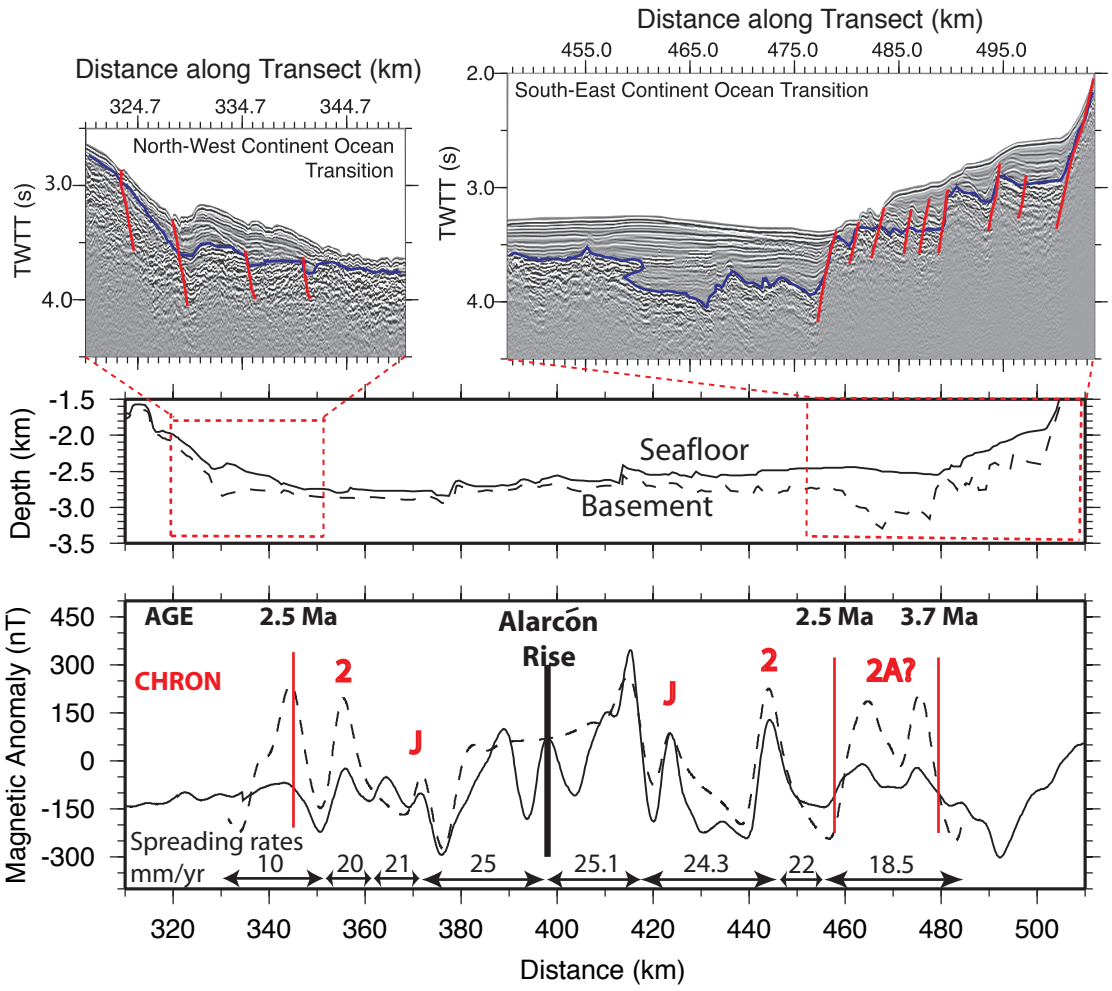

Figure II.6 Continent-ocean transitions and magnetic anomaly across the Alarcón Basin. Top plot shows MCS data in the continent-ocean transition regions, which are highlighted in the bathymetry and basement plot below. The lower plot shows the magnetic anomaly across the oceanic crust with interpretation. Observed magnetic anomaly is solid line, predicted is shown as a dashed line.

Alarcón seamounts, which are more recent than the oceanic crust and could alter the observed magnetic anomaly.

II.3.D Southeastern Margin

The Tamayo Trough (Figure II.7), located 555 km along the profile, is stratigraphically similar to the East Cerralvo Basin in that there are no discernible

basin bounding faults to create the accommodation space, only small-scale basement faulting. The basin has nearly 1.6 s of sediments but no major syn-rift sedimentary sequences, suggesting a rapid episode of faulting and accommodation. The seismic character of basement reflections also appears to be similar to the volcanic style observed on the northwestern conjugate margin. However, in the Tamayo Trough basement faulting barely produces visible offsets in the volcanic layer, in contrast to the East Cerralvo Basin (Figure II.4), where offsets up to 0.5 s (around 400 m) are seen. This suggests that deposition of the volcanic layer was after both the large-scale and some of the small-scale faulting in the Tamayo Trough, but occurred before basement faulting in the East Cerralvo Basin, making the Tamayo Trough older. We have identified three sedimentary sequences within the basin which likely document the subsidence of the basin from shallow marine to a deep marine environment, and are similar to those of the East Cerralvo Basin (Figure II.4). The lowest layer (1) is unreflective, the middle layer (2) shows some layering and may have been deposited during motion on the fault at 553 km and the youngest layer (3) consists of layered deep marine sediments similar to the post-rift packages in other basins along the transect.

Further along the transect between 585 and 600 km there are several small-offset faults before reaching the West Nayarit Ridge, which is bounded on its northern side by a large a normal fault scarp with down-to-the-northwest motion, and has accumulated only 0.25 s of sediments. A sequence of three troughs, the West Nayarit (615 km), Central Nayarit (635 km) and East Nayarit (655 km) (Figure II.8) show similar sedimentary structures: a lower syn-rift sedimentary sequence overlain by post-rift sedimentation. There seems to be a change in basement character across the Central Nayarit Ridge. The West Nayarit Trough has a discontinuous reflective basement character similar to that seen in the Tamayo Trough and further to the northwest, in contrast to the Central and East Nayarit Troughs that have a thinner, less chaotic reflective upper basement. The West Na-

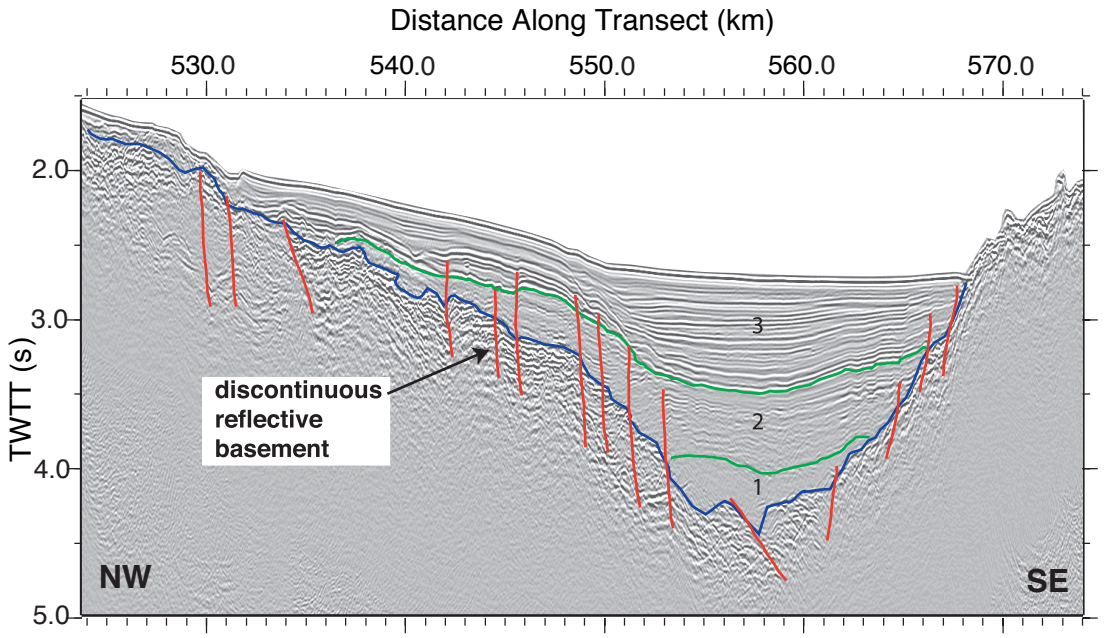

Figure II.7 Tamayo Trough. Basement is faulted but there is no major syn-rift sedimentation or a large basin-bounding fault. The basement, indicated in blue has a highly reflective "ropey" character. Sedimentary sequence boundaries are shown in green. These sequences appear similar to those in the East Cerralvo Basin (Figure II.4), with unit 1 consisting of non-layered sediments, unit 2 showing an increase in layering and unit 3 consisting of layered marine sediments.

yarit trough (615 km) has three down-to-the-northwest normal faults with up to 0.8 s sediment thickness. The Central and East Nayarit Troughs (635 km and 655 km) are opposite-sense half-grabens forming a horst, with the East Nayarit Ridge positioned between them. Sediment thickness in the Central Nayarit Trough is up to 1.1 s and, in the East Nayarit Trough, up to 1.6 s. The thickness of post-rift sedimentary sequences increases west to east. The San Blas Basin (Figure II.9) is the largest ($\sim$70 km wide) basin seen along this transect. Low-fold data and the shallow ($\leq$50 m) water depths made processing difficult and precluded the use of multiple suppression techniques, but we can see that the basement here is highly faulted, although there is no main bounding fault. There are also variations in basement character, from a highly reflective lower basement sequence in the shallow northern edge of the basin, to areas with no clear basement reflector, such as

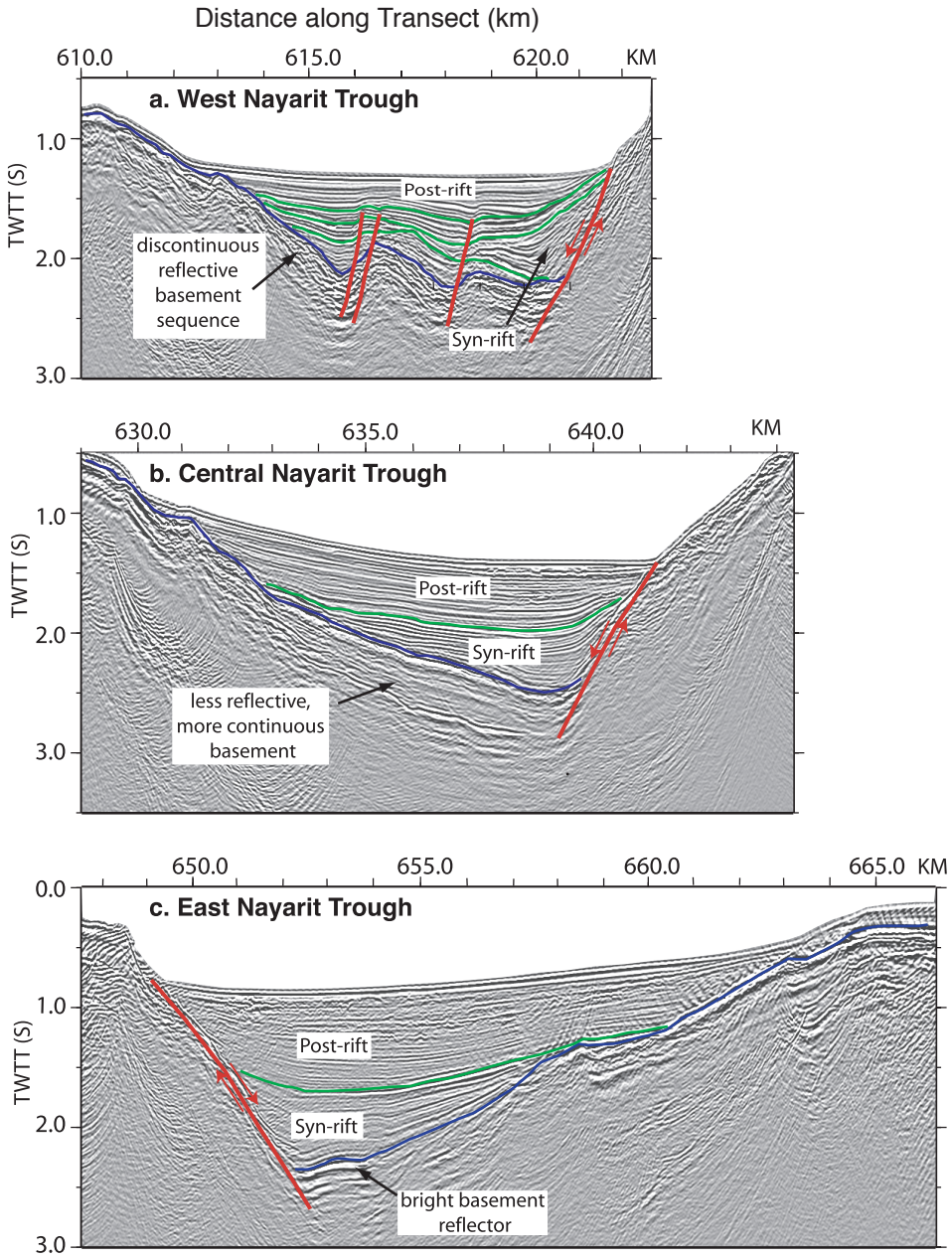

Figure II.8 The West(a), Central(b) and East(c) Nayarit Troughs. Basement is indicated in blue, faults in red and main sequence boundaries in green. The West Nayarit Trough shows the reflective, ropey character, faulted basement layer observed further to the northwest on the transect whereas the Central and East Troughs are simple half grabens with a thinner, more continuous basement reflection.

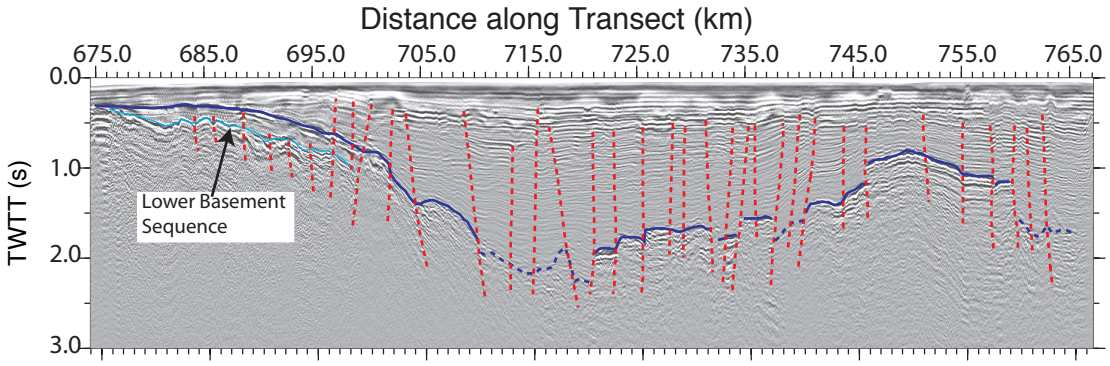

Figure II.9 San Blas Basin. This basin has several visible basement offsets but lack of quality imaging of deeper sediments prevents confident interpretation. Possible faults are shown in dashed red.

the center of the basin. The sediments reach a thickness of 2 s and reveal small-scale deformation from the faults that cross-cut conformable stratigraphy across the basin, but have no strong indication of syn-rift deposition.

II.3.E Supergather Analysis

In addition to the velocity analysis carried out to produce the stacked seismic sections, supergathers along the reflection transect were produced and modeled. The aim of the supergather analysis was to test if the ropey, volcanic character seen at the top of basement along much of the reflection profile has a distinctive velocity structure, which is indicative of volcanic or volcano-clastic deposits. A supergather takes several common midpoint (CMP) gathers along the transect and stacks on offset (or source-receiver range) to produce the equivalent of a 6 km refraction profile, with minimal subsurface smear and improved signal-to-noise (for details see Hussenoeder et al. (2002)). The supergather records the water wave reflection, subseafloor reflections, and a set of refractions, which when combined, aid in determination of a detailed velocity profile with depth. Fitting travel-time curves to these reflection and refraction arrivals produces a velocity-depth profile (Figure II.10), which can provide insight into the internal structure

of the basement. Results are best with flat structure and in shallower water depths (as more refraction arrivals below the seafloor are captured).

Our modeling shows a distinctive layer to be present beneath much of the transect, with a relatively low velocity of 2.5-2.8 km/s, and a thickness of 250-500 m (Figure II.11). In contrast, geophysical borehole logs in highly fractured granites show P-wave velocities of around 5 km/s (Boness and Zoback, 2004), indicating that this layer may be sedimentary (or volcano-clastic) in origin, not highly fractured basement. To confirm that this analysis produces reasonable results, a supergather on the oldest oceanic crust at 475 km along transect was modeled. This result shows sediments overlying basement of velocity ~4 km/s. The age of this oceanic crust should be between 3- 3.7 Ma (Figure II.6), which Hussenoeder

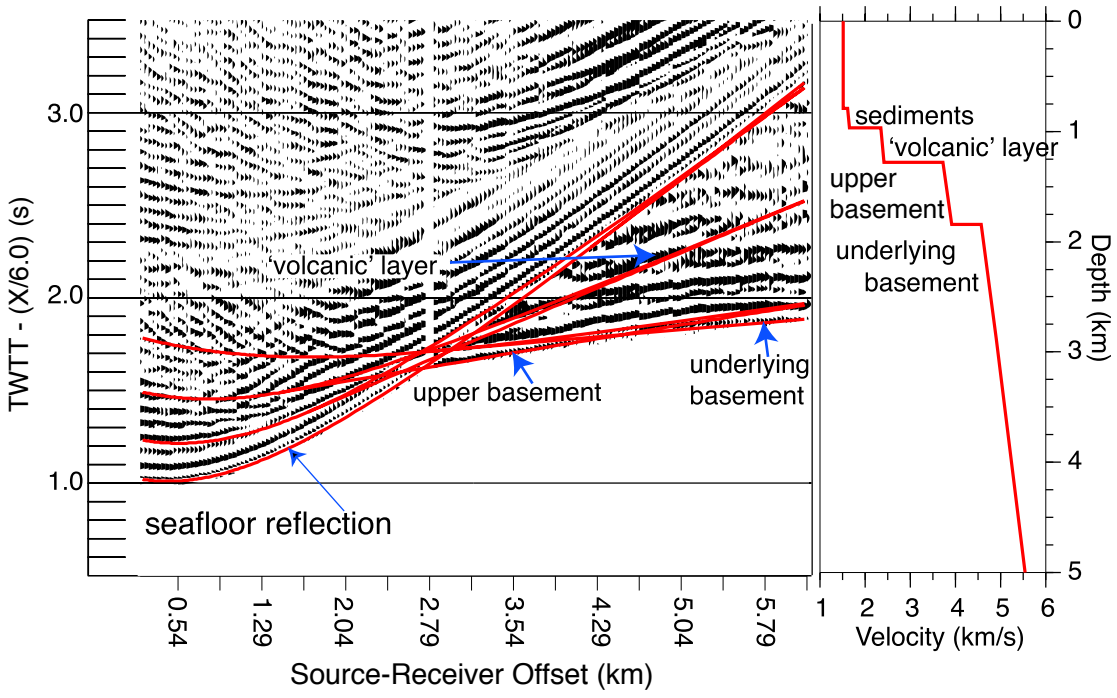

Figure II.10 Example of supergather with travel-time curve (left) and corresponding velocity-depth function (right) at 517 km along transect (Tamayo Bank). The dominant features of the supergather are the seafloor reflection, followed by reflected/refracted arrivals from three layer boundaries, which forms a triplication in travel-time.

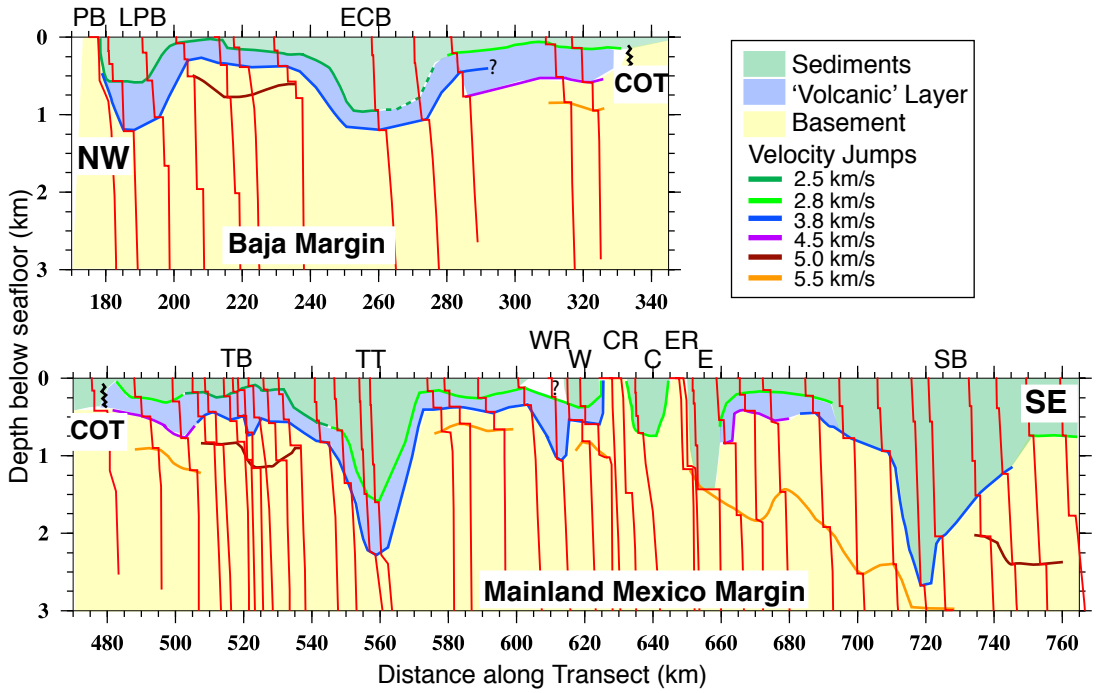

Figure II.11 Interpretation of supergather velocity results. Plotted in depth and reduced to a seafloor datum. The velocity-depth profiles are shown in red. There are two main layers: sediments (green) and the volcanic layer (blue) overlying faster basement (yellow). In some areas there is an additional layer seen in the basement, which may correspond to the upper-mid crustal boundary. Abbreviations: COT=continent-ocean transition; PB=Partida Bank; LPB=La Paz Basin; ECB=East Cerralvo Basin; TB=Tamayo Bank; TT=Tamayo Trough; WR=West Nayarit Ridge; W=West Nayarit Trough; CR=Central Nayarit Ridge; C=Central Nayarit Trough; ER=East Nayarit Ridge; E=East Nayarit Trough; SB=San Blas Basin.

et al. (2002) indicate should have a velocity of 3.75- 3.9 km/s, providing good agreement.

When velocity-depth profiles are converted back into two-way travel time, this layer clearly corresponds to the discontinuous, highly reflective layer observed. Across the Baja margin, this ropey layer is observed extending from the La Paz Basin to the continent-ocean transition, and on the mainland Mexico side, it is seen from the continent-ocean transition to the West Nayarit Trough. Closer to the continent-ocean transitions, this layer and the underlying basement is faster. The

layer does not appear to be present beneath the Central and East Nayarit Troughs (although less refractions suitable for modeling are observed in these basins, making interpretation more difficult) but reappears to the southeast for a 40 km stretch on the lip of the San Blas Basin, although it not observed beneath the San Blas Basin proper. There are three areas where 'normal' basement is present at the seafloor with no sediments or volcanic layer observed: the Partida Bank, Central Nayarit Ridge and East Nayarit Ridge. The West Nayarit Ridge has an interesting structure, with 200 m of material with a velocity of 2.2 km/s (possibly fast sediments) overlying the volcanic layer. Along much of this transect, we also observe a layer within the basement that marks a transition in velocity from around 4 km/s ("typical" crystalline basement) before a jump to 5.0+ km/s beneath. This layer is approximately 300 m thick where observed beneath the Baja margin and in the vicinity of the Tamayo Bank, and appears to thicken significantly beneath the San Blas Basin to approximately 1 km, although results in deep basins are less certain.

The Tamayo region (500- 575 km along transect) is of particular interest because of the lack of obvious faulting responsible for the accommodated structure of the basin. A more detailed interpretation of this area is shown in Figure II.12. The schematic diagram shows an interpretation of velocity-depth profiles, reduced to a seafloor datum (top), and the MCS profile shows these layers converted back into two-way travel time (bottom). We see that the volcanic layer follows the ropey basement structure and appears to be continuous from the bank down into the trough. Three main sedimentary units are observed in the Tamayo Trough: the uppermost layer has velocities similar to the recent pelagic drape seen over the entire transect, beneath this boundary velocities increase to around 2.1 km/s, and the lowest layer, corresponding to the non-reflective character seen in the seismic section, has velocities around 2.3 km/s. The volcanic layer is faster underneath the Tamayo Trough, as would be expected with compaction.

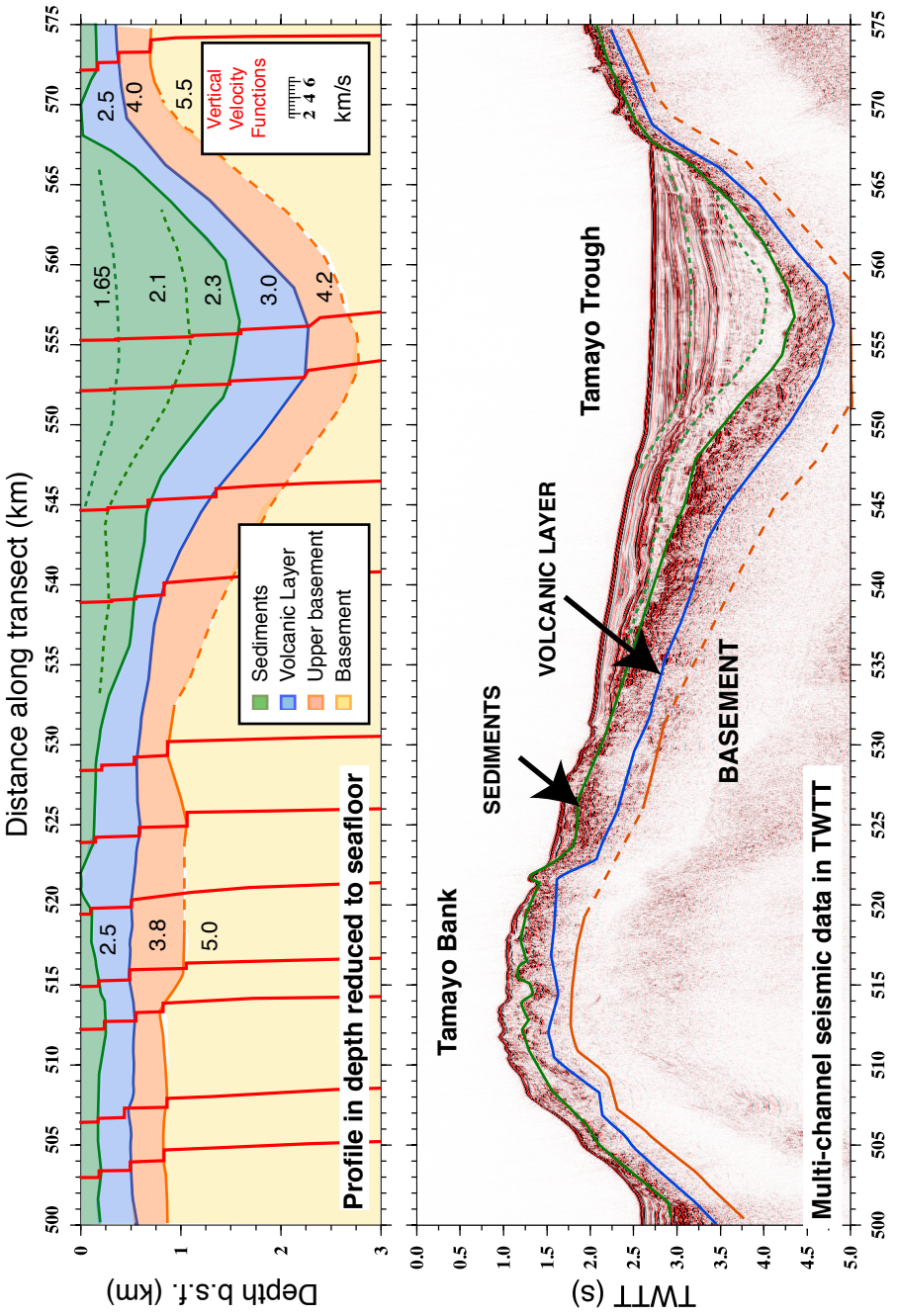

Figure II.12 Detailed supergather results and interpretation across the Tamayo Bank and Trough. Top plot shows supergathers reduced to a seafloor datum, with velocity-depth profiles in red and velocities in km/s. Sediment-basement interface is shown in green; the base of the volcanic later in blue; and the upper/mid basement boundary in orange. Lower plot shows these layers converted into TWTT and plotted over migrated MCS data.

II.4 Discussion

II.4.A Sedimentary Sequences and Fault Timing

The inferred lack of significant syn-rift sedimentary sequences in the larger basins suggests that some early large-scale faulting episodes with the southern Gulf of California occurred rapidly before being draped by volcanic or volcano-clastic deposits. In all the basins imaged, the youngest sediments are post-rift sequences, so it appears there has been little extension away from the spreading center during the past few million years. This is in agreement with the GPS and plate motion analysis of DeMets and Dixon (1999), which finds that the rate of seafloor spreading at the Alarcón Rise is consistent with total Pacific-North America displacement at the present time. We observe two styles of basin formation: (1) larger basins (East Cerralvo Basin, Tamayo Trough and San Blas Basin) characterized by small-scale basement faulting but lacking a main basin bounding fault, these basins do contain small amounts of syn-rift sedimentation (particularly the East Cerralvo), but this syn-rift sedimentation is associated with the small-scale basement faulting, not the large-scale basin formation; (2) smaller basins (La Paz Basin, Foca Trough, West, Central and East Nayarit Troughs), generally half-grabens, created by one basin-bounding normal fault with simple sedimentary sequences, including both syn-rift and post-rift sedimentary sequences. This hints at two phases of extension, one forming the larger, more complex basins, and a second phase forming the smaller, mostly more distal basins. The Alarcón Basin seems to belong in the first phase of extension: before seafloor spreading it was around 60 km wide, and shows significant small-scale faulting of the basement with no syn-rift sedimentary sequences. Without drilling we cannot be certain of sediment ages and sources, but pelagic sedimentation rates can be estimated by comparing the sediment thickness to the age of the oceanic crust, which is known from magnetic anomalies. An additional estimate is obtained from a stratigraphic section on Isla Maria Madre,

located on the southwestern edge of the San Blas Basin. Dividing the thickness of sediments by the sedimentation rate provides an estimate of time taken to deposit sediments, and hence, an estimate of the time the basin formed.

To estimate the sedimentation rate for each basin, the most geographically appropriate existing estimate was used, and the availability of sediment is considered. The sediment thickness for each basin was taken from the supergather results (Figure II.11). The northwestern side of the oceanic crust shows the lowest sedimentation rates, with a doubling of sedimentation rate from 50 to 100 m/Ma between 2.5 and 0.7 Ma. Most sediment from the Baja Peninsula is deposited near shore (Nava-Sanchez et al., 2001), so sedimentation rate along the northwest profile are likely to be low, but the northwestern oceanic crust is also further from the sediment source than the La Paz and East Cerralvo basins, so the higher rate of 100 m/Ma is considered a better estimate for the basins along the northwestern margin. The southeastern oceanic crust has significantly more sediment cover than the northwest side and as pelagic sedimentation rates will be relatively uniform, this suggests that terrestrial sediments form mainland Mexico reach the oceanic crust to account for the difference. The southeastern oceanic crust also shows an increase in average sedimentation rate over time, from 115 to 150 m/Ma over the same 2.5 to 0.7 Ma time period, and sediment ages from Isla Maria Madre (McCloy et al., 1988) show an average rate of 110 m/Ma prior to 6.7 Ma, increasing to 180 m/Ma afterwards. An average of oceanic crust sedimentation rates (115 m/Ma) is used for the Alarcón basin. An average rate of 133 m/Ma from the oceanic crust is used for the Tamayo Trough and West and Central Nayarit Troughs. The East Nayarit Trough and San Blas basin are closer to the sediment source, and an average rate of 145 m/Ma from Isla Maria Madre is used to estimate their ages. However this may be a low estimate as the San Blas basin is fed directly from land runoff and the East Nayarit Trough is fed from the overflow of the San Blas basin (Figure II.9).

The estimated ages are shown in Table II.1, with the possibility of a few million years error in basin formation. Nevertheless, as expected, the 3 larger basins (East Cerralvo, Tamayo Trough and San Blas) are also likely to be older, and the crude estimates of their ages show they formed before ∼10 Ma, probably at the onset of extension in the Gulf. Faulting near Tepic, mainland Mexico (Figure I.4) is dated to have occurred in two episodes, the first between 8-12 Ma (Ferrari and Rosas-Elguera, 1999), which overlaps with the estimated dates for the formation and faulting duration of these basins. The second episode of faulting near Tepic is 3.5-5.5 Ma (Ferrari and Rosas-Elguera, 1999), which corresponds roughly to the ages of the West Nayarit Trough, Alarcón basin and La Paz basin. With the current available data, it is impossible to say whether the age progression in the three Nayarit Troughs is purely apparent, the result of decreasing sediment supply as we move away from land, or highlights an actual east-west progression in their formation. In addition, the early date for formation of the East Nayarit Trough may be incorrect, as its history may have been complicated by its proximity to the San Blas Basin. The estimated age of first sediment deposition in the Alarcón corresponds to the onset of seafloor spreading, but obviously faulting had to have been occurring previously to accommodate the crustal thinning before the onset of seafloor spreading. Faulting may have been active in the West and Central Nayarit Troughs until the onset of seafloor spreading in the Alarcón Basin ∼3 Ma. On the Baja margin Dorsey et al. (2001) note a rapid subsidence event between 4-8 Ma, which coincides with the estimated age of the La Paz Basin and its rapidity is also consistent with the lack of syn-rift sedimentation in the basin, which is interpreted to have experienced rapid faulting and inundation.

II.4.B Upper Crustal Extension

The upper crustal extension can be estimated in two ways. The first is to sum the extension created by throw on faults that we see in the MCS data,

Table II.1 Estimated Basin Ages based on Sedimentation Rates. (*Estimate for Alarcón is likely too low because it is located furthest from sediment sources.)

Basin	Sediment Thickness	Basin Age Estimate	Post-Rift Sediment Thickness	Approx. Time Since Faulting
La Paz	500 m	5 Ma	500 m	5 Ma
East Cerralvo	1000 m	10 Ma	750 m	7.5 Ma
Alarcón	400 m	Pre-3.5 Ma*	400 m	3.5 Ma*
Tamayo	1500 m	Pre-11 Ma	1500 m	11 Ma
West Nayarit	500 m	4.0 Ma	250 m	2 Ma
Central Nayarit	1000 m	7.5 Ma	500 m	4.0 Ma
East Nayarit	1500 m	10 Ma	700 m	5 Ma
San Blas	2000 m	Pre-14 Ma	2000 m	14 Ma

which is measured by horizontal basement offset. The section of the northwestern Baja margin within the limits of the MCS data is 175 km (the profile was foreshortened by an estimated extra 125 km of extended crust), and extension created by observed faults has been estimated at 28 km, giving a stretching factor (β) of 1.2. The southeastern margin is currently 290 km wide along the extent of this MCS data (an estimated 110 km of extended crust at the southern end of the transect was not imaged), and extension on faults totals 52 km, also producing β = 1.2. Calculating extension from fault offsets in MCS data is known to be an under-estimate (Walsh et al., 1991). The second method to estimate upper crustal extension ignores the observed faults and instead uses the large-scale basement structure and bathymetry, with the assumption that the bathymetry was originally flat and close to sea level. This may be a more accurate large-scale estimate because we see large basins with no basin-bounding faults due to volcanic draping with the observed offsets on small-scale basement faults insufficient to have produced them. Higher stretching factors of β ~1.6 for the northwest margin and β ~1.5 for the southeast margin are calculated. Both estimates show similar degrees of extension on conjugate margins and although the second estimate is higher, it is still less than the whole crustal structure calculated from the coincident refraction data (Chapter III). Crustal structure shows significantly more extension,

Table II.2 Comparison of extension imaged on faults and overall accommodation scape in large basins

Basin	Current Width	Estimated Extension	Estimated sum of fault offsets	Fault offsets + 35% error	Total missing extension
San Blas	125 km	65 km	20 km	27 km	38-45 km
Tamayo	30 km	15 km	5 km	6.75 km	8.25-10 km
East Cerralvo	35 km	15 km	6 km	8 km	7-9 km

with stretching factors of around β=2.0 for both margins. The difference between the extension needed to create the basin and the amount of extension created by visible faulting is most pronounced in the San Blas, Tamayo and East Cerralvo basins, where there are no basin bounding faults. In these basins only a third of the total amount of extension seems to have been accommodated on visible faults (Table II.2), but the estimated total amount of extension individually in each of these basins does produce stretching factors of 1.75-2.0, so locally, at least there is not a discrepancy in upper crustal and whole crustal stretching factors. If the large-scale faulting occurred before the deposition of the volcanic layer, and the later, smaller-scale faulting occurs in this volcanic layer, comparisons of these two estimates of extension will indicate how much extension occurred before the deposition of the volcanic layer. Taking just the three large basins (we extrapolate the San Blas basin where we do have MCS data), there is a total of around 54-64 km extension before the volcanic layer was deposited (Table II.2).

The uniform upper crustal structure seen in supergather analysis (Figure II.11) implies symmetric extension as there is upper crustal material present across both margins. Asymmetric extension would put faster, lower crustal material near the seafloor. Symmetric extension is also seen in the crustal structure derived from the complimentary refraction dataset (Chapter III). The total amount of extension and new oceanic crust determined from refraction modeling gives an estimate of 500 km total opening across the Alarcón segment. As only 300 km of this could have been accommodated between 6-0 Ma this indicates significant

extension before 6 Ma, which agrees with both the size and the pre-Comondú age of the larger basins.

II.4.C Magmatism

The southern Gulf of California appears to be a non-volcanic margin, at least in the conventional sense as there are no seaward-dipping reflector sequences which are characteristic of the many volcanic rifted margins around the world (e.g. Mutter et al. (1982); White et al. (1987); Menzies et al. (2002)), and little evidence of underplating or magmatic intrusion. However, a continuous, uniform velocity layer, with a reflective, discontinuous ropey character is observed at the top of basement along much of our transect. The MCS data reveal a change in character within this layer at the Central Nayarit Ridge, which is consistent with results from the supergathers, which indicate that the layer is absent beneath the Central and East Nayarit Ridges and Troughs and the San Blas Basin (Figure II.11).

From the Baja margin to the West Nayarit Trough the volcanic layer varies in thickness and character to some extent, but generally is around 250 m to 500 m thick, and has an average velocity of around 2.5 km/s, with some areas as high as 3 km/s. A possible explanation for the lack of observed faulting forming the Tamayo Trough is that the start of extension and faulting overlapped with a volcanic episode, and these volcanic deposits covered the Tamayo Bank and mantled the empty basin, concealing both the true amount of extension and the major border faults which created it. The Tamayo Trough looks like a half-graben that should have a normal fault bounding its southeast side, but there are no syn-rift sedimentary sequences to show movement on this fault. There are three main geologic units, all volcanic, that are mapped on land and which could correspond to this layer. The oldest is the Comondú formation (Hausback, 1984), which consists of a series of mostly 20- 11 Ma andesite breccias, lava flows and ash falls associated with the volcanic arc during the final stages of subduction. The Comondú Arc

swept westwards covering a large geographic area, and observed thicknesses of this formation vary from 300 m to 1.5 km (Hausback, 1984; Umhoefer et al., 2001). On the Baja peninsula post-Comondú basalts and diabase dikes are dated 10- 12 Ma, and younger still are the Pliocene- present rhyolite volcanoes on the eastern edge of the Baja peninsula (Bigioggero et al., 1995). However no post-Comondú volcanism is observed south of around 25^{o}N on the Baja peninsula, and the lack of literature concerning these two younger units speaks to their sparse distribution. Hence, considering the scale of each of these deposits compared to the large-scale and continuous nature of the observed layer, and the slow velocity of the layer, the Comondú seems the most likely candidate. A low velocity of 2.5 km/s suggests a volcano-clastic sedimentary rock, such as volcanic ash and tuff or debris flow, and is less likely to be a more massive basalt flow (as demonstrated by comparison to the velocity of oceanic crust), favoring the interpretation that the Comondú is the likely source of this ropey and reflective layer in the MCS data.

As the Comondú died out at 11 Ma, the large-scale faulting in the San Blas basin, Tamayo trough and the East Cerralvo basin would have to have occurred before 11 Ma if the Comondú is covering up this faulting. As we estimate that about 60 km of extension is "missing" (i.e. needed to create the basin but not measured on the imaged faults), this extension, and deposition of the volcanic layer would have to occur before 11 Ma, suggesting that extension in the Gulf may have begun around 14 Ma, coinciding with the first marine incursion (McDougall, 2006). Although seafloor spreading on the Pacific-Farallon ridge did not completely end until 12 Ma, only small amounts of spreading are seen from 15-12 Ma (Lonsdale, 1989). If extension was not being accommodated by seafloor spreading, it may have been taken-up in the Gulf of California earlier than previously thought. But this earlier start of Gulf extension increases the total amount of dextral slip that has to be accommodated: if our clock begins at 14-15 Ma we need to account for 700 km or more of Pacific- North America plate motion (Oskin and Stock, 2003b).

With a total 500 km opening (Chapter III), we would then need 200 km dextral slip on the Tosco-Abreojos fault to take up the difference. This is less than the 300 km proposed by Yeats and Haq (1981), but still slightly more than suggested by Fletcher et al. (2006). A second option is that this layer is younger than 11 Ma: either there was a currently unknown episode of volcanism between 6-11 Ma, that is not seen on land, or the Comondú arc may have been active for longer than previously thought. The volcano-clastic/sedimentary velocity of this layer points away from typical rift-related volcanism, which consists of lava flows, not ash, so it seems the volcanism would have to be more closely related to the arc than to rifting. The age and origin of this volcanic layer is key for interpretation of the rifting history of the Gulf.

The continuous nature of the volcanic layer along 100's of kilometers produces interesting questions where it is not observed. There are two, possibly complementary, options: (1) If the layer is constructed from the Comondú volcano-clastic flows, it may be that the West Nayarit Trough is the easternmost extent of the deposits, and the re-occurrence of the layer at the northwestern lip of the San Blas Basin is a different volcanic unit, possible SMO ignimbrites. This is possible, considering the different character of the layer at 665- 690 km, which consists of a double reflector sequence (Figure II.9). The second option (2) is that the volcanic layer was laid down before the Nayarit Troughs were faulted and formed; in this mode, significant extension would have exhumed rock from depth, so the layer may have been eroded, altered or lost during rifting.

II.4.D Rifting Style

In the larger context of the Basin and Range province of western North America, the Gulf of California represents concentrated extension within a relatively narrow rift. However, the southern Gulf of California also appears to exhibit the wide mode of rifting in the sense of Buck (1991). We see different basins dis-

tributed over a wide region forming at different times, which is most often the result of extension creating mantle upwelling and strengthening in one location and the migration of rifting to a new, weaker spot (Buck, 1991). We don't see evidence, however, for the re-activation of faults, at least within the sedimentary record. Asymmetric margins (Wernicke, 1984) are created by low-angle detachment faults, which result in one margin being composed of upper crustal material and its conjugate being exhumed mid- lower crustal rocks. The presence of the volcanic layer overlying upper crustal material of around 4 km/s along both the Baja margin and the majority of the mainland Mexico margin implies that the upper layers of both margins are composed of upper crustal material. The Nayarit ridges do show a different upper crustal velocity structure, and on a local scale there may have been some exhumation of deeper crustal material in this area. However, the similar margin widths, no observed deeper crustal reflections and similar basin styles across both conjugate margins leads to the conclusion that the southern Gulf of California is, overall, a symmetric rifted margin, having undergone large-scale pure shear extension (McKenzie, 1978). This interpretation is supported by crustal structure (Chapter III), which shows similar degrees of crustal thinning on conjugate margins.

II.5 Conclusions

A migrated multi-channel seismic (MCS) profile shows multiple rifted basins spanning 600 km across conjugate rifted margins in the southern Gulf of California. Estimates of the ages of these basins based on sedimentation rates indicate two phases of basin formation: an initial phase, starting at or near 14 Ma, which formed the larger basins (San Blas Basin, Tamayo Trough and East Cerralvo Basin) with rapid extension, evidenced by the lack of observed significant syn-rift sedimentary sequences. In each basin, this initial phase of large-scale faulting was likely followed by the observed small-scale basement faulting, which

continued to accommodate extension until around 8-6 Ma, when a second phase of extension began. This second phase is inferred to have formed the smaller half-graben basins and is possibly synchronous with the formation of the basins in the central and northern Gulf. The Nayarit Troughs show lower syn-rift sedimentary sequences overlain by post-rift sediments, and this change from syn- to post-rift sedimentation likely coincides with the onset of seafloor spreading, when extension became concentrated at the Alarcón Rise. Sedimentary deposition on the sides of the Alarcón Basin itself appears to have begun at the same time as seafloor spreading, and although it seems to be the youngest basin (Table II.1, its style of extension (large basin with lots of basement faulting) is similar to the older basins. As the Alarcón is located far from land sediment sources, it may have been sediment-starved earlier in its history.

The basement along much of the transect has a distinctive highly reflective, ropey character. To investigate this layer further, vertical velocity functions were modeled from supergathers of the MCS data. The velocity-depth profiles show a volcanic layer with a velocity of $\sim$2.5 km/s comprising the uppermost few hundred meters of basement across the majority of this rifted margin. The extent and velocity structure of this layer suggests that it may be the 20-11 Ma Comondú formation. However, a volcanic arc dying out at 11 Ma, and with extension only beginning at 12 Ma in the traditional models of Gulf of California extension leaves only $\sim$1 Ma for the combination of formation of the three large basins we see along this transect, as well as deposition of around 300 m of volcano-clastic rocks. This discrepancy can be explained in two ways: either extension began earlier, around 14 Ma, or volcanism related to the arc continued for longer after the end of subduction. The evidence of 1) the 11-14 Ma marine incursion (McDougall, 2006), 2) estimated 14-10 Ma age of three oldest basins (Table II.1 and 3) the absence of Comomdú deposits younger than 11 Ma (P. Umhoefer, *pers. comm.*) hint that an earlier start of extension in the Gulf of California is more likely. In addition to the

onset of extension, the NE-SW orientation of the Tamayo bank (Figure refline20) strongly suggests that it was formed by NW-SE, not E-W extension. The volcanic layer masks early extension in the Gulf, helping to account for the discrepancy between the amount of extension measured on imaged faults and the total amount of crustal extension.

The traditional model of Gulf of California extension begins at 12 Ma; between 12-6 Ma has small amounts of E-W extension in the Gulf and 300 km dextral slip on the Tosco-Abreojos faults, and between 6-0 Ma has 300 km dextral slip and extension in the Gulf. This does not fit with our observations. To accommodate at least 60 km extension and deposition of the volcanic layer before 11 Ma, we need to start extension in the Gulf closer to 14 Ma. Between about 14 Ma to present, the total Pacific-North America plate motion has been around 700 km (100 km more than in the 12-0 Ma period). The Tamayo trough is an early basin whose large-scale faulting is masked by the volcanic layer, and the orientation of this feature indicates NW-SE extension. We also infer a significant amount of extension in the upper crust ($\sim$60 km or more) before the end of the Comondú. Our data presents a tectonic model different to the traditional model both in the timing of start of extension and the direction and magnitude of this early extension: we interpret significant dextral slip and NW-SE extension in the Gulf of California beginning at 14 Ma. This is also observed in crustal structure from seismic refraction data (Chapter III): an estimated 500 km opening has occurred across the Alarcón transect, significantly more than the 300 km needed for motion from 6-0 Ma, implying significant dextral slip and extension in the Gulf before 6 Ma. The timing of the Tamayo Trough suggests that between 14-6 Ma dextral slip was occurring simultaneously on both the Tosco Abreojos fault and in the Gulf of California. Our earlier start and increased magnitude of dextral motion in the Gulf consequently decreases the amount of slip accommodated by the Tosco-Abreojos fault, which is in agreement with Fletcher et al. (2006). Magnetic

anomalies show a possible asymmetry in the initiation of seafloor spreading.

III

Seismic velocity structure across conjugate rifted margins in the southern Gulf of California

III.1 Abstract

Ocean-bottom and land-deployed seismographs spanning an 881 km wide-angle seismic refraction profile have been used to construct a 2D velocity model across conjugate rifted margins of the Gulf of California. These data are from 64 seismographs and a total of 45,000 Pg, PmP and Pn arrivals have been used to create a velocity model, constructed using the approach of Zelt and Smith (1992). The velocity model shows symmetric continental extension, with an overall crustal stretching factor $\beta \simeq 2.0$ and a total opening of around 495 km across this transect. This model agrees with an alternative model of tectonic evolution for the Gulf of California (Gans, 1997; Fletcher et al., 2006); to accommodate around 500 km opening, which is 200 km more than required for the 6-0 Ma time-frame, the southern Gulf must have been undergoing significant NW-SE extension and dextral slip before 6 Ma, the traditional start of major extension in the Gulf. This increase

in dextral slip in the Gulf requires less total dextral slip on the San Benito and Tosco-Abreojos faults west of the Baja. There does not appear to be a single mode of rifting that explains the crustal structure seen across this margin: we observe significant preserved Moho topography, possibly created by crustal-scale brittle deformation, which indicates no significant lower crustal flow. These factors both indicate cold lithosphere, however, rifting of cold lithosphere is thought to produce a narrow mode of rifting (Buck, 1991) and we observe rifting over a region initially 350 km wide, with distributed large basins. Average lower crustal velocities are 6.3 km/s, showing no evidence for large-scale magmatism during rifting but the transition to seafloor spreading is smooth, with rapid transition to typical oceanic crust. The high degree of stretching at the continent-ocean transition (β>4), the relatively fast speed of rifting ($\sim$3 cm/yr), and the proximity of the Alarcón Basin to the East Pacific Rise may have assisted in generating a robust melt supply.

III.2 Introduction

To gain insight into rifting processes we must assess the amount and style of extension across both conjugate sides of a rifted margin. Moho structure provides the most rigorous estimate of the amount of extension across a margin, although accurate estimates depend on knowledge of original crustal thickness before the onset of rifting. Crustal structure also provides key information on rifting processes including asymmetric versus symmetric, and wide versus narrow rifting styles. The velocity structure of the crust provides additional information about the degree of magmatism experienced during rifting, as significant intrusions into the continental crust should increase its seismic velocity (McKenzie and Bickle, 1988). Constructing a model of seismic velocity and Moho depth from seismic refraction data allows us to accurately assess the rifting style, including degree of symmetry and the total amount of extension experienced across the southern Gulf of California. The total amount of extension is a key piece of evidence needed to

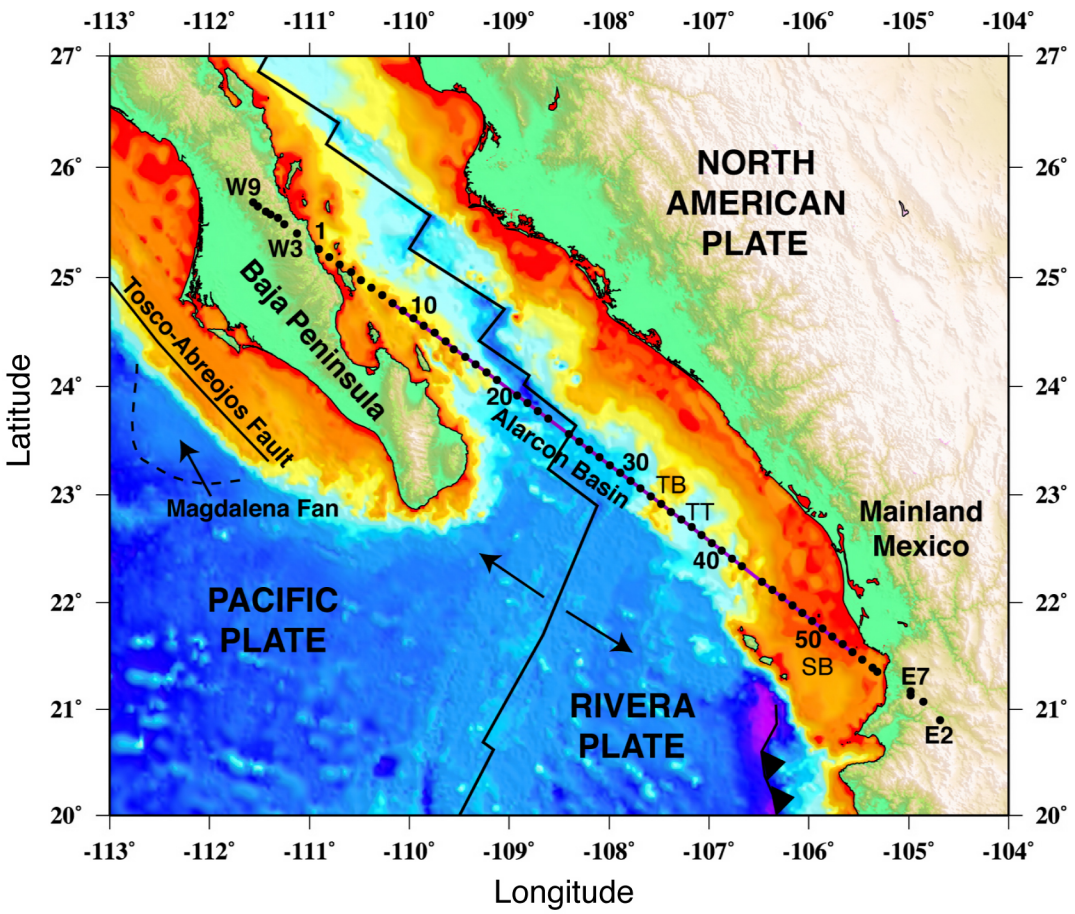

Figure III.1 Map of the southern Gulf of California showing instrument locations. PASSCAL (land) and ocean-bottom seismometers are shown in black. Shot line is shown in purple (from OBS 8 to 53). (TB= Tamayo Bank; TT= Tamayo Trough; SB= San Blas Basin).

assess the tectonic evolution of the Gulf of California (Figure I.2).

III.3 Refraction Data

The Ocean-Bottom Seismographs (OBS) deployed in this experiment were from the U.S. National Ocean Bottom Seismograph Instrument Pool (OBSIP). These OBS have two sensors: a broadband hydrophone (channel 1) and a 2 Hz vertical seismometer (channel 2). OBS were deployed from the R/V New Horizon and recorded energy from the R/V Maurice Ewing's 7860 in.^{3} array of

20 airguns, which was fired every 150 m (∼60 seconds). Refraction profiles were extended onto land using Ref-Tek 7000's from the IRIS-PASSCAL instrument center and a combination of mostly L22 (2 Hz) and some L28 (4.5 Hz) 3-component sensors. Coincident seismic reflection profiling provided depth estimates for key boundaries such as the seafloor and basement, and the velocity structure within the upper basement, which was incorporated into the velocity model *a priori*, and allows better resolution of model structure at depth than would otherwise be possible.

The 881 km wide-angle Alarcón transect consists of data from 64 working instruments: 53 OBS and 11 PASSCAL seismographs. This profile begins at 0 km on the Baja peninsula at -111.561^{o}E, 25.682^{o}N, and crosses the Gulf of California to the southeast, where it ends near the city of Tepic on mainland Mexico at -104.685^{o}E, 20.888^{o}N (Figure III.1) (see Appendix A for further details). OBS were deployed at 12.5 km intervals, and three OBS (19, 24, and 43) did not yield data, producing 25 km OBS spacing in those positions. PASSCAL seismograph spacing varied due to difficulties with land access and terrain. OBS data quality was high except in very shallow water ($<$ 50 m), with pickable arrivals recorded out to offsets of 90 km or more from the instruments. Data were processed with a 5-15 Hz minimum phase bandpass filter and predictive deconvolution. To relocate the seafloor instruments, the direct water wave was picked and iterations were started at the OBS drop point until an optimum location was found. Due to operational difficulties during the experiment, shooting only covered a 600 km central portion of the transect (Figure III.1), OBS 01-07 and 54-56, as well as all PASSCAL seismographs, had no zero-offset shots so drop point positions were used. After relocation, significant deviations from the transect were found for OBS 11, 12, 13 and 14, with 14 being the farthest off line (1 km); it seems likely that strong currents were the cause of these discrepancies. The largest off-axis deviations along the profile are from the PASSCAL seismographs, which had to be

deployed along available access roads, these problems were particularly significant for the mainland Mexico instruments, where both E7 and E9 are 5 km off-line and E8 is 2.3 km off-line.

Land-based PASSCAL seismograph locations were found with handheld GPS units, and coordinates were checked upon deployment and retrieval for accuracy. Although 3-component sensors were deployed the vertical component is all that was used for this analysis. 16 seismographs were deployed, however problems with some mainland Mexico instruments resulted in useful data on only of 4 out of 9. All 7 PASSCAL seismographs deployed on the Baja peninsula recorded shots from the R/V Ewing. The land-based data were also processed with predictive deconvolution and a 5-15 Hz minimum phase bandpass filter. Data quality varied due to differences in ground coupling, environmental noise (e.g. traffic, animals) and nearest shot offset distance. All PASSCAL seismographs recorded strong Pn arrivals.

The main crustal phases (Pg, PmP and Pn) were picked where visible. Pg (the refraction through the crust) was visible on all OBS except 01, which had low signal-to-noise and a nearest shot-offset distance of 88 km, PmP (the reflection off the Moho) was visible on 87% of OBS, and Pn (the refraction through the upper mantle) was present on about 75% OBS and was mostly lower amplitude. Assigned errors were 0.050 seconds for Pg and 0.080 seconds for PmP and Pn arrival times. The largest problems were with PmP arrivals, in part due to the difficulty in picking a secondary arrival where there is cycle-skipping due to reverberation. The OBS over the oceanic crust have a clear single PmP arrival (e.g. OBS 26 (Figure III.7)), but over the extended continental crust the PmP arrival is more complicated (e.g. OBS 8 (Figure III.6), OBS 42 (Figure III.8)). Data and picks for each instrument are shown in Appendix B.

Table III.1 Errors in travel-time fits for velocity model. Sections are divided by areas with no zero-offset shots (PASSCAL W9- OBS 7 (total 14 instruments)), extended continental crust on Baja (OBS 8-20), oceanic crust (OBS 21-31), extended continental crust on mainland margin (OBS 32-53), and instruments with no zero-offset shots on the mainland margin (OBS 54-PASSCAL E2 (total 7 instruments)). RMS error in seconds with number of data points in parentheses.

Stations	All phases	Pg error	PmP error	Pn error
Baja (W9 - 07)	0.123 (6034)	0.115 (745)	0.233 (1026)	0.085 (4298)
NW Margin (08 - 20)	0.111 (9572)	0.091 (5214)	0.136 (3667)	0.110 (1385)
Oceanic Crust (21 - 31)	0.086 (7445)	0.065 (4053)	0.117 (3282)	0.077 (920)
SE Margin (32 - 53)	0.170 (17290)	0.133 (9606)	0.181 (5886)	0.278 (1310)
Mexico (54 - E2)	0.171 (2930)	0.144 (812)	0.212 (792)	0.159 (1336)
All Instruments	**0.140** (44938)	0.112 (20636)	0.165 (14401)	0.153 (9924)

III.4 Velocity Model

A velocity model with 5 layers: ocean, sediment, upper crust, lower crust and mantle, was constructed using the ray-tracing and inversion code of Zelt and Smith (1992). Each layer is defined by a top and bottom boundary, with velocities defined at the top and base of each layer. A linear velocity gradient is imposed between the various nodes within a layer and discrete velocity jumps are allowed at layer boundaries. Initial model constraints for the seafloor/ land topography were derived from a combination of shipboard and satellite data (P. Lonsdale, *pers. comm.*, Smith and Sandwell (1997)) and basement topography from the MCS profile between 167-767 km along transect. The Pg refraction arrival at small offsets, usually less than 6 km from the instrument, constrains upper crustal velocity; the change in gradient to the main crustal Pg arrival constrains the depth of the upper crust/ lower crust boundary. Unfortunately the areas lacking MCS data

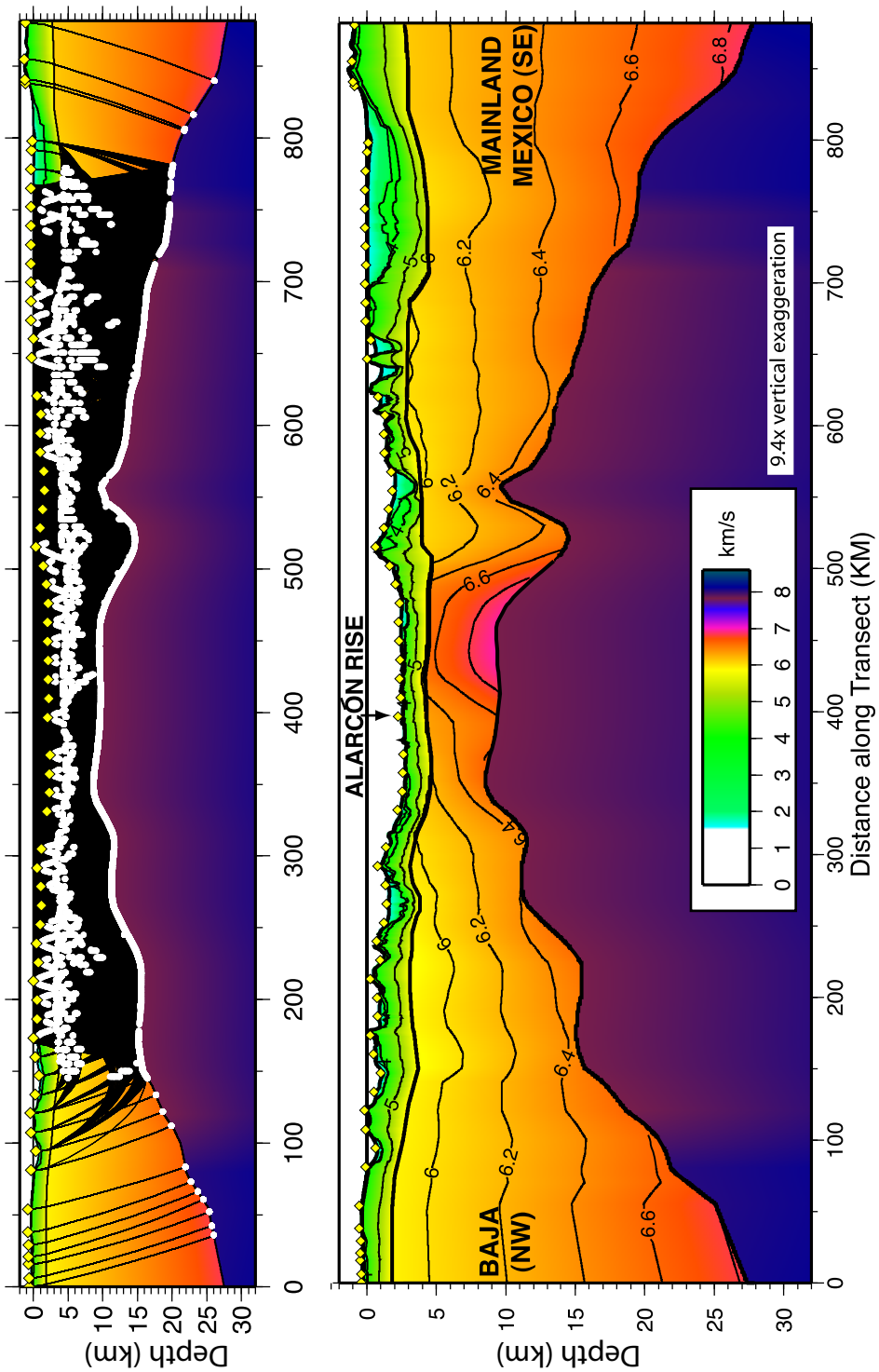

Figure III.2 Seismic velocity model across the Alarcón transect. The upper plot shows every 20th ray and its bottoming point to illustrate ray coverage.

to constrain the upper crust are also the areas where there are no corresponding refraction arrivals (no shots were fired over the instruments), consequently the upper crust before 167 km and after 767 km is poorly constrained compared to the majority of the model. After a best estimate of the upper crustal velocity structure was obtained, the Pg arrivals from the lower crust were modeled. The reflection off the Moho (PmP) and the refraction through the upper mantle (Pn) were then modeled together. The uncertainties in the predicted travel-times for both of these arrivals are larger, as they are affected by uncertainties in the crust as well as uncertainties in Moho topography and upper mantle velocity. The upper crustal velocity structure is difficult to represent accurately in this large scale model due to the sparse instrument spacing; analysis of common-midpoint (CMP) supergather results (Figure II.11) show the top of the basement is complicated with multiple layers that cannot be realistically included in a crustal-scale velocity model. The uncertainties by section and phase are shown in Table III.1. Errors on the NW side of the model and in the oceanic crust are significantly less than those on the SE margin. Larger errors on the SE margin are the result of the poorer data quality on OBS 47- 56 and difficulties in resolving the structure of the multiple deep basins. The velocity model (Figure III.2) has an overall RMS error of 0.140 seconds, χ^2 of 4, with 45,000 data points (travel-time picks).

III.4.A Crustal velocity in areas of low data coverage

The largest uncertainties in the model are past the end of the shot lines on both the Baja and mainland sides. All land seismographs recorded strong Pn arrivals (e.g. W7 shown in Figure III.6) which provide information about Moho depth, but without an independent constraint on crustal velocities, Moho depth can be traded off against crustal velocity. The final model (Figure III.2) was chosen to avoid large lateral changes in crustal velocity structure (continuous velocities and velocity gradients) between the extended margins, where we have good data

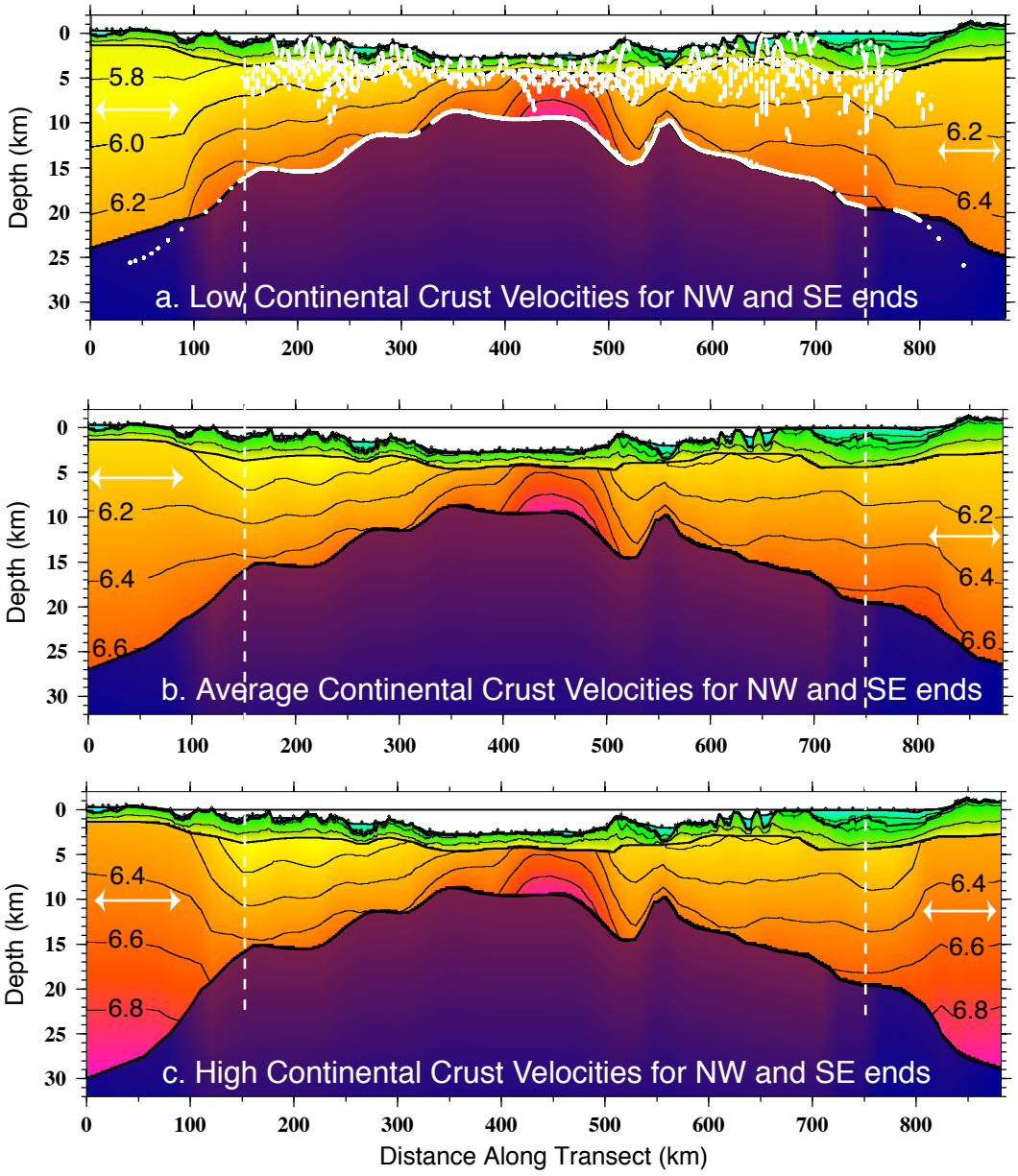

Figure III.3 Velocity models with low, average and fast continental crustal velocities at the ends of the model. Dashed white lines indicate limits of good ray coverage (150-750 km) (Figure III.2), and white arrows show the distance over which velocity was changed to match with continental velocities. Contours are labeled in km/s. (a) Crustal velocity gradient between 5 and 25 km depth is 5.7-6.3 km/s. Pg coverage on the mainland margin prohibited the lowest crustal velocities being below 6km/s. (b) Average crustal velocity with a gradient from 6.0-6.65 km/s. (c) High crustal velocities with gradient 6.25-6.95 km/s.

coverage, and the unextended continental crust at the edges of the model. To investigate the uncertainties in these regions further, low (5.7-6.3 km/s), average (6.0-6.65 km/s) and high (6.25-6.95 km/s) estimates of continental crust velocity gradients between 5 and 25 km depth from Christensen and Mooney (1995) were used to create three models (Figure III.3). Crustal velocity structure was defined from these gradients between 0-80 km and 800- 880 km, and velocity gradients between these regions and the well constrained velocities between 150 and 750 km were smoothed. The only exception was that the low velocities did not fit with the Pg arrivals for E7, E8 and E9, and hence the lowest velocity beneath mainland Mexico is 6 km/s. The Moho was adjusted accordingly to fit the data at the edges of the model. For the Baja margin these three models produce crustal thicknesses of 24, 27 and 30 km (for low, average and high lower crustal velocities respectively), and for mainland Mexico the crustal thicknesses are 25, 27 and 30 km. Overall, the data fits of high-velocity and average-velocity models are comparable to the model shown in Figure III.2, but the low continental velocities increase the RMS error to 0.153 seconds. There are two main reasons why the low velocity model (Figure III.3a) is unlikely. Firstly, unless there has been significant magmatic activity and intrusion, extended continental crust is expected to be slower than unextended crust. But the observed velocities of the extended continental crust, which average about 6.3 km/s, are not high enough to indicate significant magmatic intrusions, which typically increase velocities to around 7 km/s (McKenzie and Bickle, 1988). Secondly, 24 km crustal thickness beneath the Baja peninsula is very low for the original, unextended crustal thickness. Average continental crustal thickness worldwide is 40 km (Christensen and Mooney, 1995), and receiver functions on the Baja peninsula indicate crustal thickness in the center of the peninsula to be 27- 35 km (Persuad et al., 2005). Aside from the observation that the average continental crustal velocities (Figure III.3b) are closer to the known velocity structure in the main part of the model, there is no strong reason

to prefer either the average or high continental velocity model (Figure III.3b,c). The high continental velocities require an increase of 3 km in crustal thickness, but the gradient is lower than used in the original model; where to keep contours flat the velocity increases from 5.9 to 6.8 km/s.

III.4.B Gravity

The predicted gravity from the seismic crustal structure model was calculated to compare with the observed free-air anomaly. The primary aim of modeling gravity was to provide an additional check of Moho depth along the profile to compare with the crustal structure obtained from the refraction data and to investigate the poorly-constrained edges of the model. For the crust, velocity was converted to density using the relations of Lizarralde and Holbrook (1997). A thermal lithosphere was constructed to correspond to upwelling beneath the mid-ocean ridge and rifted margins with cooling at the edges, which fits the long-wavelength portion of the gravity anomaly. This method is only two-dimensional, and hence there are limits as to the accuracy that can be obtained in such a complex three-dimensional area, however most of the errors can be attributed to the sedimentary basins, which are associated with significant gravity anomalies.

The observed gravity anomaly is a combination of high resolution shipboard data from the R/V Ewing between 169 and 767 km, sea surface free air anomaly, and the land bouguer anomaly (Mexico 97 satellite data compiled by NOAA and INEGI on a 2' grid). Overall, the fit of the predicted gravity from the velocity model to the observed gravity shows good correlation, and is much more accurate where we have the ship data, and corresponding MCS data to provide knowledge of the sedimentary basins, than the lower resolution satellite data (Figure III.4a). The largest error is 100 mGal underneath mainland Mexico. Editing the upper crust cannot account for this discrepancy and the only way to reduce the predicted gravity anomaly by this amount is to increase Moho depth. As there

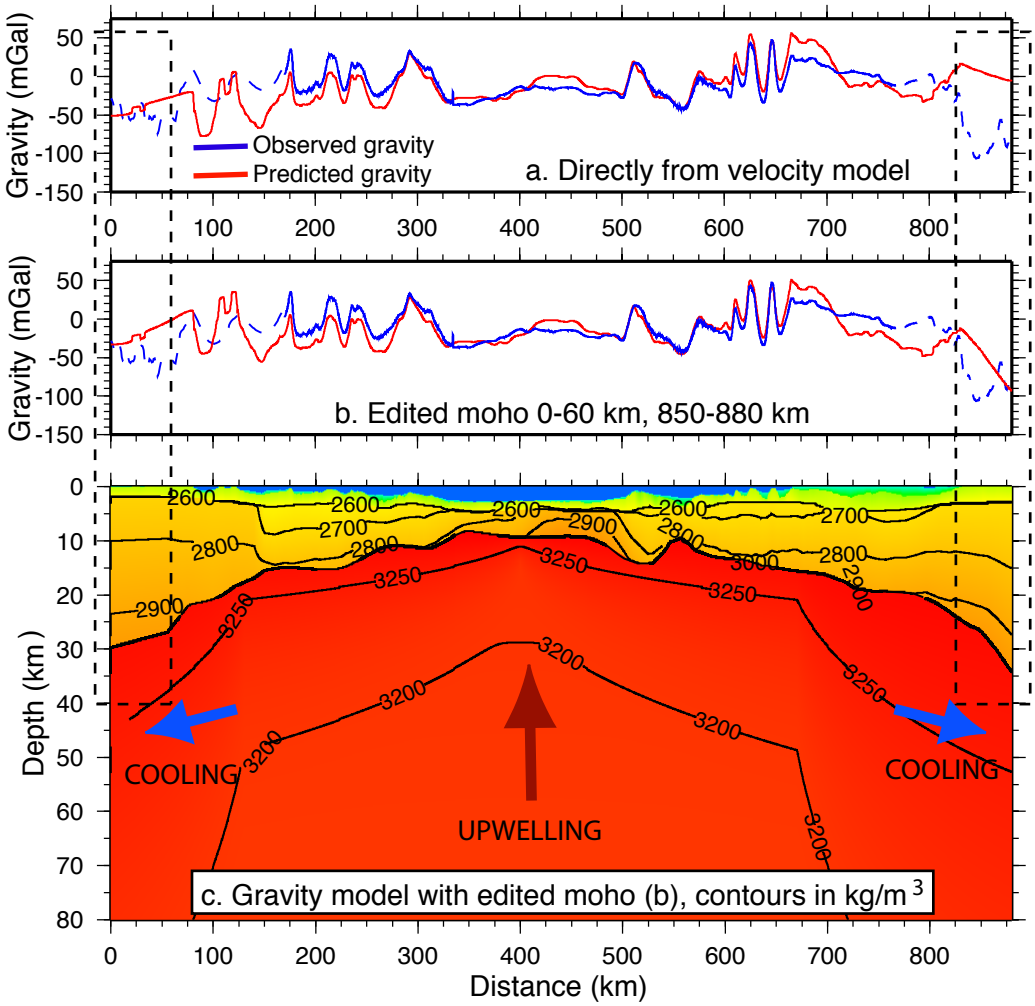

Figure III.4 Fit of predicted gravity to observed gravity for a direct conversion from velocity model (a) and after editing the Moho (b). The density model (c) consists of crust obtained by conversion from velocity to density, and including upwelling in the mantle. The solid line in plots a and b represents high resolution ship data, and the dashed line shows the 2', lower resolution satellite data.

is no seismic data coverage past 840 km (Figure III.2) on the transect, we have freedom to change this region without affecting the fit to the seismic data. On the Baja margin there is a reasonable fit to the gravity anomaly, but to explore the gravity signal of a thicker crust the increased velocity and Moho depth from the fast continental crust model (Figure III.3c) was substituted. Figure III.4c shows the density model used, with the Moho at 35 km depth at the SE end of the line,

and at 30 km at the NW end. The corresponding fit of the gravity anomalies at the SE end of the transect (Figure III.4b) is significantly improved; although there is a change in the predicted gravity anomaly beneath Baja, comparison with the long wavelength satellite data is difficult, and the fit seems to be similar in both instances. The gravity shows the overall crustal structure of the transect to be valid, and that a 27-30 km original crustal thickness under Baja is reasonable, but it is likely that the crust is still thickening past the SE end of our transect and we likely have not reached unextended crust beneath the end of the southeast conjugate margin. Thicker crust is observed further inland beneath mainland Mexico; estimates of crustal thickness in the Sierra Madre Occidental are 35-40 km (Nieto-Samaniego et al., 1999).

A third dataset that helps quantify original crustal thickness are the receiver functions calculated from the NARS-Baja seismic network (Persuad et al., 2005). This network has been installed around the Gulf of California since 2002; the stations only cover the northwest end of our transect, but there is good agreement; 24 km crustal thickness on the coastline of the Baja Peninsula is a good match to our model, and estimates in the center of the peninsula (although not close to our transect) range from 27 to 35 km, which span the estimated 27-30 km crustal thickness in the velocity model.

Gravity provides compelling evidence that, particularly on the southeast side of the profile, Moho should be deeper. Hence, our preferred crustal model is modified to correct for this, increasing original crustal thickness beneath Baja to 30 km, and beneath mainland Mexico to 35 km (Figure III.5).

III.4.C Seismic Velocity Model Description

The northwestern (Baja) rifted margin is ∼300 km wide. The limit of known extension from surface geology is the Main Gulf Escarpment on the Baja peninsula (Stock and Hodges, 1989), located on the transect between 40-60 km;

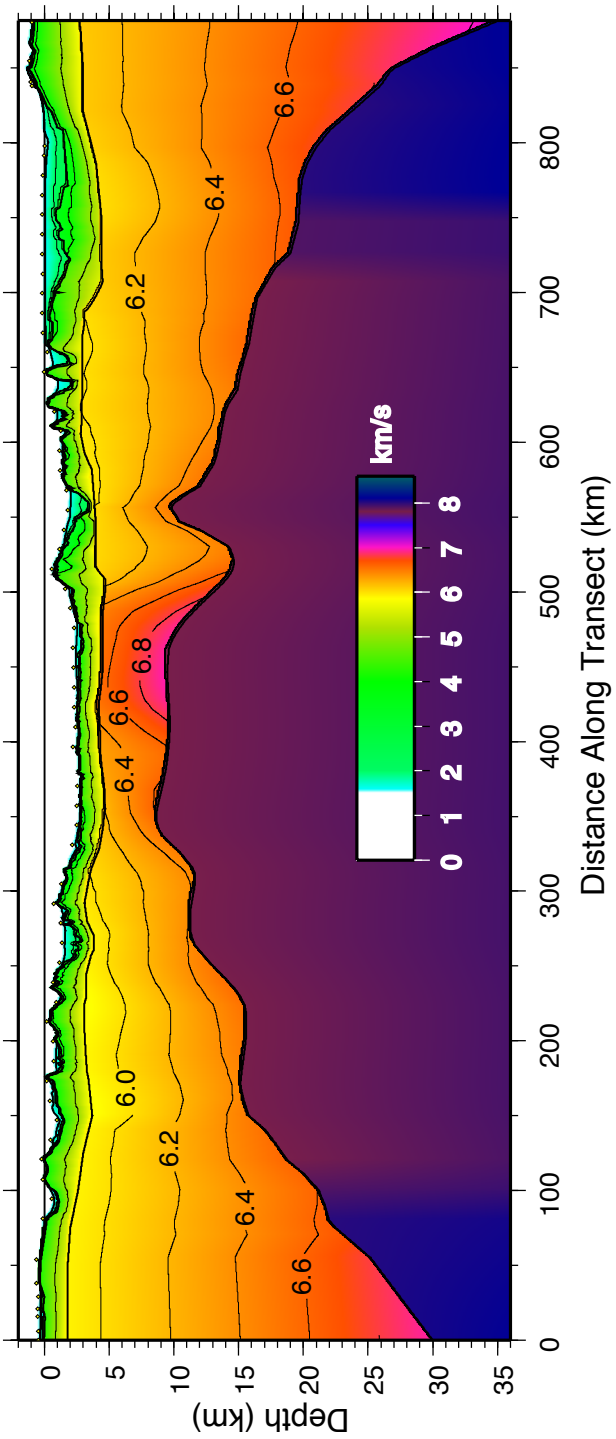

Figure III.5 Preferred seismic velocity model across the Alarcón transect updated after gravity analysis. The fit of the data to this model is the same the previous model (Figure III.2.

crustal structure indicates crustal thinning may begin around 45 km along transect. Magnetic anomalies indicate the transition to oceanic crust is complete by 345 km (Figure II.6). Underneath the Baja peninsula crustal thickness is approximately 30 km. The predicted travel-times for the preferred model (Figure III.5) produce good fits to the data: RMS error on OBS 08, the furthest northwest instrument with zero-offset data (Figure III.6) is 0.072 s and RMS error on OBS 15, located in the East Cerralvo Basin is 0.080 s. The extended continental crust on the northwestern margin has an average lower crustal velocity of 6.24 km/s (Figure III.9).

The Alarcón Basin spans 135 km and is expected to be typical oceanic crust, both based on magnetic anomalies (Figure II.6) and the chemical signature of the lavas recently erupted at the spreading center (Castillo et al., 2002). The Alarcón Rise spreading center is located 400 km along transect, and there is a marked asymmetry in the oceanic lower crust velocity structure. Northwest of the Alarcón Rise the average lower crustal velocity is 6.42 km/s and this increases rapidly south of the spreading center to 6.7 km/s. The northwestern oceanic crust is, on average, about 0.5 km thinner than that to the southeast. The good fits of the model to the data obtained for OBS arrivals over the oceanic crust provide confidence that this asymmetry is real (Table III.1), however it may be enhanced by the high velocity anomaly near the SE continent-ocean transition. Some of the details of this asymmetry were refined by tomographic modeling and will be discussed further in Chapter IV.

Southeast of the oceanic crust is the conjugate, mainland Mexico, rifted margin. This segment of the transect extends for 400 km, but it is unclear if we reach unextended continental crust or full continental crustal thickness at the southeastern end of our transect as the eastern limits of Gulf extension are not well known. The continent-ocean transition on the southeastern side is more complicated than the northwestern conjugate margin. Oceanic crustal thickness is present up to 470 km along transect, but our modeling of magnetic anomalies (Chapter

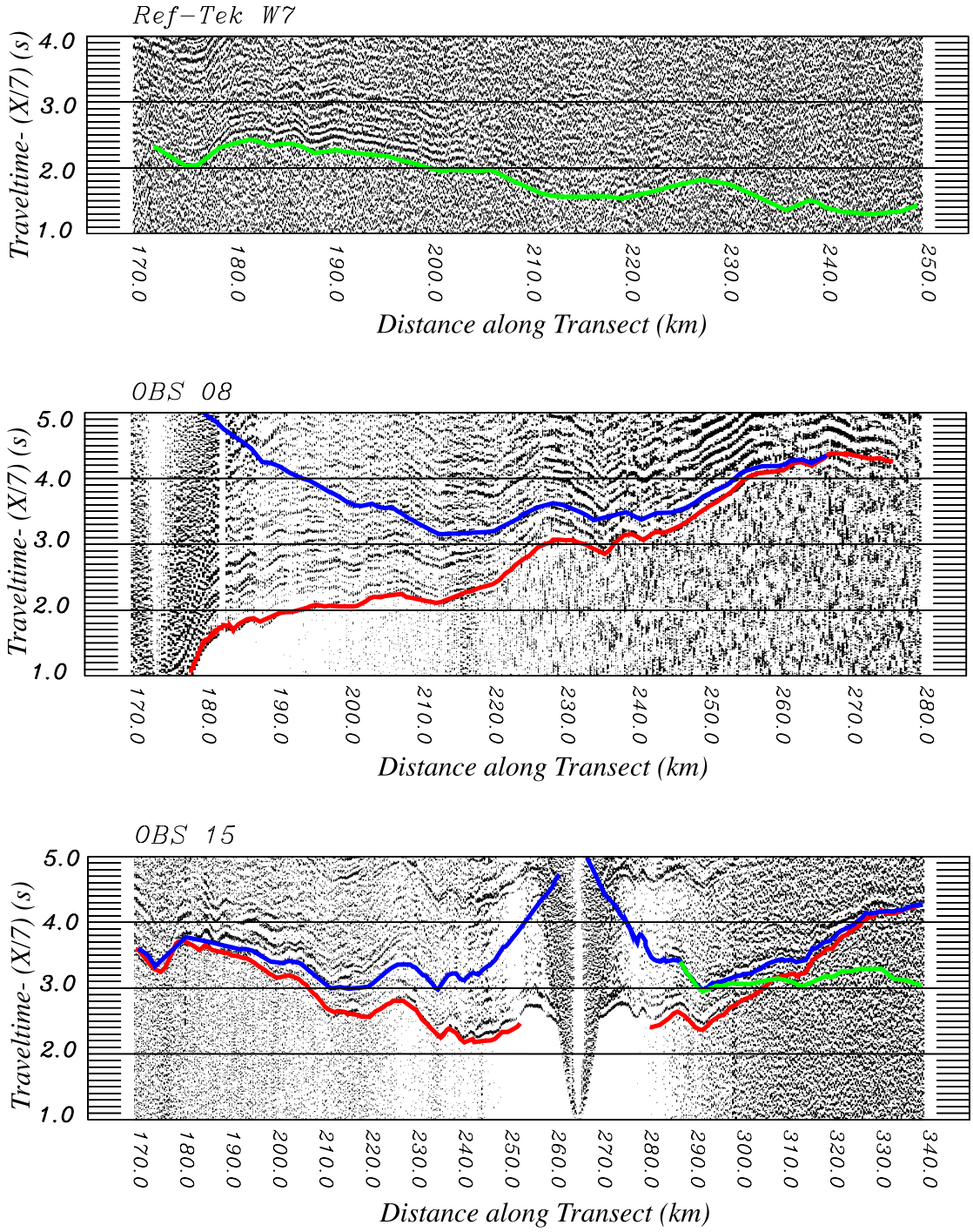

Figure III.6 Predicted travel times through velocity model (Figure III.2) for one Ref-Tek on Baja, OBS 08 and 15 on the Baja Margin. Pg(red), PmP(blue), and Pn(green) phases are shown.

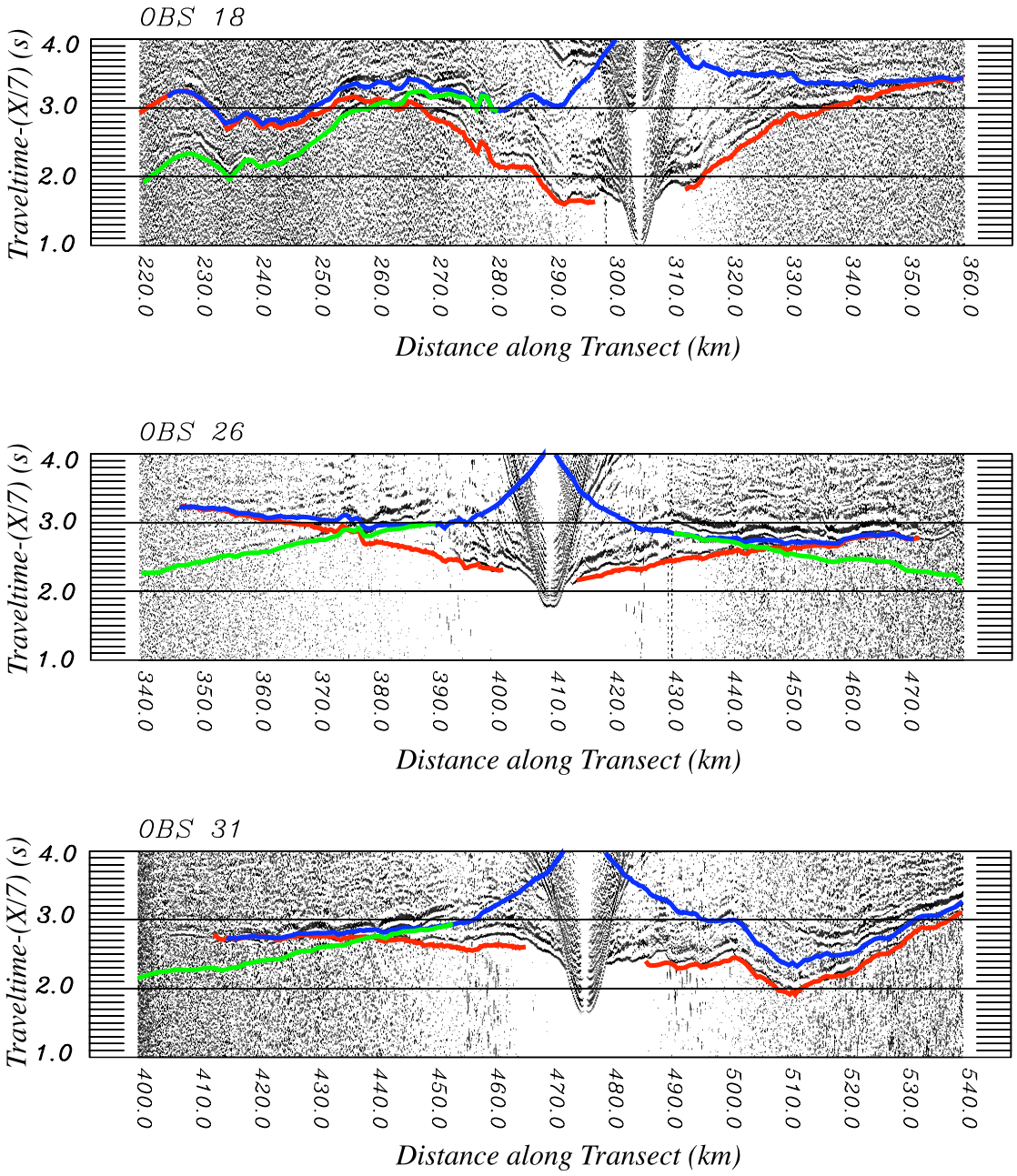

Figure III.7 Predicted travel times through velocity model (Figure III.2) for OBS 18 on the Baja Margin, OBS 26 on the oceanic crust of the Alarcón Basin and OBS 31, near the SE continent-ocean transition. Pg(red), PmP(blue), and Pn(green) phases are shown.

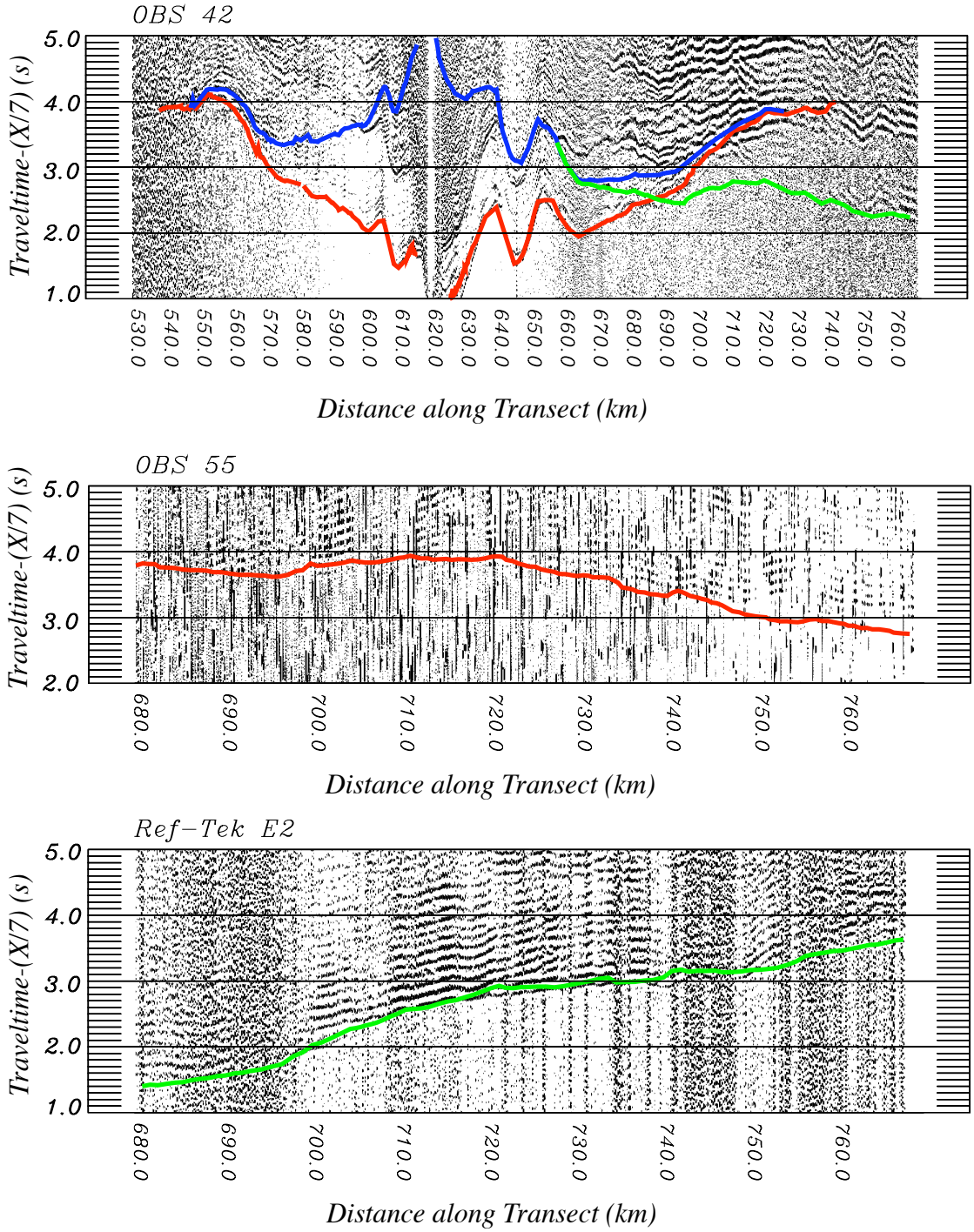

Figure III.8 Predicted travel times through velocity model (Figure III.2) for OBS 42 and 55 (in very shallow water) and Ref-Tek E2. Pg(red), PmP(blue), and Pn(green) phases are shown.

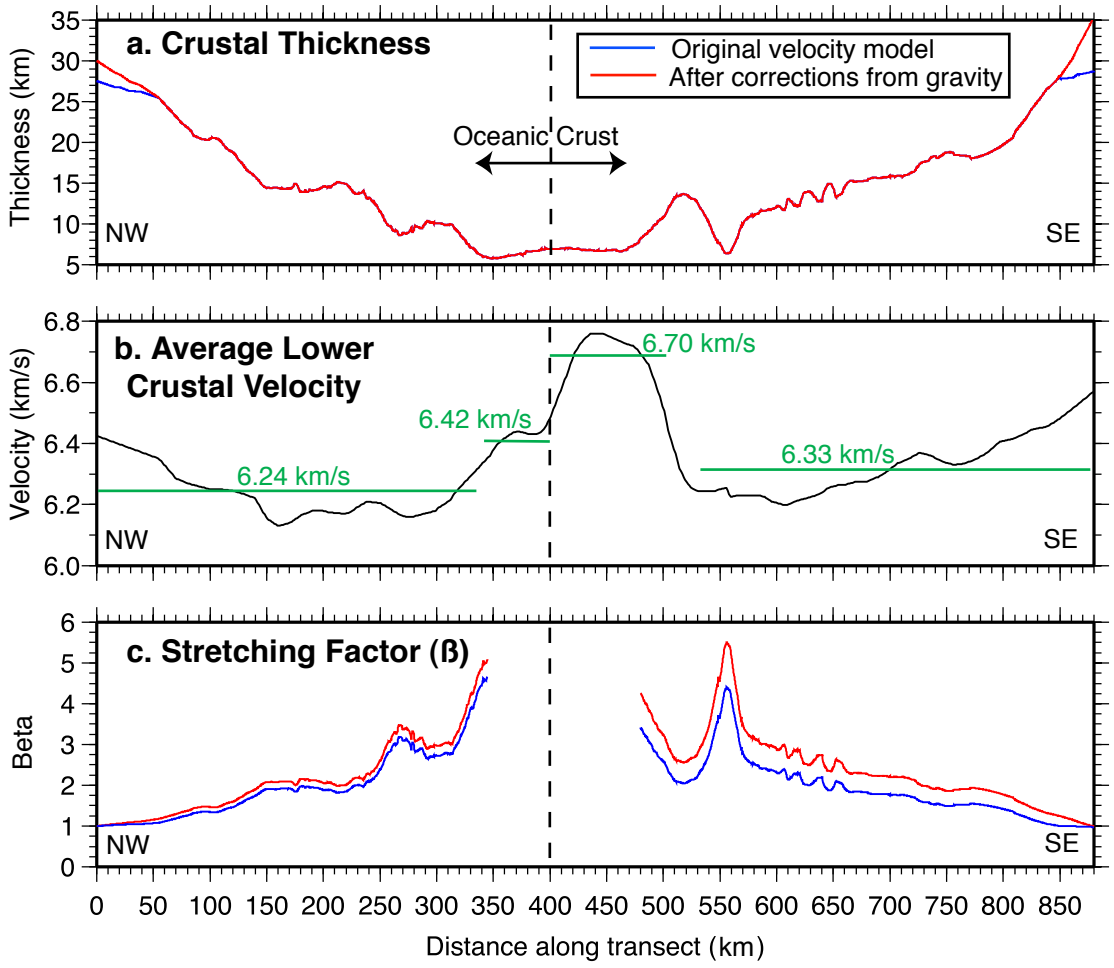

Figure III.9 Variations in crustal thickness(a), average lower crustal velocity(b) and stretching factor(c) across the Alarcón transect. Crustal thickness and stretching factors have been calculated for both the initial velocity model (blue, Figure III.2), and the preferred velocity model (red, Figure III.5). The average velocity of both margins and sides of the oceanic crust are indicated in green, and show that the northwest margin is slower than the southeast margin.

II) indicates the continent-ocean transition probably occurs 480 km along transect (Figure II.6). The high velocities associated with oceanic crust also continue out past 480 km along transect into the thicker crust, but drop off rapidly at 500 km to an average of 6.33 km/s across the extended margin (Figure III.9b). An important feature on the southeast margin is a crustal keel and high-standing continental

block 520 km along transect with ∼14 km thick crust; this feature is flanked toward the continent by crust which has been highly thinned to ∼7 km at 550 km along transect (Figure III.9a), coincident with the Tamayo Trough, a 1.5 km deep sedimentary basin. Reflections off the top of the raised Moho are shown in Figure III.7 on OBS 31. Beyond the Tamayo Trough, we observe a smooth increase in crustal thickness with an average lower crustal velocity of around 6.3 km/s. The Moho drops down around 840 km to accommodate Pn travel-times on Ref-Tek E2, and gravity beyond 840 km indicates the Moho deepens to 35 km (Figure III.9a). The inferred ∼5 km difference between original crustal thicknesses beneath Baja and mainland Mexico is probably indicative of the heterogeneous nature of the crust in the southern Gulf of California prior to rifting.

III.5 Continental Extension

III.5.A Extension across the Alarcón Transect

The overall amount of extension across the Alarcón transect is characterized by the stretching factor, denoted by β, and is simply the ratio of the width of the margin after extension divided by its width before extension. The original margin width is calculated by dividing the area of continental crust deduced from Moho and basement boundaries, by the original crustal thickness before extension, taken from the edges of the model. The final model (Figure III.5) and low, average and high continental crust velocity models (Figure III.3), are used to investigate the uncertainty in the estimates of extension. Extension on the northwestern margin is taken to begin around the main Gulf escarpment (Stock and Hodges, 1989), and from the Moho structure it appears extension begins 45 km along the Alarcón transect and continues to 345 km, where the magnetic anomaly (Figure II.6) and crustal structure indicate the transition to oceanic crust. It is unclear if unextended continental crust is reached on the conjugate southeastern

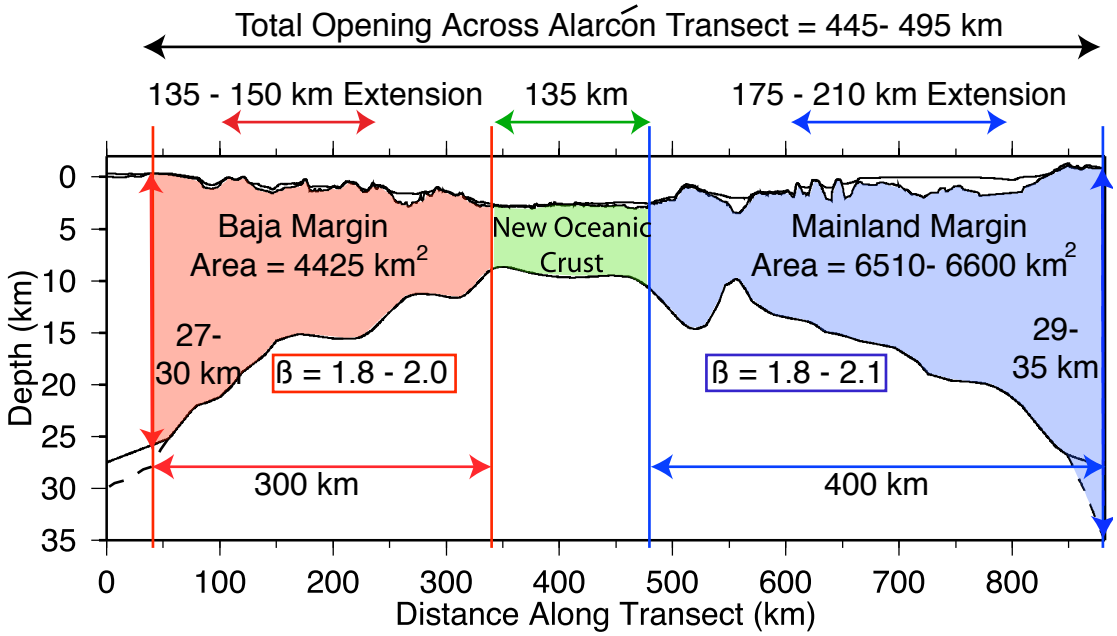

Figure III.10 Calculation of extension by area balance across the Alarcón margin. The preferred model, following gravity analysis is used (Figure III.5).

margin, but considering the normal faulting observed onshore (Ferrari and Rosas-Elguera, 1999) it seems appropriate to assume that extension continues to the end of our transect and that our calculated extension on the southeastern margin is an underestimate. The continent-ocean transition occurs 480 km along transect (Figure II.6), giving us an extended margin width of 400 km. The total opening across the transect is the sum of the extension across each margin and the width of newly created oceanic crust (135 km).

Estimates of extension from the final velocity model (Figure III.5) yield stretching factors of β=2.0 for the northwest margin and β=2.1 for the southeast margin, producing a total of 495 km total opening across the Alarcón transect (Figure III.10). The models from the low, average and high continental crust velocity estimates (Figure III.3) produce lower overall estimates: The low velocity model, with a consequently thinner original crustal thickness gives β=1.65 on the NW margin and β=1.60 on the SE margin, which produces an estimated opening of 400 km. The average model has β=1.65 (NW) and 1.80 (SE), producing 430

km opening, and the high velocity model, with a thicker crust before extension has β= 2.0 (NW) and 1.8 (SE), with a resulting total opening of 460 km. None of these models predicted 35 km crustal thickness beneath mainland Mexico, which does have a significant affect on the estimated amount of extension, increasing it by around 30 km.

The estimate from the preferred model (Figure III.5) for total opening across the Alarcón Basin is 495 km. The absolute minimum is 400 km, but, for the reasons mentioned above it is doubtful that the low velocities underlying this estimate accurately represent true crustal velocity structure. In addition, the likelihood of extension beyond the SE end of the model would likely make this a poor minimum estimate. Hence, our minumum estimate of opening across the Alarcón basin is 430 km.

III.5.B Regional Extension

The oblique nature of rifting in the Gulf of California has created three-dimensional (3D) extension, and this extension is separated in short segments, which are bounded by transform faults. To investigate if there if the amount of extension measured across the Alarcón transect is typical for the southern Gulf of California, the bathymetry/elevation and Moho information from the seismic velocity model were used to estimate 3D Moho depth. Assuming the region is isostatically balanced, a bathymetry to Moho depth relation has been calculated from the 2D transect and applied to a 3D satellite bathymetry/topography grid, producing a regional map of Moho depth from 20^o- 27^o N (Figure III.11). A second order polynomial fit was used to estimate the relation of bathymetry/topography to Moho depth from the velocity model:

$$Moho = 21.02 - 8.52z + 1.71z^2 \qquad \text{(III.1)}$$

(z=bathymetry/elevation (km))

Bathymetry depths greater than 2.45 km were taken to be oceanic crust, and assigned a Moho depth of the mean Moho depth of the Alarcón Basin (9.47 km below sea level). Calculations of extension by area balance along multiple transects parallel to Line 1 (Alarcón) (Figure III.11) were done with the original crustal thicknesses from the original model as a minimum (27 km for Baja; 29 km for mainland Mexico) and maximum crustal thicknesses (30 km for Baja; 35 km for mainland Mexico) from the preferred crustal model after gravity analysis. Results of the minimum and maximum stretching factors (β) and total opening (amount of extension on both margins plus width of oceanic crust) are shown in Table III.2. Extension is taken to begin around the main Gulf escarpment on Baja and end in an approximately equivalent position topographically to the end of Line 1. The amount of extension is under-estimated by 10-15 km for Line 1, which suggests that these results may provide a slightly low estimate of extension. To further investigate the accuracy of this analysis, the amount of extension over Line 0E, one of the additional transects of seismic data collected in the Gulf of California experiment which is oriented perpendicular to the coastline (Figure III.11), was also estimated. The amount of extension across Line 0E estimated from crustal structure is 60-90km (Paramo et al., 2006). This analysis provided estimates of 57-76 km, which is in good agreement, but also slightly lower than observed.

Transects A- F show similar results with no pattern of total opening increasing or decreasing moving from north to south, the spread of results can be attributed to errors in the bathymetry to Moho depth conversion as well as errors in the estimated geographic limits of extension. Transect G is outside of the Gulf proper, and shows asymmetrical rifting, however the total opening estimate is still in agreement with transects further north. On average rifting is quite symmetric, and each margin has experienced around 100% extension. The average minimum and maximum openings of 415 km and 475 km are in good agreement with the range of openings calculated for Line 1.

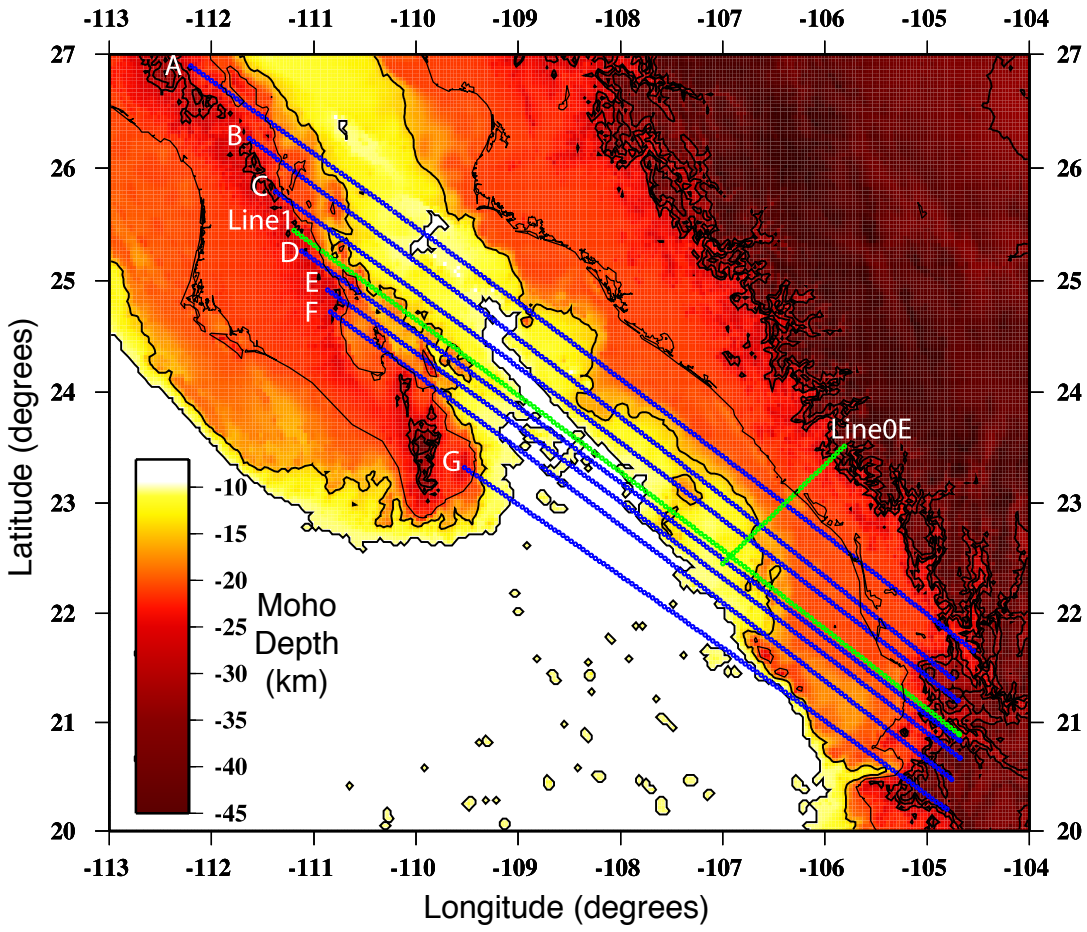

Figure III.11 Estimated Moho depth in the southern Gulf of California. The amount of extension across each transect is shown in Table III.2.

III.6 Discussion

III.6.A Rifting Style

The key observations from the model that can be used to assess rifting style are 1) similar stretching on both conjugate margins, 2) significant Moho topography (implying little to no lower crustal flow), 3) fast rifting velocity and 4) a small amount of magmatism in the areas of greatest stretching, but no large-scale rift-associated magmatism.

Table III.2 Minimum and maximum estimates of extension for multiple NW-SE transects across the Southern Gulf of California from estimates Moho depth (see Figure III.11) Average value is for transects A-F and Line 1.

Transect	Basin	Min. β NW	Min. β SE	Min. Opening (km)	Max. β NW	Max. β SE	Max. Opening (km)
A	Farallon	1.7	1.6	386	1.8	2.0	474
B	Pescadero	1.9	1.8	400	2.1	2.2	469
C	Pescadero	2.0	2.0	411	2.2	2.4	466
Line1	Alarcón	1.8	1.7	429	2.0	2.0	487
D	Alarcón	2.0	1.6	434	2.2	1.9	493
E	Alarcón	1.7	1.6	386	1.9	2.0	442
F	Alarcón	1.6	1.6	437	1.8	2.0	488
Average		1.9	1.7	415	2.0	2.1	474
G	EPR	1.4	2.4	432	1.5	3.0	451

Two end-member kinematic models are often used to characterize the extension of continental lithosphere: pure shear (McKenzie, 1978), where the whole lithosphere deforms uniformly by ductile deformation creating symmetric margins, and simple shear (Wernicke, 1984) where a large-scale detachment fault cuts through the lithosphere producing an asymmetric margin, with mid-lower crustal material on one side and faulted upper crust on the conjugate. Geodynamical models provide more realistic models and provide more insight into the factors that control rifting. For example, (Huismans and Beaumont, 2003) observe that the main controlling factors are the relative strengths of the crust and mantle; if the crust dominates the rifting process, usually asymmetric margins are produced, whereas if the ductile mantle dominates, rifting is generally symmetric.

Our interpretation is that rifting across the Alarcón Basin is symmetric, indicating a predominantly pure shear style of deformation. There is no evidence for lithospheric scale simple shear, which would move mid-lower crustal material close to the seafloor. Before the onset of seafloor spreading there appears to have been two areas of highly thinned crust (the Alarcón Basin and Tamayo Trough), separated by the strong crustal keel beneath the Tamayo Bank. Total extension

of 365 km over 11 Ma gives a strain rate of around 3 cm/yr. This is a reasonably fast rifting velocity, and the numerical models of Huismans and Beaumont (2003) suggest that a fast rifting velocity (their models use 10 cm/yr) of a cool margin always produces a symmetric result. This is because the mantle is the dominant rheology at fast speeds, and the mantle undergoes ductile deformation, which is inherently symmetric.

A key feature of this velocity model is the topography of the Moho. Moho relief implies that we have extension in the lower crust, but that we have no significant lower crustal flow. It seems likely that Moho relief, especially on the northwestern margin, was created by crustal scale faults and there has been no lower crustal flow to smooth out these features. For crustal scale brittle deformation to occur, the crust (and upper mantle) have to be cold. The Alarcón profile does not fit particularly well into the narrow, wide and core complex rifting categories of Buck (1991). We have distributed extension occurring over a region that was 350 km wide before the onset of rifting, and the extended margins now span a total of 700 km, but we have cold lithosphere and relatively thin (30-35 km) original crustal thickness, which would usually create a narrow rift. Wide rifts are typically associated with high heat flow, which produces lower crustal flow (Buck, 1991), so despite the physical scale of extension, the southern Gulf of California is in not a wide rift. It is possible that the highly oblique nature of rifting in the Gulf of California creates a wide rifting mode because we cannot have a single fault orientation to accommodate extension, and rather, requires a suite of faults (McClay and White, 1995).

Although the method of rifting itself was non-volcanic, there was significant arc volcanism immediately preceding, and likely overlapping with the onset of extension. The velocity structure of the crust does not indicate any large scale intrusions, but there is an area of higher velocity at the southeast continent ocean transition, which is likely the location of seafloor spreading initiation. The Gulf of

Table III.3 Comparison of the amounts and distribution of Pacific-North America plate separation in the traditional and alternative models for the tectonic evolution of the Gulf of California

Model	Total plate separation	Region	14-12 Ma	12-6 Ma	6-0 Ma
Traditional	600 km	Tosco-Abreojos fault	0	300 km	0
		Gulf of California	0	some E-W Extension	300 km
Alternative	700 km	Tosco-Abreojos fault	∼50 km	∼150 km	0
		Gulf of California	∼50 km	∼150 km	300 km

California has experienced a rifting duration of around 9-12 Ma. We infer from the moho structure that the lithosphere was cold, and therefore would expect no higher than normal mantle temperatures. Under these circumstances melt will only be produced in areas with stretching factors equal to or greater than 4 (Bown and White, 1995). The only regions where this occurs are the continent-ocean transitions and beneath the Tamayo trough. The Gulf of California is also a very oblique rift, where extension is concentrated along short segments with longer transform offsets and this could inhibit large-scale upwelling of mantle material, decreasing melt production.

III.6.B Implications for Tectonic Evolution

We observe around 495 km of opening (360 km extension; 135 km new oceanic crust) across the southern Gulf of California, with a minimum estimate of around 430 km opening (295 km extension). When compared to the two models of tectonic evolution (Table III.3), it is clear that this amount of opening (the distance the Baja peninsula has moved away from mainland Mexico) does not fit with the traditional model of tectonic evolution for the Gulf of California, as we observe up

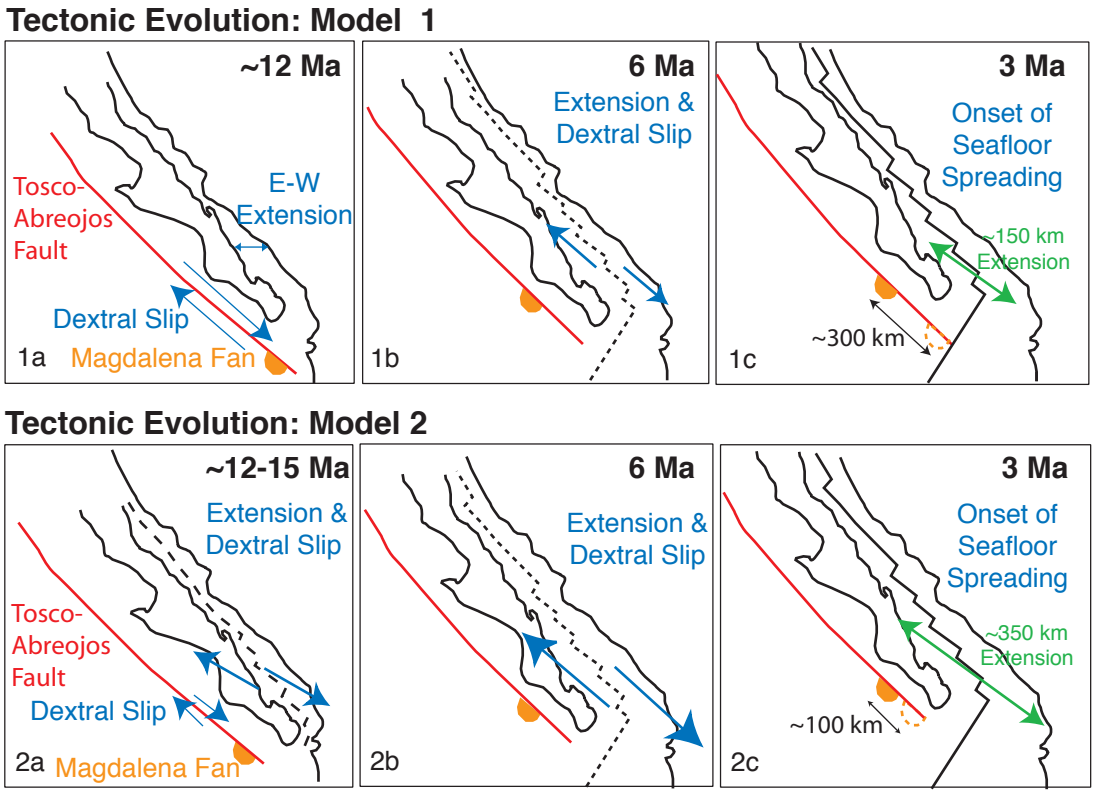

Figure III.12 Two models for the tectonic evolution of the Gulf of California. Tectonic model 1 is the traditional model, where there was limited east-west extension between 12-6 Ma in the Gulf region and 300 km slip on the Tosco-Abreojos fault. At 6 Ma the strike-slip motion jumped inboard initiating oblique extension. In this model there is ~150 km extension in the Gulf before seafloor spreading. Tectonic model 2 has oblique extension beginning around 12-15 Ma, with no 2 stage extension and ~350 km extension in the Gulf before seafloor spreading. In the two-stage model the original position of the land that now comprises the Baja Peninsula was further north than in the initial oblique rifting model.

to 200 km more extension in the Gulf than the traditional model requires. The only way to accommodate the extra 200 km extension within the Gulf in the traditional model is to place it in the earlier Basin and Range extension, before 15 Ma. Basin and Range extension was concentrated east of the Gulf of California, so overlap between Basin and Range and the Gulf extension would likely be seen at the SE end of this transect, and indeed some older, but not extensive faulting is observed on

mainland Mexico (Ferrari and Rosas-Elguera, 1999). Basin and Range extension was oriented east-west but the bathymetry of the mainland margin shows NW-SE oriented features (Figure III.1), the only exception being the San Blas Basin, which has no obvious orientation. Between the NW end of the San Blas Basin and the end of the transect (700- 880 km) average Moho depth is 22.5 km, giving a stretching factor β= 1.55, which provides 65 km extension in a NW-SE direction. This extension is not great enough to accommodate the discrepancy, leading to the conclusion that crustal structure across the Alarcón proves oblique extension and dextral slip must have begun in the Gulf of California before 6 Ma.

The mid-Miocene (11-14 Ma) marine incursion (McDougall, 2006) also suggests an early onset of extension in the Gulf of California, and along with the interpretation of extension in the upper crust (Chapter II), suggests that extension in the Gulf may have begun around 14 Ma. Starting the clock at 14 Ma increases the total amount of dextral slip between the Pacific and North American plates to 700 km. Subtracting 500 km of opening across the Alarcón segment from this 700 km leaves 200 km of Pacific-North America plate motion. This 200 km could either be accommodated by slip along the Tosco-Abreojos, or divided between the Tosco-Abreojos and extension past the southeast extent of the Alarcón profile. Either way, there is at least 100 km less slip on the Tosco-Abreojos and San Benito faults than originally thought. Some E-W extension is needed to complete the vector triangle from plate tectonic reconstructions (Atwater and Stock, 1998). North-south trending normal faults are seen at the edge of the extension zone on Baja, but these can be accommodated within the complex fault patterns of oblique rifting (McClay and White, 1995), and are observed synchronous with oblique extension along the eastern boundary of the Sierra Nevada (Unruh et al., 2003). A proposed updated model of tectonic evolution following analysis and interpretation of the MCS and wide-angle data across the Alarcón basin is shown in Figure III.13. We have the initiation of the new Pacific- North America plate

boundary at or near 14 Ma, which creates 700 km total Pacific- North America separation up to present. Between 14 and ∼6 Ma there was dextral slip on the Tosco-Abreojos fault synchronous with dextral slip and NW-SE extension in the Gulf of California. This extension began while the Comondú arc was still active and faulting produced the San Blas basin, Tamayo trough, and possibly slightly later, the East Cerralvo basin. The extension experienced was sufficient to cause enough subsidence to allow a mid-Miocene marine incursion. Around 6 Ma movement on the Tosco-Abreojos fault ended, and the Gulf of California became the only location of the Pacific-North America plate boundary. At 6 Ma the southern Gulf of California had already experienced 200 km of extension, and by the onset of seafloor spreading in the Alarcón around 2.5 Ma (Chapter II), the northwestern margin had undergone about 150 km of extension and the southeastern margin about 210 km of extension. Dating of zircons in the Magdalena fan indicate that it has translated a maximum of 150 km north from it source location (Fletcher et al., 2006), so it is possible that there is an extra 50 km of extension, possibly located to the southeast of this dataset. We do not know if movement on the Tosco-Abreojos fault and extension within the Gulf were completely synchronous, or if there was some alternation between the two: it is possible plate motion was originally located in the Gulf, then became more focused on the Tosco-Abreojos fault for a while before becoming concentrated in the Gulf again at 6 Ma.

III.6.C Comparisons to Central and Northern Gulf of California rifting

There appears to be a fundamental difference between the way the continental crust extended in the southern and northern Gulf of California. The southern Gulf (south of approximately 26.5^{o}N) consists of the Alarcón, Pescadero, Farallon and Carmen Basins. Although only the Alarcón has been shown to be undergoing magmatically robust seafloor spreading, all these basins are bathymet-

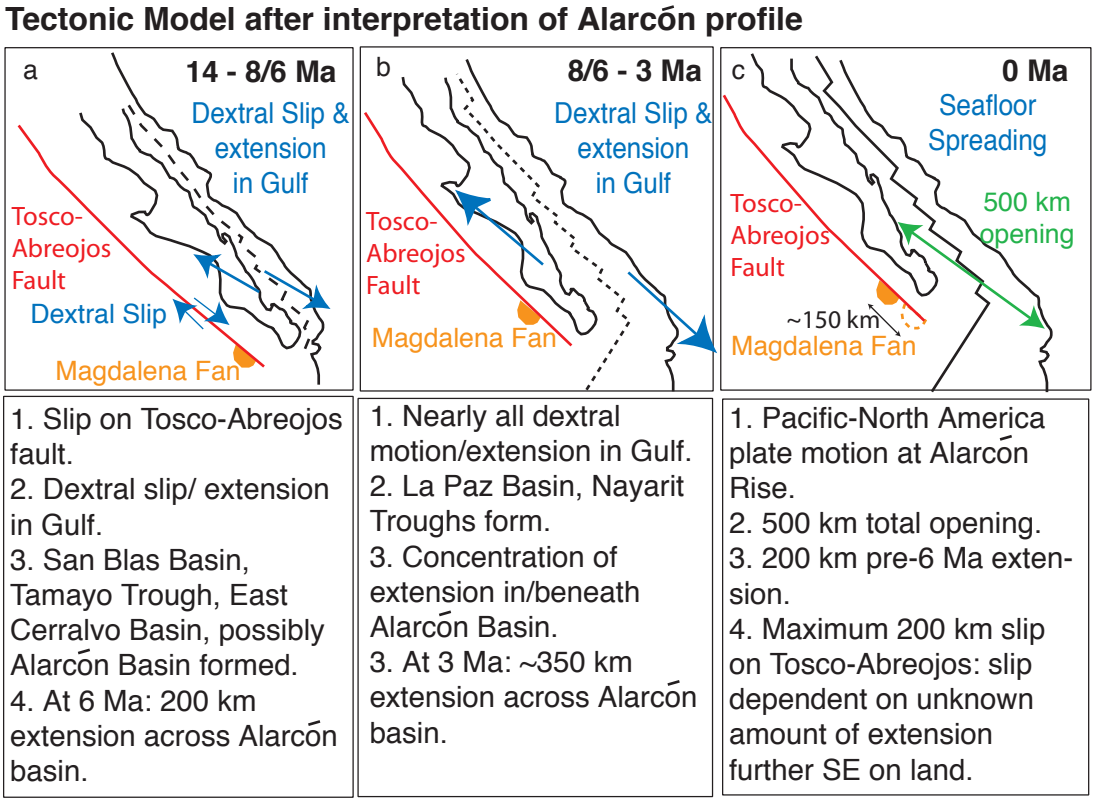

Figure III.13 Revised model of tectonic evolution of the Gulf of California.

rically deep. However it appears that the basins in the southern Gulf which are north of Alarcón may be melt-starved, which is preventing them from creating thick oceanic crust. The continent-ocean transition at Alarcón shows immediate creation of normal oceanic crust, which suggests that melt was already present at the end of rifting. Why this was not the case with the basins further north is unclear. If melt was created by decompression in areas of greater extension at Alarcón, melt would also have been created in the Pescadero, Farallon and Carmen Basins, as these basins are deeper than Alarcón, indicating high degrees of stretching (Table III.2). A more likely explanation is that the proximity of Alarcón to active seafloor spreading and upwelling at the East Pacific Rise helped with melt generation, but the long offsets between short the spreading centers inhibited melt from moving further north.

There is a significant change in rift style from the Guaymas Basin northwards. Rifting in the Guaymas Basin appears to have been quick, with none of the large extensional basins seen across Alarcón. The maximum stretching factor is β=1.75, significantly less than the regions of β>4 seen across Alarcón, and it seems new igneous crust began to be created ∼6 Ma (Lizarralde et al., 2005). However this does not appear to be normal seafloor spreading as no clear magnetic anomalies are observed and crustal thickness is about 10 km, which is significantly thicker than the ∼7 km oceanic crust of the Alarcón basin. A similar story is proposed for the northern Gulf, where there is uncertainty as to whether the crust is new igneous crust or very highly intruded, extended continental crust (Gonzalez-Fernandez et al., 2005). There is significantly more recent volcanism in the central and northern Gulf: the San Felipe Tuff, used to reconstruct the coastlines near Isla Tiburon in the northern Gulf, is 6 Ma (Oskin and Stock, 2003b) and volcanism at Reforma Caldera and at Las Tres Virgenes dates from 13- 0.6 Ma (Portugal et al., 2000). The presence of volcanic activity suggests that the difference between the southern and northern Gulf may lie in the mantle, as both areas experienced the same stress field and the same important geologic events. One hypothesis is that an asthenospheric window opened up beneath the central Gulf (Benoit et al., 2002), prompting the volcanic activity. This implies that there was no asthenospheric window under the southern Gulf, and possibly at the initiation of extension, the fossil slab was still present beneath the southern Gulf. Vigorous seafloor spreading at Alarcón hints that there is no shallow slab beneath that region of the Gulf today.

III.6.D Comparison to other Rifted Margins

Previous arc volcanism and the oblique nature of extension in the Gulf of California highlights a form of rifting where a continental sliver is transferred and translated from one tectonic plate to another. However, many features of this

rifting process, such as non-volcanic rifting, and migration of crustal thinning are also observed at other rifted margins.

The most comprehensively investigated non-volcanic margin is the West Iberia margin. The Galicia Interior Basin in the northern part of the Iberian margin is a failed rift landward of a later extension and rifting episode. It is a cold, thin and non-volcanic margin (Perez-Gussinye et al. (2003)), with a basin geometry that is about 50 km wide, 5 km deep and experienced stretching factors up to β=5. This may be analogous to the large San Blas basin we see in the southern part of the Alarcón transect, which also likely formed early during extension. But, in general, rifting processes at Iberia were very different from those in the Gulf of California: the West Iberian margin as a whole experienced significantly more stretching, over a much longer time interval with exhumation of peridotite at the seafloor (Whitmarsh et al. (1996)), indicating that it is magma-starved. This is in contrast to the smooth transition to seafloor spreading, and absence of lower crustal or upper mantle rocks near the seafloor along the Alarcón segment. The 'S' reflector observed at Galicia is interpreted as large shear zone which has rifted the continent asymmetrically, but rifting across Alarcón is symmetric. Hence, although both Alarcón and Galicia are non-volcanic rifted margins, they do not seem to have undergone similar rifting processes.

The South China Sea offers some interesting similarities; it is a non-volcanic margin and rifted a volcanic arc, although this subduction zone was long dead before the onset of extension. Upper crustal extension is estimated β=1.3 and whole crustal β=1.8 (Westaway, 1994), comparable to the observed upper crustal and whole crustal extension in the southern Gulf of California. Clift et al. (2002) conclude that extension was achieved through upper crustal normal faulting and ductile lower crustal flow, particularly near the continent-ocean transition to account for the depth-dependent extension. Hence, rifting processes in the South China Sea are likely very different to those observed in Alarcón: preserved Moho

structure along Alarcón makes ductile flow an unlikely conclusion for the primary method of lower crustal deformation, but as rifting in the Alarcón is 30 Ma more recent than seen in the South China Sea we do not know if the Moho structure will be gradually erased over time.

The thicker crust of the Tamayo Bank/crustal keel region seen on this transect just past the southeast continent-ocean transition is also observed on other margins. The Hatton Bank, which is highly volcanic margin also has a ∼100 km wide keel of crust, where Moho deepens by 7-10 km, immediately past its continent-ocean transition, before an area of thinner, extended crust (Morgan et al., 1989). The volcanism the Hatton Bank experienced during rifting resulted in higher crustal velocities than across Alarcón, but there is also a region of relatively faster lower crust stretching from the continent-ocean transition down into the crustal keel, as observed here. A crustal keel is also observed in the southern Tyrrhenian Sea. The southern Tyrrhenian Sea is also a back-arc basin and experienced almost synchronous extension and onset of seafloor spreading as the southern Gulf of California, and at a similar rifting velocity (Spadini et al., 1995). The conjugate margins of the Tyrrhenian Sea are both around 200 km, and have experienced necking, leading to seafloor spreading (Spadini et al., 1995; Pepe et al., 2000). Seismic reflection data across the Sicilian margin show that past the continent-ocean boundary the Moho deepens by 5-10 km, coincident with the Solunto High, and then thins coincident with the Cefalú Basin, which is interpreted to have been an initial focus of extension (Pepe et al., 2000). The two main areas of thinning across the Sicilian margin of the south Tyrrhenian Sea are the Cefalú Basin and the continent-ocean transition, which are analogous to the Alarcón Basin (continent-ocean transition) and the Tamayo Trough.

III.7 Conclusions

A total of 64 seismometers with an average spacing of 12.5 km form a 2D seismic refraction transect spanning 881 km across conjugate rifted margins in the southern Gulf of California. These seismometers yielded a total of 45,000 Pg, PmP and Pn arrival times, providing information on the velocity structure of the crust, the position of the Moho, and to a lesser degree, the velocity of the upper mantle. Seismic velocity structure was initially modeled using code developed by Zelt and Smith (1992). The majority of this model was devised through forward modeling, and had an overall RMS error of 140 ms. Comparison of the observed gravity anomaly to that calculated from the velocity model shows that we need around 35 km crustal thickness at the southeast end of the transect and around 30 km beneath the Baja peninsula, these regions are beyond ray coverage in the model, so the preferred seismic velocity model was adjusted to include these results.

The degree of stretching on both margins is an average of β=2.0, producing a total opening (sum of extension on both margins and the width of new oceanic crust) across the Alarcón of 495 km. A reasonable minimum opening is 430 km, corresponding to an average stretching factor of $\beta \simeq 1.7$. Rifting across the southern Gulf of California appears to have been achieved by an overall pure shear mode of extension: there are similar degrees of extension on both margins (on average crust is thinned to around 50% its original thickness); this is backed up by velocity structure in the upper crust (Chapter II), which shows similar upper crust velocities and an overlying volcanic layer across both margins.

The estimated total opening across Alarcón of around 495 km provides firm evidence in favor of the alternative model of tectonic evolution: NW-SE oblique extension and dextral slip began around 14 Ma in the Gulf and, hence, less slip occurred on the faults west of Baja (Figure III.12.2). Although the influence of earlier extension from the Basin and Range cannot be ignored, the estimated maximum magnitude of this is not sufficient to account for the $\sim$200 km discrepancy

between the amount of opening in the traditional tectonic model and the alternative tectonic model (Table III.3). However, it seems that a different story may have to explain rifting in the central and northern Gulf of California: from the Guaymas basin north only 300 km opening is observed within the Gulf (Oskin and Stock, 2003b; Lizarralde et al., 2005), although it seems likely that some extension may be located further east. Aragon-Arreola and Martin-Barajas (2005) see evidence in the northern Gulf for a westward migration of extension. We seem to observe the oldest extension to the east in the southern Gulf of California, and a westward migration of extension from the Tamayo trough to the Alarcón basin, but in the southern Gulf all the extension overlaps; possibly in the central and northern Gulf the earlier extension is separated geographically from the more recent rifting.

Significant structure on the Moho suggests brittle faulting of the entire crust, and the preservation of Moho structure implies that there is no lower crustal flow to smooth these variation out. This indicates that the lithosphere was cold at the onset of rifting, and remains cold today. The extended continental margins have average velocities of around 6.3 km/s, which do not indicate any significant magmatic intrusions, however the change from extension to seafloor spreading was smooth, with seemingly immediate onset of creation of "typical" oceanic crust. It is likely that the large degree of extension observed (β>4) at the continent-ocean transition was sufficient to create melt.

IV

Tomographic modeling

IV.1 Abstract

Seismic tomography was carried out on the 881 km-long wide-angle refraction profile using the approach of Van Avendonk et al. (2004). The initial aim of this work was to verify the structure derived after iterative forward modeling using the method of Zelt and Smith (1992) (Chapter III). We found that in even in the most rigorous test of model convergence, starting from a flat Moho, a consistent Moho structure is recovered in all areas with good, reversed ray coverage. A tomographic inversion of the profile started with our previous Moho structure, but simplified velocity structure, produces a model with similar structure and low overall error, RMS=0.073 seconds, and χ^2=1.67, compared to RMS=0.140 and χ^2=4.1 for the forward model. This gives confidence that the major features in the model and the degree of crustal extension, average lower crustal velocities and significant Moho structure are robust features. The velocity structure of the lower oceanic crust in the models is asymmetric: the northwestern side has an average velocity of 6.7 km/s and the southeastern side is faster, with an average lower crustal velocity of around 6.9 km/s. Both continent-ocean transitions show fast velocities at the base of the crust, which is indicative of magmatic intrusions, but this anomaly is

greater on the southeast side, where interpretations of magnetic anomalies indicate the initiation of seafloor spreading to have occurred. Reconstruction of the Alarcón back to 2.5 Ma (onset of seafloor spreading) shows remarkable similarity in Moho structure beneath the Alarcón Basin and Tamayo Trough. A small amount of magmatic intrusion beneath the Tamayo Trough is hinted at through a small region of higher velocities and a corresponding magnetic anomaly, but magmatic intrusions were concentrated beneath Alarcón, contributing to the onset of seafloor spreading in that location.

IV.2 Introduction

Tomographic inversions can provide a robust method for exploring the range of models that fit a dataset. For complex datasets it can produce lower errors and smoother models than can ever be produced by trial and error forward modeling, as was carried out in Chapter III using the approach of Zelt and Smith (1992). We will refer to this previous model, from forward modeling, as the rayinvr model, after the computer program name used by its original authors.

While the overall fit of the Alarcón rayinvr model is good, errors in travel-time fit are still significant in many places, even after many multiple iterations and data re-picking. The rayinvr model was largely forward modeled as the damped least squares routine at the foundation of the code produced particularly rough velocity structure and an unreliable Moho boundary at the node spacing required to fit all the features present in the data. The resulting error is likely due to the difficulty of fitting multiple datasets simultaneously by hand and in part due to underparameterization of the model, which contains only a few interfaces with sparse node spacing and linear velocity gradients between these boundaries. An alternative method for modeling the refraction data was also desirable as a means of providing a more objective test for the robustness of several notable features within the Alarcón model, such as significant Moho structure. A tomographic

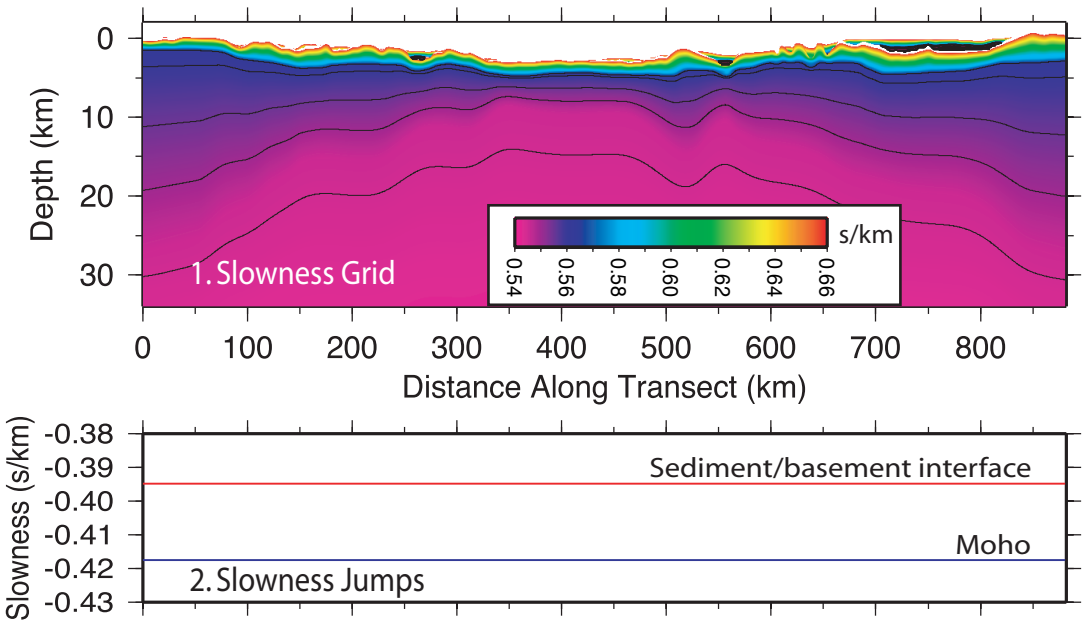

Figure IV.1 Background slowness grid and interface jumps before tomographic inversion. Starting slowness grid (1) and slowness jumps (2) across the sediment/basement interface (red) and Moho (blue) are smooth

approach was chosen to invert for both velocity and boundary structure that uses a smooth background slowness grid combined with prescribed jumps corresponding to discontinuities between boundaries such as the sediment/basement and Moho interfaces (Van Avendonk et al., 2001b, 2004). Tomographic inversions allow the user to test objectively which features of the model are required by the data, and to trade-off data fit against smoothness in a controlled manner.

IV.3 Tomography Code

Seismic tomography is a non-linear inversion process, which is accomplished iteratively through a series of linearized inversions and is an alternative to trial and error forward ray-tracing methods or partially automated inversion methods such as Rayinvr. The tomographic models consist of a smooth background slowness grid and interfaces, which are jumps in slowness (Figure IV.1). The first step in the tomographic inversion is to trace rays through the starting

model, so the differences between the data (Pg, PmP and Pn traveltimes) and the predicted traveltimes can be calculated to create the data input for the inversion. The van Avendonk tomography code uses a shortest path method (SPM) for ray-tracing on a discrete grid (Van Avendonk et al. (2001a), and references therein) and for efficiency an optimized forward star that removes redundant directions from search (Klimes and Kvasnicka, 1994). The accuracy of the SPM method depends upon the grid spacing and the size of the forward star. The grid spacing for ray-tracing is much finer than that used in the inversion.

The inversion (Van Avendonk et al., 2001b, 2004) solves for a model vector ($\mathbf{m}$), which is a combination of the slowness (the reciprocal of seismic velocity), the position of the interfaces and the jumps in slowness across those interfaces (δ $\mathbf{m}$) that minimizes a linear combinations of squared data misfit and the roughness of the model:

$$\mathrm{F}(\delta\mathbf{m})=(\mathbf{d} - \mathbf{A}\ \delta\mathbf{m})^T\ \mathbf{C}_d^{-1}\ (\mathbf{A}\delta\mathbf{m}-\mathbf{d})\ +\ \lambda(\mathbf{m}+\delta\mathbf{m})^T\mathbf{D}^T\mathbf{D}(\mathbf{m}+\delta\mathbf{m}) \quad \text{(IV.1)}$$

Where $\mathbf{d}$ is the vector of traveltime residuals; $\mathbf{A}$ is the Frechet derivative matrix, which relates model perturbations to changes in traveltime; $\mathbf{C}_d$ is the Covariance matrix, and $\mathbf{D}$ enforces the smoothing constraints. The overall Lagrange multiplier (λ) allows data to be traded off against model roughness. In general at each inversion step the desired reduction in data misfit is chosen to be small enough that the linearization used in the inversion is valid.

The matrix $\mathbf{D}$ includes 0th, 1st and 2nd order smoothing constraints, as well as the weights that, along with the Lagrange multipliers, allow the user to trade-off the relative importance of smoothing the interface, the slowness jumps at the interface and the background slowness grid.

IV.4 Tomographic Modeling

Ray-tracing was carried out on a 5525 by 361 grid (250 m horizontal spacing; 100 m vertical spacing), and the inversion was performed on a coarser 882 by 167 grid (1 km horizontal spacing; average 200 m vertical spacing). In the inversion grid the vertical grid spacing increases with depth approximately in line with the loss of vertical resolution. The initial model used for the tomography has a simple velocity structure (5.9-6.5 km/s gradient in the lower crust) and a smoothed Moho from the rayinvr model. The upper/lower crustal boundary used within the rayinvr model, which allowed for a velocity discontinuity in the mid-crust was removed, since pre- or post-critical reflections at this level of the crust were not observed, nor is such *a priori* structure required in this tomographic inversion, as the inversion is flexible enough to accommodate the change in vertical velocity gradient without an explicit boundary. The large variations in bathymetric depth across the Alarcón transect, as well as the multiple, deep sedimentary basins are important sources of travel-time variations in the data (e.g. Figure III.8). There are no turning rays in these sedimentary basins so an estimate of their structure is made from the MCS data, where we have data coverage (167-767 km along transect). If these features are not accurately accounted for, the associated travel-time signal is propagated deeper in the model, creating errors in lower crustal velocities and Moho structure. To account for these problems, static corrections were estimated (Figure IV.2). The tomographic inversion was run starting from the rayinvr Moho structure until a model with reasonable data fit was found, and then the basement depth was adjusted on a basin by basin basis to remove static errors that were common to all instruments and all phases, and can be attributed to the near surface structure. Although most of the static corrections were small and the basement used in the subsequent inversion is close to that estimated from the MCS data, in a few regions the changes were larger, for example in the San Blas Basin (Figure IV.2). These changes parameterized complex upper crustal

structure (e.g. Comondú tuffs), that would otherwise not be fully resolvable by the inversion. Static corrections were estimated for instruments beyond the ends of the shot locations, but there is a larger uncertainty in final structure at the ends of the model.

Travel-time picks, particularly PmP and Pn, were checked and iterated using reciprocity. Because we do not have true reciprocal raypaths; sources are located at the sea surface and the receivers are on the seafloor, the travel-time through the water column needed to be subtracted before we could compare reciprocal paths between instruments. To accomplish this, a reasonable model was needed to calculate reliable raypaths. The flexibility of the tomographic code made this process relatively straightforward to implement. Reciprocity allowed for identification of some very low-amplitude Pn arrivals that would not otherwise have been picked, and also improved the consistency of PmP picks. As discussed in Chapter III, many of the PmP arrivals were complicated and identifying PmP correctly was difficult; reciprocal analysis was needed to avoid cycle skips in the the picked travel-times.

IV.4.A Testing robustness of model recovery

Three starting models were created to test the robustness of the Moho structure obtained from the rayinvr model. These models were designed to be different enough that consistent features of the resulting models, after many iterations, would indicate structure that is truly required by the data. The first model has a smoothed version of the final Moho from the rayinvr model (Figure IV.3.a.1), the second model has a sloping crust/mantle interface on the continental margins and a Moho depth of 10 km between 400 and 500 km in the oceanic crustal section (Figure IV.3.b.1), and the third has a flat Moho at 15 km depth (Figure IV.3.c.1). After 12 iterations the overall χ^2 is 2.0 for each of the three models. 30% of instruments have a $\chi^2<1$, and 60% have $\chi^2<2$. Reducing the data misfit furthermore

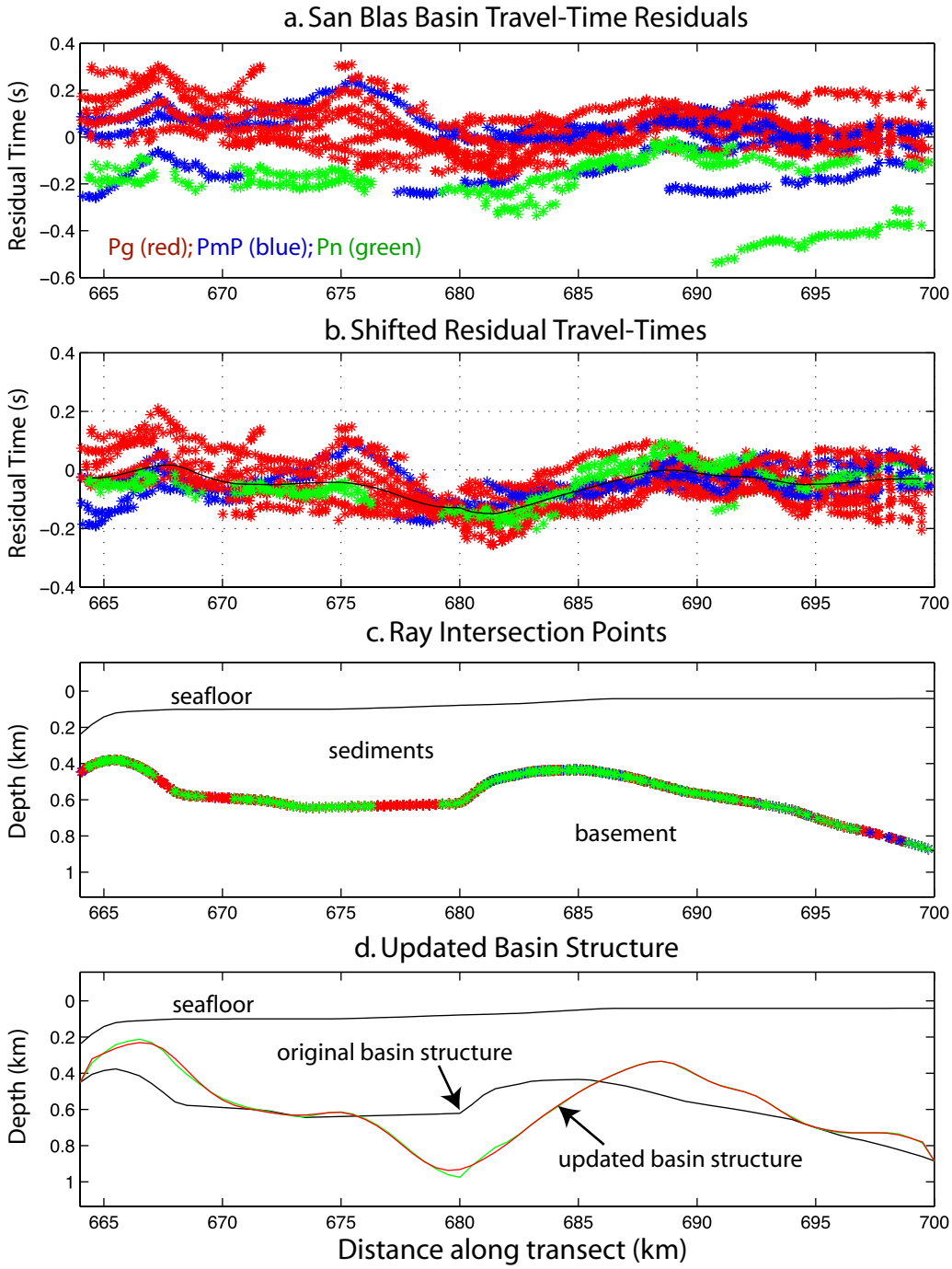

Figure IV.2 Basin static corrections over the northwest side of the San Blas basin. All picks (Pg, PmP and Pn) are used and the basement structure is updated to reduce the travel-time residuals.

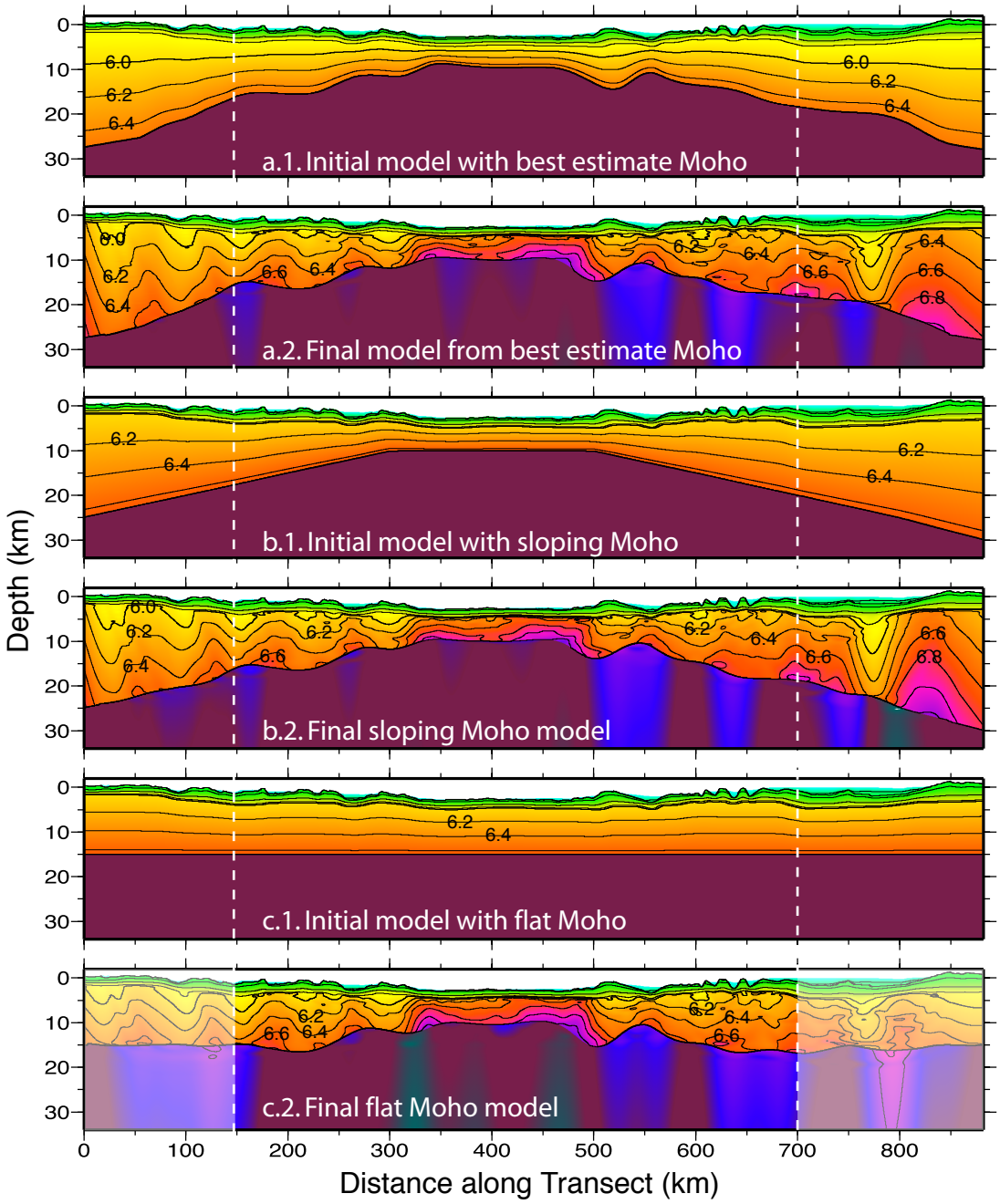

Figure IV.3 Initial and final models for three tomographic inversions. Models were inverted until a χ^2=2 was achieved. Model a.1 is the initial model with the rayinvr Moho, the final inversion is a.2. Model b.1 has a sloping Moho beneath the margins and Moho at 10 km depth beneath oceanic crust, its final inversion is b.2. Model c.1 has a flat Moho at 15 km, its final inversion is shown in c.2. Crust contours are spaced at 0.2 km/s, color scheme is from Figure III.2

(RMS errors for these models are ∼0.080 seconds) produces a significantly rougher crustal velocity structure. A slow region at 760 km is present in all models, but this is at the limit of reverse coverage, in an area with lower quality data recorded in shallow water (Figure III.8) and is likely the result of errors in upper crustal structure.

The Moho structure between 175 and 700 km, where ray coverage is good, is well resolved and similar features are seen in each model. All models produce the Moho undulation at 275 km, and the sloping and rayinvr models both resolve a second Moho undulation at 150 km at the limits of the reversed ray coverage. Moho in the oceanic section is almost identical in each model. All models produce the crustal keel and crustal thinning in the Tamayo region around 500- 550 km along transect, however mantle velocity in this area, at around 7.5 km/s, is rather low. The inversion from the flat Moho starting model (Figure IV.3.c) clearly shows the extent of good ray coverage: without PmP and Pg arrivals on the northwest end of the model the tomography cannot deepen the Moho or change bulk crustal velocity structure, but instead chooses to reduce mantle velocity to produce a good fit of travel times. A similar trade-off is seen beneath mainland Mexico, where crustal and mantle velocities are slower to compensate for thinner crust. The tomographic inversion lowered mantle velocities in both these end regions to 7.0-7.4 km/s, which are not within the observed range of upper mantle velocities (>7.6 km/s (Christensen and Mooney, 1995)). The final Moho structure produced from the originally flat Moho provides confidence that the undulating Moho is a real feature, however it also shows that it is better to begin the inversion with a closer estimate of Moho depth based on prior knowledge; even a simple sloping Moho between continental crustal thickness and oceanic crustal thickness allowed the code to produce a geologically reasonable model. The tomography recovers a consistent average crustal velocity structure, although, the oscillations seen in the lower crustal velocities are probably the smearing of small upper crustal errors

deeper into the model. The regions of low upper mantle velocities are unlikely to be real but are most likely a way for the tomography to resolve residual inconsistencies in the travel-times for this dataset.

IV.4.B Tomographic model across the Alarcón profile

A final model, started from the best estimate of Moho structure, was iterated 15 times and has errors of χ^2=1.67 and RMS error=0.073 seconds (Figure IV.4.3). Histograms of travel-time misfits by region and phase are shown in Figure IV.5. Most of these have approximately normal distribution, and the Q-Q plot (Figure IV.6) for the entire dataset shows normal distribution out to two standard deviations, but long tails, showing some large misfits between the data and model. Although mantle velocity variations continue to the bottom of the model, there is no ray coverage in this region, and estimates of upper mantle velocities seem, in places, to be geologically unreasonable. The tomography provides resolution that was not possible in the rayinvr scheme: as the depth and velocity nodes for each layer in rayinvr are provided by the user and not changed throughout modeling, small-scale features, such as the decrease in velocity at the spreading center in the oceanic crust, are missed if node spacing is too coarse.

The average crustal velocity beneath the northwest margin is 6.3 km/s, which is similar to the rayinvr model, and also in agreement with average continental crust velocities (Christensen and Mooney, 1995). The southeast extended continental margin is faster than its conjugate, and has an average velocity of 6.4 km/s, about 0.1 km/s faster than the rayinvr model. The oceanic crust is faster than in the rayinvr model, and while the asymmetry in velocity structure is still present, it is not as pronounced. There is slightly slower crust at 400 km at the position of the Alarcón Rise mid-oceanic ridge, which is not seen in the rayinvr model. The northwest side of oceanic crust has an average velocity of 6.63 km/s, which increases to 6.80 km/s on the southeast side. Many different damping and

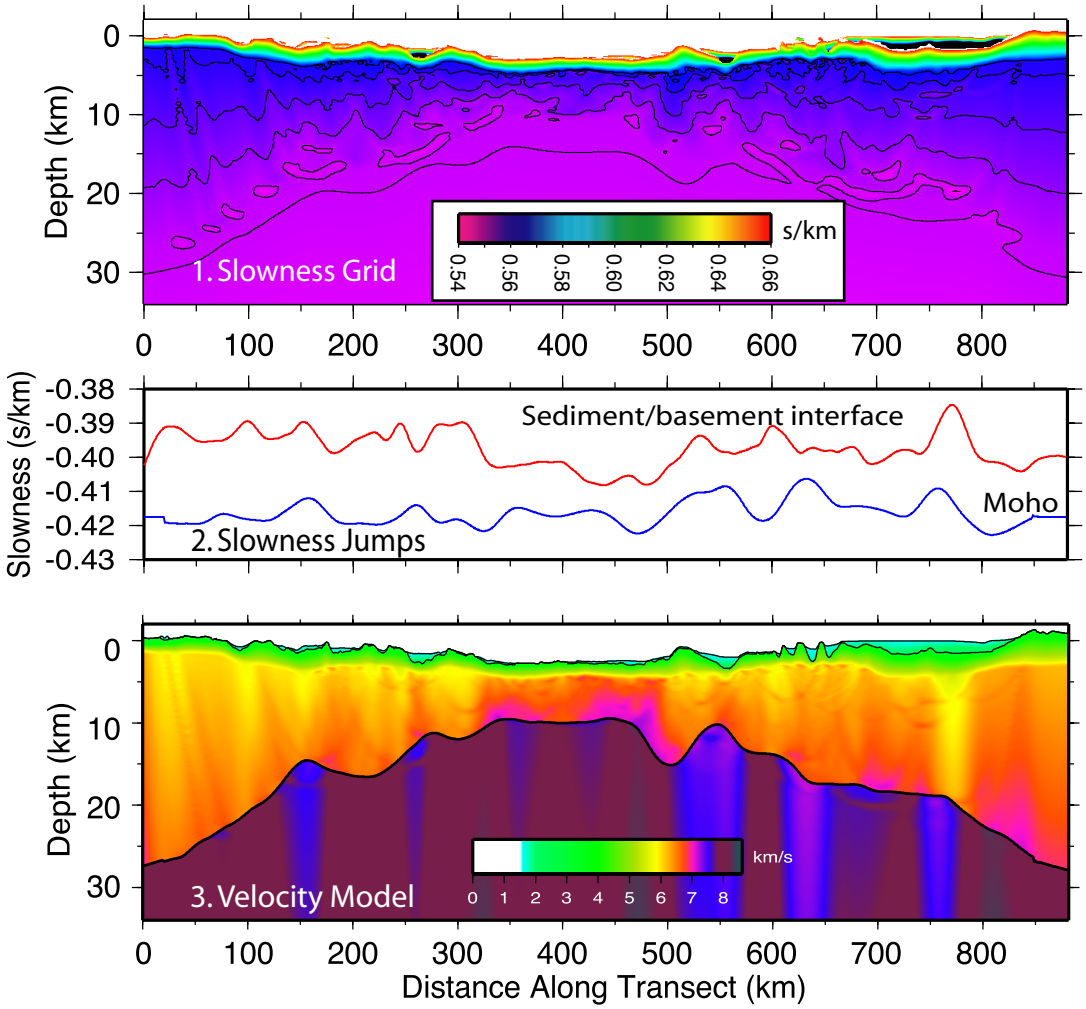

Figure IV.4 Final tomographic model across Alarcón: the background slowness grid (1), interface slowness jumps (2) and final velocity (3) are shown. Errors in this model are RMS=0.073 seconds and χ^2=1.67.

regularization parameters were tried and in each inversion, once χ^2 was pushed below 4, mantle velocities were lowered: upper mantle velocity is on average 7.8 km/s, but in some areas this is as low as 7.5 km/s, although each of the three models shown above (Figure IV.3) have areas of slow upper mantle velocity, the most pronounced and robust area of slow upper mantle velocity is in the crustal keel area.

The oscillations in crustal velocity are interesting: as the code is better

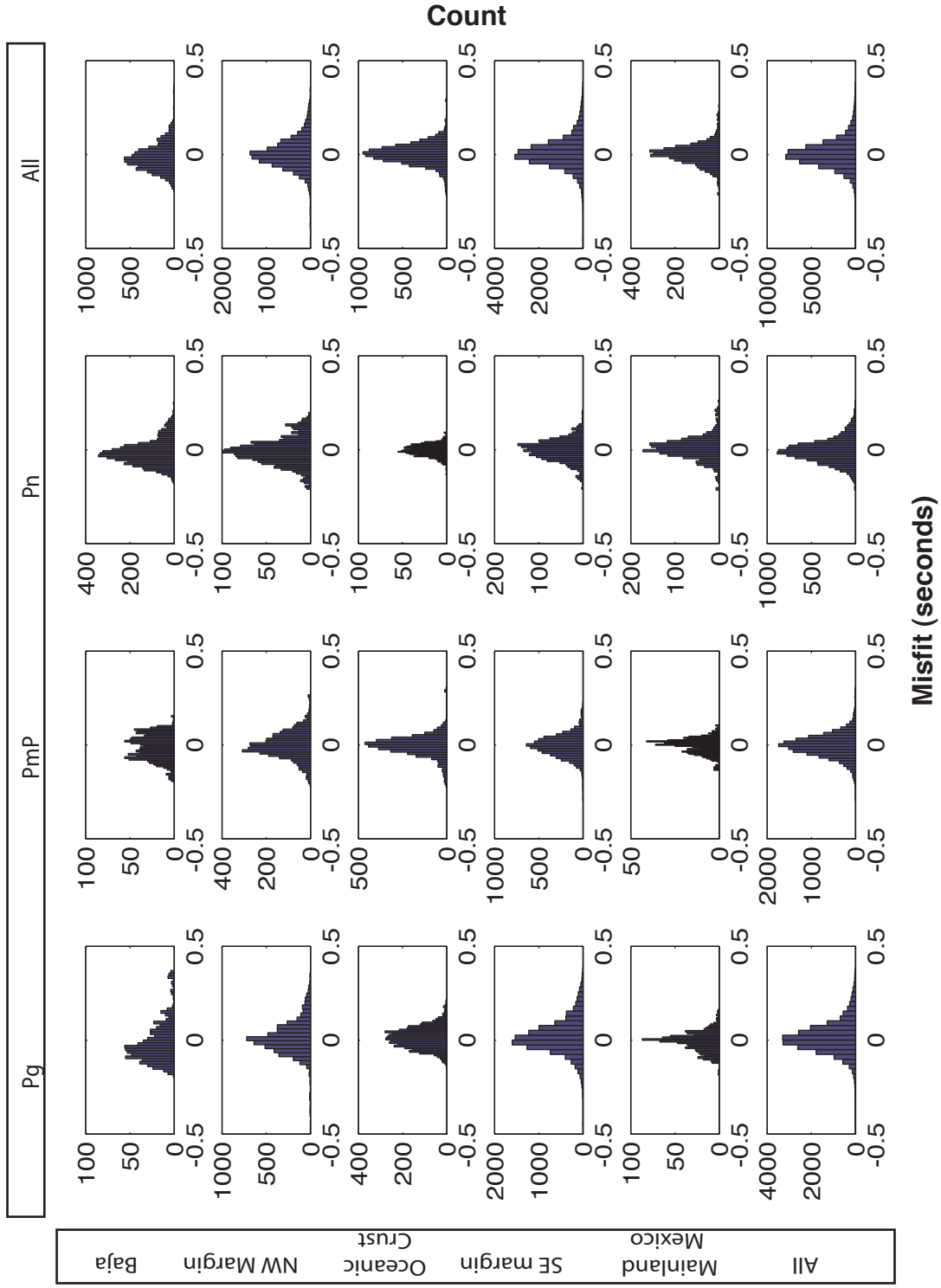

Figure IV.5 Histograms of data misfit to model (predicted traveltime-pick) IV.4 by region and phase

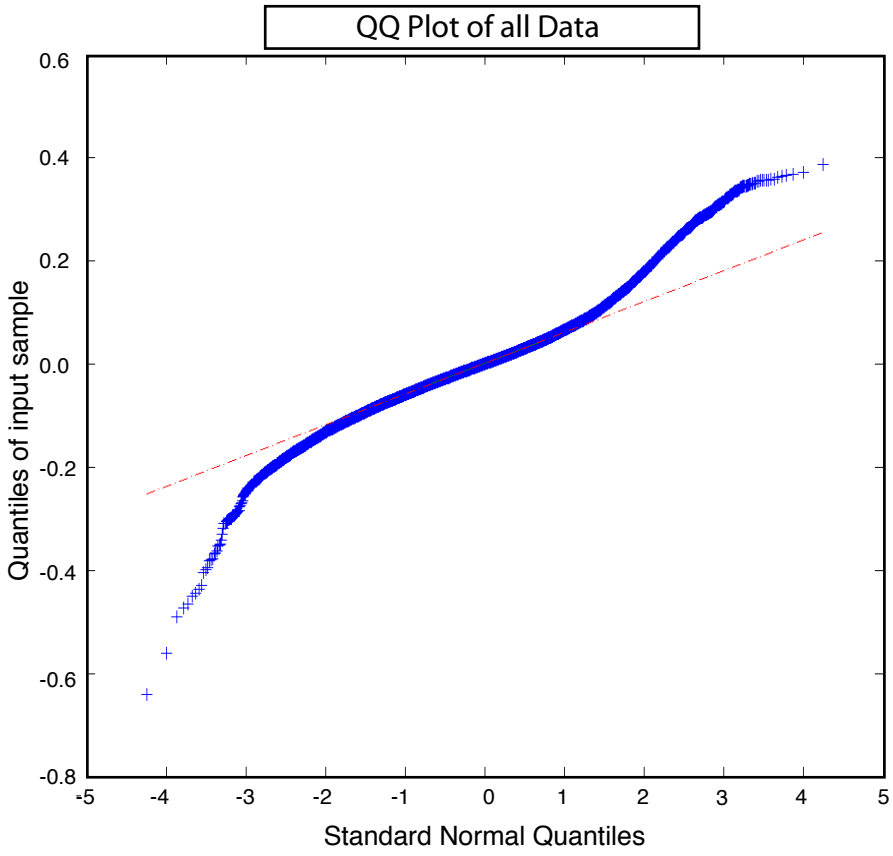

Figure IV.6 Q-Q plot for all data in model IV.4. This indicates normal distribution between about two standard deviations, but shows that the Gaussian curve has long tails, indicating some data points with large errors.

developed to produce smooth interfaces it must compensate by having a more complicated velocity structure. Small changes in slowness jumps at the basement interface (Figure IV.4.2) can propagate down to become large changes in lower crustal velocity. In the final model it seems that the oscillations are present in both the background slowness grid and in the slowness jumps. However, within the final models the higher velocities do seem to coincide with the edges of greater crustal thinning (at 175 km, 260 km, 550 km and 700 km along transect), although this may be a coincidence and not indicative of structure.

If we interpret the slower upper mantle that is resolved by the tomography

in areas of greater thinning across the margins as being as real feature, we could speculate that it may indicate the pooling of melt beneath the Moho, and that the upper mantle may have some gabbro present within it in these areas.

IV.4.C Oceanic Crust and Crustal Keel

One area where the tomographic inversion confirms the basic features of the rayinvr model is in the oceanic crust and adjacent continent-ocean transitions (Figure IV.7). Lower crustal velocity beneath the Alarcón Rise spreading ridge is 0.2 km/s slower than the older oceanic crust. In contrast to the velocity model shown in Chapter III (Figure III.5), there is also an area of fast velocity at the northwest continent-ocean transition. Intrusions into the crust would be expected in the continent-ocean transition regions, where stretching factors are high (β>4) allowing for decompression melting (Pedersen and Ro, 1992). Reconstruction of the crust at the onset of robust seafloor spreading (Figure IV.7.c), at about 2.5 Ma, shows that these regions of fast, lower crustal velocities (7.0-7.2 km/s) match up, and are concentrated on the southeast side, with a maximum lower crustal velocity (>7.2 km/s). This is in agreement with interpretation of the magnetic anomaly (Figure IV.7.a), which suggests that the anomaly at 457-480 km may be a low amplitude magnetic chron 2A, either from an asymmetric initiation of seafloor spreading, or from significant intrusions into the crust.

Reconstruction across Alarcón at the onset of seafloor spreading also demonstrates the remarkable similarity of Moho structure beneath the Alarcón Basin and Tamayo Trough before the start of seafloor spreading. There is a small region of elevated velocities above the thinned Moho, beneath the Tamayo Trough at 550 km along transect, but it seems that magmatic intrusion was concentrated beneath the Alarcón, initiating seafloor spreading there. The increased velocity beneath the Tamayo Trough is associated with a small magnetic anomaly (Figure IV.7.a), also hinting that its origin is intrusion into the crust.

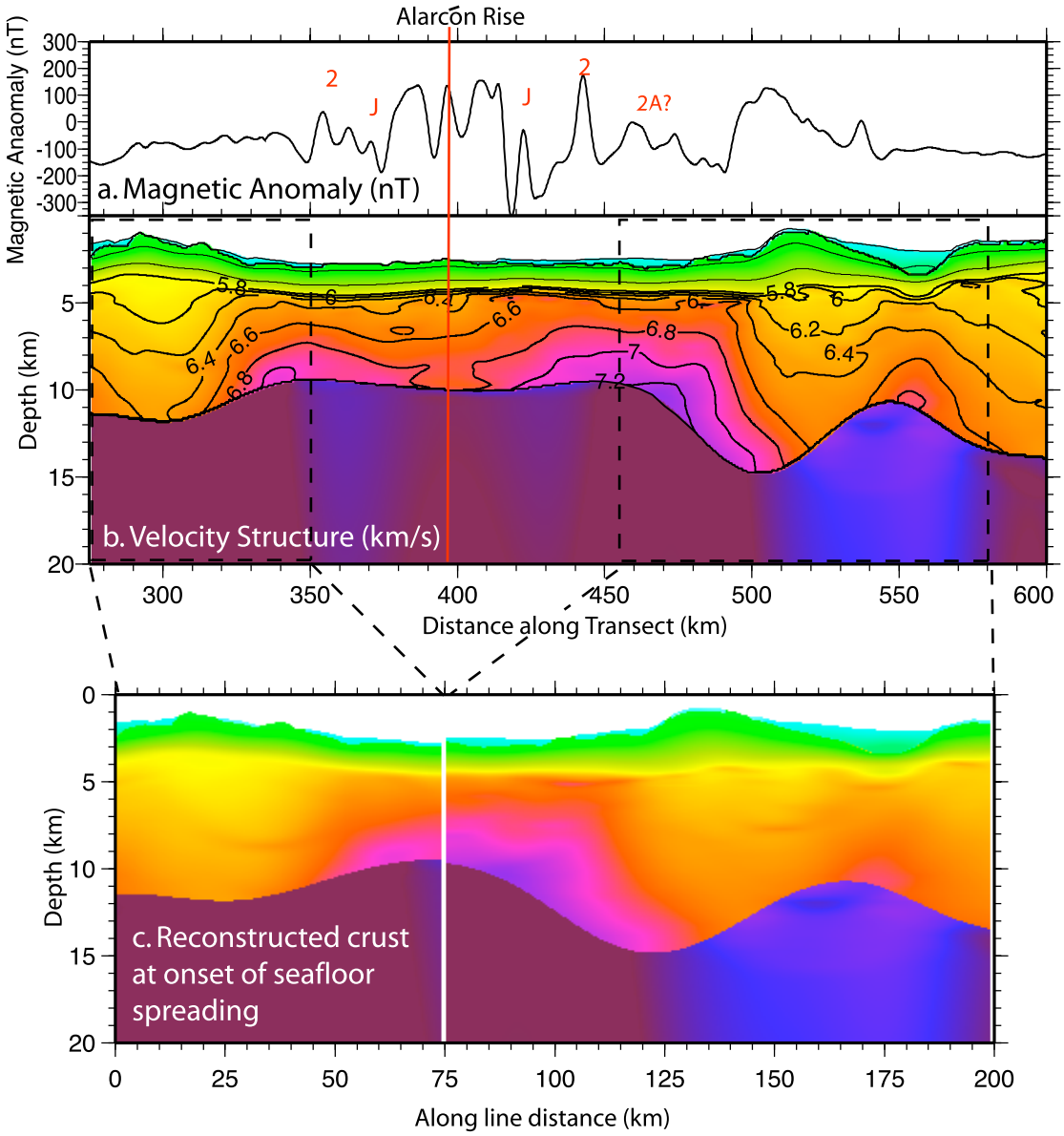

Figure IV.7 Tomographic model across the oceanic crust and crustal keel (b), with corresponding magnetic anomaly (a) and reconstruction of the crust at the onset of seafloor spreading(c). Magnetic anomaly(a) has been reduced to the pole. Reconstructed margin(c) removes crust between 350-455 km. Note the similarity between the Alarcón before seafloor spreading and the Tamayo Trough to the southeast. Areas of high velocity at the base of crust match up after reconstruction, possibly showing areas of magmatic intrusions.

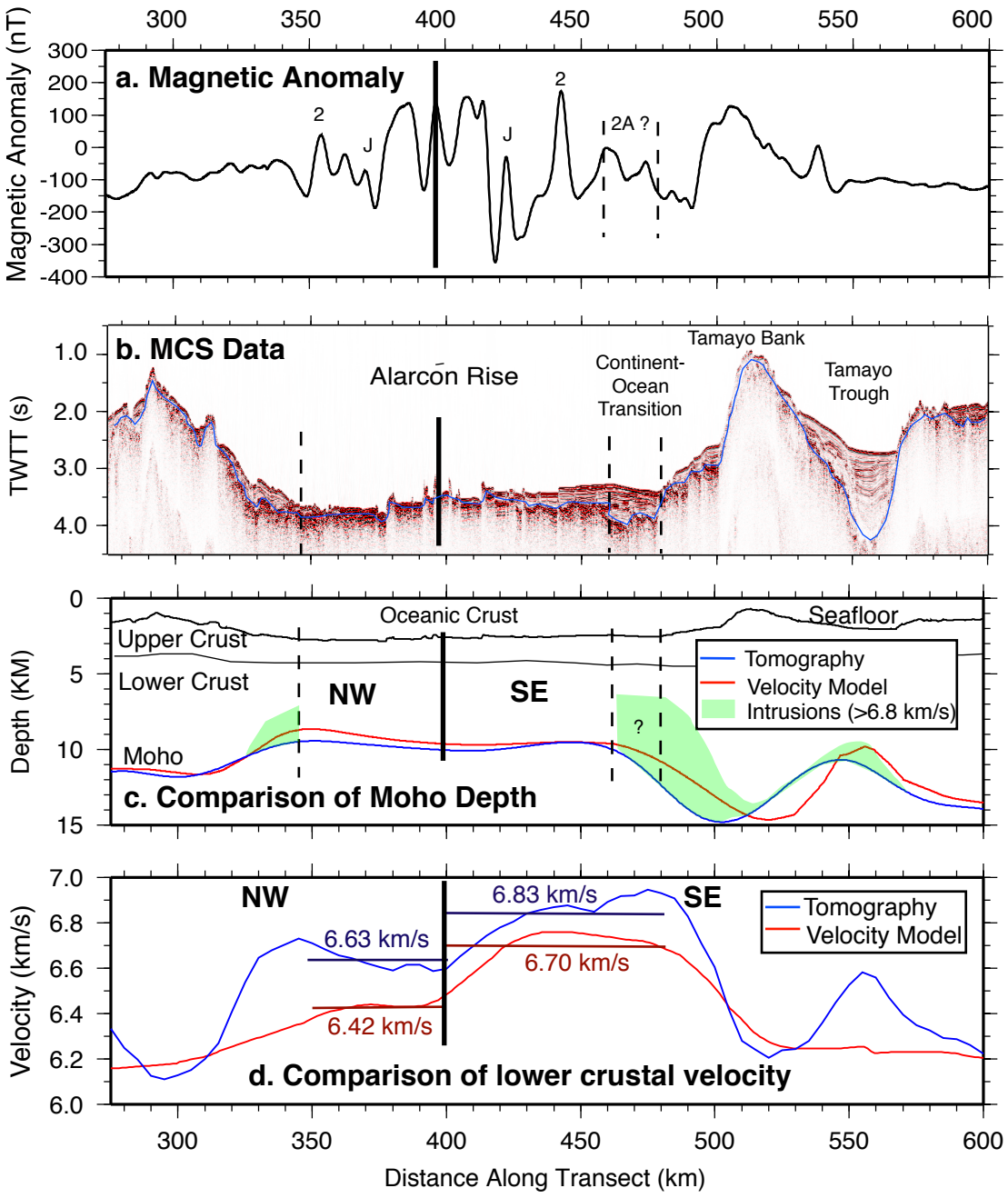

Figure IV.8 Comparison of velocity model and tomographic model in the Alarcón Basin. The magnetic anomaly (a) and MCS data (b) are shown for clarity. Differences in Moho structure (c) are greatest in depth at 350km, and the crustal keel is offset 20 km between the two models. Comparison of lower crustal velocities (d) shows a significant difference between the two models: the tomograhic model is significantly faster than the velocity model, particularly on the northwest side.

The tomographic model and the rayinvr model differ in the oceanic crust, both in Moho depth and velocity. A comparison of Moho depth (Figure IV.8.c) shows that the crust at the northwestern continent-ocean transition is 6 km thick in the rayinvr model, compared to 6.8 km thick in the tomographic model. This facilitated the low velocity for the lower crust beneath the northwestern side of the oceanic basin in the rayinvr model. The tomography model corrects this, and the oceanic crust has a more typical velocity (Figure IV.8.d). We also see that the crustal keel is offset by about 20 km between the two models, indicating the difficulty of forward modeling complicated structure. However, there are regions of fast lower crust beyond the continent-ocean transitions that likely correspond to intrusions (highlighted in green in Figure IV.8.c), and it appears that the rayinvr model compensated for these fast regions by moving the Moho shallower around 440 km, 490 km and 550 km along transect. A comparison of vertical velocity functions through the crust at 375 km and 450 km along transect (Figure IV.9) shows the differences between the rayinvr and tomographic models: the tomography has no sharp boundary at the upper/lower crust boundary and the tomography has a higher gradient and faster velocities deeper within the lower crust.

IV.5 Conclusions

To test the robustness of the crustal structure obtained from the 881 km seismic refraction profile, multiple tomographic inversions were performed. Three different starting models, one with a preferred Moho from the rayinvr model (Chapter III), one with a simple sloping Moho, and one with a flat Moho at 15 km depth, were ran for a total of 12 iterations, yielding χ^2=2. These inversions show that the main features of the model are a good fit to the data, and produced significantly lower RMS errors than the velocity model shown in Chapter III (Figure III.5), which was largely forward modeled. Between ∼150-700 km along transect (the central region with good data coverage) we obtain excellent recovery of crustal

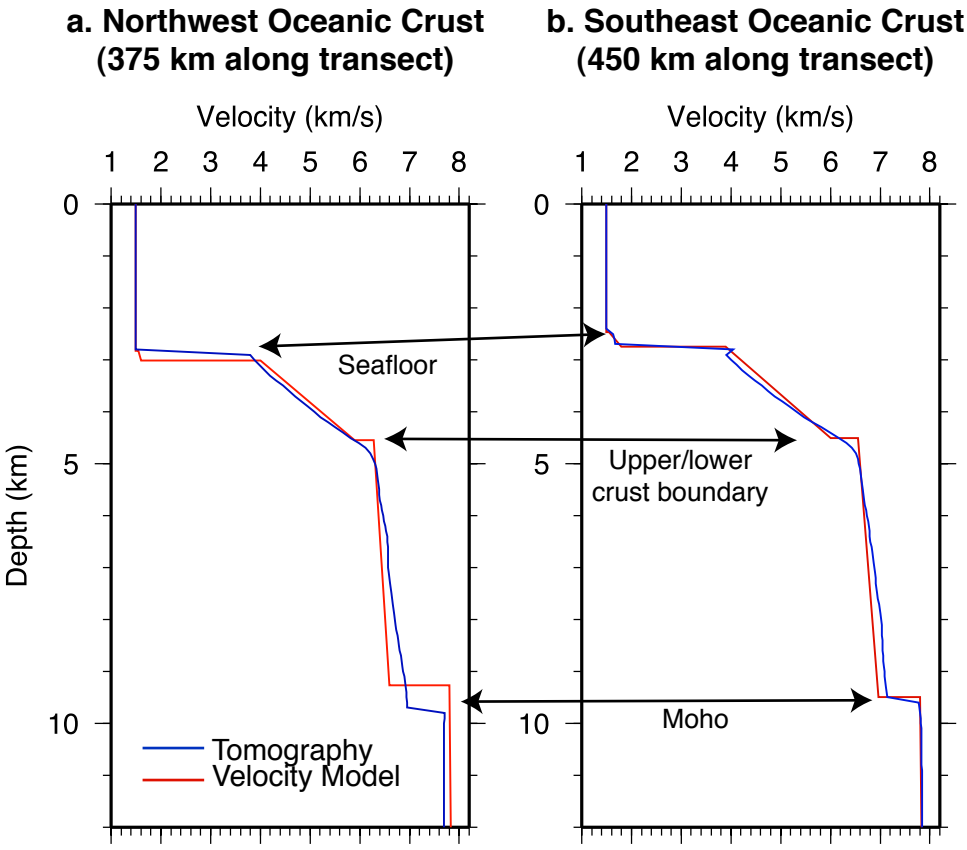

Figure IV.9 Vertical velocity functions through the NW and SE oceanic crust for both the rayinvr and tomographic models.

velocity structure and Moho topography. In all models, Moho topography, along with the crustal keel and area of thinned crust in the Tamayo region are reproduced. Confirmation of crustal structure provides confidence in our interpretation of rifting processes in the southern Gulf of California. The creation and preservation of this Moho structure implies rifting of cold lithosphere and no lower crustal flow.

The tomographic inversion of the continent-ocean transitions, oceanic crust and crustal keel region produced a more accurate and detailed model of the oceanic crust. Differences between Moho depth in the rayinvr model versus

the tomographic model appear to be due to the regions of fast velocity in the lower crust, which are likely to be intrusions. The linear gradients of the Zelt and Smith (1992) approach used in the rayinvr model do not easily accommodate these regions, and instead Moho was raised to fit the shorter travel-times. There are fast velocities at both continent-ocean transitions, but these are concentrated on the southeast side, and likely correspond to the location of seafloor spreading initiation. When oceanic crust is removed and the Alarcón Basin reconstructed back to 2.5 Ma we see a remarkable similarity in Moho structure beneath the Alarcón Basin and the Tamayo Trough. A small region of higher velocities and a small magnetic anomaly above the shallow Moho at the Tamayo Trough suggest a small amount of magmatic intrusion, which would be expected as crustal thinning (β) was >4. However, the Alarcón basin experienced greater magmatic intrusion than the Tamayo trough, which likely attributed to the onset of seafloor spreading in that location.

V

Results from OSNPE: Low Detection Threshold Magnitudes for Ocean-Bottom Recording

V.1 Introduction

The Ocean Seismic Network Pilot Experiment (OSNPE) took place from the beginning of February to early June 1998 concurrently with the PELENET experiment at the Hawaiian Islands Stephen et al. (2003). The OSNPE consisted of three broadband seismometers at site OSN-1, which is located at ODP hole 843B, 225km southwest of Oahu (see Figure V.1). Two Guralp CMG-3Ts were deployed; one on the ocean-floor (station OSN1S), similar to the deployment of an ocean-bottom seismometer, and one buried in the sediments so that the top was not visible at the seafloor (station OSN1B). A GeoTech KS-54000 was installed in the borehole 242.5m below the ocean floor at the sediment/basement interface and clamped to the borehole casing (station OSN1) (see Stephen et al. (2003) for more details), the orientations of the horizontal components on OSN-1 were BH1: 126.5^o; BH2: 216.5^o. The surface and buried seismometers both had Differential

Pressure Gages as well as 3-component seismometers within the instrument package. The horizontal components of OSN1B were BH1: 148^o; BH2: 238^o, and of OSN1S, BH1: 276.5^o; BH2: 6.5^o. The PELENET experiment (Wolfe et al., 1998) consisted of stations on each of the main Hawaiian Islands (see Figure V.1): BIG2 on Hawaii; MAUH on Maui; MOLH on Molokai; KAUH on Kauai and KIP on Oahu [a permanent Global Seismic Network (GSN) station]. The motivation for the OSNPE was to understand how to obtain high quality earthquake seismology data from the oceans through a thorough examination of all possible deployment schemes in a single location with overlapping recording windows. The ultimate aim of the GSN is a truly global network of seismometers uniformly spaced around the globe, which cannot be achieved with land sensors alone. This study has two parts:

1. To compare the data collected by the three differently situated OSN stations.
2. To compare the ocean-bottom data with those collected on the Hawaiian Islands.

Comparisons were made by calculating signal-to-noise ratios for P, S, Rayleigh and Love wave arrivals in the time domain at each station, and then inferring minimum magnitude detection thresholds.

V.2 Previous Results

A number of previous studies have examined the problem of collecting high-quality data at the ocean floor. Results from a borehole seismometer deployment in the western Pacific (Orcutt and Jordan, 1986) showed detection limits of 5.2 m_b for close teleseismic events (40^o), increasing to 5.6 m_b for distant events (80^o). This was noted to be a site with low seismic noise. In a 2 month deployment of a borehole seismometer in the NW Pacific (Butler and Duennebier, 1989), the observed threshold magnitudes were larger; the smallest observed earthquake was 5.4 m_b and all others were greater than 6.0 in magnitude. The French Pilot Exper-

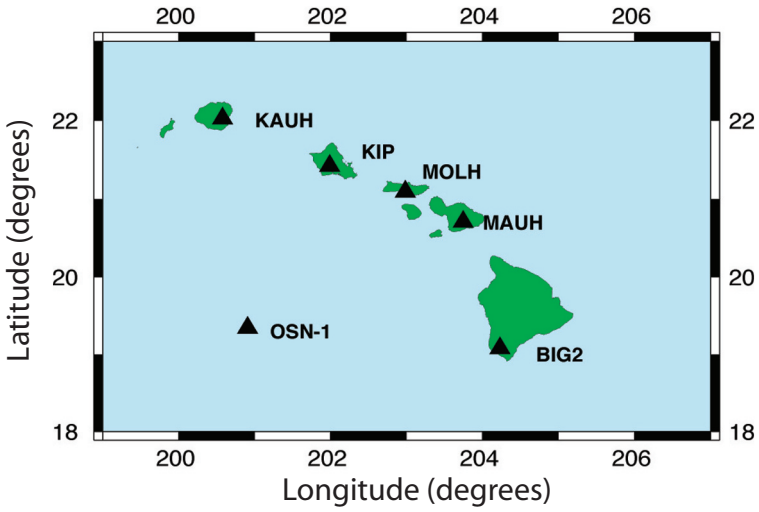

Figure V.1 Hawaii station locations and site OSN-1.

iment deployed both ocean-bottom and borehole instruments in the mid-Atlantic for 9 days, and recorded teleseismic earthquakes with a magnitude as low as 5.3 (Montagner et al., 1994). Blackman et al. (1995) examined data from OBS deployments on the East Pacific Rise, known to have high noise levels and concluded that short-period body waves would only be visible in times of low noise and for close events. For long-period body and surface waves the minimum observable magnitude was 5.7-6.0 for teleseismic events out to 100^o. Webb (1998) came to a similar conclusion by analyzing data collected at the OSN-1 site (prior to the OSNPE), which he also noted as being a particularly noisy site given its position in the trade-wind zones. A minimum m_b detection threshold there was estimated to be 7.5, dropping to 6.9 for deep events with low attenuation. However, modeling of the data showed that these levels could possibly drop down to 5.5 and 5.0 during times of low noise. Results from the MELT experiment at 17^oS on the EPR were also poor; during a 6 month deployment of 51 OBSs no clear teleseismic compressional waves at frequencies above 0.5 Hz were detected (Wilcock et al., 1999). The OSNPE was the first seafloor experiment in the deep ocean to use both a high-resolution analog-to-digital converter and sensors designed as observatory

class seismometers. This high fidelity instrumentation in conjunction with the long deployment period, allowing sampling during times of varying background noise levels are likely responsible for much of the observed improvement in detection thresholds.

V.3 Data

V.3.A P-Waves

We bandpass-filtered the seismograms between 0.8 and 3 Hz, the traditional frequency range chosen for P waves, using a 5th order Butterworth filter to pick short-period P arrivals above the noise peak. It is clear in Figure V.2 (Collins et al., 2001) that the noise power spectra are still quite high in this P-wave band. Table V.1 lists the numbers of picked arrivals and the lowest recorded magnitude events. All the lowest recorded magnitude events for P arrivals were from events in the deep subduction zones around the Pacific Rim. Both the buried and seafloor instruments (OSN1B and OSN1S) observed less than half the number of P-waves compared to the borehole seismometer, OSN1, and the Island stations. The noise levels in this frequency band on the vertical component for OSN1S and OSN1B were highest (Figure V.2), which is also clear in the time domain as shown on the seismogram (Figure V.3) from a 5.1 m_b event in Japan. The noise levels on the other stations were similar, with the borehole instrument having almost the same noise levels as MOLH on Molokai, and station KAUH being particularly quiet. For larger magnitude earthquakes high quality data was obtainable on all stations, shown in Figure V.4 from a 5.9 m_b deep trench earthquake in Tonga, where even the seafloor OBS, OSN1S, has a very high signal-to-noise ratio, in contrast to the results from MELT (Wilcock et al., 1999) where no teleseismic compressional waves were observed in this frequency range.

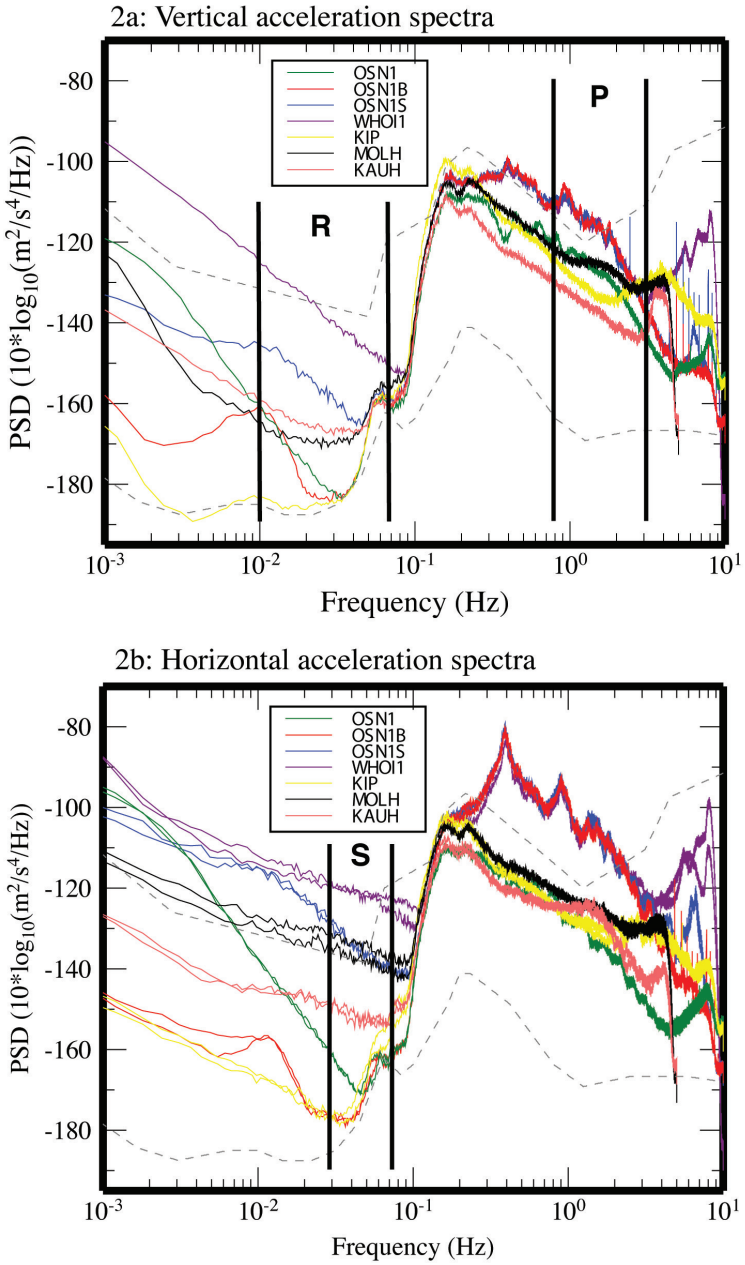

Figure V.2 (a) Vertical and (b) Horizontal component acceleration spectra for the three OSN instruments, three Island stations and a short period (1Hz) seismometer (WHOI1) (from Collins et al. (2001)).The frequency bands used to filter P-waves, S-waves and Rayleigh waves are indicated.

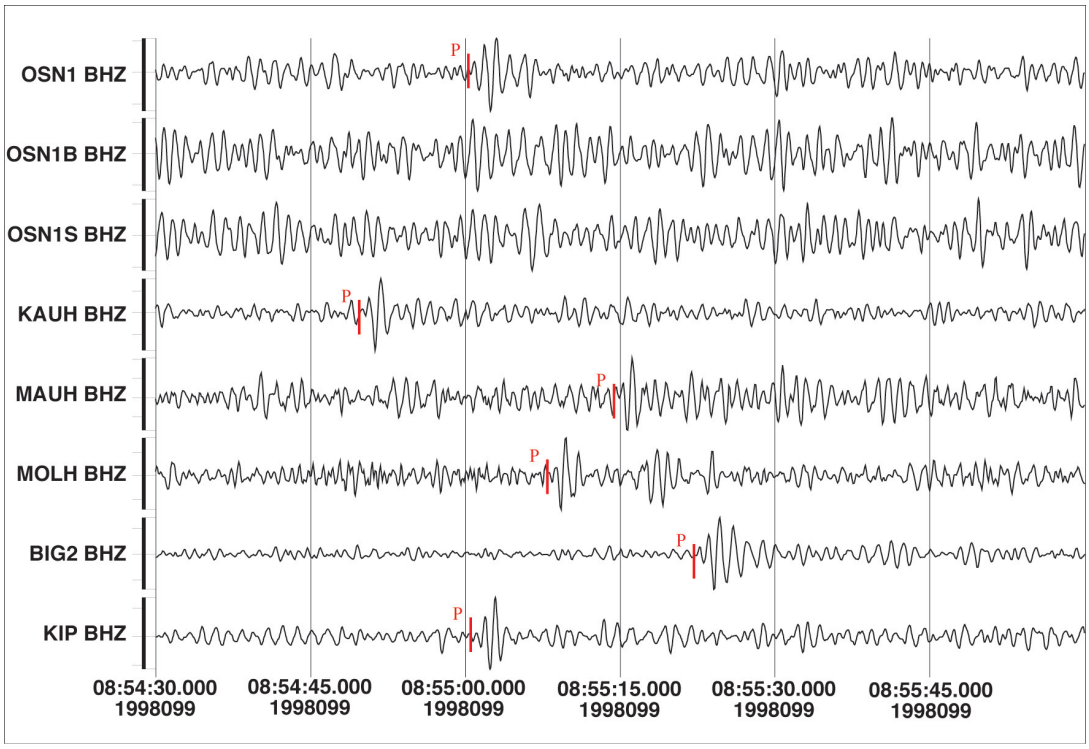

Figure V.3 Example P arrivals from a 5.1 m_b earthquake in Japan. Location 36.89N, 140.89E, 106.5km depth, 55^o from the Hawaiian Islands, at this azimuth the array aperture is approximately 5 degrees. Bandpass filtered 0.8-3.0 Hz. The signal-to-noise ratio for OSN1, the borehole sensor, is 2.3, just above the SNR=2.0 assigned detection level. Noise levels on OSN1B and OSN1S are too high to pick a P-wave arrival. SNRs for the Island Stations are: KAUH = 3,3; MAUH = 3.3; MOLH = 2.7; BIG2 = 12.2 (which was noticeably lower noise levels); KIP = 3.5.

V.3.B S-Waves

The data were filtered with a 5th order Butterworth bandpass filter designed to optimize the ocean-bottom data.. Although the horizontal components of the island stations observe low noise levels up to about 0.09 Hz with a minimum noise levels at about 0.08 Hz (Figure V.2), the horizontal components of the borehole and buried stations have their lowest noise at 0.04Hz, and the noise starts to ramp up quickly at 0.08 Hz. Therefore, we chose to bracket these low seismic noise levels between 0.03 and 0.07 Hz. The most dramatic change in the results for the OSN S-wave data, compared to the P arrivals, is on OSN1B. For P arrivals this buried sensor produced results very similar to the ocean-floor station. However,

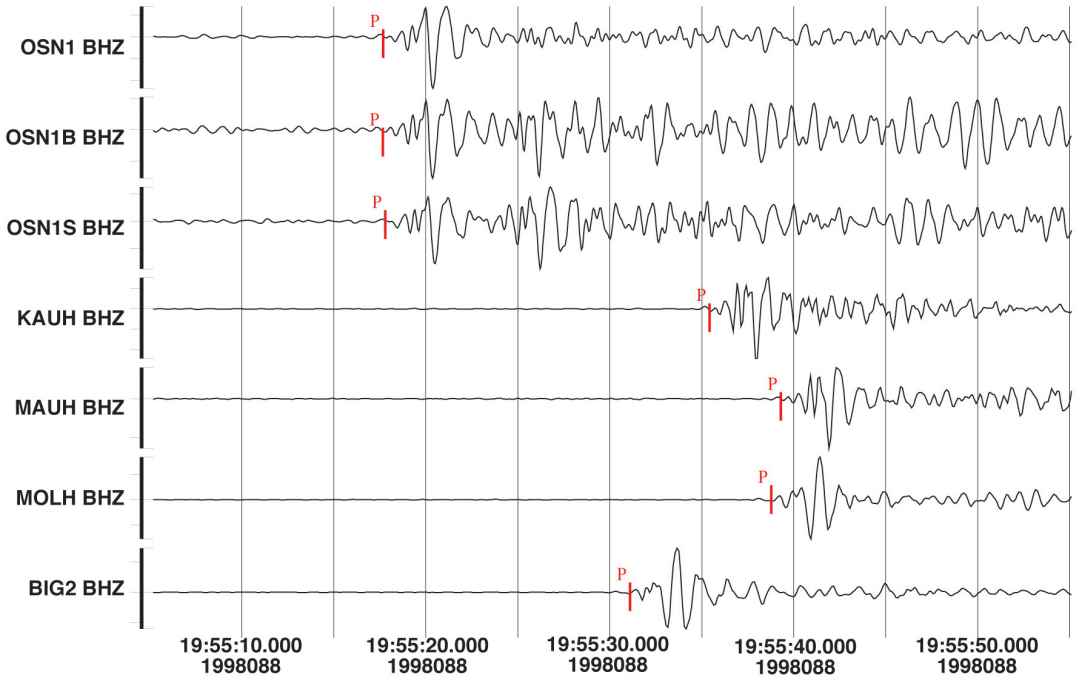

Figure V.4 P-wave arrivals from a 5.9 m_b deep(530km) Tonga earthquake. Location -17.58N, 179.00E, 42^o from the Hawaiian Islands; array aperture approximately 3 degrees. Bandpass filtered 0.8-3.0 Hz. Noise levels are average for the experiment, but the large magnitude and deep source produce high quality data for every station. Even the noisiest station, OSN1S, has SNR = 22.

at lower frequencies, the buried seismometer actually detects the largest number of S waves of any station (Table V.2), and has very low noise levels (Figure V.2). This high signal-to-noise is shown in Figure V.5, a 4.4 m_b event in Tonga. Again OSN1S has the highest noise levels and, as shown in Figure V.5, the noise can be huge and, in this example, completely obscures any signal. Most visible arrivals on OSN1S, the seafloor sensor, had a body-wave magnitude above 5.1, although 4 events below 5.1 were observed during periods of low noise. In contrast, nearly 50% of the observed S-waves on the borehole and buried sensors were from earthquakes with a body-wave magnitude less than 5.0.The smallest earthquakes from which S-waves were detected (Table V.2) were 4.0 m_b, and the same 4.0 Tonga event was the lowest detected on OSN1, OSN1B and KIP. A different 4.0 Tonga event was observed on KAUH.

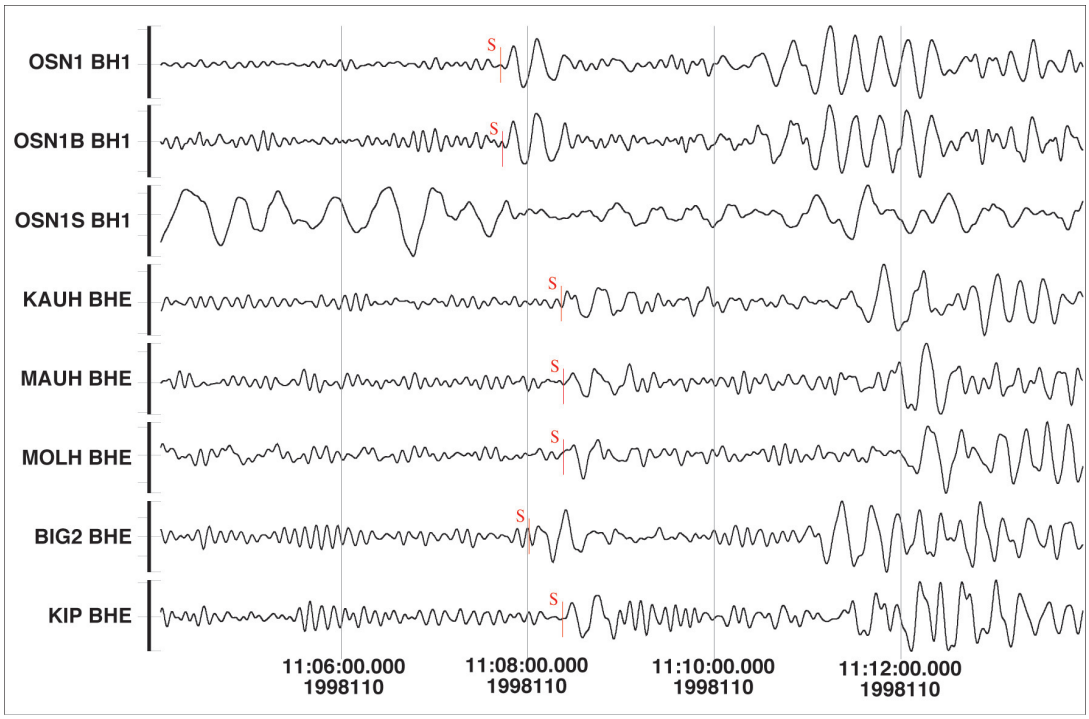

Figure V.5 S-wave data from a 4.4 m_b, 5.2 Ms shallow earthquake in Tonga. Location -17.78N, -173.18E, about 40^o from the Hawaiian Islands. Bandpass filtered 0.03-0.07 Hz. The low noise levels produce clean arrivals with good signal-to-noise levels, despite the low body-wave magnitude. OSN1S is dominated by low frequency noise.

V.3.C Rayleigh Waves

The data for surface waves were filtered with a 5th order Butterworth bandpass filter in the band 0.01-0.07 Hz, as the low noise region extends to a lower frequency on the vertical component than on the horizontal components (Figure V.2). Experiments were done with narrower passband filters for Rayleigh waves, but there was no real increase in signal-to-noise (in either the 0.03-0.07 Hz or 0.015-0.04 Hz bands that were tested), and we felt much of the frequency information was being excluded by these narrower pass bands. Higher noise levels on the horizontal components would result in increased noise levels on the rotated, radial component, canceling out the advantage of the higher signal amplitude, so the vertical component was used. Figure V.6 shows data from a 4.4 Ms event in

the Aleutian Islands- both OSN1 and OSN1B have clear Rayleigh waves, and the quality of data on those two sensors is similar to the best island station, KAUH. There is low frequency noise on OSN1S, and station MAUH is all noise- which must be localized as it is not evident on the other island stations. Both OSN1 and OSN1B exhibited noise levels lower than many of the Island stations (evident on the noise spectrum, Figure V.2). For large magnitude events, high quality data can be collected on all stations, even at large distances. Figure V.7 shows Rayleigh wave arrivals from a 6.1 Ms earthquake 92^o distant in the Southern Ocean. As well as excellent signal-to-noise, the dispersion of the Rayleigh wave can also be clearly observed. Previous studies (Blackman et al., 1995) found this magnitude to be near the limit for surface wave detection at 100^o on OBSs, so OSN1S, despite being the noisiest station here, is actually a significant improvement in data quality.

V.3.D Love Waves

For Love Wave analysis the horizontal components were rotated to transverse and radial before picking and analysis could be done. Most Love waves were not visible before rotation. The same filter was used as in the Rayleigh wave analysis. Possibly only two Love waves could be observed on the OSN1S data, but neither were of high enough quality to be used later in analysis. The best station by far was OSN1B, which recorded many Love waves at magnitudes less than 5.0, and had almost twice the number of arrivals of any other station (see Table V.4). There was a lot more variation between island stations than observed for other phases. MAUH and MOLH in general had very poor results (see Table V.4). For the other stations (OSN1, BIG2, KAUH and KIP) there were 3 events below 5.0, which they all recorded but generally the observed detection level was Ms>5.0.

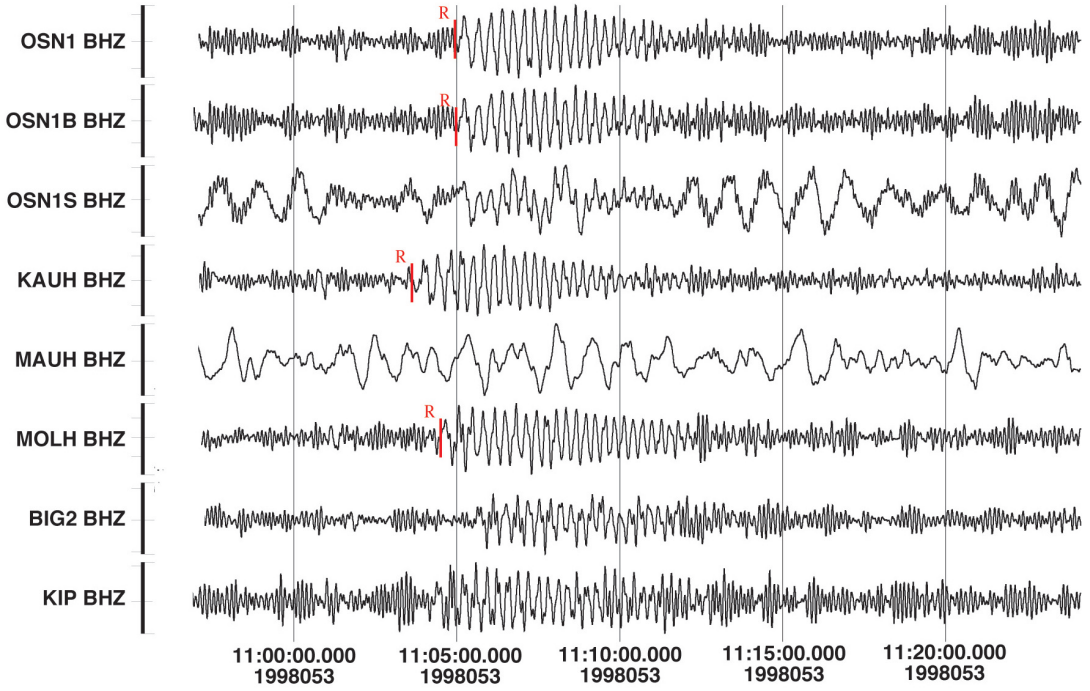

Figure V.6 Rayleigh wave arrivals from a 4.4 Ms shallow earthquake in the Aleutian Islands. Location 52.86N, -168.37E, about 35^o from the Hawaiian Islands, array aperture approximately 4 degrees. Bandpass filtered 0.01-0.07 Hz. The calculated SNR for OSN1B is at the detection limit of 1.5; SNR on OSN1, KAUH and MOLH is slightly higher- 2.0. All other stations have a SNR ¡ 1.5 and could not be used in the analysis. MAUH, in particular, has very high noise levels at this time.

V.4 Analysis

The signal and noise levels were calculated by taking the square root of the ratio of the variances over a specific time window. For the signal this window began at the picked arrival time, and for the noise, the same length window was taken 100 seconds before the P-wave onset for body waves and 1000 seconds before for surface waves (to fit in the required longer window length). Each event was checked to ensure there were no previous earthquake arrivals in the noise window. The window length used for P waves was 4 seconds, for S waves, 40 seconds, for Rayleigh waves, 1000 seconds, and varied from 100 to 500 for Love waves. There are variations in signal length, but after testing many window lengths it seemed there was little variation in relative variance between arrivals for P, S and Rayleigh

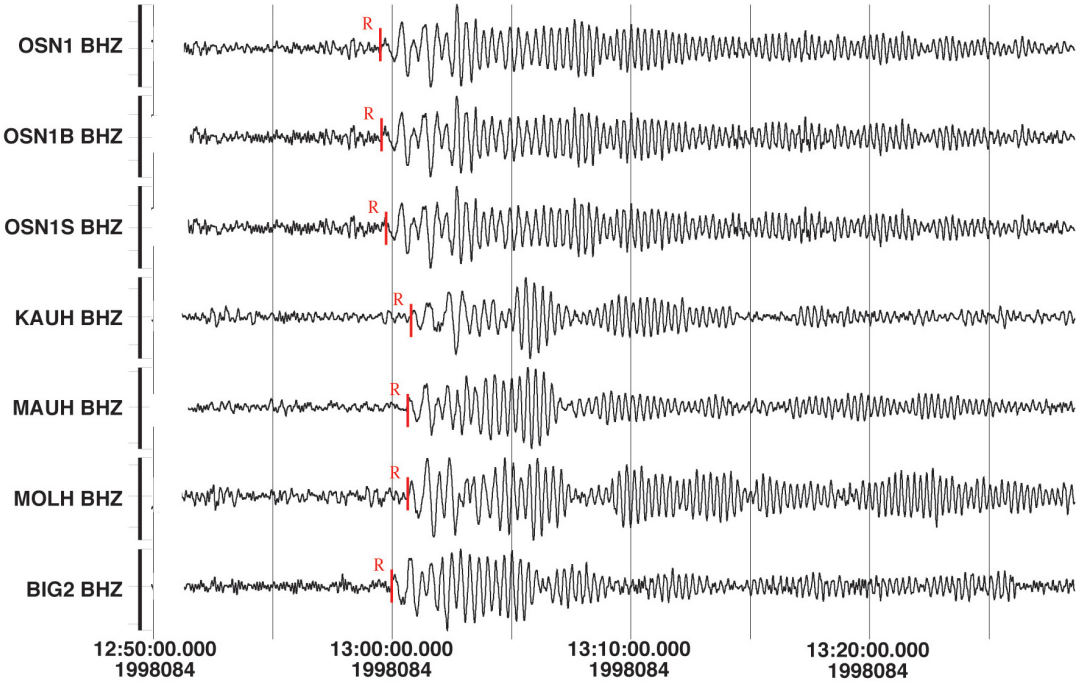

Figure V.7 High quality Rayleigh waves from a 6.1 Ms earthquake in the Southern Ocean. Location -63.56N, 148.12E, 92^o from the Hawaiian Islands; array aperture is approximately 3 degrees at this azimuth. Bandpass filtered 0.01-0.07 Hz. Despite the great distance, all sensors recorded this event with high signal-to-noise level. Noise levels at this time are about average for this experiment.

waves with changing window length. However there were distinct differences for Love waves so an appropriate window length was given to each arrival based on a visual review of the length of the Love wave.

Body Waves: To calculate minimum detection thresholds, the observed magnitudes (mb) of the arrivals were reduced to a level at which the signal-to-noise ratio (SNR) was 2.0, a minimum level at which body waves can be picked - the threshold magnitude, TM (equation 2.2). As S waves are body waves, but also low frequency, threshold body wave and surface wave magnitudes were calculated. The threshold surface wave magnitude was calculated using the method below (equations 2.3 and 2.4), but the minimum signal-to noise ratio was kept at 2.0.

$$mb = \log(\frac{A}{T}) + Q(z, \Delta) \tag{V.1}$$

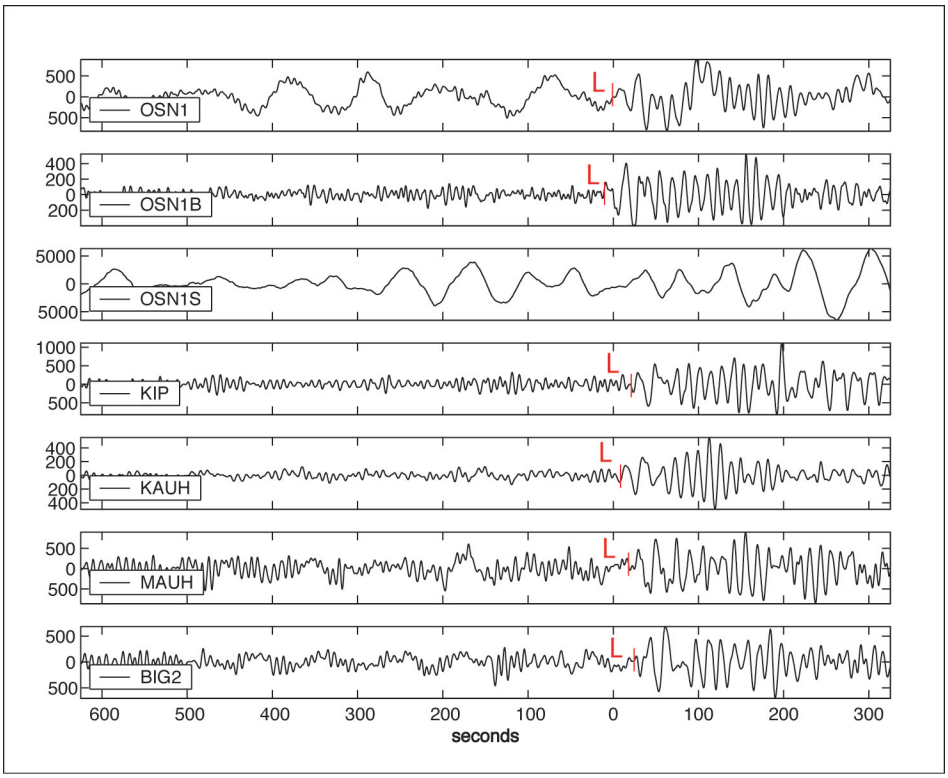

Figure V.8 Love wave arrivals from a 5.0 Ms earthquake in Tonga. Bandpass filtered 0.01-0.07 Hz. The best data are on OSN1B. Low frequency noise is evident on the borehole instrument, and OSN1S is completely dominated by noise.

$$TM = \log\left(2.0\left(\frac{10^{(mb-Q(z,\Delta))}}{snr}\right)\right) + Q(z,\Delta) \tag{V.2}$$

Surface Waves: For surface wave analysis the observed surface wave magnitudes (Ms) were reduced to a signal-to-noise ratio of 1.5. The long wave train of surface waves makes them more easily pickable than P- and S-waves on the seismogram. Only arrivals from shallow events could be used where the excitation of the fundamental mode is highest. The surface wave magnitude equation assuming shallow excitation is: For a dominant period of 20 seconds (0.05Hz).

$$Ms = \log A + 1.66 \log \Delta + 2.0 \tag{V.3}$$

$$TM = \log\left(1.5\left(\frac{10^{(Ms-1.66\log\Delta-2.0)}}{snr}\right)\right) + 1.66\log\Delta + 2.0 \tag{V.4}$$

Table V.1 P-Wave Data and Results

Sensor	Location	Obs. Events	Min. Obs. m_b	Min. TM	Mean TM	Mean SNR	Mean TM Deep	Mean TM Shallow
OSN1	Borehole	30	4.4	4.2	4.7	5.8	4.7	4.8
OSN1B	Buried	13	4.6	4.4	5.1	3.8	5.0	5.2
OSN1S	Seafloor	13	4.5	4.5	4.9	4.2	4.9	5.3
KAUH	Island-Kauai	50	3.8	3.4	4.5	10.7	4.4	4.6
MAUH	Island-Maui	30	4.5	4.0	4.9	6.5	4.7	5.1
MOLH	Island-Molokai	32	4.3	3.7	4.8	8.4	4.7	4.9
BIG2	Island-Hawaii	39	3.9	3.7	4.6	13.8	4.4	4.9
KIP*	Island-Oahu	21*	4.4*	4.1*	4.7*	4.5*	4.6*	5.0*

V.4.A P-Waves

In analyzing the results many factors have to be taken into account- most importantly the number of observed arrivals compared to the mean and minimum calculated detection threshold magnitudes. Although the mean threshold magnitude for the buried and seafloor stations are only slightly higher than some of the island stations, they observed far fewer events (see results in Table V.1). There are large noise variations on these instruments in this frequency band (0.8-3.0 Hz), so when noise levels are low they can record events reasonably well, but for a lot of the time the noise levels were simply too high. Figure V.3 shows data from a 5.1 m_b earthquake in Japan, about 55 degrees away from the Hawaiian Islands. The signal-to-noise ratio for OSN1 here is 2.3, and it is clear that even at the lower end of detectability (only slightly higher than the SNR=2 cutoff we used in the analysis), the data are of good quality. Neither OSN1B nor OSN1S observed this earthquake, which, when compared to noise levels for other events for each station,

was in a time of about average noise. The minimum calculated threshold magnitude for the borehole seismometer is 4.2, slightly higher than the island stations, but the mean detection threshold, 4.7 is the same as for the island stations, The minimum threshold magnitudes for OSN1, OSN1S and the Island stations are from deep (high signal-to-noise ratio) Pacific Rim earthquakes. In contrast, OSN1B has its minimum TM from a deep earthquake in Indonesia, 90^o away, but this event occurred during the lowest noise level for the station, illustrating how great an effect the background noise can have on observations.

Table V.2 S-Wave Data and Results

Sensor	Location	Obs. Events	Min. m_b	Min. TM m_b	Mean TM m_b	Min. Ms	Min. TM Ms	Mean TM Ms	Mean SNR
OSN1	Borehole	63	4.0	3.4	4.3	4.4	4.0	4.6	44.3
OSN1B	Buried	77	4.0	3.5	4.5	4.3	3.8	4.7	28.3
OSN1S	Seafloor	21	4.4	3.9	4.7	4.6	4.4	5.2	17.3
KAUH	Island-Kauai	61	4.0	3.6	4.5	4.3	4.0	4.8	14.8
MAUH	Island-Maui	35	4.4	3.7	4.7	4.3	4.2	5.2	13.3
MOLH	Island-Molokai	41	4.1	3.6	4.6	4.4	4.1	4.9	19.7
BIG2	Island-Hawaii	48	4.3	3.8	4.6	4.0	4.1	4.9	15.8
KIP*	Island-Oahu	26*	4.0*	3.8*	4.6*	4.4*	4.4*	4.9*	8.5*

V.4.B S-Waves

The borehole and buried instruments out-performed all of the island stations, with the two highest mean signal-to-noise ratios corresponding to the two lowest calculated minimum detection thresholds (3.4 and 3.5 respectively) as well as the most observed events (see results in Table V.2). Figure V.9 shows seismograms of S-wave arrivals from a 4.9 m_b, 5.0 Ms shallow earthquake in Central

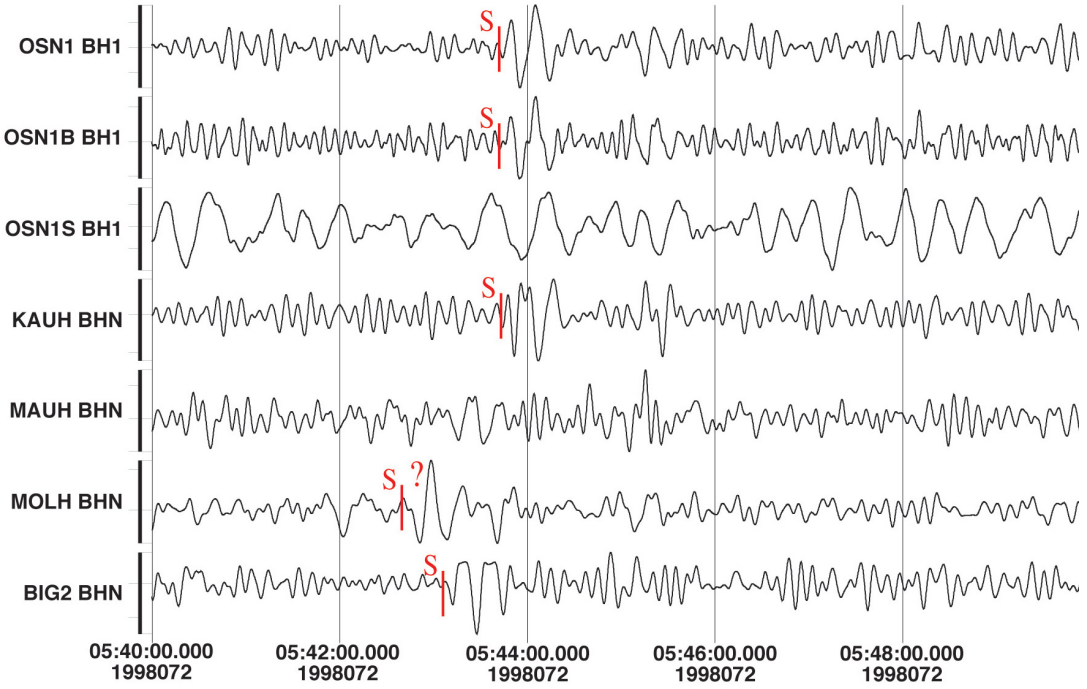

Figure V.9 S-wave data from a 4.9 m_b, 5.0 Ms shallow earthquake in Central America. Location 14.53N, -92.70E, about 60^o from the Hawaiian Islands; the array aperture is approx. 5 degrees at this azimuth. OSN1 and OSN1B have the highest signal-to-noise ratio: 2.7. BIG2 is similar at 2.6 and KAUH has only SNR = 2.0- the detection limit. MAUH and MOLH are not good (SNR ¡ 2.0), and there is nothing but low frequency noise on OSN1S.

America. SNR on the borehole and buried stations was 2.7, similar to SNR 2.6 on BIG2. KAUH was at the threshold for detection, SNR=2.0, and noise levels on station MAUH were too high, as were those on MOLH and OSN1S to produce useful data. OSN1S still yielded the poorest data of any station.

V.4.C Rayleigh Waves

The frequency band encompassing the lowest noise levels in the spectrum on the quieter, vertical component (Figure V.2) can produce over three times as many observed Rayleigh wave arrivals as S-waves. Results (Table V.3) were more uniform across the range of stations than for the body-wave phases, with the borehole and buried sensors producing results that overall were very similar to the

Table V.3 Rayleigh Wave Data and Results

Sensor	Location	Observed Events	Lowest Observed Ms	Min. TM Ms	Mean TM Ms	Mean SNR
OSN1	Borehole	154	4.1	3.8	4.5	16.2
OSN1B	Buried	165	4.2	3.8	4.7	14.3
OSN1S	Seafloor	110	4.2	4.0	4.8	9.3
KAUH	Island-Kauai	152	4.2	3.7	4.6	19.4
MAUH	Island-Maui	143	4.1	3.9	4.7	13.2
MOLH	Island-Molokai	167	4.3	3.5	4.7	13.7
BIG2	Island-Hawaii	94	4.3	4.0	4.8	15.8
KIP*	Island-Oahu	42*	4.3*	4.1*	4.8*	4.2*

Island stations, and often better. Figure V.6 shows data from a 4.4 Ms earthquake in the Aleutian Islands. The buried instrument has a signal-to-noise ratio of 1.5- at the limit of detection, but still has a clear Rayleigh wave. For this event, the borehole sensor and two of the island stations have SNR=2, but for the other stations the signal-tonoise is too low. Overall, the minimum calculated threshold magnitude is 3.8 for both the borehole and buried instruments, with the borehole having a lower mean threshold magnitude (4.5 versus 4.7 surface wave magnitude for the buried instrument) However, it is clear from Figures V.6 and V.7 that there is virtually no difference between the data on the two.

V.4.D Love Waves

Few Love waves were detected except on the buried instrument, OSN1B, which stood out as having the lowest noise levels in the 0.01-0.07Hz band on both vertical and horizontal components (see Figure V.2 and Table V.4). The minimum and mean detection thresholds for OSN1B are not any lower (in fact, are slightly

Table V.4 Love Wave Data and Results

Sensor	Location	Observed Events	Lowest Observed Ms	Min. TM	Mean TM	Mean SNR
OSN1	Borehole	24	4.4	4.4	5.1	9.4
OSN1B	Buried	44	4.4	4.0	4.7	7.3
OSN1S	Seafloor	0				
KAUH	Island-Kauai	20	4.4	3.8	4.9	15.3
MAUH	Island-Maui	12	5.0	4.8	5.6	5.2
MOLH	Island-Molokai	9	5.2	5.1	6.0	4.3
BIG2	Island-Hawaii	17	4.4	3.8	5.1	9.6
KIP*	Island-Oahu	10*	4.4*	3.6*	4.6*	9.4*

higher) than for KAUH, BIG2 and KIP which leads us to conclude that OSN1B has low variations in noise as well as a low noise level, and that noise levels fluctuate more on the Island stations, so that Love waves are only seen when signal-to-noise is particularly good, but during these periods the data is good. There is a problem with low frequency noise on the horizontal component of the borehole sensor- evident in the ramping up of the spectrum below 0.04Hz (Figure V.2), and also in the data (Figure V.8). This problem has subsequently been diagnosed and fixed.

V.5 Conclusions

It is clear that the surface sensor, OSN1S, produced low quality data for all arrivals when compared to the other sensors in the experiment because of the high noise levels directly at the seafloor. Burial of the seismometer to a shallow depth had no effect on high frequency seismic noise (Collins et al., 2001). At frequencies above 0.2 Hz, seismic noise levels observed on the buried instrument were

the same as the seafloor sensor, but the buried instrument exhibited dramatically improved noise levels at lower frequencies. This reduction in noise causes the teleseismic S wave detection threshold to improve by 0.5 magnitude units, simply by burying the sensor. Placing a broadband seismometer in a borehole reduced noise levels relative to the surface deployed OBS throughout the spectrum. When compared to the borehole sensor, the vertical component of the buried OBS had similar performance in the frequency band 0.01 to 0.2 Hz, accounting for the similarity of the Rayleigh wave detection threshold between the two instruments. Nevertheless, the borehole horizontal components were significantly noisier than the buried OBS at frequencies below 0.05 Hz, resulting in the buried sensor having better S wave and Love wave detection thresholds. For the Hawaiian Island stations, KAUH on the island of Kauai produced the best results, and had especially low noise levels at higher frequencies. The thresholds for detecting body waves at the seafloor are much lower than those reported in any past studies. Using a borehole instrument, P-waves for 4.4 m_b earthquakes have been detected with decent quality results, and we estimate that data at a SNR=2.0 level should be obtainable for magnitude 4.2 events, an order of magnitude improvement over published observations. The signal-to-noise ratios are even better for S-waves, with observed events at 4.0 m_b and calculated thresholds as low as 3.5 m_b, an even greater improvement over previous studies. We have also shown that high quality surface wave data at teleseismic distances can be obtained at levels lower than previously thought, and that Rayleigh waves should be readily detectable with either a borehole or buried seismometer at magnitude 4.5.

V.5.A Summary

Based on the observations made in this paper and the results from Collins et al. (2001), the best system to record high quality teleseismic P waves at the OSN1 site was the borehole seismometer that was coupled to the basalt at the base

of the sediments. The preferred system to record teleseismic S- and Love waves was the buried broadband OBS which had the best horizontal noise performance at frequencies below 0.04 Hz. For observing Rayleigh waves, both the buried and the borehole seismometer performed comparably. The seafloor broadband sensor had the highest detection threshold for each of the four types of measurements made. When compared to nearby island stations, the borehole system provided similar results for the magnitude detection thresholds for teleseismic P, S, Rayleigh and Love waves, while the buried broadband sensor gave improved detection thresholds for teleseismic S, Rayleigh, and in particular, Love waves but significantly higher detection thresholds for teleseismic P waves. In all cases, the use of buried or borehole broadband seismometers on the seafloor yielded remarkable decreases in detection thresholds over previous observations and theoretical estimates, so that in the future large datasets will be obtainable in shorter amounts of time, saving money and greatly improving research.

V.6 Acknowledgements

We would like to thank the masters and crews of the R/V *Thomson* and R/V *Melville* and Dr. Sean C. Solomon for providing the PELENET data. This work was supported by the National Science Foundation under Grant Number OCE-0002595.

The text in this chapter, in full, is a reprint of material as it appears in: Sutherland, F.H., Vernon, F.L., Orcutt, J.A., Collins, J.A., Stephen, R.A. Results from OSNPE: Improved Teleseismic Earthquake Detection at the Seafloor, Bulletin of the Seismological Society of America, vol. 94, No 5, pp. 1868-1878, 2004. The dissertation author was the primary investigator and author of this paper.

Appendix A

Instrument Locations

A.1 Instrument Location

The transects for the Gulf of California experiment were located on great circle paths. The best fit great circle path for Line 1 (the Alarcón line) was -111.561E, 25.682N to -104.685E, 20.888N giving a total transect length of 881.4 km. A total of 64 instruments yielded data for the refraction survey. There were 7 PASSCAL (land seismometers) on the Baja peninsula, labeled W9 (furthest to the northwest) to W3. On mainland Mexico 9 PASSCAL seismographs were deployed, however numbers E1, E3 and E6 did not function properly and out of the remaining instruments only E7, E8, E9 and E2 (listed in west- east order) actually recorded shots from the ship. 56 OBS were deployed from the New Horizon, of which three (OBS 19, 24 and 43) either were not retrieved from the seafloor or contained no data.

All OBS that were directly shot over were relocated to obtain a best estimate of their position on the seafloor. Shots were only fired between 169 km and 767 km along line, covering OBS 8- 53. To relocate the water wave was picked. The water wave should be symmetric if the correct position is used to convert the raw data into SEG-Y format. A combination of an inversion routine and simple

grid-search were used to find the best position. Most OBS were relocated to within 100 m from their drop/ pick-up positions (Tables A.1, A.2, A.3). The final location of the instruments relative to the great circle path are shown in Figure A.1. OBS 12, 13 and 14 are significantly off-line.

We had multiple, often slightly differing estimates of depth along transect and at the positions of the instruments. Many of the depths noted on OBS deployment were incorrect because the R/V New Horizon has limited depth-ranging capabilities in deeper water and no multi-beam system. There are 5 estimates of depth of each OBS (Tables A.1, A.2, A.3): the first is the deployment depth from the R/V New Horizon, the second is the depth after instrument relocation (8-53 only). The third is the minimum travel time on the OBS record section (see Appendix B) converted to depth (08-53 only). The fourth estimate is the depth of a bathymetry grid at the instrument location. Many of the instruments in the center of the transect were covered by Peter Lonsdale's high resolution bathymetry grid, and these estimates are accurate, but elsewere the satellite-derived bathymetry is used, which is not so accurate (around 1 km grid spacing, values indicated with *). The final estimate is from the centerbeam of R/V Maurice Ewing, which is logged every minute (again, only 08-53). Elevations of the land-based seismographs were measured using hand-held GPS units, and were checked on deployment and pick-up (Table A.4). The Lonsdale bathymetry depths were used where possible, and elsewhere deployment depths from the R/V New Horizon were taken.

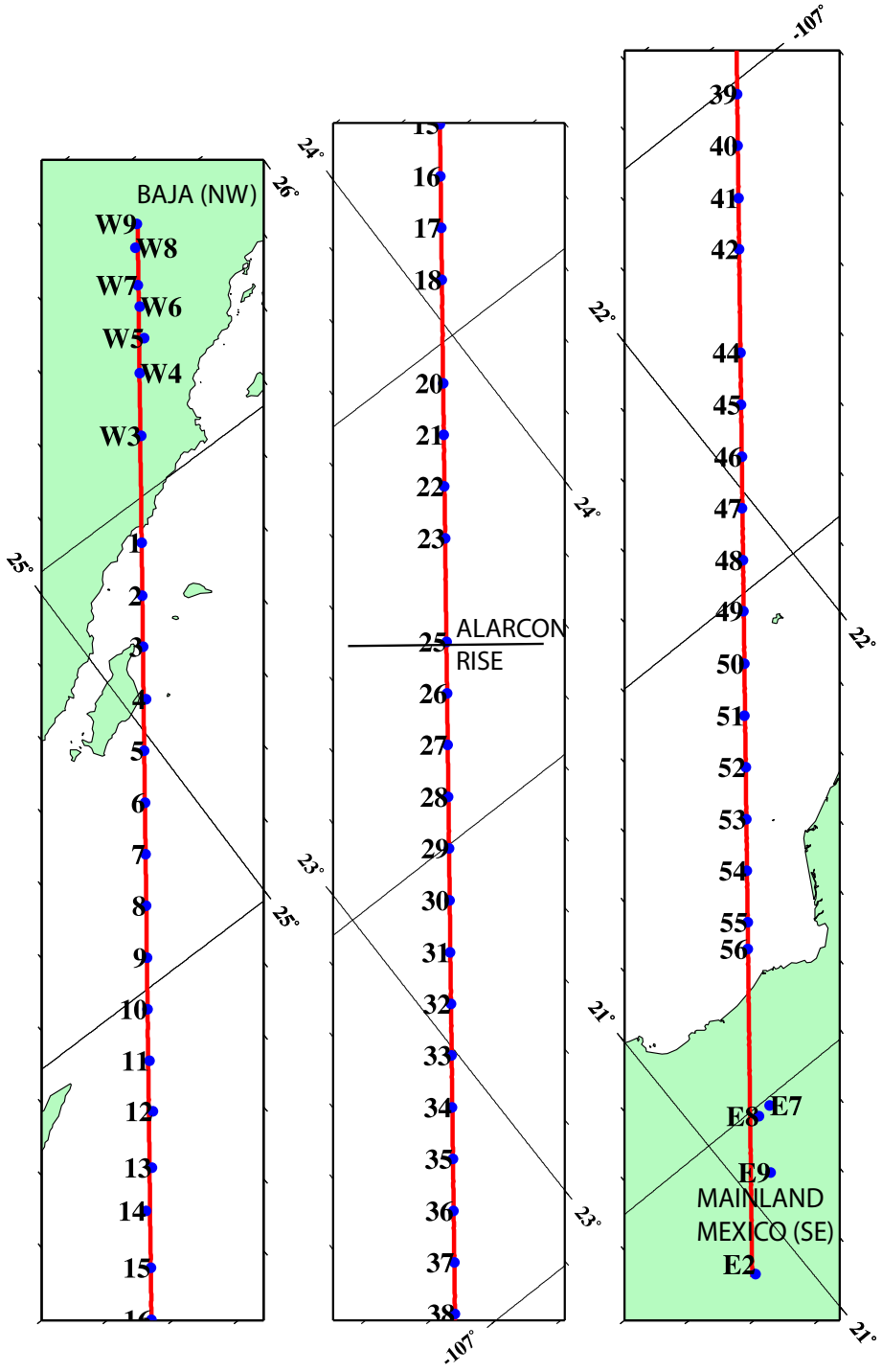

Figure A.1 Location of Alarcón transect (red) and instruments used in refraction survey (blue). W9 is located on the Baja peninsula, OBS 25 is at the Alarcón Rise and E2 is near Tepic on mainland Mexico.

Table A.1 OBS location information 01 -25

OBS	X (km)	Deploy lon.	Deploy lat.	Deploy Depth (km)	Reloc longitude	Reloc latitude	Reloc Depth	min TT. Depth	Bathy Grid Depth	Center-beam Depth
1	81.102	-110.9066	25.2543	0.100					0.104*	
2	94.497	-110.7992	25.1831	0.783					0.759*	
3	107.446	-110.6954	25.1143	0.071					0.033*	
4	120.837	-110.5847	25.0474	0.073					-0.005*	
5	133.901	-110.4834	24.9739	0.774					0.685*	
6	147.073	-110.378	24.9039	0.850					1.192	
7	160.147	-110.2738	24.834	0.660					0.662	
8	173.362	-110.1693	24.7641	0.490	-110.1684	24.7635	0.45	0.384	0.228*	0.4269
9	186.577	-110.064	24.6938	0.856	-110.0629	24.6932	0.85	0.900	0.942	0.9316
10	199.582	-109.9599	24.6234	0.930	-109.9594	24.6237	0.89	0.900	0.929	0.9306
11	212.782	-109.8536	24.5559	0.410	-109.8538	24.5539	0.35	0.372	0.417	0.4039
12	225.914	-109.7471	24.4917	1.140	-109.7468	24.4869	0.98	1.092	1.154	1.1313
13	239.256	-109.6363	24.4122	0.840	-109.6403	24.4162	0.80	0.804	0.888	0.8505
14	252.262	-109.5584	24.3414	1.430	-109.5451	24.3368	1.28		1.414	1.4261
15	265.459	-109.4379	24.2709	1.570	-109.4383	24.2688	1.50	1.536	1.578	1.5626
16	278.624	-109.3337	24.2003	1.495	-109.3330	24.1995	1.467	1.464	1.511	1.5033
17	291.744	-109.2295	24.1294	0.950	-109.2293	24.1290	0.927	0.936	0.969	0.9622
18	304.874	-109.1259	24.0585	1.550	-109.1257	24.0583	1.514	1.500	1.555	1.5189
20	331.061	-108.9185	23.9167	1.960	-108.9194	23.9171	2.362	2.340	2.393	2.3747
21	344.145	-108.8157	23.8454	2.720	-108.8167	23.8462	2.697	2.688	2.717	2.6774
22	357.071	-108.7129	23.7746	2.740	-108.7132	23.7787	2.68	2.688	2.754	2.7199
23	370.18	-108.6089	23.7033	2.760	-108.6108	23.7072	2.74	2.736	2.795	2.7704
25	396.586	-108.4028	23.5606	2.560	-108.4045	23.5634	2.378	2.376	2.428	2.4212

Table A.2 OBS location information 26 -49

OBS	X (km)	Deploy longitude	Deploy latitude	Deploy Depth (km)	Reloc longitude	Reloc latitude	Reloc Depth	min TT. Depth	Bathy Grid Depth	Center-beam Depth
26	409.763	-108.3001	23.4893	2.610	-108.3011	23.4923	2.700	2.676	2.633	2.6141
27	423.072	-108.1982	23.4176	2.616	-108.1987	23.4181	2.488	2.484	2.554	2.5033
28	436.349	-108.0948	23.346	2.550	-108.0955	23.3454	2.480	2.496	2.559	2.5478
29	449.479	-107.9928	23.2747	2.460	-107.9926	23.2746	2.427	2.424	2.485	2.4608
30	462.706	-107.8894	23.203	2.450	-107.8893	23.2029	2.413	2.412	2.456	2.4459
31	475.875	-107.7874	23.131	2.530	-107.7871	23.1308	2.499	2.508	2.556	2.528
32	489.035	-107.6854	23.0593	2.220	-107.6849	23.0589	2.192	2.196	2.096*	2.2125
33	502.084	-107.5837	22.9875	1.830	-107.5838	22.9874	1.794	1.800	1.829	1.8148
34	515.250	-107.4816	22.9155	0.790	-107.4818	22.9153	0.761	0.744	0.788	0.7862
35	528.357	-107.3797	22.8437	1.390	-107.3800	22.8439	1.356	1.344	1.288*	1.4004
36	541.525	-107.2776	22.7716	1.710	-107.2780	22.7719	1.676	1.680	1.733	1.712
37	554.735	-107.1758	22.6995	2.000	-107.1758	22.6996	1.976	1.980	2.021	2.0137
38	567.840	-107.0749	22.6274	1.870	-107.0751	22.6271	1.897	1.896	1.934	1.9108
39	581.145	-106.9732	22.5546	1.465	-106.9735	22.5528	1.402	1.404	1.445	1.4469
40	594.260	-106.8719	22.4827	1.420	-106.8712	22.4822	1.386	1.380	1.412	1.4083
41	607.540	-106.7693	22.4094	1.350	-106.7691	22.4090	1.43	1.428	1.479	1.4612
42	620.523	-106.6699	22.3379	1.000	-106.6692	22.3376	0.90	0.912	0.987	0.9869
44	646.835	-106.4673	22.1924	0.190	-106.4673	22.1924	0.190		0.391	0.2011
45	660.106	-106.366	22.1193	0.472	-106.3656	22.1191	0.458	0.432	0.402*	0.4806
46	673.178	-106.2654	22.047	0.092	-106.2654	22.0470	0.092		0.053*	0.0955
47	686.232	-106.165	21.9737	0.056	-106.1658	21.9745	0.04	0.048	0.063*	0.0577
48	699.484	-106.0647	21.9014	0.051	-106.0645	21.9012	0.04	0.024	0.058*	0.0523
49	712.536	-105.9654	21.8286	0.051	-105.9646	21.8292	0.049	0.072	0.046*	0.0523

Table A.3 OBS location information 50-56

OBS	X (km)	Deploy longitude	Deploy latitude	Deploy Depth (km)	Reloc longitude	Reloc latitude	Reloc Depth	min TT. Depth	Bathy Grid Depth	Center-beam Depth
50	725.696	-105.8642	21.7556	0.049	-105.8647	21.7557	0.04	0.036	0.038*	0.0507
51	738.828	-105.7642	21.6817	0.048	-105.7646	21.6829	0.035	0	0.030*	0.0499
52	752.035	-105.6638	21.6101	0.047	-105.6638	21.6099	0.035	0	0.033*	0.0491
53	765.216	-105.5634	21.5367	0.043	-105.5638	21.5364	0.03	0	0.056*	0.0458
54	778.295	-105.4645	21.4636	0.049					0.091*	
55	791.472	-105.3643	21.3905	0.041					0.194*	
56	798.151	-105.314	21.3529	0.033					0.267*	

Table A.4 Ref-Tek Locations

Ref-Tek	X (km)	longitude	latitude	Elevation (km)
W9	0.211	-111.5610	25.6801	0.210
W8	6.194	-111.5150	25.6448	0.222
W7	15.629	-111.4351	25.5991	0.279
W6	21.066	-111.3893	25.5728	0.294
W5	29.156	-111.3180	25.5380	0.248
W4	38.058	-111.2529	25.4822	0.361
W3	53.981	-111.1236	25.3993	0.358
E7	837.981	-104.9823	21.16653	0.820
E8	840.709	-104.9781	21.1318	0.917
E9	855.029	-104.8534	21.0714	0.712
E2	880.659	-104.6855	20.898	0.726

Appendix B

Refraction Data by Instrument

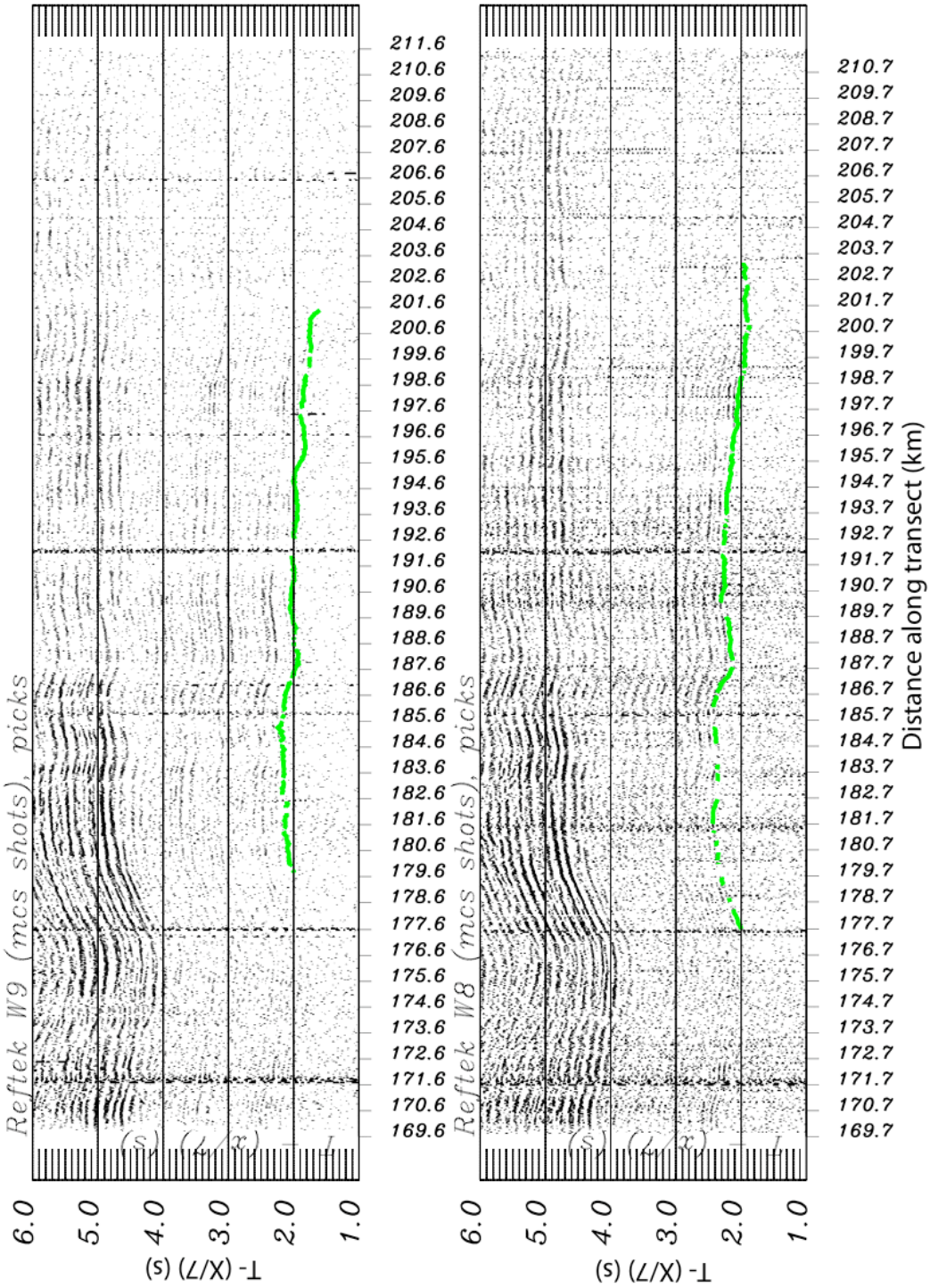

Figure B.1 PASSCAL seismographs W9 and W8 plotted with a reduction velocity of 7 km/s

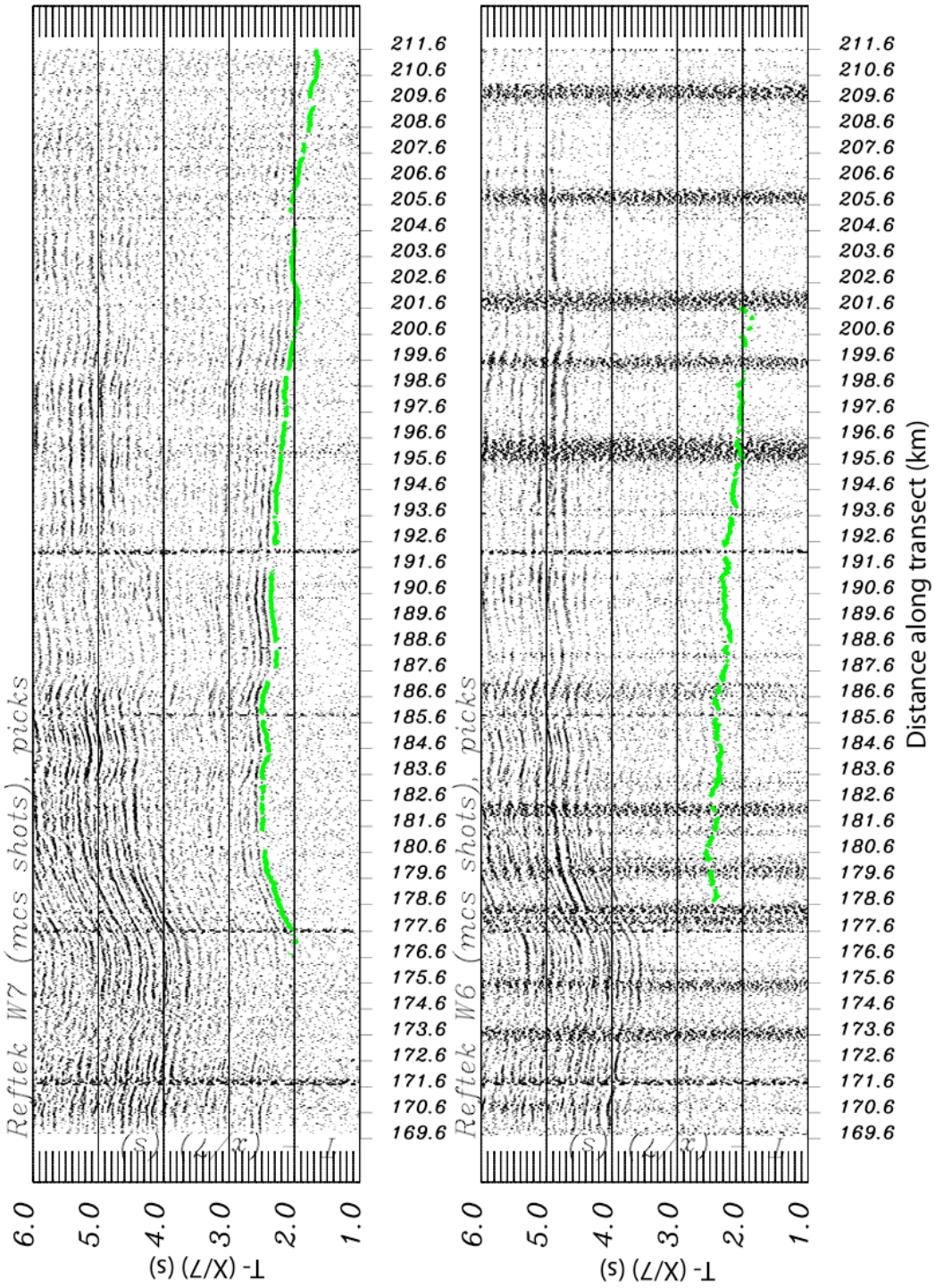

Figure B.2 PASSCAL seismographs W7 and W6 plotted with a reduction velocity of 7 km/s

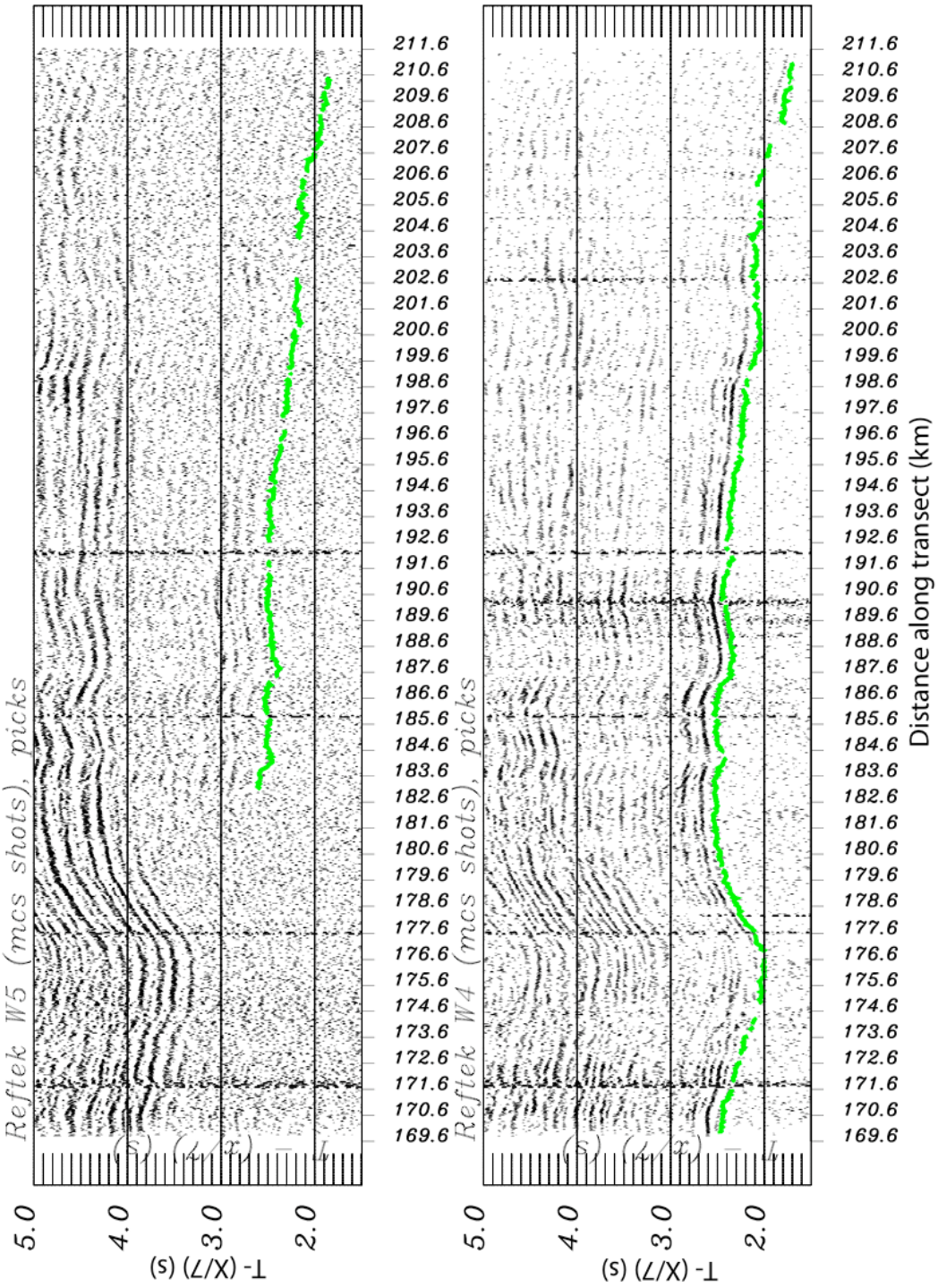

Figure B.3 PASSCAL seismographs W5 and W4 plotted with a reduction velocity of 7 km/s

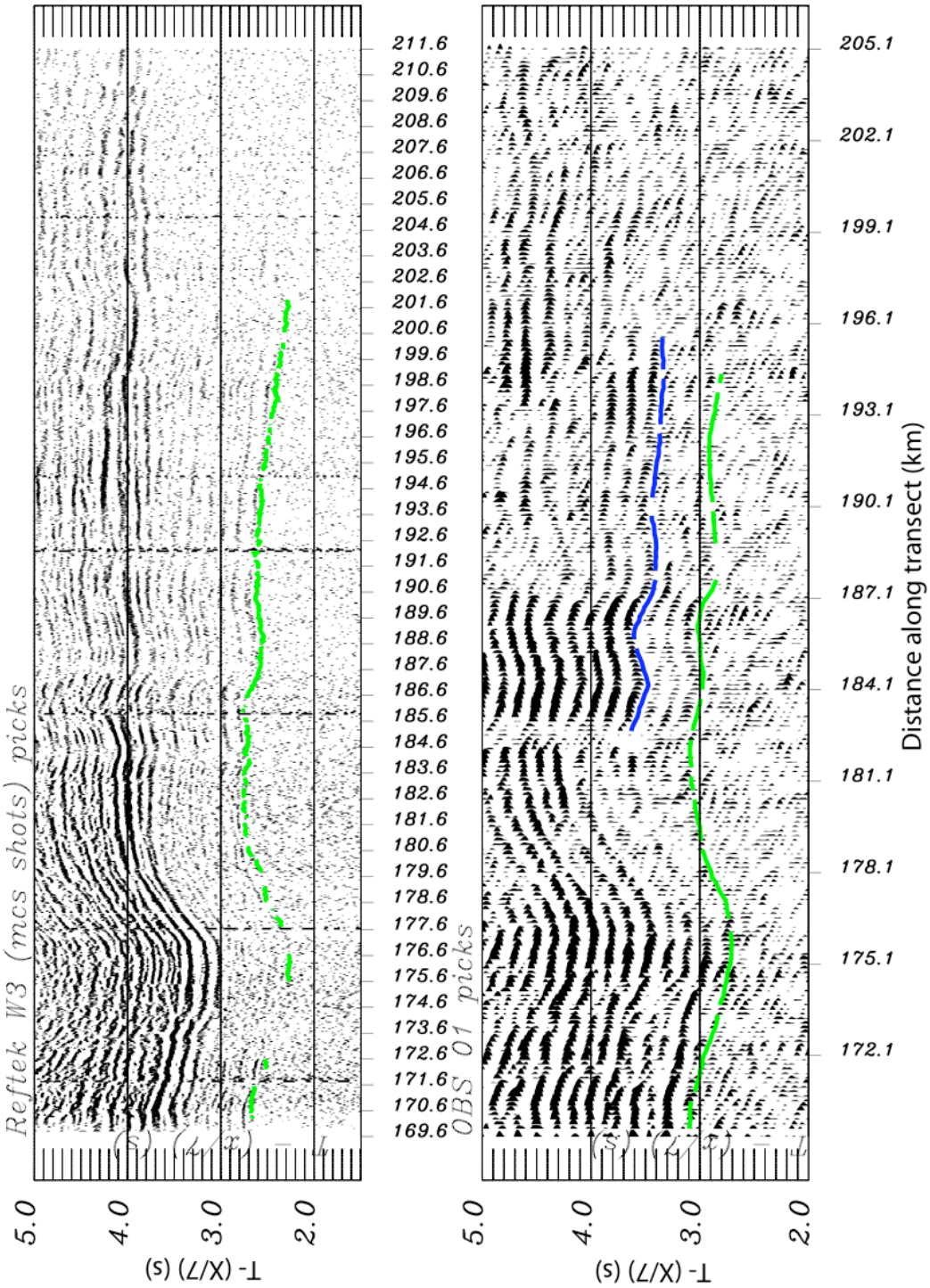

Figure B.4 PASSCAL seismograph W3 and OBS 01 plotted with a reduction velocity of 7 km/s

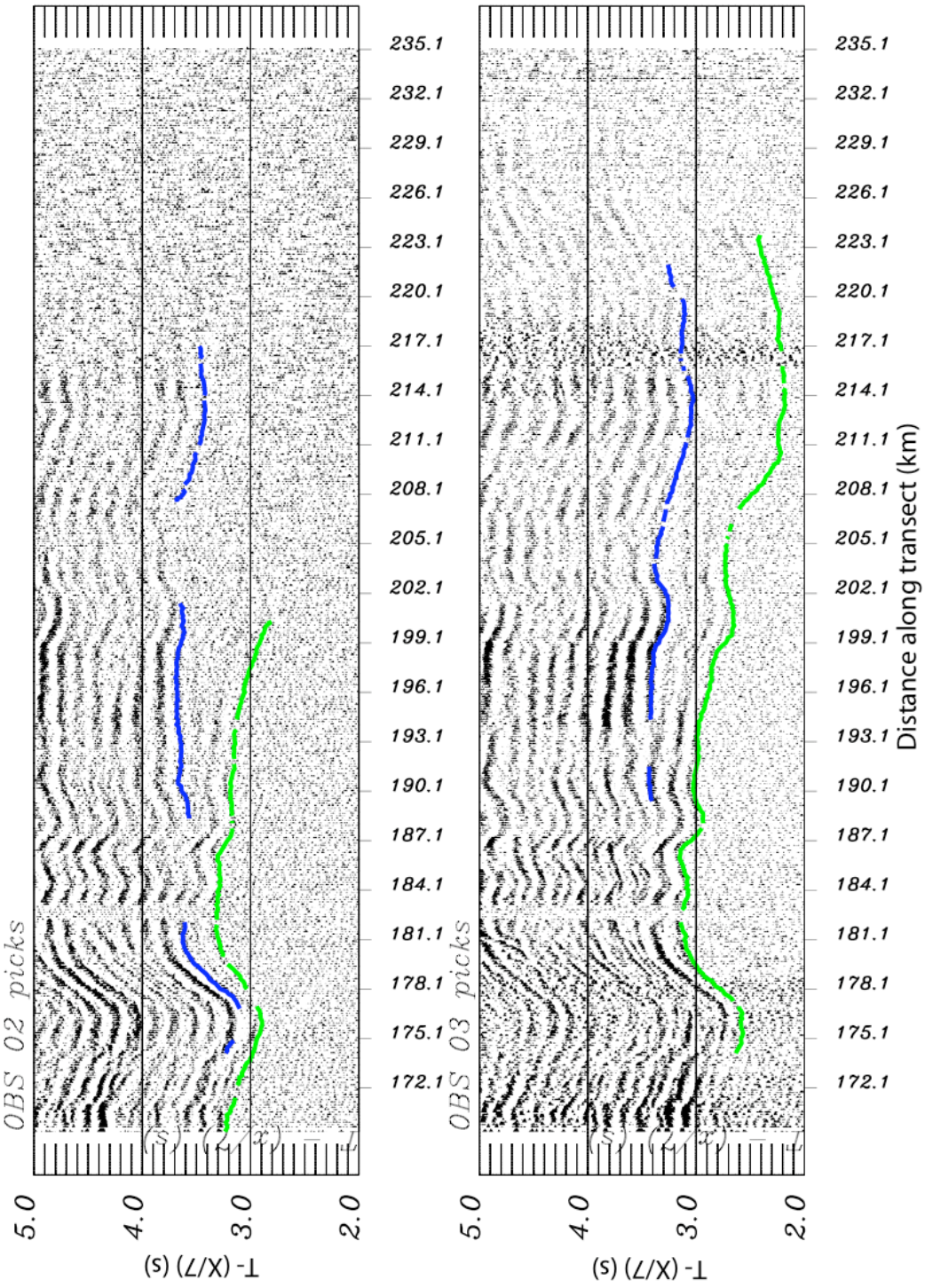

Figure B.5 OBS 02 and 03 plotted with a reduction velocity of 7 km/s

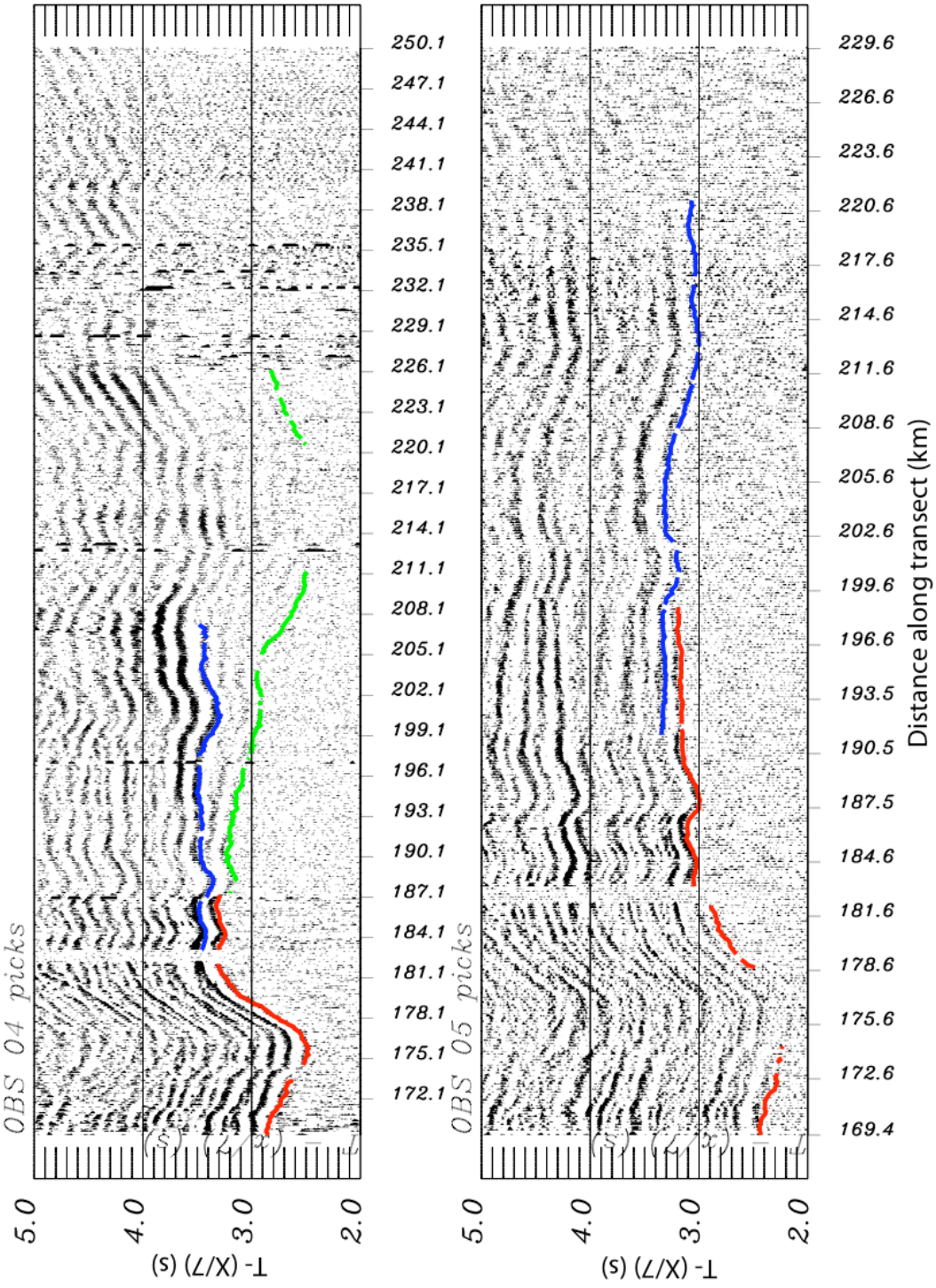

Figure B.6 OBS 04 and 05 plotted with a reduction velocity of 7 km/s

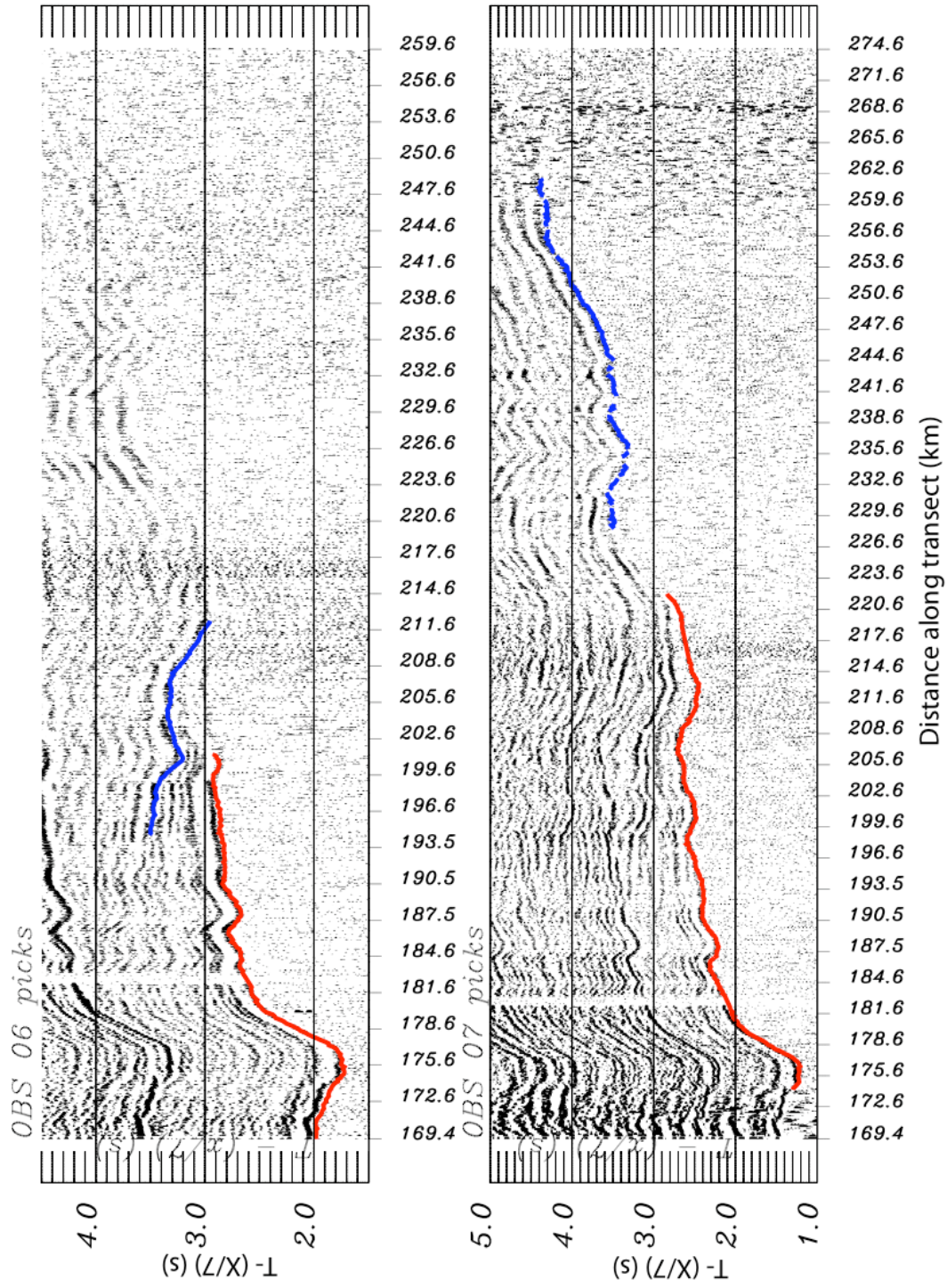

Figure B.7 OBS 06 and 07 plotted with a reduction velocity of 7 km/s

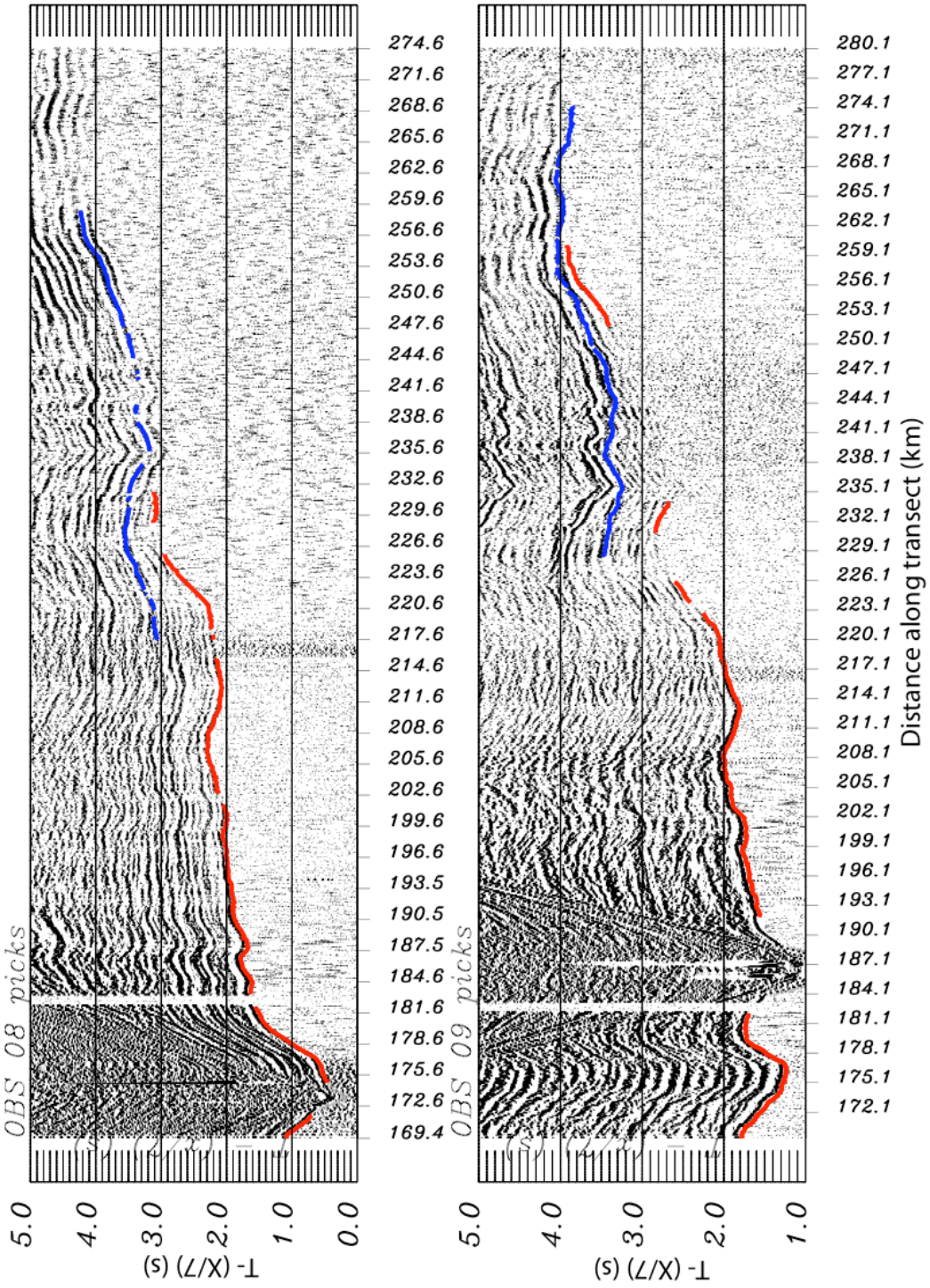

Figure B.8 OBS 08 and 09 plotted with a reduction velocity of 7 km/s

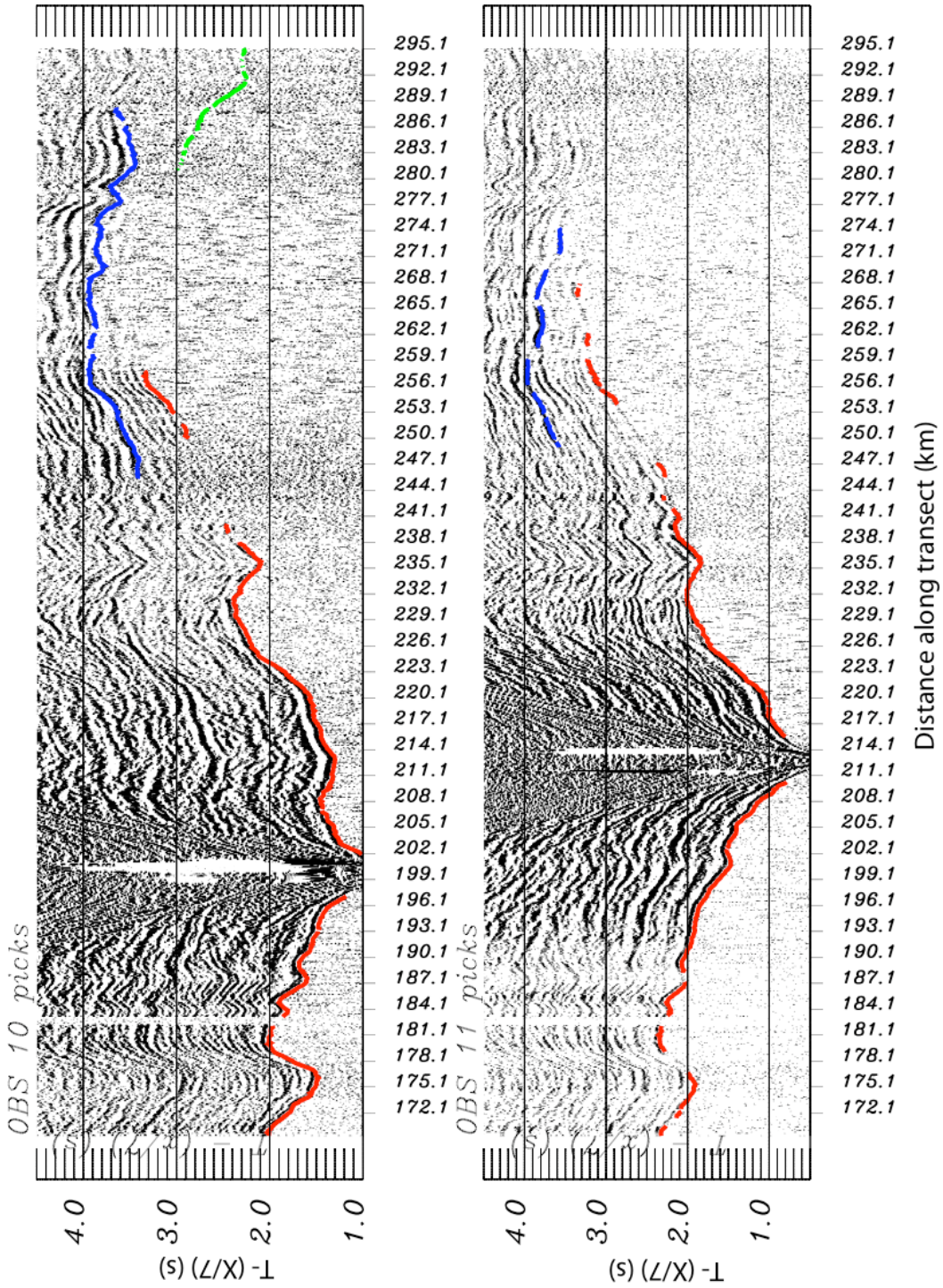

Figure B.9 OBS 10 and 11 plotted with a reduction velocity of 7 km/s

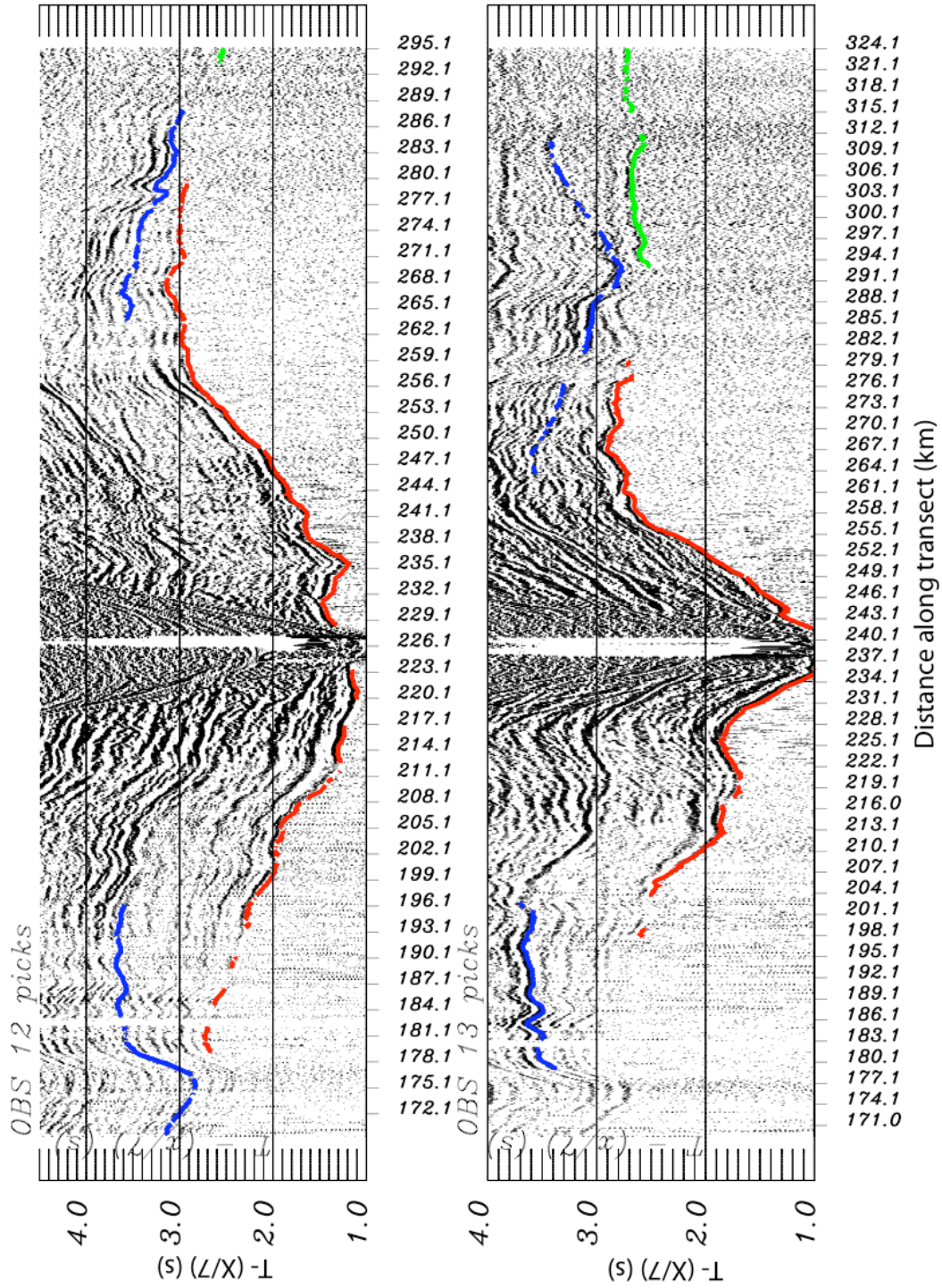

Figure B.10 OBS 12 and 13 plotted with a reduction velocity of 7 km/s

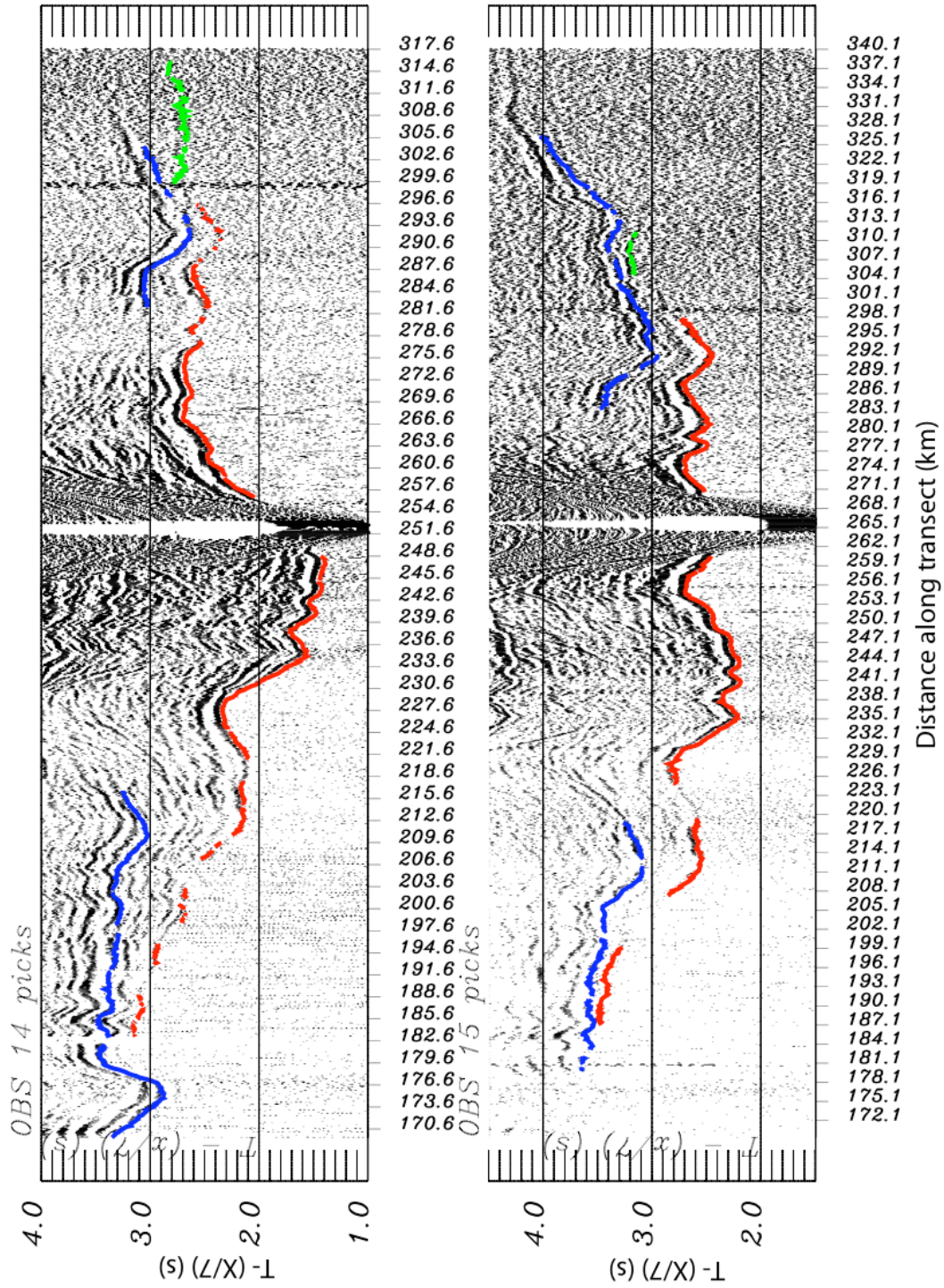

Figure B.11 OBS 14 and 15 plotted with a reduction velocity of 7 km/s

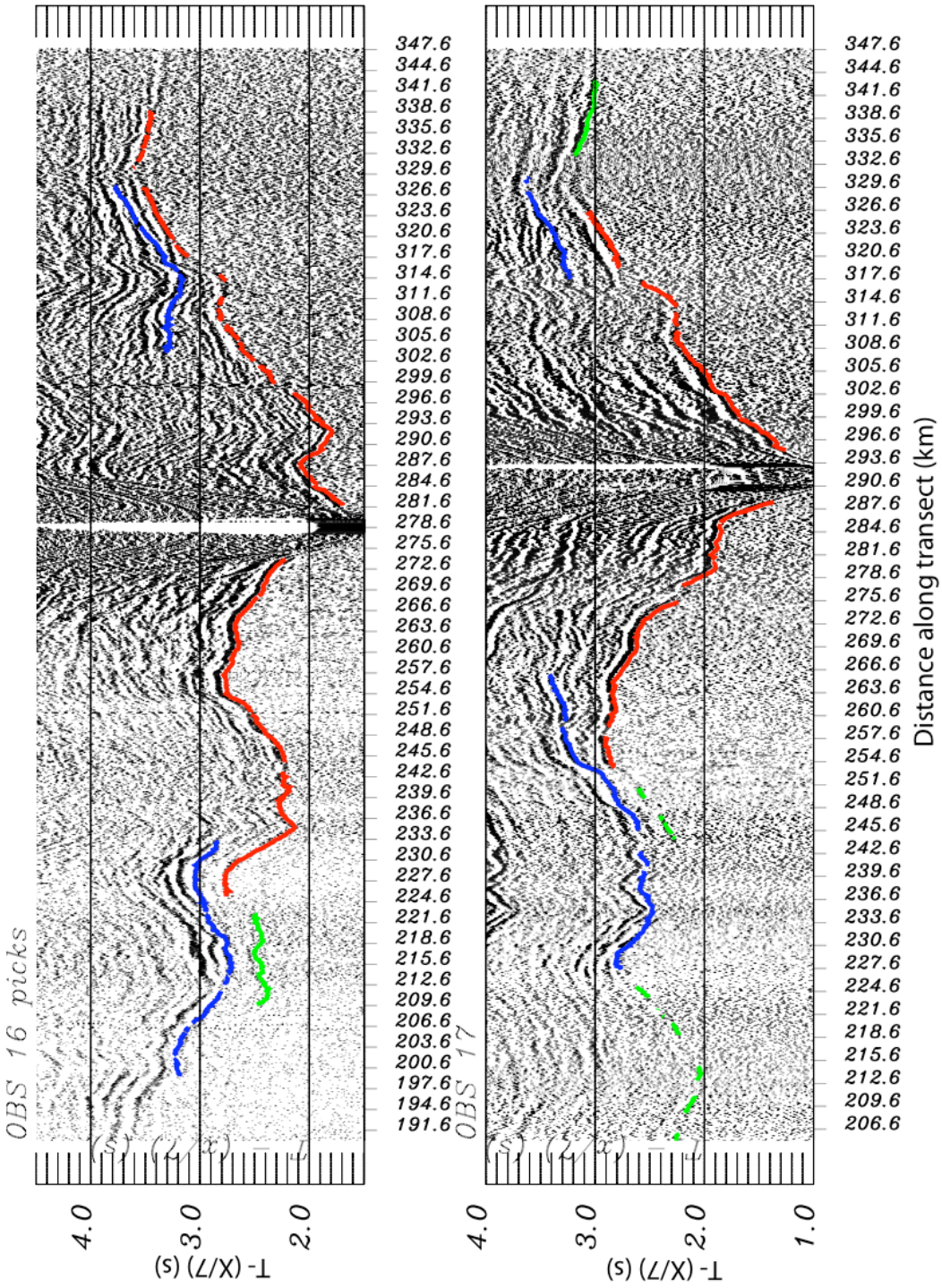

Figure B.12 OBS 16 and 17 plotted with a reduction velocity of 7 km/s

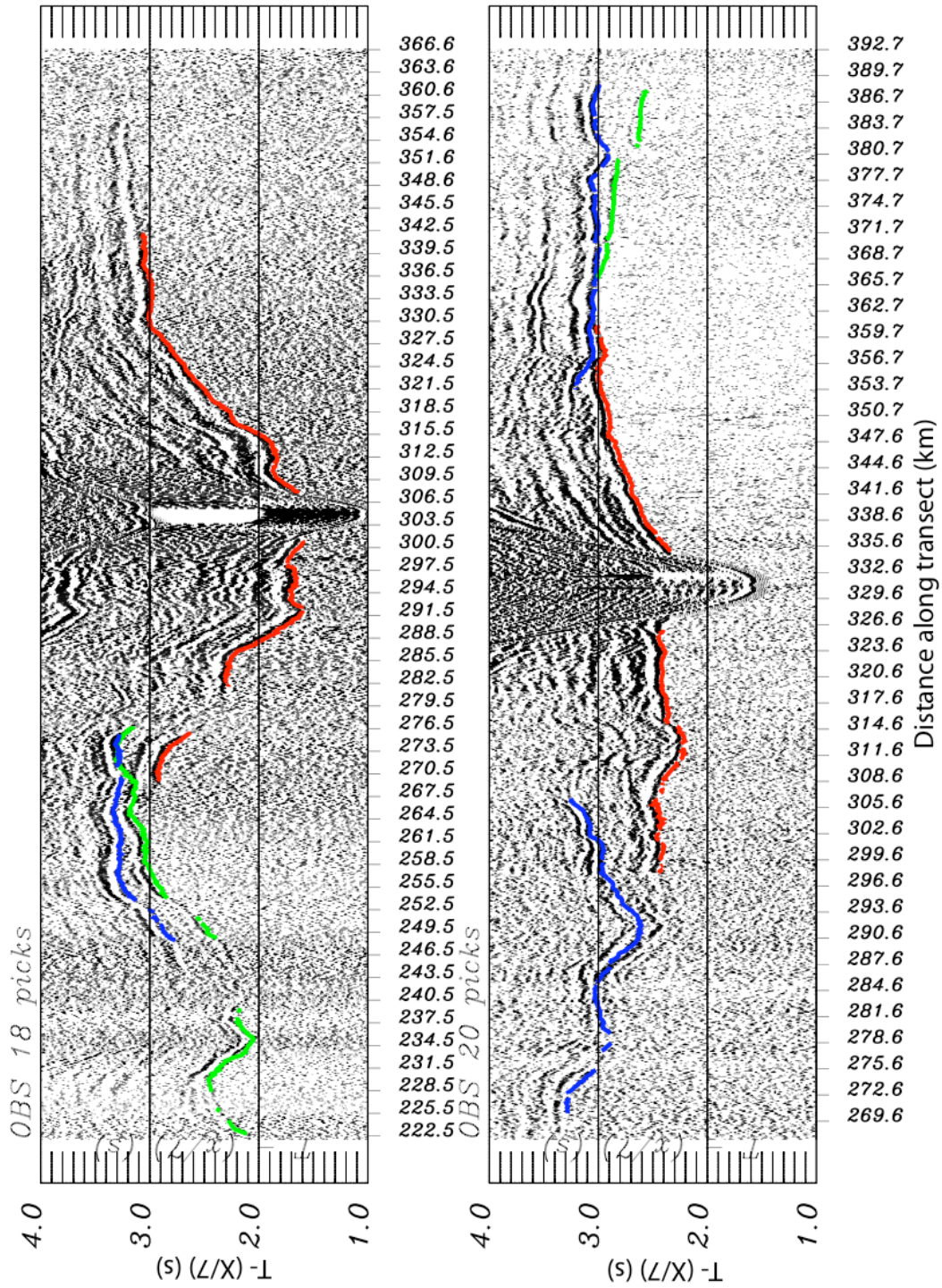

Figure B.13 OBS 18 and 20 plotted with a reduction velocity of 7 km/s

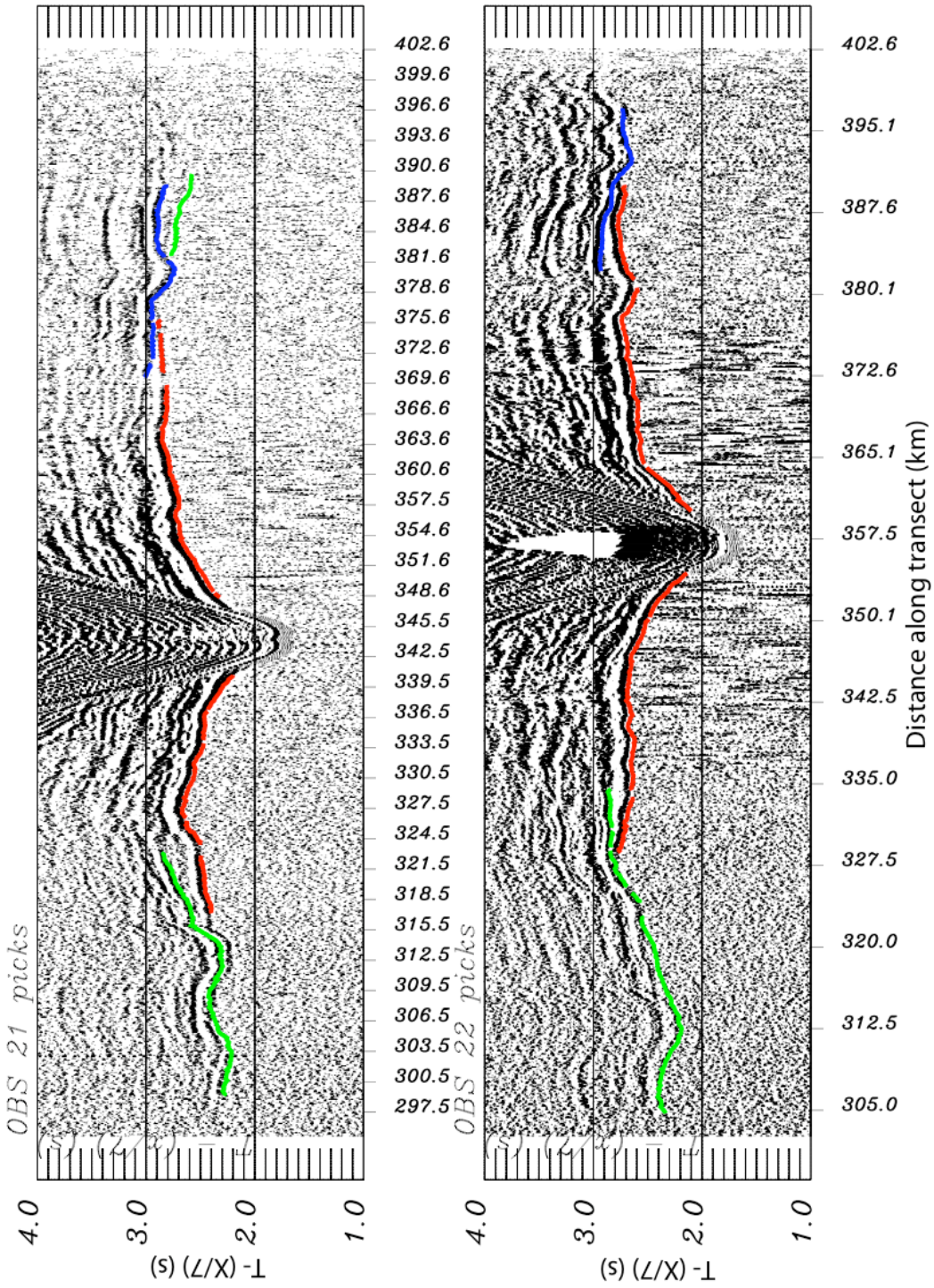

Figure B.14 OBS 21 and 22 plotted with a reduction velocity of 7 km/s

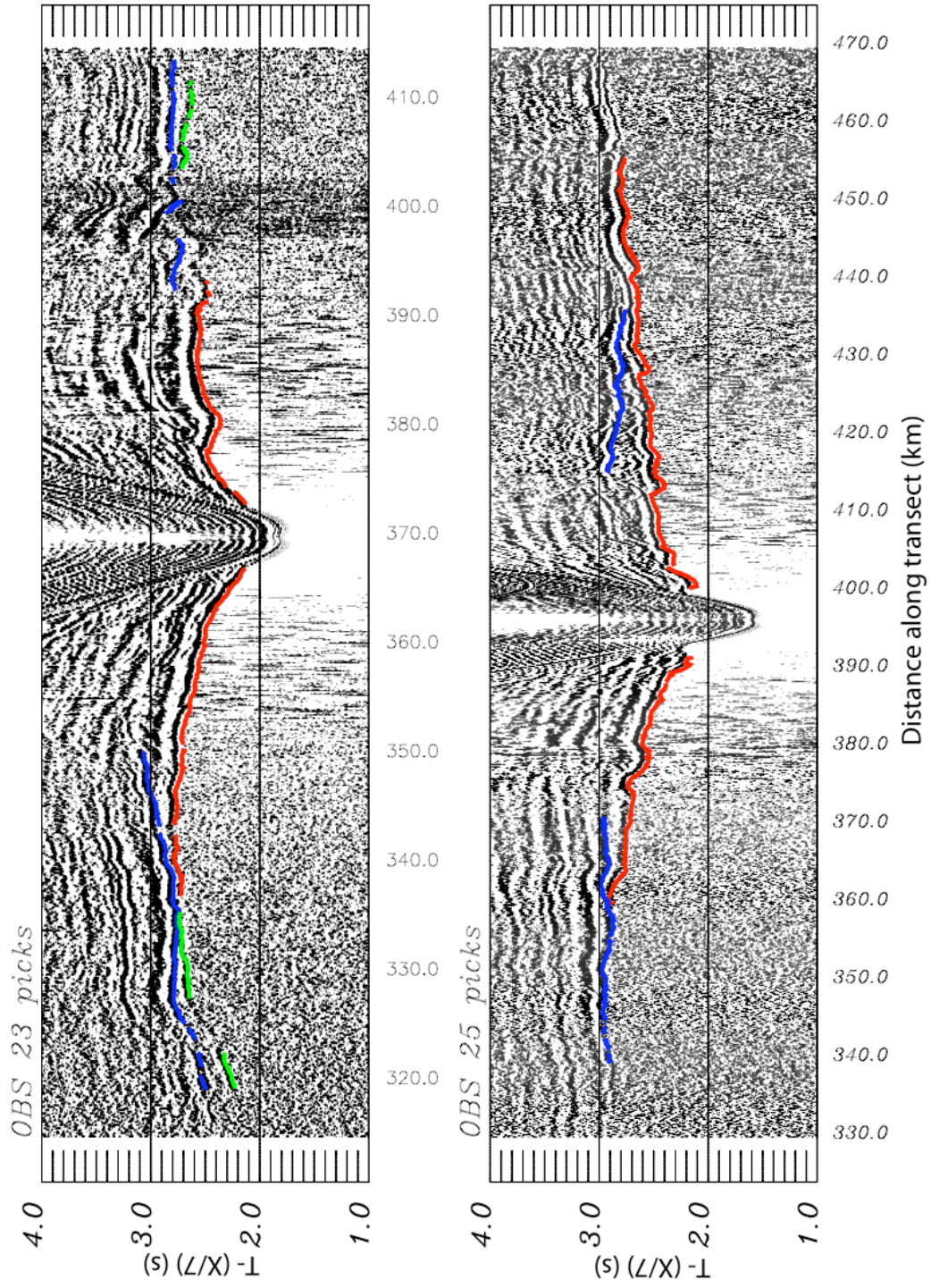

Figure B.15 OBS 23 and 25 plotted with a reduction velocity of 7 km/s

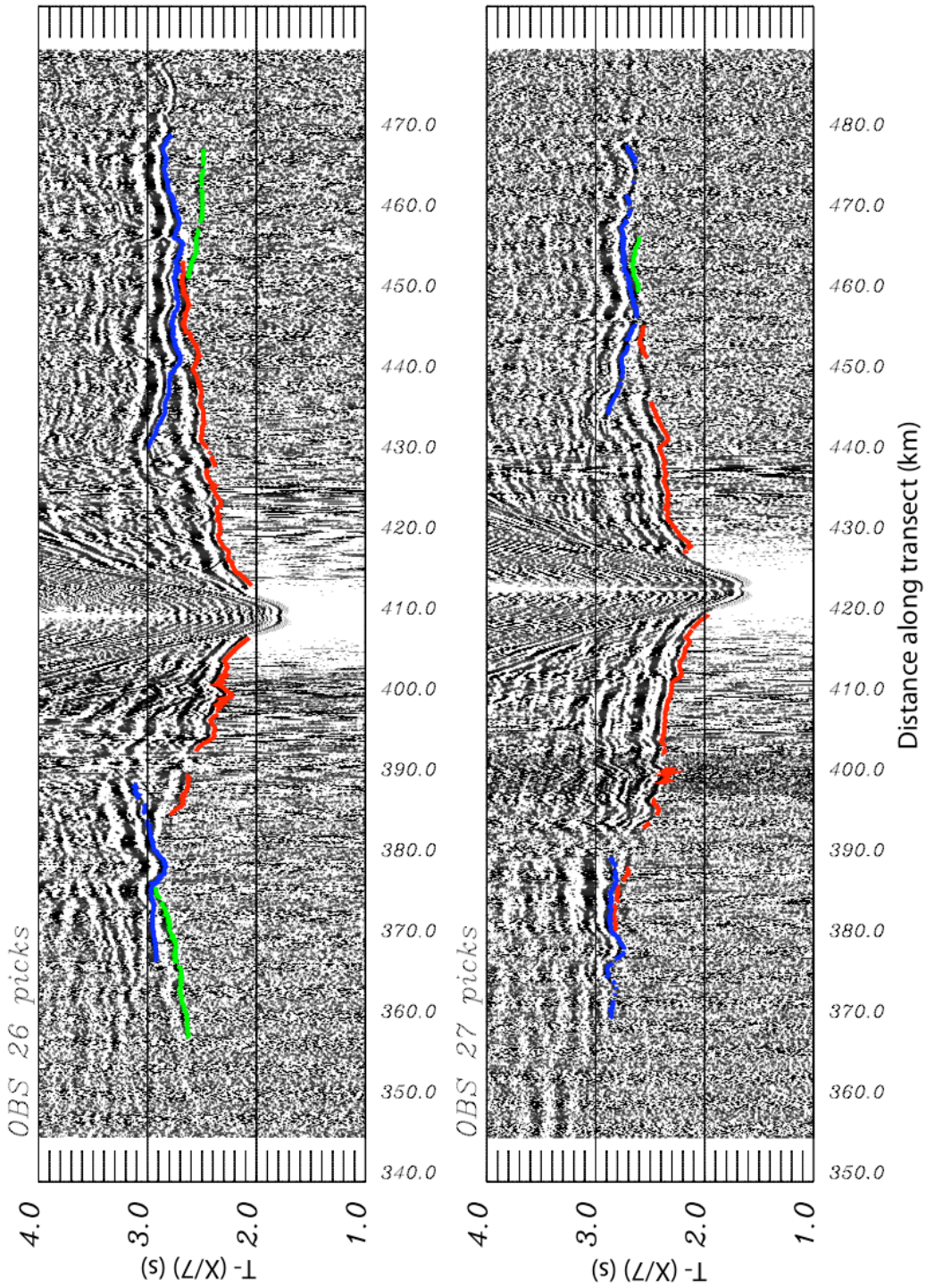

Figure B.16 OBS 26 and 27 plotted with a reduction velocity of 7 km/s

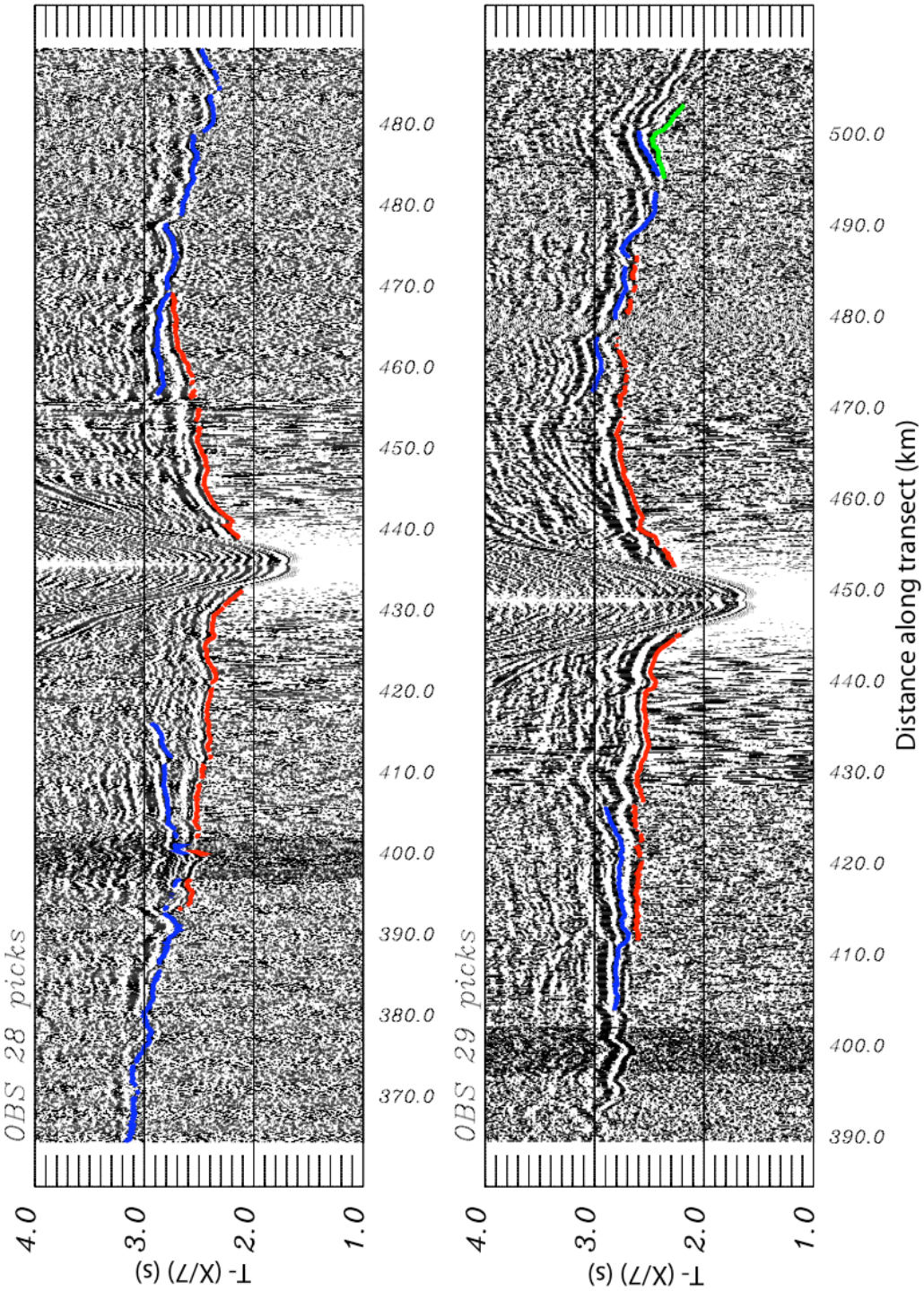

Figure B.17 OBS 28 and 29 plotted with a reduction velocity of 7 km/s

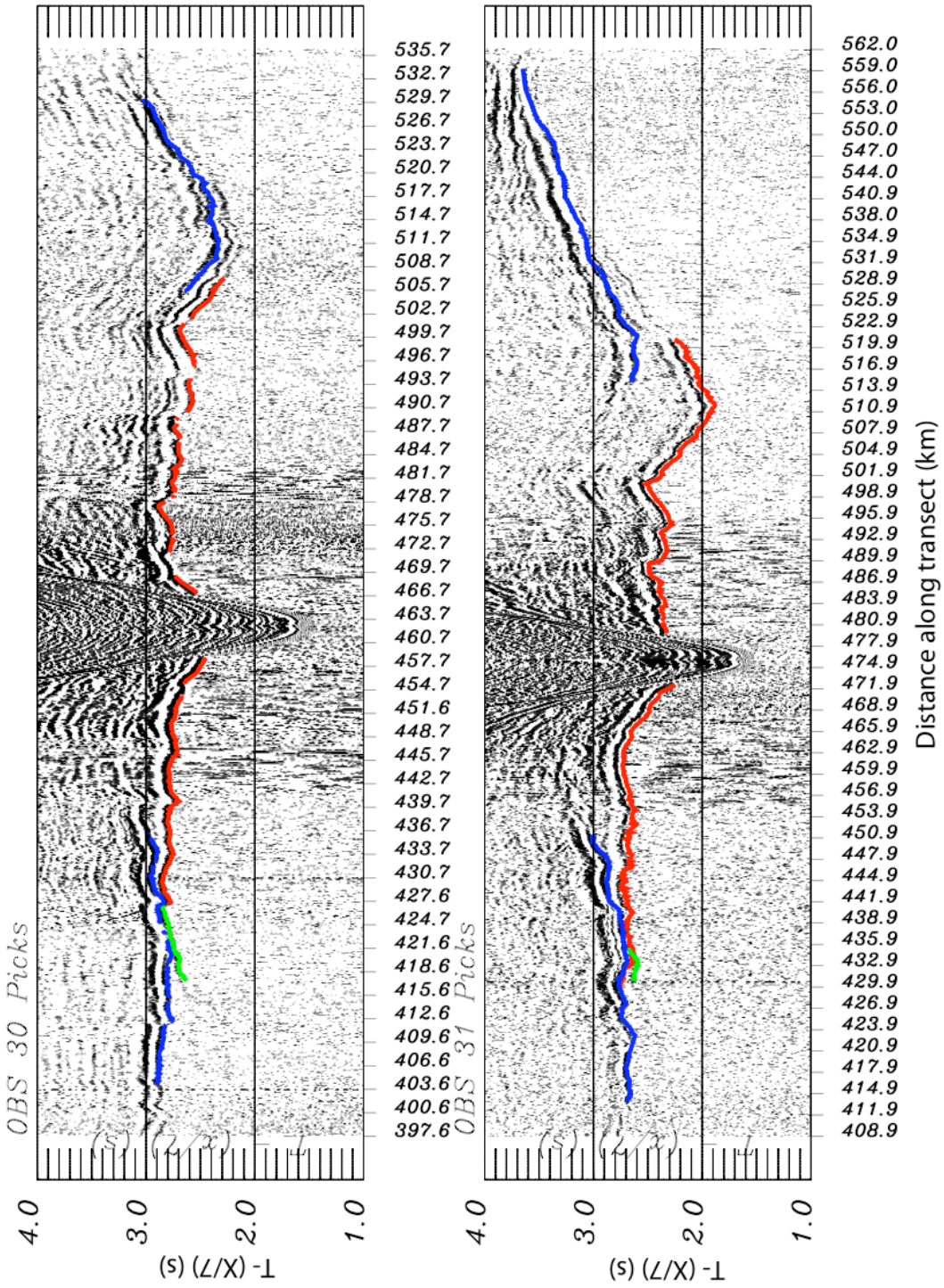

Figure B.18 OBS 30 and 31 plotted with a reduction velocity of 7 km/s

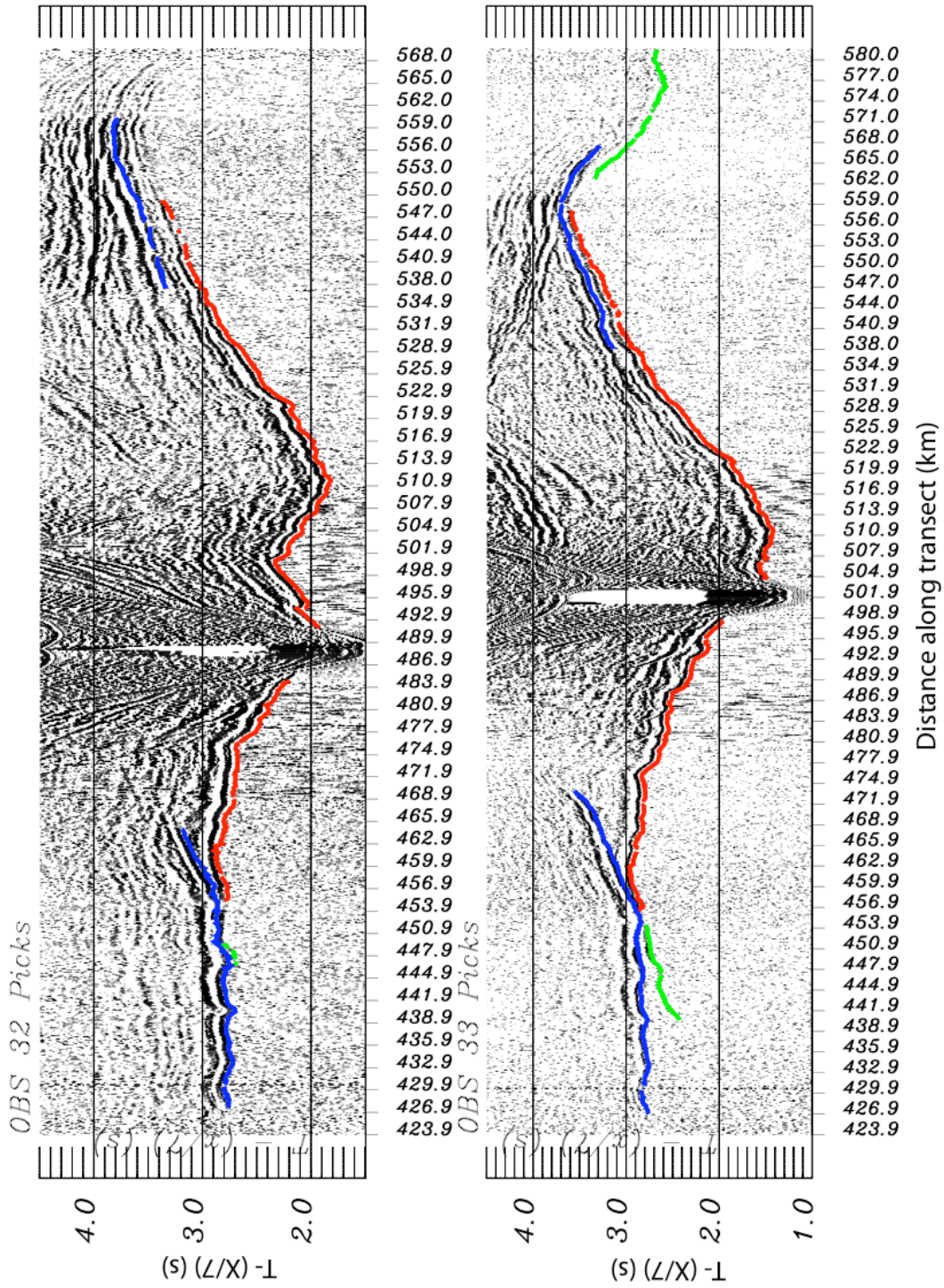

Figure B.19 OBS 32 and 33 plotted with a reduction velocity of 7 km/s

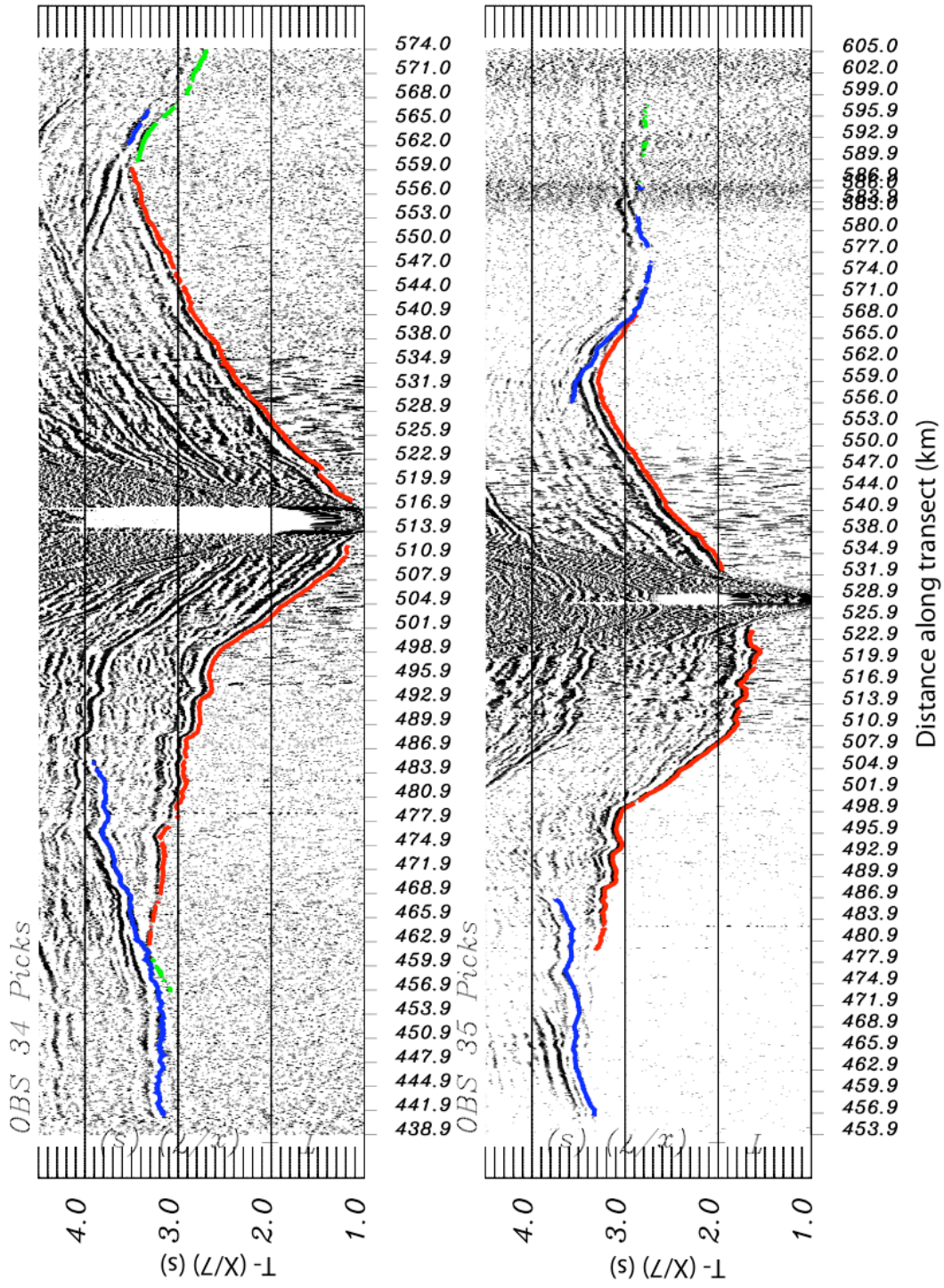

Figure B.20 OBS 34 and 35 plotted with a reduction velocity of 7 km/s

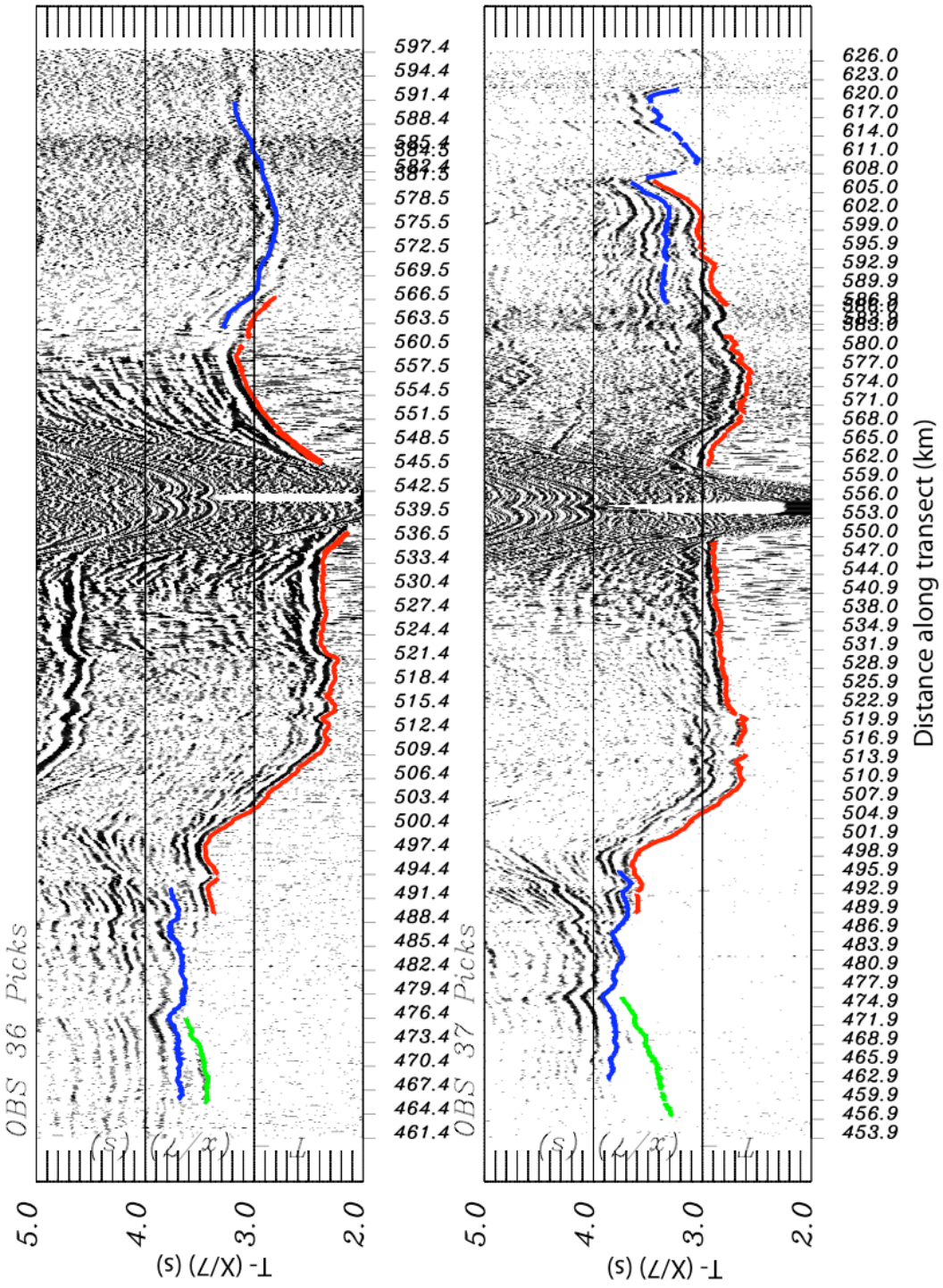

Figure B.21 OBS 36 and 37 plotted with a reduction velocity of 7 km/s

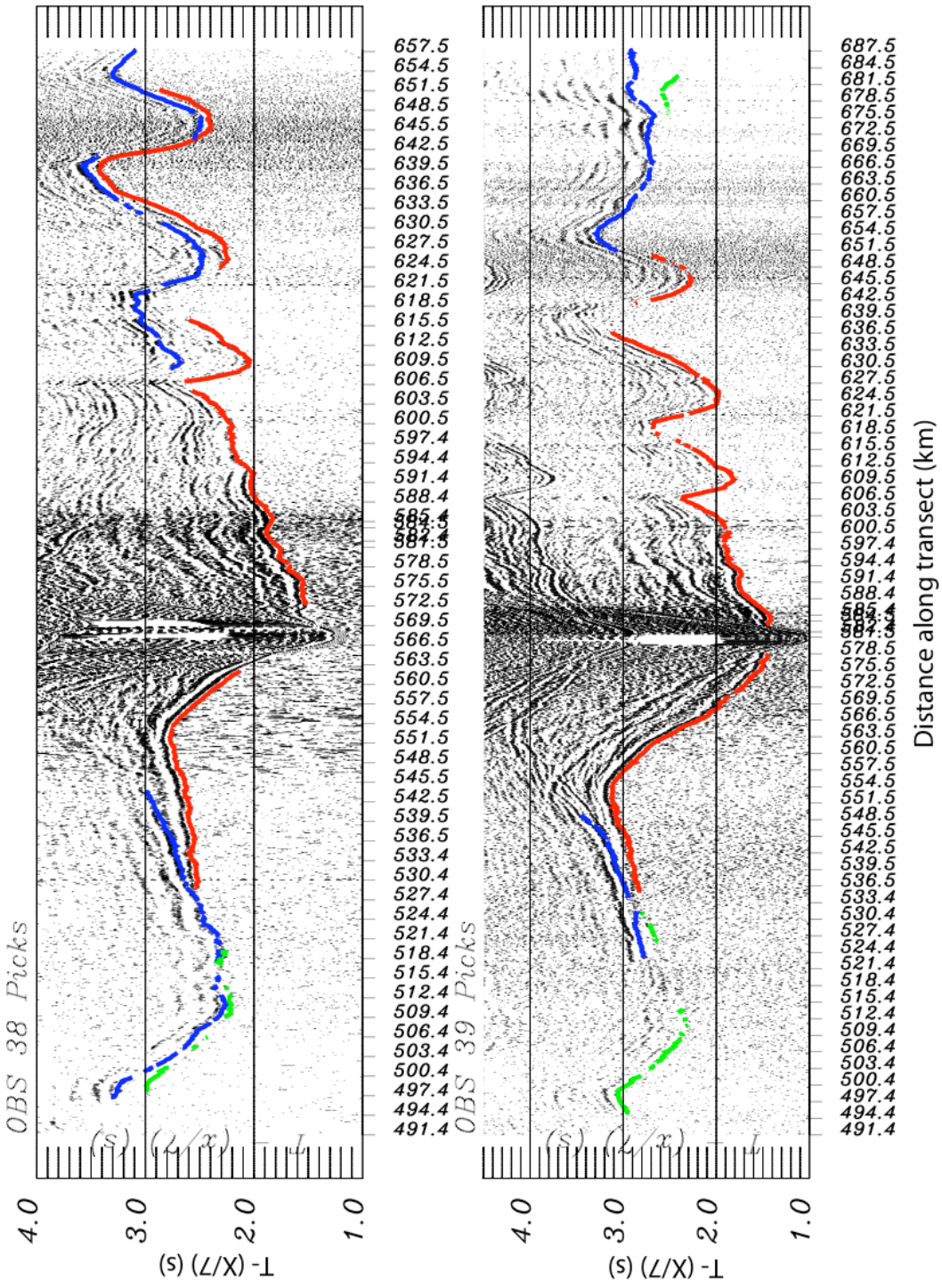

Figure B.22 OBS 38 and 39 plotted with a reduction velocity of 7 km/s

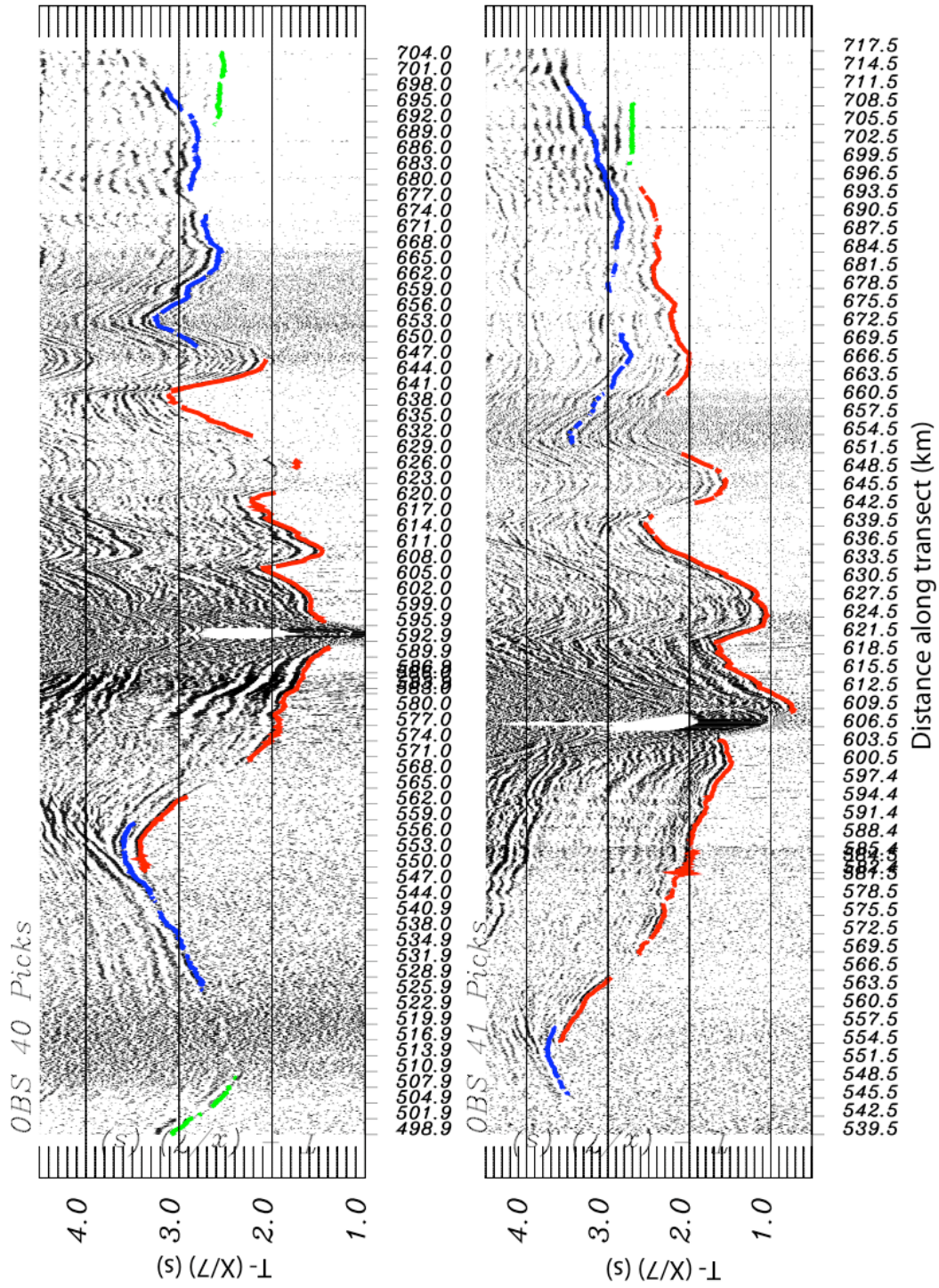

Figure B.23 OBS 40 and 41 plotted with a reduction velocity of 7 km/s

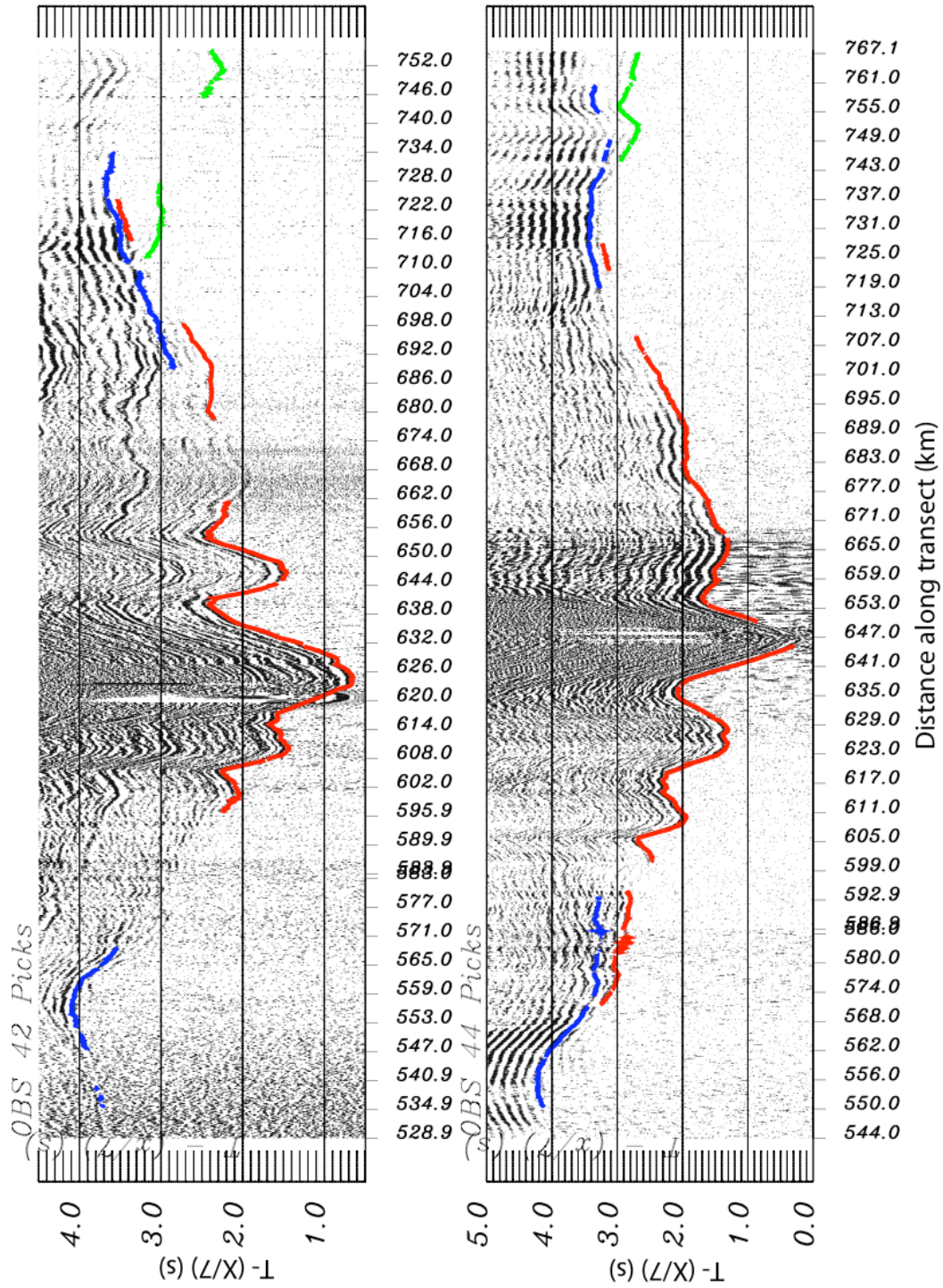

Figure B.24 OBS 42 and 44 plotted with a reduction velocity of 7 km/s

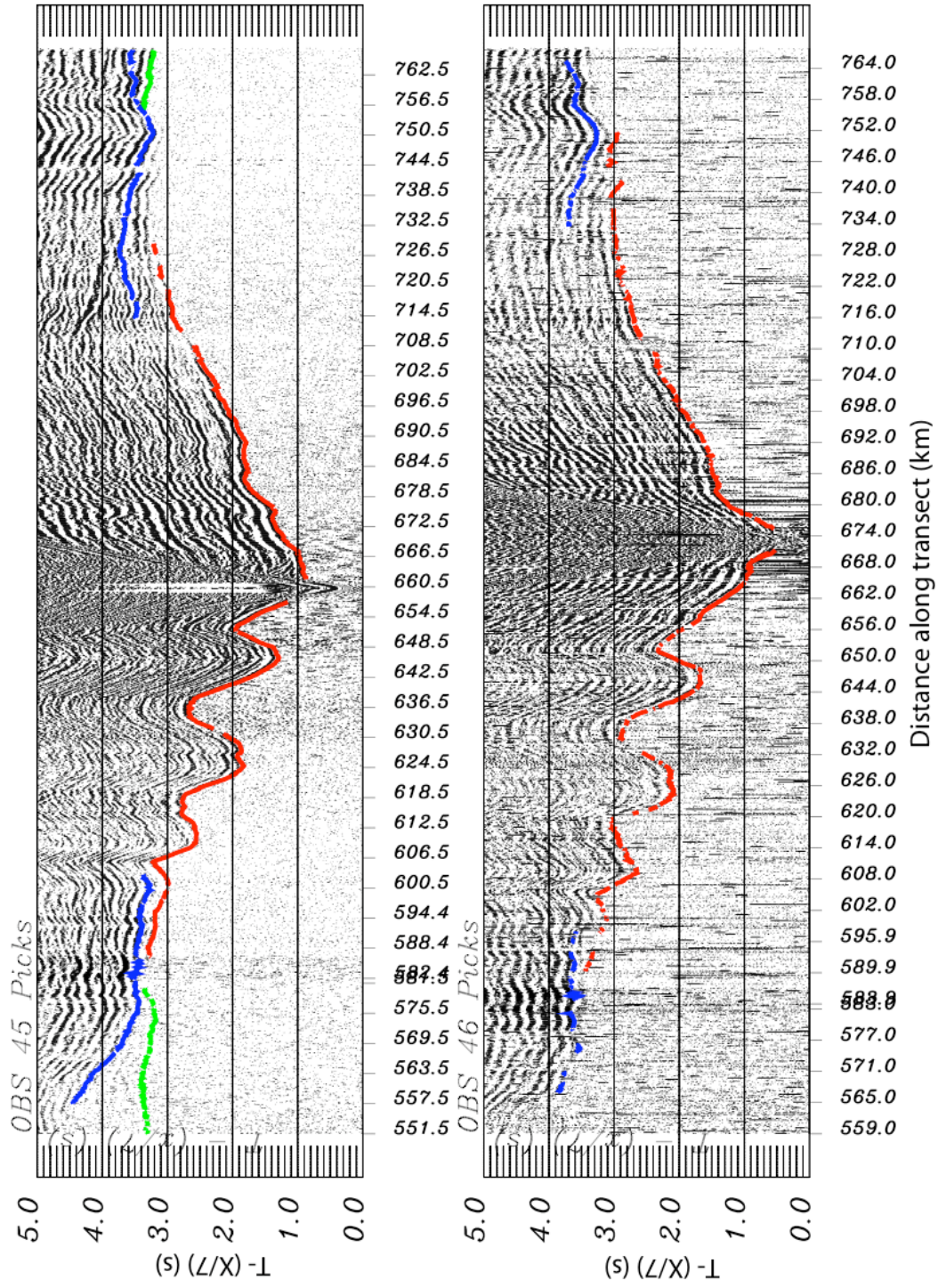

Figure B.25 OBS 45 and 46 plotted with a reduction velocity of 7 km/s

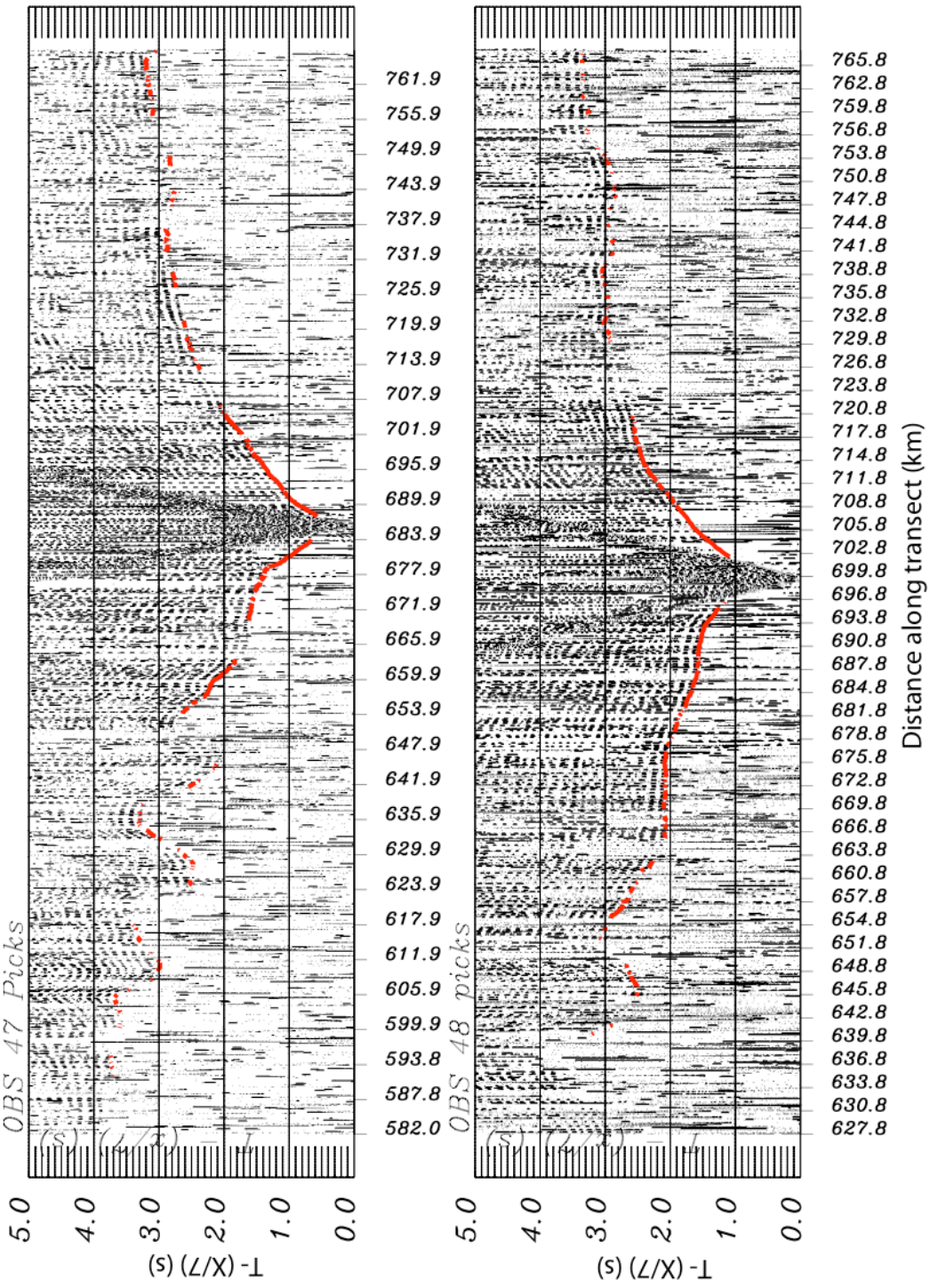

Figure B.26 OBS 47 and 48 plotted with a reduction velocity of 7 km/s

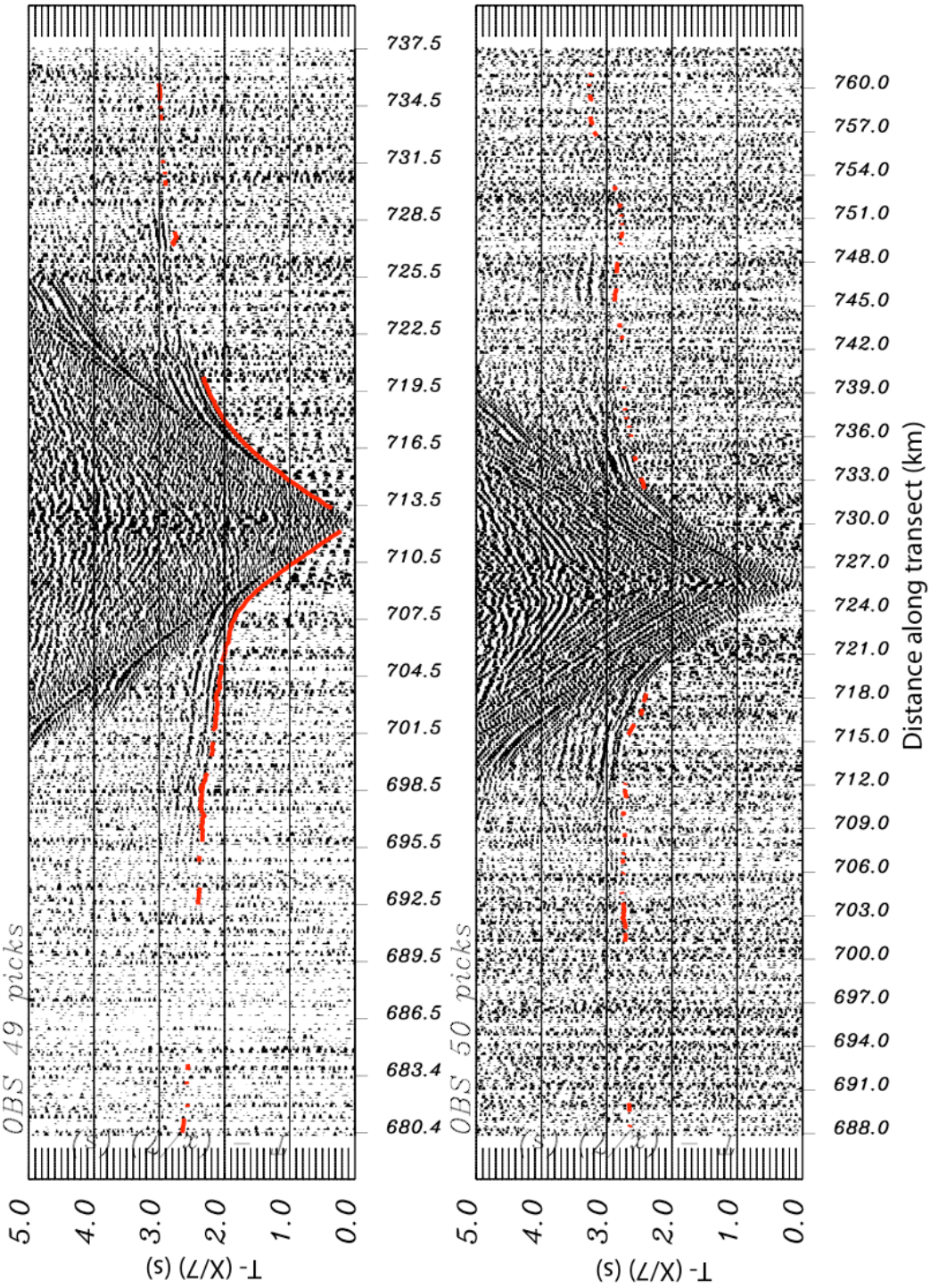

Figure B.27 OBS 49 and 50 plotted with a reduction velocity of 7 km/s

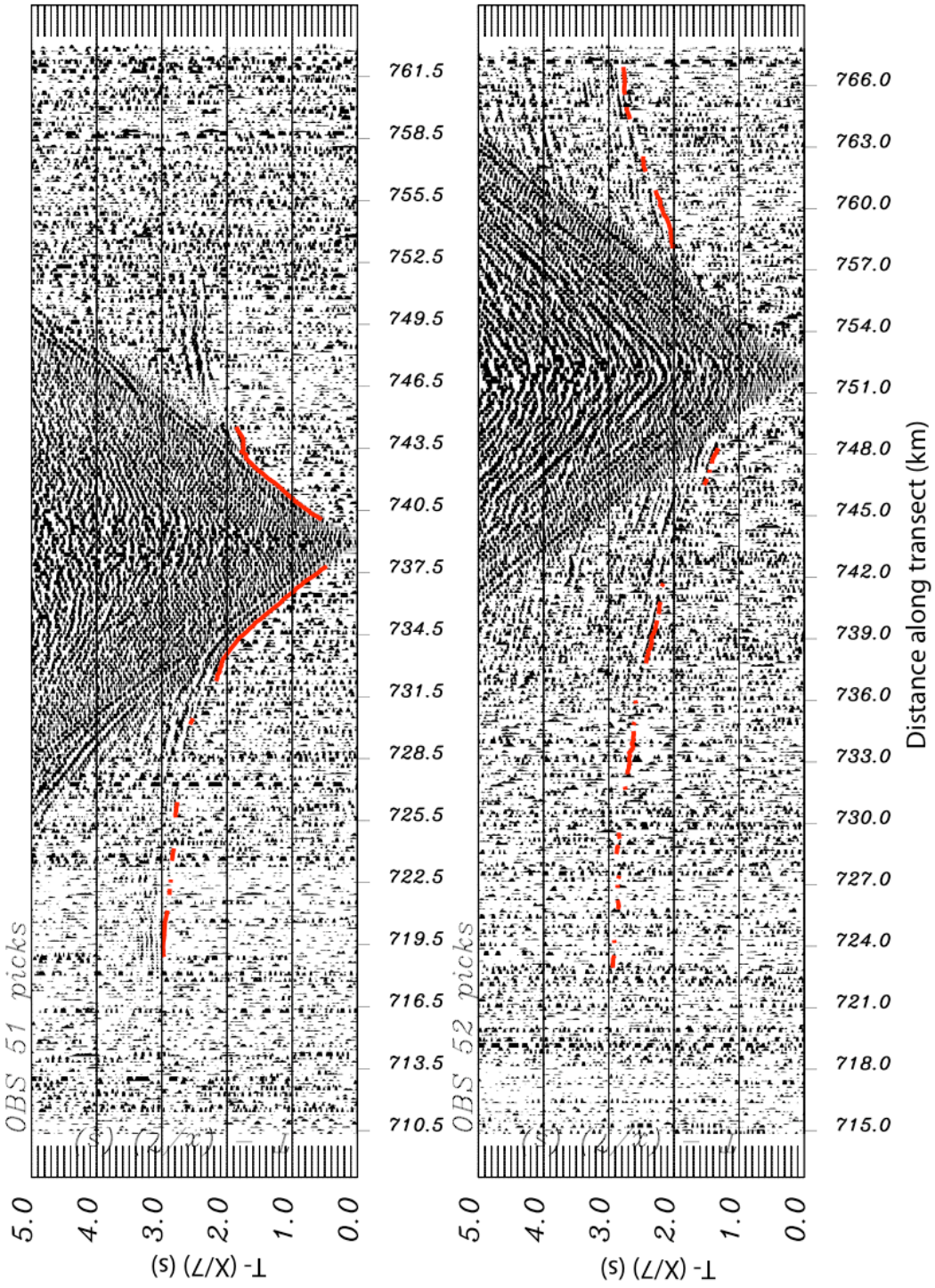

Figure B.28 OBS 51 and 52 plotted with a reduction velocity of 7 km/s

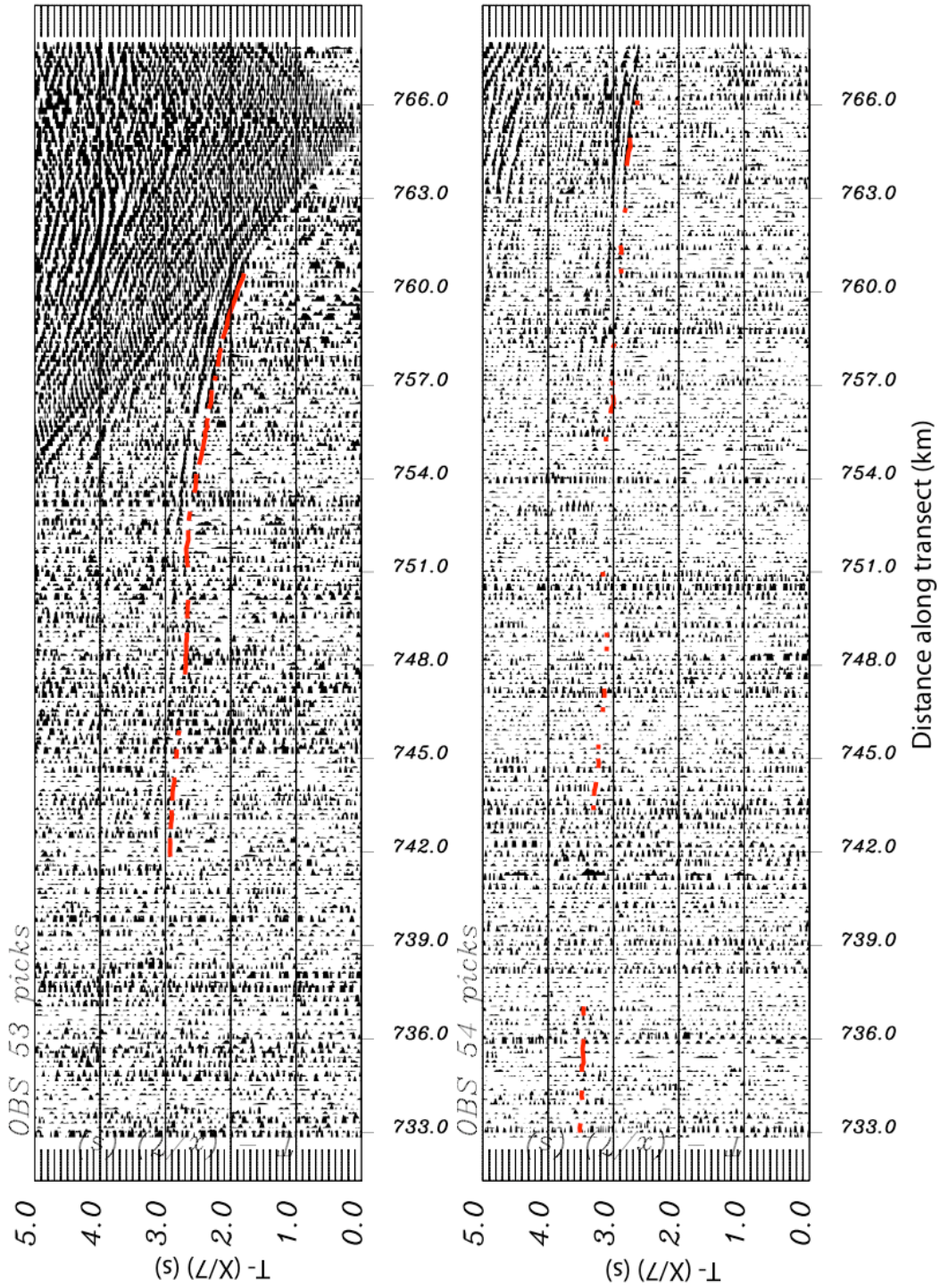

Figure B.29 OBS 53 and 54 plotted with a reduction velocity of 7 km/s

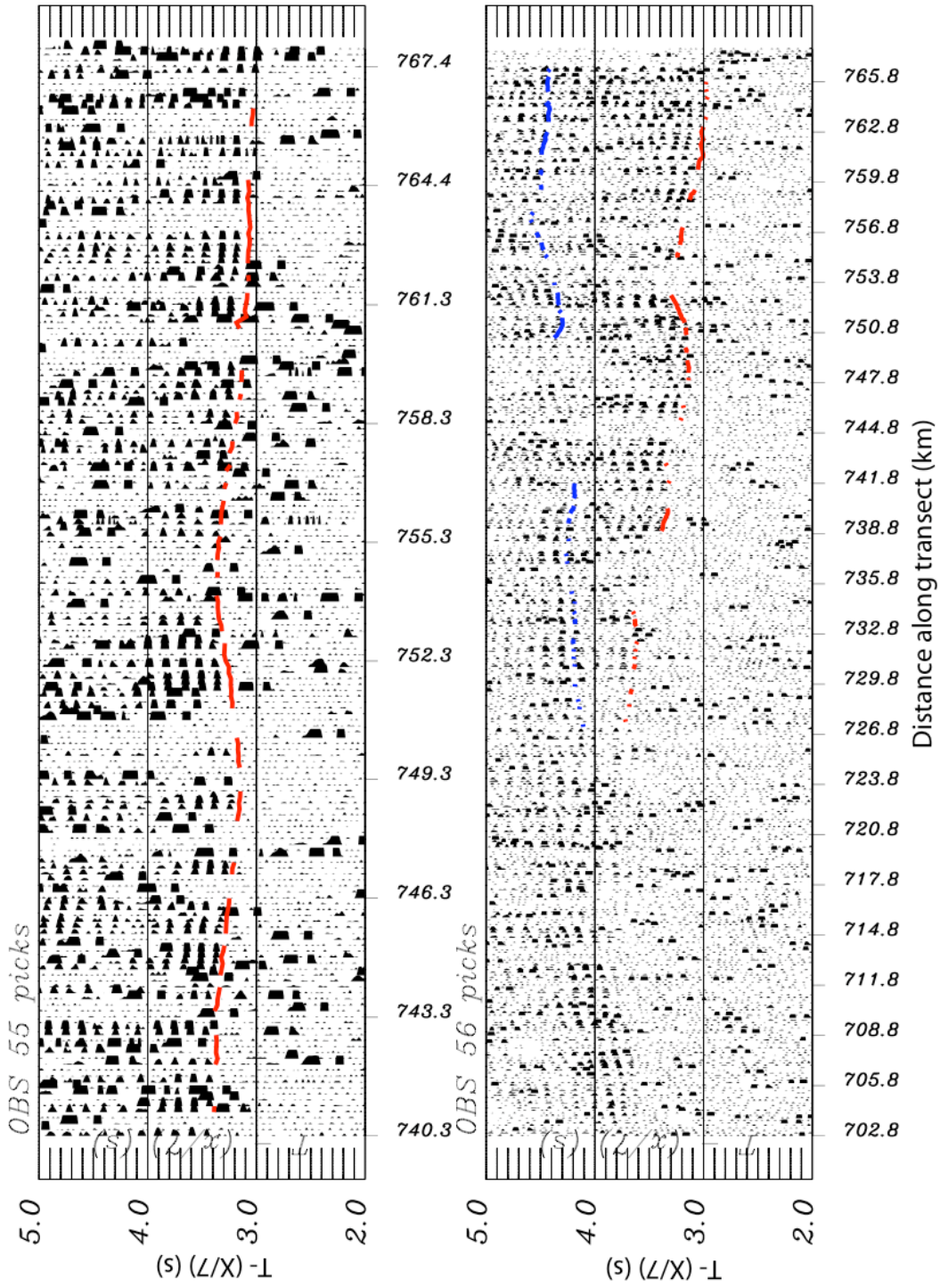

Figure B.30 OBS 55 and 56 plotted with a reduction velocity of 7 km/s

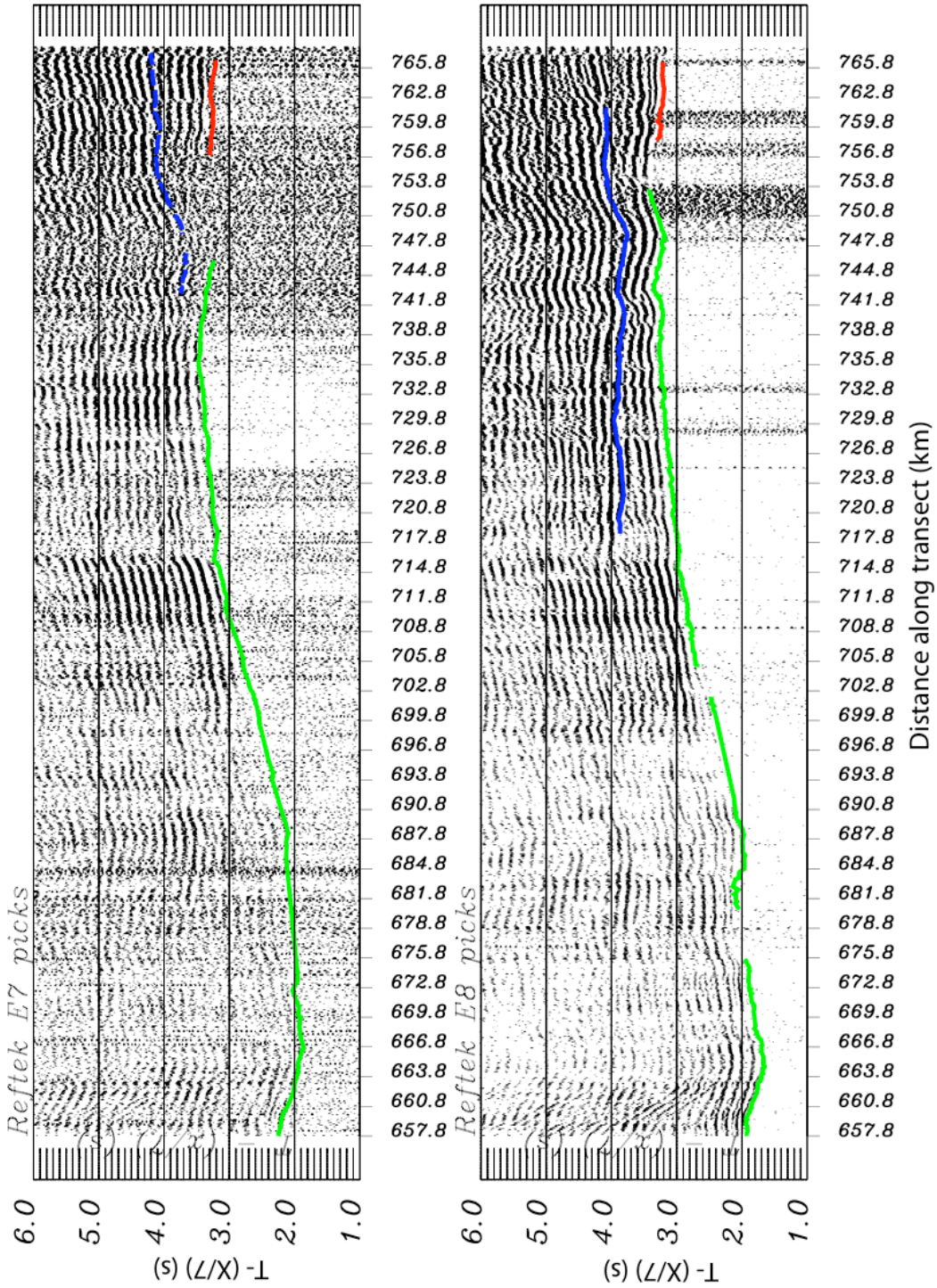

Figure B.31 PASSCAL seismographs E7 and E8 plotted with a reduction velocity of 7 km/s

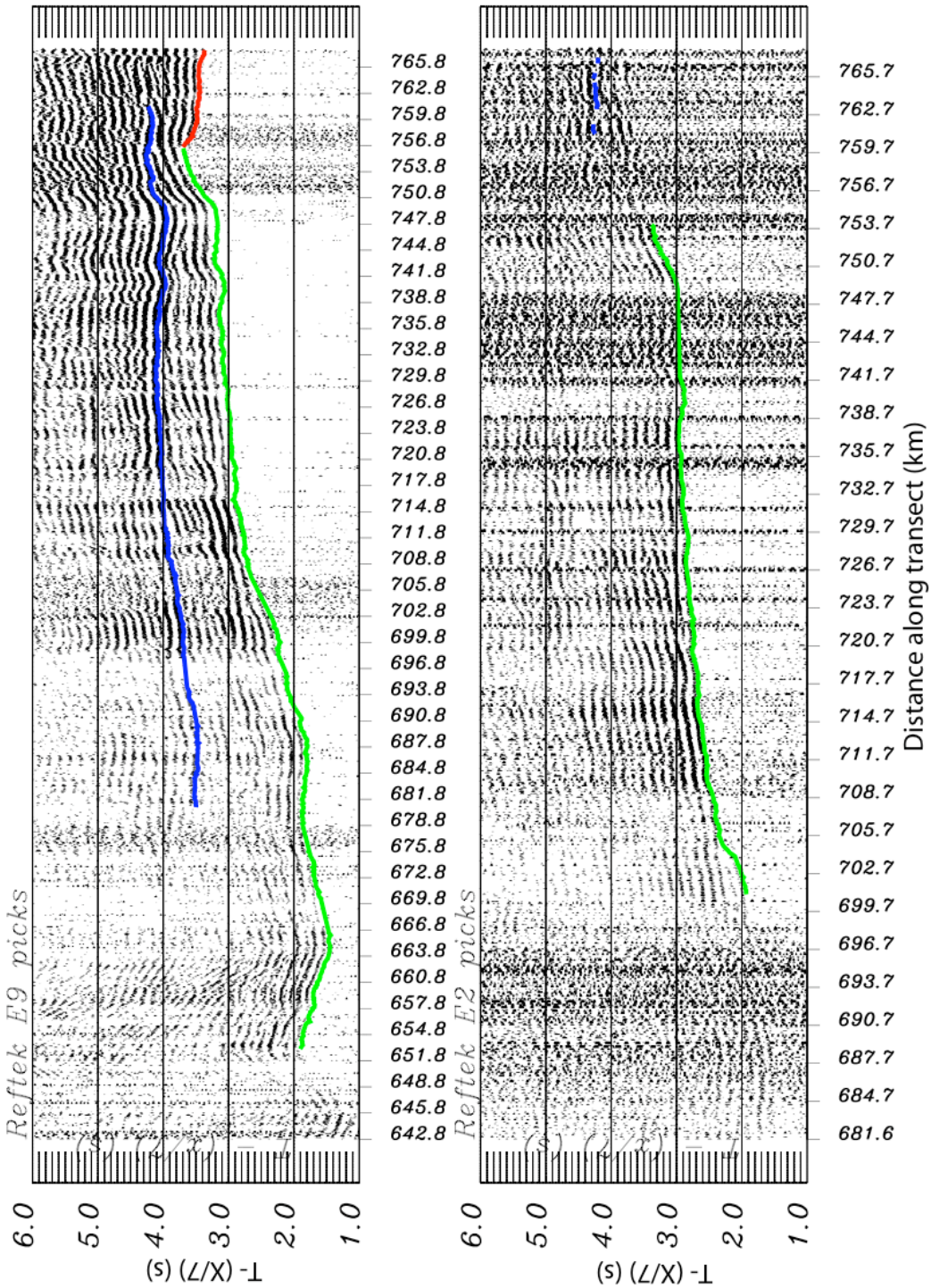

Figure B.32 PASSCAL seismographs E9 and E2 plotted with a reduction velocity of 7 km/s

References

Abers, G. A., Ferris, A., Craig, M., Davies, H., Lerner-Lam, A., Mutter, J., and Taylor, B., 2002: Mantle compensation of active metamorphic core complexes at Woodlark rift in Papua New Guinea. *Nature*, **418**(6900), 862–865.

Aragon-Arreola, M., and Martin-Barajas, A., 2005: Rift-to-drift transition in the northern Gulf of California. *GSA Annual Meeting Salt Lake City abstract*, (122-6).

Atwater, T., 1970: Implications of Plate Tectonics for the Cenozoic Tectonic Evolution of Western North America. *Geological Society of America Bulletin*, **81**, 3513–3536.

Atwater, T., and Stock, J., 1998: Pacific-North America Plate Tectonics of the Neogene Southwestern United States: An Update. *Int. Geol. Rev.*, **40**, 375–402.

Backus, D., Ledesma-Vázquez, J., Johnson, M., and Lopez-Perez, R., 2005: Geologic history of the Isla Coronados, Baja California Sur, Mexico. abstract with program, VII International Meeting on the Geology of the Baja California Peninsula. Ensenada, Baja California, Mexico. April 3-6 2005.

Benoit, M., Aguillon-Robles, A., Calmus, T., Maury, R., Bellon, H., Cotten, J., Bourgois, J., and Michaud, F., 2002: Geochemical Diversity of Late Miocene Volcanism in Southern Baja California, Mexico: Implication of Mantle and Crustal Sources during the Opening of an Asthenospheric Window. *Geology*, **110**, 627–648.

Bigioggero, B., Chiesa, S., Zanchi, A., Montrasio, A., and Vezzoli, L., 1995: The Cerro Mencenares volcanic center, Baja California Sur: Source and tectonic control on postsubduction magmatism within the Gulf Rift. *GSA Bulletin*, **107**(9), 1108–1122.

Blackman, D., Orcutt, J., and Forsyth, D., 1995: Teleseismic detection using ocean bottom seismometers at Mid-Ocean Ridges. *Bull. Seis. Soc. Am.*, **85**, 1648–1664.

Bohannon, C., R.G. Naeser, Schmidt, D., and Zimmermann, R., 1989: The timing of uplift, volcanism and rifting peripheral to the Red Sea: A case for passive rifting. *J. Geophys. Res.*, **94**(B2), 1683–1701.

Bonatti, E., 1985: Punctiform initiation of seafloor spreading in the Red Sea during transiton from a continental to an oceanic rift. *Nature*, **316**, 33–37.

Boness, N., and Zoback, M., 2004: Stress-induced seismic velocity anisotropy and physical properties in the SAFOD Pilot Hole in Parkfield, CA. *Geophys. Res. Lett.*, **31**, L15AS17. doi:10.1029/2003GL019020.

Bown, J., and White, R., 1995: Effect of finite extension rate on melt generation at rifted continental margins. *J. Geophys. Res.*, **100**(B9), 18,001–18,029.

Brun, J.-P., 1999: Narrow rifts versus wide rifts: inferences for the mechanics of rifting from laboratory experiments. *Phil. Trans. R. Soc. Lond. A*, **357**, 695–712.

Brun, J.-P., and Beslier, M., 1996: Mantle Exhumation at Passive Margins. *Earth Plan. Sci. Lett.*, **142**, 161–173.

Buck, W., 1991: Modes of Continental Lithospheric Extension. *J. Geophys. Res.*, **96**(B12), 20,161–20,178.

Buck, W., 2004: *Consequences of asthenospheric variability on continental rifting*, chapter Rheology and deformation of the lithosphere at continental margins, 1–30. Columbia University Press, New York, NY, United States (USA).

Butler, R., and Duennebier, F., 1989: Teleseismic Observations from OSS IV. *Initial Rep. Deep Sea Drill Proj.*, **88**, 147–153.

Cande, S., and Kent, D., 1995: Revised calibration of the geomagnetic polarity timescale for the Late Cretaceous and Cenozoic. *J. Geophys. Res.*, **100**, 6093–6096.

Castillo, P., Hawkins, J., Lonsdale, P., Hilton, D., Shaw, A., and Glascock, M., 2002: Petrology of Alarcon Rise lavas, Gulf of California: Nascent intracontinental ocean crust. *J. Geophys. Res.*, **107**(B10), 2222. doi:10.1029/2001JB000666.

Chand, S., and Subrahmanyam, C., 2003: Rifting between India and Madagascar-mechanism and isostasy. *Earth Planet Sci. Lett.*, (210), 317–332.

Chian, D., and Louden, K., 1994: The continent-ocean transition across the southwest Greenland margin. *J. Geophys. Res.*, **99**(B5), 9117–9135.

Christensen, N., and Mooney, W., 1995: Seismic velocity structure and composition of the continental crust: A global view. *J. Geophys. Res.*, **100**(B7), 9761–9788.

Clift, P., Lin, J., and Barckhausen, U., 2002: Evidence of low flexural rigidity and low viscosity lower continental crust during continental break-up in the South China Sea. *Marine and Petroleum Geology*, (19), 951–970.

Collins, J., Vernon, F., Orcutt, J., Stephen, R., Peal, K., Wooding, F., Speiss, F., and Hildebrand, J., 2001: Broadband Seismology in the Oceans: Lessons from the Ocean Seismic Network Pilot Experiment. *Geophys. Res. Lett.*, **28**, 49–52.

DeMets, C., and Dixon, T., 1999: New kinematic models for Pacific-North America motion from 3 Ma to present, I: Evidence for steady motion and biases in the NUVEL-1A model. *Geophys. Res. Lett.*, **26**(13), 1921–1924.

Dickinson, W., and Snyder, W., 1978: Plate Tectonics of the Laramide Orogeny. *Geol. Soc. Am. Mem.*, (151), 355–366.

Dorsey, R., and Kidwell, S., 1999: Mixed carbonate-siliciclastic sedimentation on a tectonically active margin: Example from the Pliocene of Baja California Sur, Mexico. *Geology*, **27**(10), 934–938.

Dorsey, R., Umhoefer, P., Ingle, J., and Mayer, L., 2001: Late Miocene to Pliocene stratigraphic evolution of northest Carmen Island, Gulf of California: implications for oblique-rifting tectonic. *Sedimentary Geology*, (144), 97–123.

Driscoll, N., and Karner, G., 1998: Lower crustal extension across the Northern Carnarvon basin, Australia: Evidence for an eastward dipping detachment. *J. Geophys. Res.*, **103**(B3), 4975–4991.

Ebinger, C. J., 1989: Tectonic development of the western branch of the East African rift system. *Geological Society of America Bulletin*, **101**, 885–903.

Ferrari, L., Lopez-Martinez, M., and Rosas-Elguera, J., 2002: Ignimbrite flare-up and deformation in the southern Sierra Madre Occidental, western Mexico: Implications for the late subduction history of the Farallon plate. *Tectonics*, **21**(4), 1035. doi:10.1029/2001TC001302.

Ferrari, L., and Rosas-Elguera, J., 1999: Late Miocene to Quaternary extension at the northern boundary of the Jalisco block, western Mexico: The Tepic-Zacoalco rift revised. *in Delgado-Granados, H., Aguirre-Diaz, G., and Stock, J.M., eds, Cenozoic Tectonics and Volcanism of Mexico: Geol. Soc. Am. Special Paper 334.*

Fletcher, J., Grove, M., Kimbrough, D., and Lovera, O., 2006: Neogene Tectonic Evolution of the Magdalena shelf and southern Gulf of California: Insights from detrital Zircon U-Pb ages from the Magdalena fan and adjacent areas. *GSA Bulletin*, **in press**.

Fletcher, J., Kohn, B., Foster, D., and Gleadow, A., 2000: Heterogeneous Neogene cooling and exhumation of the Los Cabos block, southern Baja California: Evidence from fission-track thermochronology. *Geology*, **283**(2), 107–110.

Fournier, M., Bellahsen, N., Fabbri, O., and Gunnell, Y., 2004: Oblique rifting and segmentation of the NE Gulf of Aden passive margin. *Geochem., Geophys., Geosys.*, **5**(11), Q11005. doi:10.1029/2004GC000731.

Funck, T., Hopper, J., Larsen, H., Louden, K., Tucholke, B., and Holbrook, W., 2003: Crustal structure of the ocean-continent transition at Flemish Cap: Seismic refraction results. *J. Geophys. Res.*, (B11), 2531. doi:10.1029/2003JB002434.

Gans, P., 1997: Large-magnitude Oligo-Miocene extension in southern Sonora: Implications for the tectonic evolution of northwest Mexico. *Tectonics*, **16**(3), 388–408.

Gastil, G., Krummenacher, D., and Minch, J., 1979: The record of Cenzoic volcanism around the Gulf of California. *Geological Society of America Bulletin*, **90**(9), 1839–1857.

Gastil, G., Morgan, G., and Krummanacher, D., 1978: Mesozoic history of the Peninsular California and related areas east of the Gulf of California. *in Howell, D.G. and McDougall, K.A. (eds), Mesozoic paleogeography of the western United States: Soc. of Econ. Paleon. and Mineral., Pacific Coast Paleogeography Symposium 2*, 107–115.

Gonzalez-Fernandez, A., Danobeitia, J., Delgado-Argote, L., Michaud, F., Cordoba, D., and Bartolome, R., 2005: Mode of extension and rifting history of the upper Tiburon and upper Delfin basins, northern Gulf of California. *J. Geophys. Res.*, **110**, B01313. doi:10.1029/2003JB002941.

Grove, M., Kimbrough, D., Perez-Venzor, J., Fletcher, J., and Kohn, B., 2005: Basement evolution of Isla Cerralvo. abstract with program, VII International Meeting on the Geology of the Baja California Peninsula. Ensenada.

Hausback, B., 1984: Cenozoic Volcanic and Tectonic Evolution of Baja California Sur, Mexico. *Geology of the Baja California Peninsula: Pacific Section S.E.P.M.*, **39**, 219–236.

Henstock, T., and Minshull, T., 2004: Localized rifting at Chagos Bank in the India-Capricorn plate boundary zone. *Geology*, (357), 237–240.

Holbrook, W., and Kelemen, P., 1993: Large igneous province on the US Atlantic margin and implicatons for magmatism during continental breakup. *Nature*, **364**, 433–436.

Holbrook, W., Larsen, H., Korenaga, J., Dahl-Jensen, T., Reid, I., Kelemen, P., Hopper, J., Kent, G., Lizarralde, D., Bernstein, S., and Detrick, R., 2001: Mantle thermal structure and active upwelling during continental breakup in the North Atlantic. *Earth Planet Sci. Lett.*, (190), 251–266.

Holbrook, W., Reiter, E., Purdy, G., Sawyer, D., Stoffa, P., Jr, J. A., Oh, J., and Makris, J., 1994: Deep structure of the U.S. Atlantic continental margin, offshore South Caolina, from conincident ocean bottom and multichannel seismic data. *J. Geophys. Res.*, **99**(B5), 9155–9178.

Huismans, R., and Beaumont, C., 2002: Asymmetric lithospheric extension: The role of frictional plastic strain softening inferred from numerical experiments. *Geology*, (3), 211–214.

Huismans, R., and Beaumont, C., 2003: Symmetric and assymetric lithospheric extension: Relative effects of frictional-plastic and viscous strain softening. *J. Geophys. Res.*, **108**(108), 2496. doi:10.1029/2002JB002026.

Hussenoeder, S., Detrick, R., Kent, G., Schouten, H., and Harding, A., 2002: Fine-scale seismic structure of young upper crust at 17 20S on the fast spreading East Pacific Rise. *J. Geophys. Res.*, **107**(B8), 2158. doi:10.1029/2001JB001688.

Johnson, M., Backus, D., Eros, J., and Lopez-Perez, R., 2005: Pliocene to recent carbonate deposits, Islas Carmen and Monserrat, Gulf of California. abstract with program, VII International Meeting on the Geology of the Baja California Peninsula. Ensenada.

Kelemen, P., and Holbrook, W., 1995: Origin od thick, high-velocity igneous crust along the U.S. East Coast Margin. *J. Geophys. Res.*, **100**(B7), 10,077–10,094.

Kendall, J.-M., Stuart, G., Ebinger, C., Barstow, I., and Keir, D., 2005: Magma-assisted rifting in Ethiopia. *Nature*, **433**, 146–148.

Klimes, L., and Kvasnicka, M., 1994: 3-D network ray-tracing. *Geophys. J. Int.*, **116**, 726–738.

Korenaga, J., Holbrook, W., Kent, G., Kelemen, P., Detrick, R., Larsen, H.-C., Hopper, J., and Dahl-Jensen, T., 2000: Crustal structure of the southeast Greenland margin from joint refraction and reflection seismic tomography. *J. Geophys. Res.*, **105**(B9), 21,591–21,614.

Larson, R., 1972: Bathymetry, Magnetic Anomalies, and Plate Tectonic History of the Mouth of the Gulf of California. *GSA Bulletin*, **83**, 3345–3360.

Lizarralde, D., Axen, G., Fletcher, J., Gonzalez-Fernandez, A., Harding, A., Holbrook, W., Kent, G., Umhoefer, P., Brown, H., Paramo, P., and Sutherland, F.,

2005: Gulf of California Rift Structure and Magmatism: Guaymas Basin and Comparison With Southern Basins. *AGU Fall Meeting Abstracts*, **T51E-01**.

Lizarralde, D., and Holbrook, W., 1997: Structure and early thermal evolution of the U.S. Mid Atlantic margin. *J. Geophys. Res.*, **102**, 22,855–22,875.

Lonsdale, P., 1989: Geology and Tectonic history of the Gulf of California. *in Winterer E.L., Hussong, D.M. and Decker, R.W., eds., The Eastern Pacific Ocean and Hawaii: Boulder, Colorado, Geological Society of America, the Geology of North America, v. N.*

Lonsdale, P., 1995: Segmentation and Disruption of the East Pacific Rise in the Mouth of the Gulf of California. *Marine Geophysical Researches*, (17), 323–359.

Mackenzie, G., Thybo, H., and Maguire, P., 2005: Crustal velocity structure across the Main Ethiopian Rift: results from two-dimensional wide-angle seismic modelling. *Geophys. J. Int.*, **162**(3), 994–1006.

Manatschal, G., and Bernoulli, D., 1999: Architecture and tectonic evolution of nonvolcanic margins: Present-day Galicia and ancient Adria. *Tectonics*, **18**(6), 1099–1119.

McClay, K., and White, M., 1995: Analogue modelling of orthogonal and oblique rifting. *Marine and Petroleum Geology*, **12**(2), 137–151.

McCloy, C., Ingle, J. C., and Barron, J. A., 1988: Neogene Stratigraphy, Foraminifera, Diatoms, and Depositional History of Maria Madre Island, Mexico: Evidence of Early Neogene Marine Conditions in the Southern Gulf of California. *Marine Micropaleontology*, **13**(3), 193–212.

McDougall, K., 2006: Marine Incursions: Implications for crustal thinning and regional strain. *Margins RCL-Cortez Workshop.*

McKenzie, D., 1978: Some Remarks on the Development of Sedimentary Basins. *Earth Planet Sci. Lett.*, (40), 25–32.

McKenzie, D., and Bickle, M., 1988: The Volume and Composition of Melt Generated by Extension of the Lithosphere. *Journal of Petrology*, (Part 3), 625–679.

McKenzie, D., Davies, D., and Molnar, P., 1970: Plate Tectonics of the Red Sea and East Africa. *Nature*, **226**, 243–248.

Menzies, M., Klemperer, S., Ebinger, C., and Baker, J., 2002: Characteristics of Volcanic Rifted Margins. *in Volcanic Rifted Margins, Spec. Paper Geol. Soc. Am.,*, (362), 1–14.

Montagner, J.-P., Karczewski, J.-F., Romanowicz, B., Bouaricha, S., Lognonne, P., Roult, G., Stutzmann, E., Thirot, J.-L., Brion, J., Dole, B., Fouassier, D., Koenig, J.-C., Savary, J., Floury, L., Dupond, J., Echardour, A., and Floc'h, H., 1994: The French Pilot Experiment OFM-SISMOBS: First scientific results on noise level and event detection. *Phys. Earth Planet Inter*, **84**, 321–336.

Moore, J., and Davidson, A., 1978: Rift structure in southern Ethiopia. *Tectonophysics*, **46**, 159–173.

Morgan, J., Barton, P., and White, R., 1989: The Hatton Bank continental margin-III. Structure from wide-angle OBS and multichannel seismic refraction profiles. *Geophys. J. Int.*, **98**(2), 367–384.

Mutter, J., and Larson, R., 1989: Extension of the Exmouth Plateau, offshore northwestern Australia: Deep seismic reflection/refraction evidence for simple and pure shear mechanisms. *Geology*, **17**, 15–18.

Mutter, J., Talwani, M., and Stoffa, P., 1982: Origin of seaward-dipping reflectors in oceanic crust off the Norwegian margin by "subaerial sea-floor spreading". *Geology*, **10**, 353–357.

Nagy, E., and Stock, J., 2000: Structural controls on the continent-ocean transition in the northern Gulf of California. *J. Geophys. Res.*, **105**(B7), 16,251–16,269.

Nava-Sanchez, E., Gorsline, D., and Molina-Cruz, A., 2001: The Baja California peninsula borderland: structural and sedimentological characteristic. *Sedimentary Geology*, **144**, 63–82.

Nielsen, T., Larsen, H.-C., and Hopper, J., 2002: Contrasting rifted margin styles south of Greenland: implications for mantle plume dynamics. *Earth Planet Sci. Lett.*, (200), 271–286.

Nieto-Samaniego, A., Ferrari, L., Alazniz-Alvarez, S., Labarthe-Hernandez, G., and Rosas-Elguera, J., 1999: Variation of Cenozoic extension and volcanism across the southern Sierra Madre Occidental volcanic province, Mexico. *GSA Bulletin*, **111**(3), 347–363.

Orcutt, J., and Jordan, T., 1986: MSS and OBS Data from the Ngendi experiment in the southwest Pacific. *in The Vela Program, edited by A. Kerr Def. Adv. Res. Proj. Agency, Washington, D.C.*, 758–770.

Ortlieb, L., 1991: Quaternary vertical movements along the coasts of Baja California and Sonora. In *The Gulf and Peninsular Province of the Californias*, editors J. P. Dauphin, and B. R. T. Simoneit, volume 47 of *AAPG Memoir*, 447–480. The American Association of Petroleum Geologists, Tulsa, Oklahoma.

Oskin, M., and Stock, J., 2003a: Marine incursion synchronous with plate-boundary localization in the Gulf of California. *Geology*, **31**(1), 23–26.

Oskin, M., and Stock, J., 2003b: Pacific–North America plate motion and opening of the Upper Delfin basin, northern Gulf of California, Mexico. *GSA Bulletin*, **115**(10), 1173–1190.

Paramo, P., Holbrook, W., Brown, H., Lizarralde, D., Fletcher, J., Umhoefer, P., Kent, G., Harding, A., Gonzalez-Fernandez, A., and Axen, G., 2006: Seismic structure in the direction of proto-gulf extension in the Southern Gulf of California. *J. Geophys. Res.*, **in preparation**.

Pedersen, T., and Ro, H., 1992: Finite duration of extension and decompression melting. *Earth Plan. Sci. Lett.*, **113**, 15–22.

Pepe, F., Bertotti, G., Cella, F., and Marsella, E., 2000: Rifted margin formation in the south Tyrrhenian Sea: A high-resolution seismic profile across the north Sicily passive continental margin. *Tectonics*, **19**(2), 241–257.

Perez-Gussinye, M., Ranero, C., Reston, T., and Sawyer, D., 2003: Mechanisms of extension at nonvolcanic margins: Evidence from the Galicia interior basin, west of Iberia. *J. Geophys. Res.*, **108**(B5), 2245. doi:10.1029/2001JB000901.

Persaud, P., Stock, J., Steckler, M., Martin-Barajas, A., Diebold, J., Gonzalez-Fernandez, A., and Mountain, G., 2003: Active deformation and shallow structure of the Wagner, Consag, and Delfin Basins, northern Gulf of California, Mexico. *J. Geophys. Res.*, **108**(B7), 2355. doi:10.1029/2002JB001937.

Persuad, P., Perez-Campos, X., and Clayton, R., 2005: Crustal Thickness Variations in the Margins of the Gulf of California from Receiver Functions. *Geophys. J. Int.*, **submitted**.

Phillips, R., 1964: Seismic refraction studies in the Gulf of California. *in van Andel, T.H. and Shor, G.G., eds., Marine Geology of the Gulf of California AAPG Memoir 3*, 90–121.

Portugal, E., Birkle, P., Barragan, R., Arellano G., V., Tello, E., and Tello, M., 2000: Hydrochemical-isotopic and hydrogeological conceptual model of the Las Tres Virgenes geothermal field, Baja California Sur, Mexico. *J. Volcanol. Geotherm. Res.*, **101**(3-4), 223–244.

Rusnak, G., Fisher, R., and Shepard, F., 1964: Bathymetry and faults of the Gulf of California. *in van Andel, T.H. and Shor, G.G., eds., Marine Geology of the Gulf of California*, 59–75.

Schwennicke, T., Ruiz-Geraldo, G., Umhoefer, P., and Ingle, J., 2005: Evolution of terrestrial and marine depositional environments in the transtensional Pliocene Punta Colorada Basin, Isla San Jose, Gulf of California. abstract with program, VII International Meeting on the Geology of the Baja California Peninsula. Ensenada.

Smith, W., and Sandwell, D., 1997: Global seafloor topography from satellite altimetry and ship depth soundings. *Science*, **277**, 1957–1962.

Spadini, G., Cloetingh, S., and Bertotti, G., 1995: Thermo-mechanical modeling of the Tyrrhenian Sea: Lithospheric necking and kinematics of rifting. *Tectonics*, **14**(3), 629–644.

Spencer, J., and Normark, W., 1979: Tosco-Abreojos fault zone: A Neogene transform plate boundary within the Pacific margin of southern Baja California, Mexico. *Geology*, **7**, 554–557.

Stephen, R., Speiss, F., Collins, J., Hildebrand, J., Orcutt, J., Peal, K., Vernon, F., and Wooding, F., 2003: Ocean Seismic Network Pilot Experiment. *Geochem. Geophys. Geosyst*, **4**(10), 1092. doi:10.1029/2002GC000485.

Stock, J., and Hodges, K., 1989: Pre-Pliocene Extension around the Gulf of California and the Transfer of Baja California to the Pacific Plate. *Tectonics*, **8**(1), 99–115.

Sutherland, F., Vernon, F., Orcutt, J., Collins, J., and Stephen, R., 2004: Results from OSNPE: Improved Teleseismic Earthquake Detection at the Seafloor. *Bull. Seis. Soc. Am.*, **94**(5), 1868–1878.

Taylor, B., Goodliffe, A., and Martinez, F., 1999: How continents break up: Insights from Papua New Guinea. *J. Geophys. Res.*, **104**(B4), 7497–7512.

Taylor, B., Goodliffe, A., Martinez, F., and Hey, R., 1995: Continental rifting and inital seafloor spreading in the Woodlark basin. *Nature*, **374**, 534–537.

Umhoefer, P., Dorsey, R., Willsey, S., Mayer, L., and Renne, P., 2001: Stratigraphy and geochronology of the Comondu Group near Loreto, Baja California sur, Mexico. *Sedimentary Geology*, (144), 125–147.

Unruh, J., Humphrey, J., and Barron, A., 2003: Transtensional model for the Sierra Nevada frontal fault system, eastern California. *Geology*, **31**(4), 327–300.

van Andel, T., and Shor, G., editors, 1964: *Marine Geology of the Gulf of California*. AAPG Memoir 3.

Van Avendonk, H., Harding, A., Orcutt, J., and Holbrook, W., 2001a: Hybrid shortest path and ray bending method for traveltime and raypath calculations. *Geophysics*, **66**(2), 648–653.

Van Avendonk, H., Harding, A., Orcutt, J., and McClain, J., 2001b: Contrast in crustal structure across the Clipperton transform fault from travel time tomography. *J. Geophys. Res.*, **106**(B6), 10,961–10,981.

Van Avendonk, H., Holbrook, W., Okaya, D., Austin, J., Davey, F., and Stern, T., 2004: Continental crust under compression: A seismic refraction study of South Island Geophysical Transect I, South Island, New Zealand. *J. Geophys. Res.*, **109**, B06302. doi:10.1029/2003JB002790.

Walsh, J., Waterrson, J., and Yielding, G., 1991: The importance of small-scale faulting in regional extension. *Nature*, **351**, 391–393.

Webb, S., 1998: Broadband Seismology and Noise Under the Ocean. *Rev. Geophysics*, **36**, 105–142.

Wernicke, B., 1984: Uniform-sense normal simple shear of the continental lithosphere. *Can. J. Earth Sci.*, **22**, 108–125.

Westaway, R., 1994: Re-evaluation of extension across the Pearl River Mouth Basin, South China Sea: implications for continental lithosphere deformation mechanisms. *J. Struct. Geol*, **16**(6), 823–838.

White, R., Spence, G., Fowler, S., McKenzie, D., Westbrook, G., and Bowen, A., 1987: Magmatism at rifted continental margins. *Nature*, **330**, 439–444.

Whitmarsh, R., White, R., Horsefield, S., Sibuet, J.-C., Recq, M., and Louvel, V., 1996: The ocean-continent boundary off the western continental margin of Iberia: Crustal structure west of Galicia Bank. *J. Geophys. Res.*, **101**(B12), 28,291–28,314.

Wilcock, W., Webb, S., and Bjarnason, I., 1999: The Effect of Local Wind on Seismic Noise near 1Hz at the MELT site and in Iceland. *Bull. Seis. Soc. Am.*, **89**(6), 1543–1557.

Wilson, J., 1966: Did the Atlantic close and then re-open? *Nature*, **211**, 676–681.

Wolfe, C., Yang, S., Solomon, S., and Silver, P., 1998: Initial Results from the PELENET Experiment along the Hawaiian Islands; body-wave delay times and P-to-S conversions at the 410- and 660-km discontinuities. *Eos, Transactions, AGU*, **79**(17), 208.

Yeats, R., and Haq, B., 1981: Deep-Sea Drilling off the Californias: Implications of Leg 63. *Init. Repts. DSDP*, **63**, 949–961.

Zelt, C., and Smith, R., 1992: Seismic traveltime inversion for 2-D crustal velocity structure. *Geophys. J. Int.*, (108), 16–34.